Department of Electronics and Nanoengineering

Amorphous molybdenum-based thin films for surface micromachining

Mari Laamanen

Aalto University

DOCTORAL DISSERTATIONS

Aalto University publication series
DOCTORAL DISSERTATIONS 23/2017
VTT SCIENCE 147

Amorphous molybdenum-based thin films for surface micromachining

Mari Laamanen

A doctoral dissertation completed for the degree of Doctor of Science (Technology) to be defended, with the permission of the Aalto University School of Electrical Engineering, at a public examination held at the lecture hall T2 (Computer Science Building, Konemiehentie 2, Espoo) on 10th March 2017 at 12:15.

Aalto University
School of Electrical Engineering
Department of Electronics and Nanoengineering

Supervising professors
Associate professor Hele Savin
Micro and Nanoelectronics
School of Electrical Engineering
Aalto University, Finland

Preliminary examiners
Professor Krisztián Kordás
Micro- and nanoelectronic materials and components for ICT applications
Microelectronics Research Unit
University of Oulu, Finland

Dr. Claudia Wiemer
Laboratorio MDM, Unit of Agrate Brianza
CNR Institute for Microelectronics and Microsystems (IMM), Italy

Opponents
Assistant professor Kristinn B. Gylfason
Micro and Nanosystems
School of Electrical Engineering
KTH Royal Institute of Technology, Sweden

Aalto University publication series
DOCTORAL DISSERTATIONS 23/2017

VTT SCIENCE 147

© Mari Laamanen

ISBN 978-952-60-7289-0 (printed)
ISBN 978-952-60-7288-3 (pdf)
ISSN-L 1799-4934
ISSN 1799-4934 (printed)
ISSN 1799-4942 (pdf)
http://urn.fi/URN:ISBN:978-952-60-7288-3

ISBN 978-951-38-8512-0 (printed)
ISBN 978-951-38-8509-0 (pdf)
ISSN-L 2242-119X
ISSN 2242-119X (printed)
ISSN 2242-1203 (pdf)
http://urn.fi/URN:ISBN:978-951-38-8509-0

Unigrafia Oy
Helsinki 2017

Finland

A! Aalto University

Aalto University, P.O. Box 11000, FI-00076 Aalto www.aalto.fi

Abstract

Author
Mari Laamanen

Name of the doctoral dissertation
Amorphous molybdenum-based thin films for surface micromachining

Publisher School of Electrical Engineering

Unit Department of Electronics and Nanoengineering

Series Aalto University publication series DOCTORAL DISSERTATIONS 23/2017

Field of research Micro and Nanosciences

Manuscript submitted 5 September 2016 **Date of the defence** 10 March 2017

Permission to publish granted (date) 17 November 2016 **Language** English

☒ **Monograph** ☐ **Article dissertation** ☐ **Essay dissertation**

Abstract

Microelectromechanical systems (MEMS) are often based on silicon technology. This thesis studies two molybdenum-based thin films, amorphous Mo-N and Mo-Si-N deposited by reactive sputtering, for an alternative material choice for surface micromachining.

Bulk amorphous metals stand out from other engineering materials because of their high elasticity, which would be an interesting feature for the structural layer of MEMS devices. Since elemental metal films are practically always polycrystalline, molybdenum was amorphised first by nitrogen. The resulting Mo-N films were characterised for their deposition and etch rates, composition, resistivity and residual stress. Because the amorphisation was incomplete, silicon was added. The Mo-Si-N films were characterised for their deposition and etch rates, composition, resistivity, residual stress, microstructure, surface roughness, elastic modulus, hardness, elastic recovery, coefficient of thermal expansion, temperature coefficient of resistance and complex refractive index. It was found the resistivity of these amorphous Mo-Si-N films is 1...2 mΩcm, and their residual stress can be tuned to low tensile values (around 100 MPa) by the sputtering pressure.

The thermal stability of Mo-N and Mo-Si-N films was studied in particular. The first signs of oxidation were observed at 350°C, and structural changes even below. The unsealing surface oxidation can be prevented by a thin protective silicon cap on top of the films. The residual stress of the Mo-Si-N films sputtered from separate Mo and Si targets depends on the post-deposition annealing temperature, while the Mo-Si-N films sputtered from a Mo_5Si_3 compound target are more resistant to annealing-induced structural changes.

By the end of this study, surface micromachined MEMS devices with Mo-Si-N films as their structural layer were demonstrated. The capacitive RF MEMS devices operated at frequencies up to 110 GHz, and were fully functional after the actuation of 50 million cycles between the up- and down-states of their MEMS bridges. Mo-Si-N films were also applied to thin film absorbers designed for the visible and near-infrared wavelengths (350...2000 nm). The absorption was measured to be higher than 93 % over the whole spectrum of interest.

In conclusion, amorphous Mo-N and Mo-Si-N films are suitable for several kinds of MEMS devices on condition that they are not exposed to increased temperatures in an oxidising atmosphere without a protective silicon cap. Their integration with conventional MEMS processes is convenient, as they can be deposited by sputtering and patterned with common dry and wet etch chemistries. The demonstrated MEMS fabrication process was CMOS compatible. The low process temperature enables the use of a polymeric sacrificial layer and provides an opportunity for the monolithic integration of MEMS and CMOS.

Keywords Mo-N, Mo-Si-N, mictamict alloy, amorphous, thin film, sputtering, residual stress, thermal stability, MEMS

ISBN (printed) 978-952-60-7289-0 **ISBN (pdf)** 978-952-60-7288-3

ISSN-L 1799-4934 **ISSN (printed)** 1799-4934 **ISSN (pdf)** 1799-4942

Location of publisher Helsinki **Location of printing** Helsinki **Year** 2017

Pages 199 **urn** http://urn.fi/URN:ISBN:978-952-60-7288-3

Aalto-yliopisto

Aalto-yliopisto, PL 11000, 00076 Aalto www.aalto.fi

Tiivistelmä

Tekijä
Mari Laamanen

Väitöskirjan nimi
Amorfiset molybdeenipohjaiset ohutkalvot pintamikromekaniikassa

Julkaisija Sähkötekniikan korkeakoulu

Yksikkö Elektroniikan ja nanotekniikan laitos

Sarja Aalto University publication series DOCTORAL DISSERTATIONS 23/2017

Tutkimusala Mikro- ja nanotekniikka

Käsikirjoituksen pvm 05.09.2016 **Väitöspäivä** 10.03.2017

Julkaisuluvan myöntämispäivä 17.11.2016 **Kieli** Englanti

☒ **Monografia** ☐ **Artikkeliväitöskirja** ☐ **Esseeväitöskirja**

Tiivistelmä

Mikroelektromekaanisten MEMS-komponenttien valmistamiseen käytetään yleisesti piitä. Tässä väitöskirjassa tutkittiin kahden vaihtoehtoisen materiaalin soveltuvuutta pintamikromekaniikkaan: tutkittavina olivat reaktiivisella sputteroinnilla kasvatetut amorfiset, molybdeenipohjaiset Mo-N– ja Mo-Si-N–ohutkalvot.

Yhdestä alkuaineesta sputteroidut metalliohutkalvot ovat rakenteeltaan monikiteisiä. Työssä molybdeenikalvot seostettiin ensin typellä (Mo-N) ja sitten lisäksi piillä (Mo-Si-N). Kalvojen ominaisuuksia karakterisoitiin usein eri menetelmin. Niistä määritettiin kasvu- ja etsausnopeudet, kemiallinen koostumus, mikrorakenne, resistiivisyys lämpötilakertoimineen, jäännösjännitys, pinnankarheus, kimmokerroin, kovuus, lämpölaajenemiskerroin ja kompleksinen taitekerroin. Amorfisten Mo-Si-N–kalvojen resistiivisyydeksi mitattiin 1...2 mΩcm, ja niiden jäännösjännitys voitiin säätää matalaan vetojännitykseen (noin 100 MPa) sputterointipainetta muuttamalla.

Sekä Mo-N– että Mo-Si-N–kalvojen pintaan muodostui oksidikerros, jos kalvoja kuumennettiin yli 350°C lämpötilassa ilma ympäröivänä atmosfäärinä. Oksidoituminen oli estettävissä ohuella suojaavalla piikerroksella. Erillisistä Mo- ja Si-kohtioista kasvatettujen Mo-Si-N–kalvojen jäännösjännitys riippui kuumennuslämpötilasta. Sen sijaan Mo_5Si_3-yhdistekohtiosta kasvatettujen kalvojen jännitys säilyi kuumennettaessa miltei muuttumattomana.

Väitöstyössä kehitettiin pintamikromekaaninen MEMS-valmistusprosessi, joka hyödynsi Mo-Si-N–kalvoja komponenttien rakennekerroksena. Kapasitiiviset RF MEMS–komponentit oli suunniteltu toimimaan enimmillään 110 GHz taajuudelle saakka, ja ne säilyivät täysin toimintakykyisinä rasituskokeessa, jossa niiden MEMS-siltoja liikutettiin 50 miljoonaa kertaa ääriasentojensa välillä. Mo-Si-N–kalvoja käytettiin myös ohutkalvoabsorbaattoreissa, jotka toimivat näkyvän valon ja lähi-infrapunan aallonpituuksilla (350...2000 nm), ja joiden absorptio oli vähintään 93 % koko tällä alueella.

Työn johtopäätöksenä todettiin, että amorfisia Mo-N– ja Mo-Si-N–ohutkalvoja on mahdollista käyttää hyväksi useissa MEMS-komponenteissa ehdolla, että ne eivät valmistuksen tai käytön aikana altistu korkeille lämpötiloille hapettavissa olosuhteissa ilman suojakerrosta. Materiaalien käyttö perinteisten MEMS-valmistusprosessien yhteydessä on sujuvaa, koska ne kasvatetaan sputteroinnilla ja voidaan kuvioida yleisillä kuiva- ja märkäetsausmenetelmillä. Matala kasvatuslämpötila mahdollistaa polymeeripohjaisten uhrautuvien kerrosten käytön ja MEMS-komponenttien monoliittisen integroinnin mikropiirien päälle.

Avainsanat Mo-N, Mo-Si-N, mictamict-seos, amorfinen, ohutkalvo, sputterointi, jäännösjännitys, terminen stabiilisuus, MEMS

ISBN (painettu) 978-952-60-7289-0 **ISBN (pdf)** 978-952-60-7288-3

ISSN-L 1799-4934 **ISSN (painettu)** 1799-4934 **ISSN (pdf)** 1799-4942

Julkaisupaikka Helsinki **Painopaikka** Helsinki **Vuosi** 2017

Sivumäärä 199 **urn** http://urn.fi/URN:ISBN:978-952-60-7288-3

Preface

The experimental part of this work was carried out between 2002 and 2010 at VTT Technical Research Centre of Finland, on the premises of Micronova (Centre for Micro and Nanotechnology), progressing piece by piece besides several other research projects and activities. The manuscript was finally completed during the maternity leave with my third child in 2016, after this academic hobby had been already doomed to the X-files for several times in my mind. Since the topic turned out to be niche one, the findings had luckily not become outdated in the meanwhile, leaving the door still open for a dissertation. It was upon this reactivation when Prof. Hele Savin came in. I warmly thank her for her unconditioned support to this project as well as valuable insight she provided at the point the manuscript was being finalised. I also warmly thank Prof. Kristinn B. Gylfason for acting as the opponent in the public defence of this thesis, and Prof. Krisztián Kordás and Dr. Claudia Wiemer for their careful reviews and insightful comments as pre-examiners.

A major part of this work has been already published in [1-16] (note that the majority has been authored under my maiden name Ylönen). However, I decided to write this dissertation as a monograph for three reasons. First, I wanted to include rather extensive literature reviews of mictamict, Mo-N and Mo-Si-N films in this work because such reviews have not been published earlier from a MEMS perspective. Secondly, this monograph includes experimental results, particularly of the thermal stability of Mo-N and Mo-Si-N films, that have not been published in [1-16]. These results modified considerably my understanding of the applicability of these films, why they deserved to be added in. Thirdly, a monograph provided a means of clarifying the distribution of work between several research team members, and including in this dissertation for defence only the contribution of my own.

For a long time, I was frozen by an idea of *writing a dissertation*. The lock was opened only after I realised there is no need to *sell* anything, but just to give a plain and humble story of what was done and what was learnt. After saying the above, this thesis is my heritage to anybody who might consider using these materials in MEMS or relating fields, covering “all” that I know about this unconventional material choice. If this report facilitated anyone’s effort to assess different material options or practically use these films, my goals to write this would be fully satisfied.

There is a large number of present and former colleagues at VTT to thank for their contribution. Prof. Hannu Kattelus, Lic.Sc. Martti Blomberg, Dr. Jyrki Kiihamäki

and Dr. Anu Kärkkäinen have acted as the team leaders during my years at VTT. In particular, I acknowledge Hannu Kattelus for introducing the topic of amorphous Mo-N and Mo-Si-N films in 2002-2003, and Jyrki Kiihamäki for proof-reading the manuscript in 2016, ensuring the technical contents have no conflicts with proprietary information. I also acknowledge Martti Blomberg for all the general MEMS knowledge he has provided me during the years, such abundant in amount that it is impossible to trace everything back in detail. Dr. Tauno Vähä-Heikkilä, Dr. Jyrki Molarius, Dr. Tommi Riekkinen, Dr. James Dekker, Dr. Kai Kolari, Dr. Heini Saloniemi, Dr. Tomi Haatainen, Dr. Tuomas Pensala, Dr. Arto Nurmela, Dr. Kimmo Solehmainen, Mr. Sami Ylinen, Mr. Markku Kapulainen, Dr. Anna Rissanen, Dr. Riikka Puurunen, Mr. Antti Tolkki, Mr. Pekka Ikonen, Ms. Meeri Partanen, Ms. Kirsi Järvi, Ms. Riitta Lindman and Ms. Kristiina Rutanen are acknowledged for all their technical expertise and diligent work, as specified in more detail in Section 1.2. Outside VTT, Dr. Timo Sajavaara, Dr. Antti Niskanen, Mr. Pasi Kostamo, Mr. Tatu Muukkonen, Dr. Silja Holopainen, Dr. Alexander Savin and Ms. Fang Tuurnala are acknowledged for the same. Particularly, I want to thank Tauno Vähä-Heikkilä for the collaboration on RF MEMS in 2003-2007, which resulted in a number of publications, admiring the talent and the wide-ranging understanding of the field Tauno proved in his work. I want also specially thank Meeri Partanen for all those years she has processed my samples in the cleanroom, politely revising the stupid plans of the once young researcher, and skilfully carrying out dozens of experiments and MEMS processes we have worked through. In addition, all other present and former colleagues at VTT deserve thanks for the knowledge and information they have shared with me, to mention by name Dr. Panu Pekko, Dr. Jaakko Saarilahti and Mr. Gao Feng as long-time team colleagues.

Besides the above, I would like to thank Riikka, Panu, James, Anna, Sari and any featuring guest stars for the most cheerful conversations we used to have at the pea soup and pancake, Neste pizza and other lunches. Thank you for sharing your most interesting news and experiences, the latest updates of the official Stupidity Control DataBase (SCDB), contemplation of the way of the world and human nature, and various events of family life (from which I apparently did not fully learn the lesson), as well as for showing continued interest in List™ items and dedicating yourselves to the careful consideration of the philosophical questions I kept posing. Come what may, these are the best memories I carry with me from the years at VTT.

Writing a doctoral thesis during a maternity leave is not possible without the support of the family. Alexander: thank you for letting me take this preoccupation to the end regardless of the bustle at home. Mum and Dad: thank you for “spending quality time” repeatedly with your grandchildren, and still saying you enjoy it. Kiitos äiti ja isä. Our sweeties Eva (now aged 5), Otto (aged 3) and Ester (aged 1): you are a trio who definitely keep us remembering there is Life Outside Of Work.

Finally, Alexander, once again: thank you for everything. Up to now, right now, and in the future.

Espoo, 29th January 2017
Mari Laamanen

Contents

Preface vii

Contents ix

List of abbreviations xi

List of symbols xiv

1. Introduction 1

1.1 Background and objectives 1
1.2 Author's contribution 3

2. Technological background 5

2.1 Surface micromachining 5
2.1.1 Outline 5
2.1.2 Material selection 7
2.2 Thin films 9
2.2.1 Sputtering 9
2.2.2 Stresses in thin films 10
2.2.3 Measurement of residual stress 13
2.3 Amorphous metals 14
2.3.1 History and development 14
2.3.2 Structure and properties 17
2.3.3 Applications 18

3. Review of mictamict alloys 20

3.1 Introduction 20
3.2 Composition and structure 21
3.3 Thermal stability 22
3.4 Mechanical properties 25
3.5 Electrical properties 26
3.6 Process technology 28
3.7 Applications 29

4. Mo-N thin films 31

4.1 Introduction 31
4.2 Review 32
4.2.1 Process technology 32
4.2.2 Composition and structure 33
4.2.3 Thermal stability 34
4.2.4 Mechanical properties 35
4.2.5 Other properties 36
4.2.6 Applications 37

4.3 Experimental procedure ... 37
4.4 Properties of as-deposited films ... 42
4.5 Thermal stability ... 49
4.6 Conclusions ... 53

5. Mo-Si-N thin films ... 55

5.1 Introduction ... 55
5.2 Review ... 56
5.2.1 Process technology ... 56
5.2.2 Composition and structure ... 57
5.2.3 Thermal stability ... 57
5.2.4 Mechanical properties ... 61
5.2.5 Other properties ... 62
5.2.6 Applications ... 62
5.3 Experimental procedure ... 63
5.3.1 Analysis of as-deposited films ... 63
5.3.2 High and low temperature experiments ... 68
5.4 Properties of as-deposited films ... 71
5.5 Thermal stability ... 84
5.6 Low temperature behaviour ... 103
5.7 Conclusions ... 106

6. MEMS devices ... 110

6.1 Process technology ... 110
6.1.1 Patterning ... 110
6.1.2 MEMS structures ... 114
6.2 RF MEMS ... 119
6.2.1 Introduction ... 119
6.2.2 Fabrication ... 120
6.2.3 Performance ... 125
6.3 Thin film absorber for optical MEMS ... 133
6.3.1 Introduction ... 133
6.3.2 Experimental procedure ... 134
6.3.3 Results ... 135

7. Conclusions and outlook ... 137

References ... 142

List of abbreviations

AC	Alternating current
AES	Auger electron spectroscopy
AFM	Atomic force microscopy
AIP	Arc ion plating
ALD	Atomic layer deposition
BAW	Bulk acoustic wave
BGA	Bulk glassy alloy
BHF	Buffered HF
BioMEMS	Biomedical microelectromechanical systems
BMG	Bulk metallic glass
CMOS	Complementary metal-oxide-semiconductor
CMP	Chemical mechanical polishing
CMUT	Capacitive micromachined ultrasonic transducer
CP	Critical pressure
CPW	Coplanar waveguide
CVD	Chemical vapour deposition
DC	Direct current
DF	Dark field
DI	Deionised
DMD	Digital micromirror device
DMTL	Distributed MEMS tranmission line
DRPHS	Dense random packing of hard spheres
DSP	Double side polished
DTA	Differential thermal analysis
EBL	Electron beam lithography
EDX	Energy-dispersive X-ray spectroscopy
ER	Elastic recovery
FIB	Focused ion beam

f.c.c.	Face-centred cubic
GFA	Glass forming ability
HF	Hydrofluoric acid
HMDS	Hexamethyldisilazane
HVOF	High velocity oxygen fuel
IC	Integrated circuit
ICP	Inductively coupled plasma
IR	Infrared
LF	Light field
Ln	Lanthanide
LPCVD	Low-pressure chemical vapour deposition
LTM	Late transition metal
LTO	Low temperature oxide
MEMS	Microelectromechanical systems
MG	Metallic glass
MOEMS	Micro-optoelectromechanical systems
MOS	Metal-oxide-semiconductor
MRO	Medium-range order
NIL	Nanoimprint lithography
NIR	Near-infrared
PEB	Post-exposure bake
PECVD	Plasma-enhanced chemical vapour deposition
PMMA	Polymethyl methacrylate
PSG	Phosphorus doped silica glass
PVD	Physical vapour deposition
RBS	Rutherford backscattering spectrometry
RCA	Radio Corporation of America (a company after which a standard clean was named)
RF	Radio frequency
RFID	Radio frequency identification

RF MEMS	Radio frequency microelectromechanical systems
RIE	Reactive ion etching
RMS	Root mean square
RT	Room temperature
RTA	Rapid thermal annealing
R&D	Research and development
SC	Standard clean
SCLR	Supercooled liquid region
SEM	Scanning electron microscopy
SIMS	Secondary ion mass spectrometry
SM	System monitor
SRO	Short-range order
SSP	Single side polished
STP	Standard temperature and pressure
SWIR	Short-wavelength infrared
TCR	Temperature coefficient of resistance
TDEAT	Tetrakis(diethylamido) titanium
TEM	Transmission electron microscopy
TFMG	Thin film metallic glass
TG	Thermogravimetry
TM	Early transition metal
TPF	Thermoplastic forming
UV	Ultraviolet
VTT	Technical Research Centre of Finland
XPS	X-ray photoelectron spectroscopy
XRD	X-ray diffraction
3D	Three-dimensional

List of symbols

A	Absorption
A_V	Constant
C_{MEMS}	Capacitance of a MEMS bridge
E	Elastic modulus (Young's modulus)
E_a	Activation energy (in the Arrhenius equation)
E_s	Elastic modulus (Young's modulus) of the substrate
h_C	Contact depth
h_F	Final displacement
h_{MAX}	Maximum displacement
I	Current
I_V	Nucleation rate per unit volume
k	Extinction coefficient
k_B	Boltzmann constant
L	Length
L_{MEMS}	Inductance of a MEMS bridge
n	Refractive index
$\tilde{n}$	Complex index of refraction
P	(Electric) power
p	Pressure
p_{N2}	Partial pressure of nitrogen
Q	Quality factor
R	Reflection
R_a	Average roughness
R_f	Radius of curvature of the wafer with the stressed film
R_{MEMS}	Resistance of a MEMS bridge
R_q	Root mean square (RMS) roughness
R_S	Sheet resistance
R_0	Radius of curvature of the wafer without the stressed film

R^2	Coefficient of determination
S_{11}, S_{21}	Elements of a scattering matrix
s_{11}, s_{12}	Elastic compliances of single crystal silicon
T	Absolute temperature
T_g	Glass transition temperature
T_m	Melting temperature (liquidus temperature)
T_{rg}	Reduced glass transition temperature
T_x	Onset temperature for crystallisation
t_f	Thickness of the film
t_s	Thickness of the substrate
U_r	Modulus of resilience
V	Voltage
y	The bending of a substrate
α_F	Coefficient of thermal expansion of the film
α_S	Coefficient of thermal expansion of the substrate
ΔG^*	Activation energy for forming a stable nucleus
Δm	The mass change due to oxidation
δ	Displacement
ε	Strain
ε_{el}	Elastic strain limit
η	Viscosity
λ	Wavelength
v	Poisson's ratio
v_s	Poisson's ratio of the substrate
ρ	Resistivity
σ	Stress
σ_c	Conductivity
σ_e	Extrinsic stress
σ_{ext}	External stress
σ_f	Residual stress (internal stress)

σ_i	Intrinsic stress
σ_{th}	Thermal stress
σ_{tot}	Total stress
σ_y	Yield strength

1. Introduction

1.1 Background and objectives

MEMS is an abbreviation for microelectromechanical systems, and refers to micro-sized devices that inherently combine electrical and mechanical functions. MEMS has inherited a lot from silicon-based microelectronics. This goes for the material selection as well as the process technology. While the onset of microelectronics was in the invention of the transistor in 1947, MEMS was born in the 1970s [17]. Compared to the integrated circuit (IC) industry, the production volumes of MEMS are low. MEMS is lagging behind the IC industry regarding also the minimum line-width (broader) and the average wafer size (smaller). In 2016, a typical linewidth and a wafer size for MEMS is 0.5 μm and 150 mm, respectively, while advanced IC fabrication plants reach the 14 nm node and use 300 mm wafers. Consequently, the old fabs and equipment of IC manufacturers have often been passed to MEMS fabrication, when the former have moved to newer technologies. The scarcity of standard MEMS processes means that each fab and application tends to have a process technology of its own, adding to the diversity of the field. The average times from the research and development (R&D) phase to commercialisation are also long (e.g. [18]).

The best known commercial MEMS products are possibly ink-jet printer nozzles [19], digital micromirrors for video projectors [20], and accelerometers for airbag launchers (e.g. [21]). These applications are such widely spread that anybody may make use of MEMS devices, aware or not. MEMS has been employed in various sensors (like pressure gauges, gyroscopes and microphones), optical devices (MOEMS = micro-optoelectromechanical systems), communication technology (RF MEMS = radio frequency MEMS), and biomedical devices (bioMEMS). By tradition, the interest in MEMS has been justified by the small size and low cost per unit. The small size enables functionality in size-critical cases, and is useful in portable devices. The low cost per unit, however, materialises only in large production volumes. As the emphasis has been shifting from industrial applications to consumer devices, there is pressure to introduce new products fast, and push the costs further down. This is a challenge to the field. Since the year 2000, the MEMS market has always been expected to boom within the next five years ([22] in 2002, [23] in 2006, and [18] in 2014). In reality, the total global market stagnated below $10 billion for years

[24], begging the question if MEMS remains only a perennial promise. However, the recent times have been positive to MEMS, with the market indeed growing with double-digit numbers in the 2010s [25, 26]. The future will show if this positive trend continues.

This dissertation deals with amorphous metallic thin films for surface micromachining. The purpose is to introduce a new choice to the material selection among which the best alternative for each application is chosen. The topic is a jump out of the mainstream of MEMS technologies which still rely heavily on the use of silicon. But what was the origin for the interest in amorphous metals? There was a demonstration that had a metal disc in a transparent tube, and a little steel ball bouncing on the disc [27]. Unlike the common materials we know from our everyday life, the ball kept bouncing and bouncing on the metal disc made of $Zr_{41.2}Be_{22.5}Ti_{13.8}Cu_{12.5}Ni_{10.0}$ (“Vitreloy 1”), an amorphous metal in a bulk form. Such a highly elastic material might be very interesting as a structural MEMS material, although the potential has not been recognised very widely within the MEMS community.

The selection of bulk amorphous metals is large [28]. To keep the scope of this thesis focused enough, two materials were picked for a closer look. The choice was made by the compatibility with the conventional MEMS processes, and easy availability in our premises. In addition, it was known that certain amorphous metal alloys were introduced for diffusion barriers in the IC technology already in the 1980s [29], although not widely used. IC compatibility is certainly a bonus. On these bases, sputter deposition was selected for the process technology, and molybdenum for the main metal ingredient. Since elemental metals take a polycrystalline structure, molybdenum was amorphised by nitrogen and silicon.

By the time this research was started, the attempts to apply amorphous sputtered metal films to MEMS were rather few. There was much unknown even in the material properties of these films, which became a substantial part of this work. However, a key objective was to move forward to MEMS process integration and real MEMS devices. By the end of the experimental work, indeed, MEMS devices with amorphous Mo-Si-N films were demonstrated. This experience was used to gain an understanding of the strengths and weaknesses of these films. Do they really contribute something useful to MEMS, and if yes, what are the limitations?

The dissertation begins with an overview of the relevant aspects of MEMS technologies and thin films in general, and a brief review of bulk amorphous metals that served as an inspiration for the study. The review continues with a survey of *mictamict* alloys, which Mo-Si-N films belong to. Chapters 3–5 review mictamict, Mo-N and Mo-Si-N films in detail with the purpose not only to constitute the necessary background for the experimental part of the dissertation, but also to provide a more generic reference if one intends to apply these films to MEMS. The experimental part presents the material properties and the process technology relating to the Mo-N and Mo-Si-N films. Finally, the thesis describes the use of these materials in true devices, providing an assessment of their applicability to MEMS.

1.2 Author's contribution

The research topic, amorphous Mo-N and Mo-Si-N films for MEMS, was suggested and introduced by Research Professor Hannu Kattelus. A basic characterisation of Mo-N films had been done before the author joined the work, albeit excluding considerations of the thermal stability [30]. A characterisation of Mo-Si-N films had also been started; the role of the author was to release and analyse the micromechanical beams that were the first MEMS structures made of Mo-Si-N [1, 2]. The characterisation of Mo-N and Mo-Si-N films was repeated and extended by the author after the deposition system was updated, and is reported only in this thesis.

The reviews in Chapters 2–5 are based on the judgement of the author alone. The author was assisted with the experimental work of Chapters 4–6 by several people. Mr. Antti Tolkki, Dr. Jyrki Molarius and Dr. Tommi Riekkinen gave practical advice on sputter depositions; in addition, Mr. Antti Tolkki sputtered some of the samples and Mr. Pekka Ikonen made technical arrangements for the sputtering tool. The deposition and etch rates, resistivity and residual stress were measured by the author; Dr. James Dekker, Dr. Kai Kolari and Dr. Heini Saloniemi assisted with the etching experiments. The scanning electron microscopy (SEM) and atomic force microscopy (AFM) analyses were made by the author with some assistance by Dr. Tomi Haatainen and Dr. Tuomas Pensala. Dr. Tomi Haatainen performed also an energy-dispersive X-ray spectroscopy (EDX) analysis and patterned the nanowires with electron beam lithography (EBL). Dr. Arto Nurmela and Dr. Timo Sajavaara (University of Jyväskylä) performed the Rutherford backscattering spectrometry (RBS) analyses, Dr. Antti Niskanen (University of Helsinki) and Mr. Pasi Kostamo (Aalto University) the X-ray diffraction (XRD) analyses, and Mr. Tatu Muukkonen the nanoindentation. The measurements with spectroscopic reflectometry were made by Dr. Kimmo Solehmainen and Mr. Sami Ylinen, the measurements with gonioreflectometry and transfer standard spectrometry by Dr. Silja Holopainen (MIKES, Finnish Centre for Metrology and Accreditation), and the optical modelling by Mr. Markku Kapulainen. Dr. Alexander Savin (Low Temperature Laboratory, Aalto University) measured Mo-Si-N samples at low (cryogenic) temperatures. Results of the materials research have been reported in [3, 4, 6, 14-16].

The author was the first to observe the low temperature (< 400°C) oxidation of our Mo-N and Mo-Si-N films. The subsequent experiments on the thermal stability were planned, executed and analysed solely by the author except for one set of Mo-Si-N samples that was annealed and photographed by Dr. Anna Rissanen following the plan of the author. Ms. Fang Tuurnala assisted in using the Tencor FLX-2320 stress measurement instrument. The results of the thermal stability are reported mainly in this thesis only (Chapters 4 and 5).

The photoresist process for the sacrificial layer and a few workable etch chemistries for Mo-N and Mo-Si-N films were known before this work was begun [4, 6, 30]. The author tested more etch chemistries, demonstrated the stepped and corrugated membranes, and experimented the hermetic sealing of free-standing amorphous metal membranes (Section 6.1). The author's contribution is reported mainly in this thesis only.

In the end, Mo-Si-N films were applied to RF MEMS (Section 6.2). The application field was suggested by Research Professor Hannu Kattelus, while the work itself was conducted with Dr. Tauno Vähä-Heikkilä. The latter carried out the RF design and measurements, and made suggestions for useful test structures. The author planned and refined the fabrication process and was responsible for the actual fabrication. Ms. Meeri Partanen suggested a couple of practical improvements on the fabrication process. The results have been published in [5, 7-13].

The thin film absorbers of Section 6.3 were designed by Lic.Sc. Martti Blomberg, while Dr. Riikka Puurunen was responsible for the atomic layer deposition (ALD) process. The author organised the fabrication and the measurements of the absorbers, and reported the results. They have been published in [14, 15] also.

Routine cleanroom operations such as cleans and lithography were performed by Ms. Meeri Partanen, Ms. Kirsi Järvi, Ms. Riitta Lindman and Ms. Kristiina Rutanen by the instructions of the author throughout the work.

2. Technological background

This chapter is an introduction to surface micromachining, thin films and amorphous metals, and provides a basic understanding of the technological background of this study. The surface micromachining section 2.1 outlines the framework in which MEMS material candidates will be assessed. The thin films section 2.2 discusses sputter deposition and thin film stresses because they were such an essential part of the experimental work, and the section 2.3 gives an overview of bulk amorphous metals that served as an inspiration for this study. Thin films and MEMS fabrication are covered in detail in many textbooks, such as [31] on thin films, [32] on silicon IC process technology, [33-36] on microfabrication, and [37] on measurement methods. Also amorphous metals are reviewed by several sources, such as [28, 38-47]. Mictamict alloys, the closest relatives of Mo-Si-N films studied in this thesis, will be discussed separately in Chapter 3.

2.1 Surface micromachining

2.1.1 Outline

The amorphous metal films of this study were developed for surface micromachining. When MEMS was born in the 1970s, the fabrication of MEMS devices was based on bulk micromachining where three-dimensional (3D) structures were formed into silicon substrates by anisotropic wet etching. The resulting structures were restricted by the crystallography of single crystal silicon, and tended to be relatively large in size. Surface micromachining emerged in the 1980s. Now the substrate was merely a carrier on top of which thin films were deposited and patterned, forming the desired structures. All functionality lay on one side of a wafer, on its surface.

Greatly simplified, the fabrication of surface micromachined MEMS devices consists in the repetition of thin film deposition, patterning (by optical lithography), and etching (Figure 1). These basic steps are supplemented by cleaning and other surface preparation, doping, annealing, and sometimes – if a broader definition is accepted – polishing and wafer bonding. Surface micromachined MEMS structures take their form when the structural parts are released by removing the sacrificial layer, both comprised of thin films. Several structural and sacrificial layers can be

used as well. The mechanical properties of a structural layer must be good, and the electrical properties appropriate. Especially, the structural layer must usually have a low biaxial residual stress and a low stress gradient in the vertical direction [48]. The sacrificial layer must bear the process temperatures of the structural layer, and there must be an etch process to remove it in a selective and isotropic manner. The latter results in deliberate undercutting and the concurrent release of MEMS structures. During and after the release, stiction must be avoided. Stiction means undesirable and permanent adhering of free-standing MEMS structures to the substrate, or each other. The likelihood of stiction can be reduced by replacing wet sacrificial etching with dry or vapour phase etching, using critical point drying or sublimation after the wet release etching, modifying the surfaces mechanically or chemically, or designing stiffer structures.

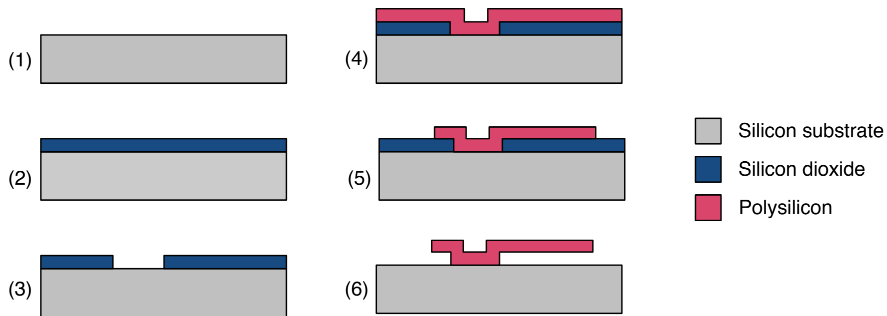

Figure 1. An example of a simple surface micromachining process to fabricate a cantilever beam.

When emerging, surface micromachining was an advance over bulk micromachining in terms of the size of devices (smaller), integration with electronics (easier), and design freedom (in certain aspects). The design of MEMS devices was no longer complicated by the crystal plane anisotropy of single crystal silicon, and multilayer structures became possible [36]. On the other hand, the maximum thicknesses of thin films are limited, and their properties are often poorly defined and far from ideal. The properties of thin films are usually different from those of bulk materials, and strongly dependent on the deposition process. In addition, they are impacted by the thermal load the film has experienced. For a successful realisation of surface micromachined MEMS, the ability to control thin film properties is hence essential.

For a long time, MEMS has been praised for its easy integration with integrated circuits, especially in the case of surface micromachining. Integrated MEMS devices exist indeed [49] but, in many cases, monolithic integration is not profitable. The monolithic integration may enable functionality that would be otherwise unattainable, and it may reduce packaging costs, bearing in mind that the packaging may be

the most expensive part of a MEMS component. On the other hand, the total process gets easily long and complex when MEMS and IC are combined on a same chip, and the yield may get poor, both increasing the costs. Therefore, so called hybrid integration is still widely used. It means that MEMS and IC are fabricated separately, and the integration happens at the package level, e.g. by flip chip bonding. Flexibility is gained if MEMS and electronics can be developed and manufactured independent of each other. [50, 51]

2.1.2 Material selection

Thin films for surface micromachining have to meet manifold requirements. Good mechanical properties, especially residual stress, are usually essential. Resistivity (or the total resistance), permittivity (or the dielectric constant), tensile strength, hardness, the refractive index, surface roughness and conformal step coverage are relevant depending on the application. The films shall be uniform in composition and thickness, and have a low defect density, acceptable thermal stability, and adequate adhesion to the substrate or the underlying film. A feasible etch process for patterning must be available, and the selected deposition method has to provide films with the desired properties in a reproducible manner.

MEMS is often based on silicon technology. The dominating position of silicon stems from its good material properties together with easy availability and the well established process technology. Silicon is a semiconductor with a high melting point (1414°C) [52]. The resistivity is widely tailorable by doping. Single crystal silicon is a strong but brittle material; at room temperature, it elongates elastically until it fractures [52], with the fracture strain as high as 4 % [36]. Silicon is widely accompanied by its dielectrics, silicon dioxide (SiO_2) and silicon nitride (Si_3N_4), which are used for electric insulation, chemical passivation, mechanical protection, dielectric films, mask materials, and optical layers [36]. Silicon oxide is also a common choice for the sacrificial layer in MEMS.

The polycrystalline thin film form of silicon, polysilicon, is the most widely used material for the structural layer in surface micromachining. It is paired with silicon oxide as the sacrificial layer. Other conceivable pairs are silicon nitride (as the structural layer) together with silicon oxide (as the sacrificial layer), poly-SiGe together with CVD oxide [36], polysilicon together with poly-SiGe [50] and PECVD oxide together with polyimide [48], where CVD stands for chemical vapour deposition, and PECVD stands for plasma-enhanced CVD. Metal films (aluminium, gold, copper and nickel) as structural layers are often deposited on top of photoresist or polyimide as the sacrificial layer. Other possibilities are gold (as the structural layer) together with PECVD oxide (as the sacrificial layer) [48], and gold, nickel or diamond (as the structural layer) together with copper (as the sacrificial layer) [36]. The metal films can be deposited by sputtering or electroplating.

In the first edition of his famous MEMS book in 1997 [53], M.J. Madou regarded the material properties of polysilicon as “far superior” to those of metal films, stating also that “because of fatigue problems, metals are not typically used as mechanical

components". Since then, metals have been accepted for MEMS, showing their usefulness e.g. in the commercial success story of Texas Instruments' digital micromirrors with amorphous Ti-Al structural parts [20]. It is true that metal films suffer from fatigue and memory effects [36], as well as the direction dependent mechanical properties in the microscale [53]. Aluminium is widely used although its mechanical stability and temperature tolerance are quite poor, and thermal stresses are relaxed with hillocks and whiskers [50]. As a counterbalance, metals certainly have benefits, too. First, the conductivity of metal films is notably higher than that of polysilicon. The resistivity of even heavily doped polysilicon exceeds 1 mΩcm, while the corresponding values are 2.8 μΩcm for aluminium, 2.4 μΩcm for gold, 1.7 μΩcm for copper, and 6 μΩcm for molybdenum [50], that is, the common metals conduct electricity almost 1000 times better than polysilicon at its best. High conductivity is a crucial requirement e.g. in RF MEMS. Second, thick metal films up to tens of micrometers can be produced easily by electroplating [36], while LPCVD (low-pressure CVD), which is the usual deposition method for polysilicon films, is not well suited for films thicker than 2 μm. Third, the deposition temperature of metals is significantly lower than that of polysilicon: sputtering and electroplating take place at or near room temperature, while LPCVD polysilicon is synthesised at around 600°C. The low deposition temperature enables the use of polymers instead of silicon oxide as the sacrificial layer. The maximum temperature polymers can stand is generally between 100 and 200°C, and 400°C at the utmost [36].

Polymers such as photoresist and polyimide are appealing for the sacrificial layer because of their easy removal compared to silicon oxide. Polymers can be removed in oxygen plasma that is gentle to the other structures on the wafer, while silicon oxide needs to be etched by HF (hydrofluoric acid) that is an aggressive acid towards several common MEMS materials. The use of the polymer technology thus extends the selection of other materials that can be incorporated into the devices. Another advantage is that the monolithic integration of MEMS and IC is possible when the process temperatures of MEMS fabrication stay low (as in the case of metals and polymers). The approach is then MEMS post-processing on top of IC electronics. The limit for the low temperature processing is 450°C [36] which stems from the thermal stability of aluminium that is widely used in CMOS (complementary metal-oxide-semiconductor) electronics. When the sacrificial etching is done by the oxygen plasma, no extra protection is needed.

The study with amorphous molybdenum-based thin films was initiated because they were anticipated to benefit from good mechanical properties (better than those of elemental metal films), relatively low resistivity (lower than that of polysilicon), a low deposition temperature (when deposited by sputtering), and consequently the possibility to have a polymeric sacrificial layer.

2.2 Thin films

2.2.1 Sputtering

The amorphous metal films of this study are deposited by sputtering which is the most important physical vapour deposition (PVD) method today. Sputter deposition is favoured by the broad material selection, as sputtering targets of almost any engineering material are commercially available. [31] The advantages of sputtering include also the low deposition temperature, good adhesion, and a better step coverage than what is achieved by evaporation. However, the films deposited by chemical vapour deposition (CVD) techniques are usually superior in terms of conformality.

Sputtering is defined as a process where an energetic particle hits a surface and dislodges an atom from it [54]. When such ejected atoms are transported to a nearby substrate, condense onto it, and form a thin solid film, the process is called sputter deposition [32]. A sputter deposition set-up consists of a target (a solid plate of the source material) on a negatively charged cathode, and a substrate on a grounded or positively charged anode (Figure 2). They are located in a sputtering chamber that is typically filled by argon gas and kept in a low pressure of the mTorr region. Positively charged argon ions are produced in a glow discharge. When such argon ions strike the target, they dislodge atoms from it by physical momentum transfer [54]. Secondary electrons are also created; they are needed to sustain the glow discharge and keep the process on. The dislodged atoms are transported to the substrate through the low pressure chamber, usually experiencing several collisions during their flight. Upon they condense onto the surface, a solid film is formed. When a metal film is deposited on an oxide surface (like was often done in the experimental part of this study), the island growth is usually the predominant growth mode [31]. In the island (Volmer–Weber) mode, deposit atoms are bound more strongly to each other than to the substrate, leading to the formation of three-dimensional islands that later merge [31, 36]. For sputtered films, a film may be 10…20 nm thick before it gets continuous [36]. – As the above was a simplified description of the sputtering process, references [31], [32] and [54] can be recommended for thorough reviews of the rather many-sided sputtering physics.

The variables through which sputtering processes can be tuned are the pressure and the flow rate of argon gas, a purpose introduction of reactive gases, the bias voltage, the sputtering power, substrate heating and the details of the sputtering configuration (such as the distance between the electrodes). Besides argon, the inert working gas can be e.g. of neon or krypton [54], albeit argon is almost solely used. The bias voltage can be of DC (direct current) or RF (radio frequency); however, DC biasing is not practical for the sputtering of insulators. Whichever the choice, the ionisation efficiency is often improved by the presence of a magnetic field, leading to magnetron sputtering. A depositing film is bombarded by energetic particles during its formation. Ion bombardment can modify the structure of the film in terms of surface topography, crystallography, grain size, texture and residual

stress [31]. It can increase the density and improve the adhesion [36]; on the other hand, defects may form as well. Properties like adhesion, step coverage and residual stress can be adjusted also by substrate heating [32, 53]. In general, sputter deposition is yet a low temperature process which is often performed at room temperature or slightly above.

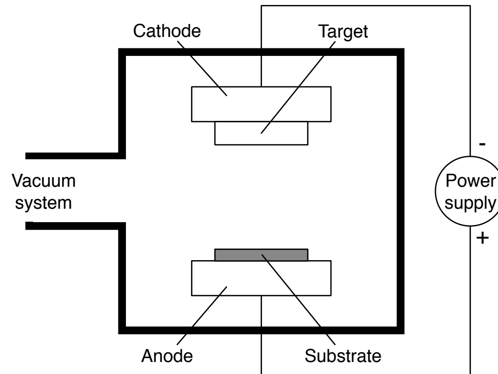

Figure 2. A schematic picture of a simple sputtering equipment. Redrawn after Rossnagel, S. (2002) [54] with permission of Elsevier.

It is quite common that some argon is trapped in a sputter deposited film but mostly the effects are small [36]. The incorporation of a reactive gas like oxygen affects the properties of the depositing film much more and is usually undesirable. If one wants to prevent oxygen from incorporating, its partial pressure must be kept low (by having a low background pressure). If reactive sputtering is aimed, however, it is done by the purpose introduction of one or more reactive gases. Doing that, compounds like oxides, nitrides, carbides, sulfides and oxynitrides can be produced [31]. Other ways to have composite films are co-sputtering of two (or more) targets, the use of a composite target, or even a combination of the above. The reactive sputtering is complicated by the fact that the target tends to react as well, leading e.g. to a reduced deposition rate and arc formation [54].

2.2.2 Stresses in thin films

Mastering the mechanical stresses of metal films is essential in this study. The total stress σ_{tot} of a film is

$$\sigma_{tot} = \sigma_{ext} + \sigma_f = \sigma_{ext} + (\sigma_e + \sigma_i) \tag{1}$$

where σ_{ext} is the external stress, σ_f the residual stress (also known as the internal stress), σ_e the extrinsic stress, and σ_i the intrinsic stress. σ_{ext} refers to the stress caused by intentionally applied external forces [34]. The residual stress σ_f includes two terms: the extrinsic and the intrinsic. The extrinsic stress covers the thermal

stress σ_{th} resulting from the thermal expansion mismatch between the film and the substrate, and the stress caused by any unintentional external forces like package-induced ones [34]. The intrinsic stresses arise from the film itself: its deposition process and microstructure. They often result from the fact that the energy minimum is not reached during the film deposition. In more detail, the intrinsic stresses can ensue from process-related factors like atomic peening, the lattice mismatch between the film and the substrate, doping, point defects like voids or impurities, grain boundaries, and recrystallisation, phase transformations or chemical reactions leading to volume changes [31, 34, 36, 55].

The stress of a thin film can be either compressive or tensile. If a film is under compressive stress, it would expand if detached from the substrate (Figure 3). Respectively, a film under tensile stress would contract. Both kind of films make the underlying substrate to curve: the former in a convex way, the latter in a concave way. A usual measure of stress is MPa (1 MPa = 10^6 Pa), that is, the same as for pressure. There is a convention to use a positive sign for tensile stress, and a negative sign for compressive stress. The typical stresses in thin films are a few GPa in magnitude at the most.

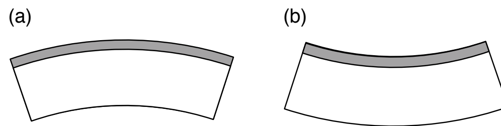

Figure 3. A thin film under (a) compressive and (b) tensile residual stress deposited onto a substrate.

When thin films are used for surface micromachining, low biaxial residual stress and a low stress gradient in the vertical direction [48] are normally desired. Large compressive stress can make a MEMS structure to buckle, and large tensile stress to crack. If the stress varies with depth (i.e. if there is a stress gradient) a released MEMS structure may warp. All these effects are usually unwanted. In general, thin film stresses affect the performance of MEMS devices as they are capable of shifting the pull-in voltage and the resonant frequency, and increasing film resistivity [34]. The yield and the reliability are degraded if stresses cause the loss of adhesion (delamination or blistering [34]) or an increased risk of corrosion [32].

From the above, it is obvious that an ability to adjust residual stress is important. The residual stress of a thin film depends on its composition, the deposition method, the process details (including the deposition temperature and the deposition rate), the substrate, and possible impurities [32, 34]. In the case of sputtering, there is a multitude of process variables affecting the residual stress: the gas pressure, the substrate bias, the atomic masses of the gas and the target, the angles of deposition and emission, the target shape, the cathode power, the proximity and the motion of the substrate, and reactive contamination [56]. As Hoffman states, it is possible to

bring about a stress reversal from compressive to tensile by almost any of the above listed variables [56]; however, the gas pressure is the most frequently used with quite a sharp reversal (Figure 4). Besides tuning the stress state of an individual film, the stress of a MEMS structure can be adjusted by layering several differently stressed films one on the other, or by executing structural stress relief by mechanical design like in the case of corrugated membranes [53].

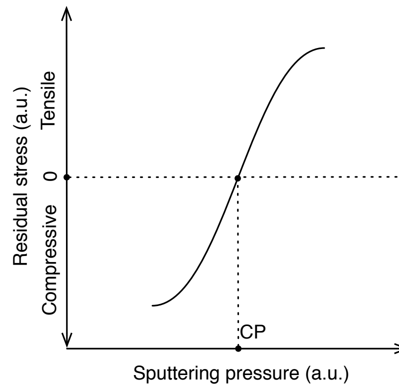

Figure 4. A typical curve for the residual stress vs. the argon sputtering pressure for metal films. CP is the critical pressure for the compression-to-tensile stress transition. Redrawn after Hoffman, D.W. (1994) [56], with the permission of American Vacuum Society.

The residual stress of evaporated metal films is usually tensile [31]. Such a generalisation cannot be made for sputtered metal films whose stress can equally be compressive or tensile. It is claimed the metal films deposited at low temperatures have typically tensile stress, and the stress decreases and finally turns compressive as the deposition temperature is increased [32, 34]. Furthermore, the refractory metals with a high melting point and low atomic mobility tend to have higher tensile stress than the soft metals with a low melting point and high mobility [34]. One should bear in mind the residual stress of a film does not only depend on its composition and deposition variables, but also on its thickness [57-59] and the thermal load the film has experienced. It is common that the stress varies with depth, reflecting a change in the microstructure [32]. The thinner the film, the larger influence the film-substrate interface may have. Stress relaxation, for one, may take place already during a high-temperature deposition process or by subsequent annealing through mechanisms like grain growth, grain-boundary relaxation, recrystallisation or even film cracking [31].

2.2.3 Measurement of residual stress

The residual stress of thin films was frequently measured in the experimental part of this work. In practice, the common stress measurement methods are indirect by nature, i.e. stress is deduced from strain measurements. The most common method is to detect the stress induced change in the substrate bow. The residual stress in a thin film deposited on a disc substrate is obtained by the famous Stoney equation (e.g. [36]):

$$\sigma_f = \frac{E_s}{6(1-\nu_s)}\frac{t_s^2}{t_f}\left(\frac{1}{R_f} - \frac{1}{R_0}\right) \qquad (2)$$

where E_s, ν_s and t_s are the Young's modulus, the Poisson's ratio and the thickness of the substrate, t_f the thickness of the film, and R_0 and R_f the radii of curvature of the wafer without and with the stressed film. The signs of R_0 and R_f should be positive if the substrate is concave (bending downward) and negative if the substrate is convex (bending upward). This agreement leads to a positive sign for tensile stress, and a negative sign for compressive stress. One should note the above formula gives the average stress of the film, while in practice the stress is often thickness dependent. For a stack of n stressed films, the Stoney equation gets a form (assuming R_0 can be neglected) [31]:

$$\frac{1}{R_1} + \frac{1}{R_2} + \cdots \frac{1}{R_n} = \frac{6(1-\nu_s)(\sigma_1 t_1 + \sigma_2 t_2 + \cdots \sigma_n t_n)}{E_s t_s^2} \qquad (3)$$

The Stoney equation has been derived based on the fact that both the net force and the net bending moment on any film/substrate cross-section must vanish in mechanical equilibrium [57]. The equation assumes the film stiffness can be neglected [55], the film thickness is uniform and much less than the substrate thickness, there are no temperature gradients, the film–substrate system is mechanically free, and the stress is homogeneous over the measurement area [53]. The equation does not reveal if there is a stress gradient in the vertical direction, but the average value is given. The reference [57] shows how the traditional Stoney equation above neglects the elastic anisotropy of single crystal silicon (used as the substrate), with E_s and ν_s being averaged values. This is not a problem with [111] silicon wafers whose in-plane stiffness does not depend on the in-plane direction. If one wants to be precise, the neglect can be corrected for other silicon wafers by replacing the biaxial modulus $E_s/(1 - \nu_s)$ with $1/(s_{11} + s_{12})$ where s_{11} and s_{12} are elastic compliances of silicon (the values given in [57]).

The substrate bending for a stress measurement can be detected optically (by a laser beam) or by stylus profilometry. To record the change in the substrate bow, two curvature measurements are needed for each wafer: with and without the stressed film. It does not matter if the reference measurement of the blank wafer is done before the film deposition, or after the film has been deposited and then removed. To have a good measurement resolution, the substrate should not be too thick: a thin wafer bends more than a thick one. Also the thickness variation of the

substrate (from the nominal value given by the wafer manufacturer) should be minimised since it contributes to the measurement uncertainty. Besides a disc substrate, the stress can be determined from the deflection of a cantilever beam when the equation (2) changes to a form [31]:

$$\sigma_f = \frac{\delta E_s t_s^2}{3L^2(1-\nu_s)t_f} \tag{4}$$

where δ is the free-end displacement of a cantilever of length L.

The deflection methods described above are not the only way to measure stress in thin films. Elastic strains can be observed directly by X-ray diffraction detecting the slight stress induced changes in the interplanar spacing of crystal planes [31]. Different kinds of micromachined test structures (like the so-called Guckel rings [60]) are also possible. The drawbacks of such released test structures are that an array of them is needed if one wants to measure the stress accurately (instead of knowing whether a certain threshold value is exceeded or not), such arrays take a large surface area (making their integration onto a MEMS production wafer uneconomic), and several fabrication steps are needed to complete them (instead of analysing blank, non-patterned films). Other stress measurement methods are bulge testing, Raman spectroscopy, ultrasonic techniques, nanoindentation, and a method based on electrostatic actuation of MEMS test structures [55]. Although it would be useful, there is no good method for measuring a through-film stress gradient without releasing the film [61]. Some data could be acquired by depositing films of varied thicknesses, and analysing them one by one. A set of samples would be needed, however, and it would not be sure if the obtained results really corresponded to the stress gradient of one thick film.

2.3 Amorphous metals

This study was initially inspired by *bulk amorphous metals* that are also known as *amorphous metal alloys*, *bulk metallic glasses* (BMG), *bulk glassy alloys* (BGA), *bulk amorphous alloys*, *glassy metals*, and sometimes *metglasses* or even *liquid metals* although the latter is confusing. The terms are generally used as synonyms. The key concepts are defined in Table 1.

2.3.1 History and development

Elemental metals are crystalline in the solid state except for very rare occasions [31, 64, 68]. To obtain an amorphous microstructure, metals must be alloyed. Most references credit W. Klement and P. Duwez with producing the first amorphous metal $Au_{75}Si_{25}$ in 1960 [69], although there are some earlier mentions of amorphous metals starting from 1930 [31, 68-71]. The early amorphous metals had to be cooled extremely rapidly to avoid crystallisation upon solidification. The cooling rate was as high as $10^5 \ldots 10^6$ K/s, and at least one dimension had to be small (50 µm or below)

Table 1. The key concepts related to amorphous metals.

Concept	Definition
Alloy	A metallic substance that is composed of two or more elements [62]. At least one of the elements must be a metal, and the alloyed substance must have metallic properties.
Amorphous	A synonym for *non-crystalline*. A solid material has either a crystalline or an amorphous structure depending on the regularity with which its atoms are spatially arranged. Contrary to crystalline materials, an amorphous solid has a random atomic-scale structure lacking a long-range translational order (periodicity). It resembles a frozen liquid configuration. An amorphous structure forms if the constituent atoms do not have enough time or energy to rearrange for crystal nucleation. [62, 63]
Amorphous metal alloy	A system which is either (a) composed of at least two different metals, or (b) composed of at least one metallic and one non-metallic 'metalloid' compound, and which is stable in the amorphous state at room temperature, or at least metastable with lifetimes up to years or decades [64].
Bulk	In relation to amorphous metals, a material is called bulk if it can be made amorphous with a thickness of 10 mm [40, 41] or at least 1 mm [42, 65, 66] in all dimensions. Consequently, the critical cooling rate must be in the order of 100 K/s or below. The amorphous metals with a high critical cooling rate and a low casting thickness are sometimes called *conventional metallic glasses*.
Glass	An amorphous solid which exhibits a glass transition. A solid is defined as a material whose shear viscosity exceeds $10^{13.6}$ Nsm^{-2}. A glass transition is a phenomenon in which a solid amorphous phase exhibits a relatively abrupt change in the *derivative* thermodynamic properties (such as heat capacity or thermal expansivity) from solid-like to liquid-like values with the change of temperature. [63] Sometimes a glass is defined simply as an amorphous product produced by rapid quenching of a melt. The latter definition, however, is less accurate than the former.
Metal	An electropositive element or an alloy based on these elements. The electropositive elements are capable of giving up their few valence electrons to become positively charged ions. Metals have a large number of non-localised electrons, and their electron band structure is characterised by a partially filled valence band. [62]
Metalloid	An element whose chemical properties are intermediate between those of metals and non-metals. The exact members of the group slightly differ depending on the reference cited. For example, W.D. Callister counts in B, C, Si, Ge, As, Se and Te [62]. M.-A. Nicolet counts in also N and P [67].

[28, 42, 46, 71]. This was a severe limitation since only ribbons and foils could be produced.

Accordingly, there has been a continuous endeavour to find new compositions with higher glass forming ability (GFA), i.e. the tendency of a material to solidify into an amorphous state, and lower critical cooling rates. H.S. Chen achieved the casting thickness of 1 mm in 1974 with a ternary Pd-Fe-P alloy [40, 41], and D. Turnbull *et al.* the casting thickness of 1 cm in 1984 with a Pd-Ni-P alloy [72]. The critical cooling rate of the latter was only 1 K/s [72]. Because of the high cost of palladium, the achievements remained mainly of academic interest [42, 46]. The breakthrough

in the development of bulk amorphous metals was made around 1990, when A. Inoue *et al.* at Tohoku University (Japan) discovered the Ln-Al-LTM alloys, where Ln stands for a lanthanide and LTM for a late transition metal (LTM = Fe, Co, Ni, Cu) [28, 38, 73], and W.L. Johnson *et al.* at California Institute of Technology (USA) discovered the family of Zr-Ti-Cu-Ni-Be metallic glasses [74]. BMGs can be manufactured nowadays with a casting thickness of several centimetres, e.g. a sample of the $Pd_{42.5}Cu_{30}Ni_{7.5}P_{20}$ alloy with a critical cooling rate of 0.067 K/s was 80 mm in diameter and 3430 g in weight [28, 75, 76]. Despite lower GFA, iron-based BMGs attract engineering interest due to their low cost and very high strength [28, 77-79]. Figure 5 illustrates the development of the casting thickness following an exponential growth during the past decades.

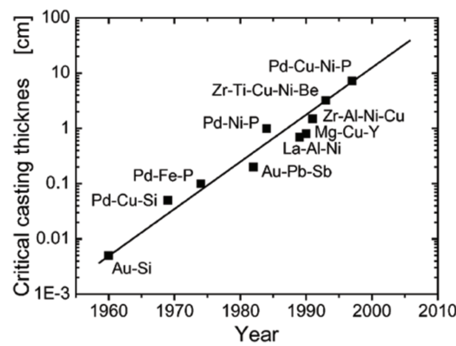

Figure 5. The increase in the critical casting thickness since the discovery of amorphous metals. Reprinted from Löffler, J.F. (2003) [40] with permission of Elsevier.

In search of new amorphous compositions, scientists have proposed several empirical rules to predict alloy systems with high GFA. The early work of D. Turnbull advised looking for alloys with high $T_{rg} = T_g/T_m$, where T_{rg} is the reduced glass transition temperature, T_g the glass transition temperature, and T_m the melting temperature. This often means deep eutectic compositions. [38, 40, 42] A. Inoue *et al.* have presented a set of three rules: (1) the multi-component alloy should contain at least three elements, (2) the difference in the atomic size between the main constituents should exceed 12 %, and (3) the heat of mixing should be negative (i.e. energy is released) [28, 45, 65, 79]. W.L. Johnson *et al.* developed the so called confusion principle: they suggest selecting multiple chemically different atoms that cannot arrange into a simple crystalline structure [38, 40].

Also the processing methods have developed over the years. The historical $Au_{75}Si_{25}$ alloy was produced by splat quenching, by which droplets of the molten alloy were propelled onto a cold copper plate [46, 71]. In the 1970s, amorphous metal filaments and ribbons were produced by melt spinning that employed a cooled rotating wheel [41, 64, 71]. Today, bulk specimens can be prepared by methods such as copper mould casting, high-pressure die casting, injection moulding, arc melting and thermoplastic forming (TPF), or hot pressing and mechanical alloying

from powders [42, 45, 79-81]. TPF takes advantage of the softening and viscous flow of BMGs in their supercooled liquid region (SCLR), i.e. the temperature region between T_g and T_x, where T_x is the onset temperature for crystallisation ($T_g<T_x$), similar to the manufacturing of plastic articles [38, 45, 82]. The joining of BMG parts is possible by welding without crystallisation or visible defects by the attendant heat [42, 83]. Thin films and coatings can be prepared by high velocity oxygen fuel (HVOF) thermal spraying [41, 84-87] and sputtering [88-98]. Although the latter is a common film deposition method, the sputtering of thin film metallic glasses (TFMGs) is complicated by the facts that usually BMG sputtering targets are not commercially available, and significant differences between the compositions of the multi-element sputtering targets and the resulting films may be observed [45].

2.3.2 Structure and properties

When conventional and amorphous metals are cooled from a liquid melt, they behave differently. A conventional metal crystallises right below the melting temperature T_m. An amorphous metal can be cooled below T_m without solidification. The viscosity of the undercooled melt increases until the glass transition. If the cooling rate is high enough, the melt solidifies into an amorphous state without crystallisation, resembling a frozen liquid configuration. [38, 45] The glass transition temperature T_g is neither discrete nor constant. It is rather a narrow temperature range whose location depends on the thermal history of the material, able to vary even 10…20 %. [38, 45, 63]

An amorphous structure is obtained only if the crystallisation in the undercooled liquid is suppressed. With the assumption of steady-state nucleation, the nucleation rate per unit volume is:

$$I_V = \frac{A_V}{\eta(T)} exp\left(-\frac{\Delta G^*}{k_B T}\right) \tag{5}$$

where A_V is a constant, $\eta(T)$ the viscosity, ΔG^* the activation energy for forming a stable nucleus, k_B the Boltzmann constant, and T the absolute temperature. The first factor of I_V is kinetic and depends on the viscosity, or atomic diffusion. (Viscosity and diffusivity are inversely proportional by the Stokes-Einstein relation.) The second factor is thermodynamic. The activation energy ΔG^* is determined by two competing forces: the free energy difference between the liquid and a crystal provides a driving force for crystal nucleation, whereas the interfacial energy between the liquid phase and nuclei creates an energy barrier which must be overcome. [40, 42] The crystallisation depends also on pressure and the susceptibility to phase separation [40, 42]. The latter is relevant since many good glass formers have a eutectic composition, and eutectic alloys possess an intrinsic tendency towards phase separation [38].

Although amorphous metals are characterised by the lack of long-range atomic order, their structure is not entirely random [47, 99-105]. The complex topic has been reviewed extensively by Cheng and Ma in 2011 [104]. It was earlier believed that the atomic order of metallic glasses (MGs) would correspond to Bernal's model

of the dense random packing of hard spheres (DRPHS) but the model has now been rejected as too simplistic [46, 68, 101, 102, 104]. The current models are based on some local structural motif (such as icosahedral clusters) as a basic building block, representing the short-range order (SRO) of MGs [42, 46, 99, 102, 104]. The medium-range order (MRO) concerns the positioning of the neighbouring building blocks in order to obtain efficient filling of space, e.g. face-centred cubic (f.c.c.) packing of overlapping clusters [100, 102]. Different types of MGs have different characteristic structural motifs, and there is local structural heterogeneity even inside each MG [104]. Structural relaxation is induced by annealing [44, 104] and polyamorphism (i.e. the transition between distinct and differently ordered amorphous phases) by pressure [106, 107].

Bulk amorphous metals possess certain outstanding mechanical properties. They have high elasticity, high yield and tensile strength, and high hardness [40-43, 46, 47]. They can sustain an elastic strain of ca. 2 %, while the elastic strain limit ε_{el} of common crystalline metal alloys is typically about 0.5 % [38, 40, 41, 45, 62]. Consequently, the modulus of resilience U_r, which represents the maximum elastic energy density stored in a material, is very high for amorphous metals, as it combines the yield strength σ_y and the elastic strain limit ε_{el}:

$$U_r = \int_0^{\varepsilon_{el}} \sigma \, d\varepsilon = \frac{1}{2}\sigma_y \varepsilon_{el} \tag{6}$$

where σ is the instantaneous stress, ε the instantaneous strain, and a linear elastic region is assumed [38, 40, 62]. In addition, amorphous metals are resistant to corrosion and wear [42, 45, 46], and iron-based compositions possess good soft magnetic properties [28, 40, 45, 71].

On the other hand, amorphous metals suffer from brittleness and low ductility at room temperature. Unlike conventional metals, they are vulnerable to strain-induced work-softening and highly localised shear bands, giving rise to catastrophic failure once yielding has begun. [40-44, 46, 108]. These shortcomings have led to the development of composite alloys with a two-phase microstructure: an amorphous matrix of BMG reinforced with a ductile crystalline material, so as to combine the high strength of BMGs with the ductility, fracture toughness and plastic strain-to-failure of conventional metals [39-42, 44, 46, 47, 108, 109].

2.3.3 Applications

The unique mechanical properties of amorphous metals have been utilised in sporting goods such as golf clubs and tennis rackets [28, 39, 41, 42], and they are suitable for the casings of electronic devices as well [41, 42, 45]. For example, Apple Inc. has acquired an exclusive licence to use certain BMG alloys in consumer electronics although the exact use is only being speculated [110, 111]. The magnetic properties have been exploited in magnetic cores for distribution transformers, sensors such as magnetic recording heads, and radio frequency identification (RFID) systems [28, 40, 71, 112]. The medical applications include e.g. prosthetic or biodegradable implants, pacemaker casings, and surgical instruments like ophthalmic

scalpel blades [41, 42, 46, 47, 113, 114]. Amorphous metals have been used also for industrial coatings, jewellery, and military and space applications [41, 42, 47]. Nanostructured amorphous metals have been studied as catalysts [114-116]. Despite the variety of applications, amorphous metals are found on the market mainly as niche products because of the lack of ductility, limited fracture toughness, high price and size restrictions [109]. They have been commercialised under the trade names of Vitreloy, Liquidmetal, Metglas and Liqualloy.

MEMS and nanotechnologies can take advantage of the structural homogeneity of amorphous metals. With dimensions below one micron, the grain size of polycrystalline materials start to be comparable to the feature size of devices, resulting in remarkable anisotropy of properties [45]. In the absence of a crystalline microstructure, such anisotropy is absent. Miniaturisation is favoured by the lack of grain morphology, grain boundaries and crystal defects. Importantly, the tendency of amorphous metals towards low ductility and brittle fracture, which severely hampers the use of BMGs, is mitigated in micro- and nanoscale dimensions [43, 108, 117, 118]. MEMS applications often make use of amorphous metals in their thin film form, i.e. as thin film metallic glasses (TFMGs) [88, 89].

The digital micromirror device (DMD) of Texas Instruments is the most successful MEMS application of amorphous metals. A large array of micromirrors with hinges made of an amorphous sputter deposited Ti-Al alloy is a critical part of the digital light projectors produced more than 35 million pieces by 2015 [20, 119-121]. The hinges were previously made of a crystalline aluminium alloy but they suffered from poor mechanical reliability, including considerable hinge memory [20]. An amorphous sputtered Ti-Al alloy has been applied also to the fabrication of the spatial light modulators and the capacitive micromachined ultrasonic transducers (CMUTs) by Fraunhofer IPMS [122-125]. These Ti-Al films are not direct counterparts of any of the BMGs discussed in Section 2.3.1, however.

In general, BMGs have been used for the fabrication of MEMS devices such as microgeared motors, pressure sensors, microlens arrays, micropillars, variable inductors and conical spring actuators [45, 88, 126, 127]. A variety of fabrication methods is available for micro- and nanodevices: thermoplastic forming (TPF), nanoimprinting lithography (NIL) (or hot embossing), focused ion beam (FIB) milling, as well as microextrusion, -forging and -molding [45, 97, 118, 128-135]. Most of these methods take advantage of the supercooled liquid region of BMGs, in which they are highly malleable. For example, the SCLR of $Zr_{41.2}Ti_{13.8}Cu_{12.5}Ni_{10}Be_{22.5}$ ("Vitreloy 1") is between 349 and 426°C [118].

3. Review of mictamict alloys

3.1 Introduction

The concept of *mictamict alloys* was first introduced in 1999 by Marc-A. Nicolet [136], a professor at California Institute of Technology (Caltech) and a leading character to study these materials in the 1980s and 1990s. He and his research group had recognised already some years earlier that ternary thin films comprising of an early transition metal, silicon and nitrogen possessed a few striking properties in common [137]. In particular, those films had an amorphous microstructure, and were remarkably stable against crystallisation when annealed. Soon, it was realised that other three-element systems with similar features might exist as well [138, 139], leading to a more mature understanding of the field [140]. The concept of mictamict alloys is noteworthy because Mo-Si-N, the key material studied in this thesis, belongs to the group. The other key material of this thesis, Mo-N, is not a representative of the mictamict alloys.

By their narrow definition, the mictamict alloys are "ternary thin films of the generic composition (early transition metal)–Si–(nitrogen or oxygen) that have an amorphous or near-amorphous structure and are highly resistant to crystallisation upon thermal annealing" [140], also abbreviated to TM-Si-N or TM-Si-O where TM stands for an early transition metal [141]. The broader definition generalises the concept also across other highly metastable amorphous or near-amorphous ternary films that comprise of two dissimilar compounds with one common species, resulting in a quasi-binary system [140]. An example of the latter is W-B-N (comprising of W-N and B-N) [139].

Chapter 3 is a review of the mictamict alloys in general, while Mo-Si-N films are discussed in Chapter 5 in more detail. Chapter 3 itemises the currently known representatives of the mictamict alloys, and covers what is known about their structure and thermal stability as these are the characteristics by which the group is defined. The chapter continues with a discussion on the mechanical and electrical properties of the mictamict alloys. By the end of the chapter, we take a look at the processing methods and the practical applications of these films.

3.2 Composition and structure

By the definition, a main feature of the mictamict alloys is their amorphous or near-amorphous structure. To have such, grain growth during film deposition must be suppressed. Elemental metal films are practically always crystalline. The production of amorphous transition metal silicides is rather easy, while the same is more difficult for transition metal nitrides [142]. Adding silicon to a metal nitride often makes the structure more amorphous by nature [140]. Sputter deposition (a common method for producing mictamict alloys) further promotes the formation of an amorphous structure as it is a low temperature process impeding atomic diffusion during deposition. By Nicolet, quasi-binary systems should be examined in the search for possible mictamict alloys [140]. He concluded that an amorphous structure is favoured if one mixes two binary compounds that are dissimilar in terms of their crystal structure and bonding character, and whose mutual solubility is limited. In the case of ternary films, the two compounds should have one element in common. Nicolet supported his idea of quasi-binary systems with the example of TM-Si-N films: the nitrides of early transition metals are refractory metallic compounds with a simple crystal structure, while Si_3N_4 is a covalent compound with a complex structure [140]. Mixed together, there is a good chance that TM-Si-N films are amorphous.

When the concept of mictamict alloys was introduced in 1999, amorphous TM-Si-N films with (TM = Ta, Ti, Mo, W) had been already demonstrated [136-139]. Amongst those early representatives of the mictamict alloys, Ta-Si-N [142-185] and Ti-Si-N films [142, 183, 186-220] have been studied the most, while Mo-Si-N [142, 221-239] and W-Si-N films [142, 156, 190, 229, 231-233, 240-249] somewhat less. The fact that Ti-N films have been employed widely as diffusion barriers in the semiconductor industry has probably added to the early interest in Ti-Si-N films [139]. Nicolet predicted in 2001 that also Sc, V, Cr, Y, Zr, Nb and Hf could form mictamict alloys together with silicon and nitrogen [140]. Indeed, Cr-Si-N [250-255], Hf-Si-N [236, 256], Nb-Si-N [254, 257-260], V-Si-N [261, 262] and Zr-Si-N [229, 254, 263-277] films have been synthesised since that, albeit only certain Zr-Si-N compositions [264-266, 268, 270, 271, 276, 277] were amorphous. More generally, Nicolet forecast that TM-Si-O as well as several combinations of early transition metals with boron, carbon, silicon, phosphorus and nitrogen might meet the definition of mictamict alloys [136, 138, 141]. The possible combinations can be written in the form TM-(Si,B,C)-(B,C,N) [136]. Amongst them, Ir-Si-O [278, 279], Ru-Si-O [279-282], Ti-Si-O [283, 284], W-B-N [142, 190, 285] and Ti-P-N [162] have been realised. The elements that may form mictamict alloys are highlighted in the periodic table of Figure 6.

	1	2	3	4	5	6	7	8	9	10	11	12	13	14	15	16	17	18
1	1 H																	2 He
2	3 Li	4 Be											5 B	6 C	7 N	8 O	9 F	10 Ne
3	11 Na	12 Mg											13 Al	14 Si	15 P	16 S	17 Cl	18 Ar
4	19 K	20 Ca	21 Sc	22 Ti	23 V	24 Cr	25 Mn	26 Fe	27 Co	28 Ni	29 Cu	30 Zn	31 Ga	32 Ge	33 As	34 Se	35 Br	36 Kr
5	37 Rb	38 Sr	39 Y	40 Zr	41 Nb	42 Mo	43 Tc	44 Ru	45 Rh	46 Pd	47 Ag	48 Cd	49 In	50 Sn	51 Sb	52 Te	53 I	54 Xe
6	55 Cs	56 Ba	*	72 Hf	73 Ta	74 W	75 Re	76 Os	77 Ir	78 Pt	79 Au	80 Hg	81 Tl	82 Pb	83 Bi	84 Po	85 At	86 Rn
7	87 Fr	88 Ra	**															

* Lanthanides

** Actinides

Figure 6. The periodic table showing the elements that may form mictamict alloys.

Yet, mixing right constituents together does not guarantee the resultant film is amorphous and highly metastable. Several films referenced above were nanocomposites having small crystallites embedded in an amorphous matrix, or nanocrystalline. Reid found that most of his sputter deposited (Mo,Ta,Ti,W)-Si-N and W-B-N films had local order of 0.5…1.5 nm, thus being only marginally amorphous [142]. Among the most studied mictamict alloys, Ti-Si-N films seem to be more susceptible to incomplete amorphousness than the others. The microstructure of a film often varies with its exact composition, like in the case of Oizumi *et al.* whose Ta-Si-N films turned from crystalline into amorphous as their Si/(Si+Ta) ratio exceeded 25 % [174, 175]. If a film is sputter deposited, the composition of the sputtering target as well as the use and the flow rate of any reactive gas impact the composition of the film. In addition, it is quite common that sputter deposited mictamict films incorporate a few percents of argon and oxygen as impurities [142]. One should not ignore the role of the analysis method either: a film may look amorphous by XRD but prove partially crystalline by transmission electron microscopy (TEM), the latter being more accurate.

It was observed that the atomic density of (Ta,Ti,Mo,W)-Si-N films rose with the increasing nitrogen concentration, starting from $6…7\cdot10^{22}$ atoms/cm^3 of the silicide films (with no nitrogen), and ending up to $8…9\cdot10^{22}$ atoms/cm^3 of the ternary films with about 50 at.% of nitrogen [142, 165]. The same trend applied to W-B-N films [142, 285]. As an example of mass density, the density of Ti-Si-N films by Vaz *et al.* varied from 3.4 to 5.1 g/cm^3 depending on their composition [215].

3.3 Thermal stability

By the definition, another main feature of the mictamict alloys is their high metastability, i.e. their high resistance to crystallisation upon thermal annealing. It requires

a strong kinetic barrier against nucleation and the subsequent formation of crystalline phases [140]. Even so, amorphous structures are unstable by nature and crystallise if annealed heavily enough [137]. Thus the crucial question is: at which temperature, and how fast?

In general, many originally amorphous mictamict films of the type TM-Si-N start to crystallise at 800...900°C. It is well above the melting point of aluminium (650°C [36]), enabling the use of the mictamict alloys as diffusion barriers. There are a few studies claiming that TM-Si-N films with favourable compositions survived even higher temperatures without crystallisation like illustrated in Figure 7: $Ta_{0.24}Si_{0.10}N_{0.66}$ and $Ta_{0.24}Si_{0.12}N_{0.64}$ at 1100°C for 1 hour [176], $Zr_{15}Si_{25}N_{60}$ at 1100°C for 30 min [264], Mo-Si-N films with the Mo/Si ratio of ½ and 50 at.% N at 1000°C for 1 hour [222], and $W_{24}Si_{21}N_{55}$ at 1000°C (the time was not specified) [247]. However, XRD was used as the analysis method in all these cases. If high-resolution TEM and electron diffraction are used, the onset of crystallisation is typically observed at a 100...200°C lower temperature [140], as TEM is more sensitive to structural changes than XRD. Other mictamict alloys are slightly less stable at elevated temperatures: $Ru_{17}Si_{16}O_{67}$ survived at 800°C for 5 hours without crystallisation [282], Ti_3SiO_8 only at 500°C for 30 min [283, 284], and W-B-N films (of several compositions) at 700°C for 1 hour [285]. It is possible that the crystallisation temperature depends on the substrate the film is lying on: the $Ta_{36}Si_{14}N_{50}$ films by Kolawa *et al.* crystallised at 1100°C on a sapphire substrate, but at 900°C when in contact with copper [164]. As long as the crystallisation temperature is not exceeded, even an extended heat treatment close to that temperature does not necessarily induce crystallisation, e.g. $Ta_{27}Si_{20}N_{53}$ and $Ta_{30}Si_{18}N_{52}$ maintained their amorphous structures at 600°C for 100 hours [146, 157]. Finally, thin films seldom crystallise all at once. The process is more like progressive with some amorphous structure remaining after the onset of crystallisation, and disappearing only gradually.

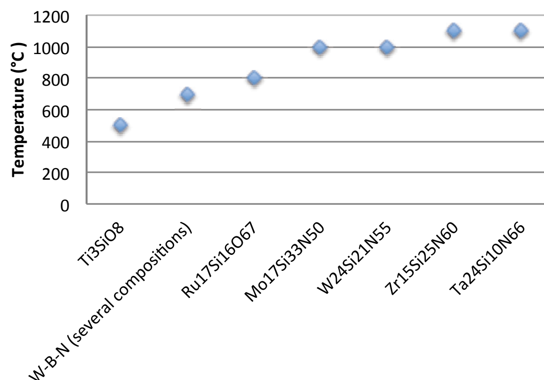

Figure 7. The temperatures at which mictamict films have been reported to remain amorphous at their best. See the text for the references.

Several studies have shown that the composition affects the crystallisation temperature of a mictamict film. Reid proved that any of his (Mo,Ta,Ti,W)-Si-N films could be made stable at least up to 800°C if the nitrogen concentration was just raised high enough [142]. The increase in the crystallisation temperature with a rising nitrogen concentration was observed also by Kuchuk *et al.* [165] with their Ta-Si-N films, by Louro *et al.* [245] and Marques *et al.* [248] with their W-Si-N films, and by Daniel *et al.* with their Zr-Si-N films [264]. In a similar way, higher oxygen content was able to stabilise Ru-Si-O films [282], as well as a higher Si/Ta ratio stabilised Ta-Si-N films [176]. It is possible that thermal annealing induces a loss of nitrogen or oxygen from mictamict films, which has been observed with Ta-Si-N [142], W-Si-N [142, 243, 246], W-B-N [142], Ru-Si-O [282], and especially clearly with Mo-Si-N films [142]. The loss of nitrogen often initiates crystallisation [138]. Consequently, the crystallisation temperature is dependent on the bond strength of nitrogen (or oxygen) to the film at issue [137].

While the mictamict alloys have been praised for their high structural metastability, their propensity for oxidation has gained somewhat less attention. The fact that transition metal nitrides are prone to oxidation at elevated temperatures [138, 179] cast doubt on the chemical stability of the mictamict alloys, too. The mictamict alloys of the type TM-Si-N oxidise indeed [140]. At room temperature in the air, a thin native oxide film is formed on their surface [140] similarly to the classic examples of silicon or aluminium. For $Ta_{36}Si_{14}N_{50}$, the thickness of such surface native oxide was 2 nm [168, 169]. Intentional dry and/or wet oxidation has been proved possible for Ta-Si-N films at 650...850°C [179], and Ti-Si-N films at 500...1000°C [193-195]. When picking the oxidation method, one might prefer wet oxidation because its reproducibility is better than that of dry oxidation with the latter being sensitive to even small amounts of residual moisture [194]. If thick enough, an oxide scale on top of a metallic film can be seen with a colour change of the film surface.

The propensity for *unintentional* oxidation at elevated temperatures is relevant to the real life applications of the mictamict alloys. In these cases, the surrounding atmosphere is often of air. The rather few studies of the topic have considered Ta-Si-N, Zr-Si-N and Mo-Si-N films the best among the mictamict alloys in this respect. The $Ta_{12}Si_{26}N_{62}$ films by Zeman *et al.* [185] started oxidising in flowing air only above 800°C, and had an excellent oxidation resistance up to 1300°C when compared to several other hard coatings. When Ta-Si-N films are oxidised, they transform into Ta-Si-O [179]. The Zr-Si-N films by Musil *et al.* [268, 277] exhibited a high oxidation resistance likewise up to 1300°C. Also the Mo-Si-N films with a high nitrogen concentration (50 at.%) by Hirvonen *et al.* [222] were highly resistant to oxidation up to 800°C under wet oxidation conditions. At the opposite end, Ru-Si-O films have proved quite unstable in oxidising environs [280-282]. For example, the $Ru_{20}Si_{15}O_{65}$ films by Gasser *et al.* [281] oxidised already at 600°C in 30 minutes or less when exposed to dry oxygen. Annealing of Ir-Si-O films in dry oxygen at 700°C, instead, did not induce changes in their composition [278]. Ti-Si-N films were able to resist oxidation up to 900°C at their best [187], but unfavourable compositions oxidised already at 500°C in the air [212, 213]. Yet they are more stable than their nitride counterpart, TiN [202, 211-213]. When Ti-Si-N films are oxidised, they

change into Ti-Si-O comprising of TiO_2 and SiO_2 [187, 194, 195]. Finally, W-Si-N films with their most optimum composition were able to stand 800°C without oxidation, but even a high Si_3N_4 content did not raise the stability above that [249].

When a low oxidation rate is pursued, raising the silicon content of TM-Si-N films is an option. Several studies have shown that an increase in the silicon concentration was able to improve the oxidation resistance of the film: [185] for Ta-Si-N, [187] and [213] for Ti-Si-N, and [266] for Zr-Si-N. A silicon oxide layer on the surface of a TM-Si-N film acts as an oxygen diffusion barrier retarding the further oxidation of the underlying film in a rather efficient way [187, 202, 247]. Another option to improve the oxidation resistance of TM-Si-N films is their pre-annealing in a vacuum or an inert atmosphere like Kacsich *et al.* did [195]. Pre-annealing at 800°C altered the microstructure of their Ti-Si-N films resulting in TiN-like grains growing in an amorphous SiN_x matrix. As the matrix was depleted of titanium, the oxidation rate of the film was decreased significantly. Kacsich *et al.* supposed the same could work for other TM-Si-N alloys as well.

3.4 Mechanical properties

The amorphous metals, discussed in Section 2.3, have certain outstanding mechanical properties; especially, they are highly elastic. Similar to them, the mictamict alloys have an amorphous microstructure and a metallic ingredient (an early transition metal). The fact is followed by an immediate question: Could the mictamict alloys possess similar unique properties, but as thin films with easy MEMS process integration? If the answer was yes, they would be a truly interesting material candidate for MEMS.

Among the mechanical properties of the mictamict alloys, elastic modulus (Young's modulus), hardness and residual stress have been surveyed the most. A major part of these studies concern Ti-Si-N films because of their role as hard, wear-resistant coatings (see Section 3.7). Elastic modulus and hardness often correlate, i.e. they increase together [248, 249]. Both are dependent on the microstructure, and consequently on the deposition conditions such as the deposition temperature [188, 201, 211, 219], the substrate bias voltage [188, 201, 211, 215], the silicon target current [241], and the nitrogen partial pressure [217, 249] (all related to TM-Si-N films). Several studies show the elastic modulus and the hardness of TM-Si-N films rise with the increasing silicon content. However, this trend holds only at low silicon concentrations: after a certain concentration limit is exceeded (typically between 5 and 15 at.%), the values of these parameters turn down again. [186, 197, 201, 202, 204, 211, 213, 217-219, 265, 266] The elastic moduli of Ti-Si-N films are usually in the range of 200…300 GPa [186, 200, 201, 204, 214, 215], albeit a value of 700 GPa has been reported at the most [188]. The few reported values for W-Si-N films are of the same order [246, 248]. The typical hardness values of Ti-Si-N and W-Si-N films fall between 20 and 50 GPa [197, 200-202, 204, 211, 213, 217-219, 241, 242, 245, 246, 248, 249]. For a comparison, the elastic modulus of single crystal silicon is 130…190 GPa depending on the crystal orientation, and its Knoop

hardness 850 kg/mm^2 (8.3 GPa) [36, 52, 286]. Elastic modulus and hardness are prone to change if a film is annealed at temperature high enough to change its microstructure. For example, the hardness of $W_{26}Si_{28}N_{46}$ films increased from 27 to 45 GPa when annealed at 900°C [245]. The study repeated the general trend: the hardness of W-Si-N films increases with annealing temperature until a turning point (usually around 1000°C) is reached, after which lower hardness is observed again [245, 246, 248].

When a film is supposed to serve as a structural part of a MEMS device, its residual stress gets significant; commonly, low tensile stress is aimed at. As-deposited mictamict alloy films have been frequently reported to have compressive residual stress ([142, 151, 154, 155, 165, 167] for Ta-Si-N, [197, 201, 214, 219] for Ti-Si-N, [142, 240-242, 249] for W-Si-N, and [264, 270] for Zr-Si-N), while the films under tensile stress are few ([198] for Ti-Si-N, [249] for W-Si-N, and [264] for Zr-Si-N). Like for elastic modulus and hardness, residual stress is affected by the deposition conditions such as the N_2/Ar gas flow ratio [154, 165] or the sputtering pressure [240]. Especially, the residual stress of TM-Si-N films appears to change with their silicon content [197, 201, 214] albeit Musil *et al.* concluded just the opposite [249]. Their W-Si-N films with identical N/Si ratios could have unequal residual stress if sputtered with dissimilar values of the substrate ion current density. Subsequently, they concluded it is not the silicon content but rather the phase composition that is decisive. The frequently encountered compressive stress of the mictamict alloys can be relaxed or turned tensile by thermal annealing [142, 151, 155, 167, 214, 240], and even while the amorphous microstructure is maintained [142, 151, 240]. Because the eventual residual stress is a function of the annealing temperature, the stress can be tuned to a specific value by carrying out an appropriate heat treatment [151]. A subsequent heat treatment does not alter the stress state as long as the primary annealing temperature is not exceeded [151]. Reid explained the irreversible stress changes observed in TM-Si-N films by densification and plastic deformation [142]. Besides annealing, it is possible to adjust the residual stress of the mictamict alloys by their deposition parameters, particularly the sputtering pressure (see Section 2.2.2).

The measured data on the surface roughness of mictamict alloys is few and inconsistent. The reported roughness values range from 0.2 % of the film thickness (0.2 nm for 100 nm thick Ta-Si-N films [154]) to more than 5 % of the film thickness (3 nm for 45 nm thick amorphous $W_2NSi_{0.15}$ films [243]). Thus an amorphous microstructure in itself does not seem to guarantee a particularly flat film surface. However, the surface roughness of nanocomposite Nb-Si-N films proved to decrease with the increasing N_2 partial pressure during sputter deposition, owing to a smaller grain size (a more amorphous nature) of the films [259].

3.5 Electrical properties

TM-Si-N films, the most important embodiments of the mictamict alloys, can be perceived as quasi-binary systems of a transition metal nitride and Si_3N_4 [140]. They

are often deposited by sputtering a silicide target (like Mo_5Si_3) in nitrogen gas. On this background, one could expect the electrical properties of TM-Si-N films reflect those of the constituting binary compounds. The resistivities of transition metal silicides and nitrides are typically a few hundred μΩcm [142], while Si_3N_4 is an insulator. For a comparison, many elemental metals have a resistivity of a few μΩcm (see Section 2.1.2). The resistivities of as-deposited mictamict alloys comply with the above expectation indeed. The reported values range from 140 μΩcm of $Zr_{41}Si_{11}N_{48}$ [274] to even 40 mΩcm of $Ti_{17}Si_{35}N_{48}$ [208] and 100 mΩcm of Ru-Si-O films with 50 at.% oxygen [282]; however, the usual resistivities of mictamict alloys fall between 200 μΩcm and 2 mΩcm. This is lower than for polysilicon, albeit the resistivity of heavily doped polysilicon may overlap with that of a mictamict alloy with a high nitrogen (or oxygen) content.

The resistivity of a particular mictamict alloy film depends on its composition and structure, the ambient temperature, and the potential heat treatment it has experienced. The most obvious trend is confirmed by numerous studies: the resistivity of mictamict alloys increases as their nitrogen (or oxygen) content rises. This is understandable as Si_3N_4 and SiO_2 are insulators. The resistivity rise with the increasing nitrogen content is monotonic but not linear: a sharp rise is often encountered when the nitrogen concentration exceeds about 50 % (e.g. [142, 161, 208]). Reid explained this by a change in the local chemical ordering of the amorphous films [142]. The trend of a monotonic rise did not apply to Ru-Si-O films whose resistivity had a peak at 50 at.% of oxygen and decreased beyond that [282]. Besides nitrogen, a rise in the silicon content or the silicon to metal ratio of TM-Si-N films also made the resistivity go up [176, 190, 207, 208]. The effects of different constituents are dependent on each other. Having Ti-Si-N as an example, the adding of nitrogen increased the resistivity faster for Si-rich than for Ti-rich compounds [208]. In general, a change in the composition is capable of turning a mictamict alloy from metallic to semiconductive, and further to insulating [140].

The resistivity of TM-Si-N films tends to decrease with the increasing ambient temperature, in other words, their temperature coefficient of resistance (TCR) is negative [142, 147, 175, 176, 191]. Apart from few exceptions, high temperature annealing induces a resistivity drop for TM-Si-N [142, 207, 208] as well as for Ru-Si-O films [282]. Reid found that when his $Mo_{35}Si_{17}N_{48}$ films were annealed at 900°C for 1 hour, their resistivity decreased to about one tenth of the as-deposited value, while the corresponding change for $Ta_{36}Si_{14}N_{50}$ films was less than 20 % [142]. The annealing-induced resistivity drop has been explained by a relaxation of the atomic disorder and the intergranular strain, or by grain growth (in the case of crystalline films) [208].

When a mictamict alloy film (or any other conductive film) gets thin enough its electrical behaviour is likely to change. In general, the resistivity of a metal film increases due to surface scattering as the film thickness approaches the electron mean free path [32]. Aouadi *et al.* determined the resistivity of ultrathin (≤ 10 nm) Ta-Si-N films as a function of thickness [144]. Started at zero thickness, they found the resistivity decreased rapidly for the first 5…7 nm, after which the fall-off was slower. The authors explained the thinnest films were composed of discrete islands,

and their electrical conduction took place through quantum mechanical tunnelling and thermionic emission. As the islands coalesced, the classical conduction mechanisms with scattering effects started to dominate.

3.6 Process technology

Reactive sputtering in the presence of nitrogen (or oxygen) gas is by far the most common method to deposit mictamict films. The use of a compound target (like Ta_5Si_3 or $TaSi_2$) or two separate targets (like Ta and Si) is equally possible. The former choice is simpler, while the latter enables the tuning of the metal to silicon ratio in a less limited way. The nitrogen concentration in the depositing film can be adjusted by the nitrogen flow rate. Alternatively, it is possible to co-sputter a metal and a Si_3N_4 target to produce TM-Si-N films [218]. For a given target composition, the increase in the nitrogen content (through changing the flow rate) took place at the expense of a decreased metal to silicon ratio in the case of Mo-Si-N, Ta-Si-N, W-Si-N and W-B-N systems [142]. For a given nitrogen flow, on the other hand, the nitrogen incorporation into the film was dependent on the target composition [142]. In some cases, conventional sputter deposition was combined with arc ion plating (AIP) [188], or a depositing film was bombarded purposely with an ion flux [197, 217]. The aim of these experiments was to synthesise hard nanocomposite Ti-Si-N coatings. Sputter deposition in general was discussed in Section 2.2.1.

Mictamict alloys can be synthesised also by CVD, albeit these examples are much fewer in number. The use of CVD methods is motivated by their high deposition rate [243] and good step coverage. Ti-Si-N films were deposited by thermal CVD from TiI_4, SiI_4 and NH_3 [189] or from tetrakis(diethylamido) titanium (TDEAT), NH_3 and SiH_4 [190] as precursors, W-Si-N films from WF_6, NH_3 and Si_2H_6 [190, 243], and W-B-N films from WF_6, SiH_4, B_2H_6 and NH_3 [190]. A typical deposition temperature was 350°C. The structure, resistivity and diffusion barrier properties of these films resembled closely those of their PVD deposited counterparts [190]. Ti-Si-N films were also deposited by PECVD at 500°C in a gaseous mixture of $TiCl_4$, $SiCl_4$, N_2, H_2 and Ar [202], and by an inductively coupled plasma (ICP) assisted CVD/PVD hybrid tool [200, 219].

Among the mictamict alloys, the etching behaviour of only Ta-Si-N and Ti-Si-N films has been studied. There are several plasma chemistries by which the etching of Ta-Si-N films is possible: CF_4/O_2 [168, 169], CHF_3/O_2 [170], SF_6/O_2 [155, 167], and C_2ClF_5/SF_6 [155, 167]. In the case of the first two options, etching began only after a native surface oxide was broken through, resulting in an initial delay time quite typical of reactive ion etching (RIE). Between the last two options, C_2ClF_5/SF_6 proved better than SF_6/O_2 in terms of uniformity [155], selectivity and undercutting [167]. The etch rates varied around 100 nm/min depending on the exact values of the process parameters. Important to micromachining, Ta-Si-N films were proved to withstand H_3PO_4+HNO_3 (the wet aluminium etchant) [155, 167], buffered HF (BHF) (7:1), HNO_3 and H_2SO_4+H_2O_2 (Piranha) [155], enabling selective aluminium etching, the wet release etching of sacrificial silicon oxide layers, as well as cleaning

and photoresist stripping. The etching of Ti-Si-N films was possible by BCl_3/Cl_2 plasma with a rather low etch rate of 23 nm/min, and a selectivity of 5:1 over fused silica [198, 199].

3.7 Applications

The two most important applications of the mictamict alloys are diffusion barriers and hard coatings. While diffusion barriers were studied intensively in the 1990s, hard coatings have attracted research interest in the 2000s. Amorphous films are a tempting choice for diffusion barriers in integrated circuits because grain boundaries, which act as fast diffusion paths, are absent. Mictamict alloys are interesting for barriers also because of their high thermal stability. Indeed, several amorphous mictamict alloys have proved to work as diffusion barriers in Al/Si and Cu/Si contacts (e.g. [138]), with Ta-Si-N being the most frequently studied. An old but extensive research of Reid showed that Ta-Si-N, Ti-Si-N and W-Si-N barriers were stable in contact with copper for 900°C/30 min at their best, and Mo-Si-N and W-B-N barriers for 800°C/30 min at their best [142]. The thickness of these films was about 100 nm. It is not a limit, however: 10 nm thick Ta-Si-N films acted as efficient diffusion barriers for copper for 800°C/90 min as well [144]. In contact with aluminium, Ta-Si-N barriers stood for 700°C/20 min and Mo-Si-N and W-Si-N barriers for 675°C/10 min without a failure, that is, aluminium could be melted on top of them [138, 142]. Ta-Si-N films have also served as diffusion barriers for gold [165, 177, 178, 181, 182], bearing 750°C/30 min in Au/Si contacts [177]. A failure often coincides with the crystallisation of the barrier film (e.g. [138]). Whether the resistivity of a particular mictamict alloy film is acceptable for use as a diffusion barrier depends on its composition; however, the resistivities of mictamict alloys are always a few hundred μΩcm at least (see Section 3.5).

Hard, wear-resistant coatings are the other main application of the mictamict alloys. Besides excellent mechanical properties, hard coatings must be thermally stable and have high oxidation resistance at high temperatures. Transition metal nitride films, above all Ti-N, are frequently used for protective coatings [185, 201, 202, 287]. The addition of silicon is anticipated to further improve the properties of these films, especially in relation to their oxidation resistance [201, 202, 215]. Being a direct derivative of Ti-N, Ti-Si-N films have been studied by far the most for protective coatings among the mictamict alloys (e.g. [192, 197, 200-202, 210, 211, 215, 217]) but studies of W-Si-N [242, 245, 246, 248], Ta-Si-N [185] and Zr-Si-N [266] films also exist. However, these TM-Si-N films are commonly not amorphous but nanocomposite, i.e. they have nanocrystallites embedded in an amorphous matrix. The nanostructured two-phase systems are developed so as to avoid the usual fracture mechanisms of both crystalline and amorphous materials [211, 215].

The MEMS applications of the mictamict alloys have been few in number. Linder *et al.* [167], Grétillat *et al.* [155] and Dubois *et al.* [153] each fabricated free-standing surface micromachined structures of 1…3 μm thick sputter-deposited Ta-Si-N films, resulting in beams and bridges [155, 167] and a gas microvalve [153]. Aluminium

[153, 167] and phosphorus doped silica glass (PSG) [155] served as sacrificial layers. The former was selectively removed by wet aluminium etchant (H_3PO_4+HNO_3) and the latter by BHF without a deterioration of the Ta-Si-N films. The Ta-Si-N films themselves could be patterned by standard photolithography and plasma etching (see Section 3.6). The compressive stress of the as-deposited Ta-Si-N films was reduced by annealing at 450°C, alleviating the unwanted buckling of the free-standing MEMS structures [155, 167]. The lifetime of the electrostatically actuated microvalves was over 1 million cycles, and not limited by the Ta-Si-N structural layers [153]. The interest in Ta-Si-N films was awoken by their IC compatibility [155], low resistivity [153, 155, 167], Young's modulus (being close to that of silicon) [153, 167], and the possibility to control their residual stress [153]. Moreover, it was speculated that the amorphous structure of Ta-Si-N films would hamper fatigue and wear [155, 167], leading to better mechanical reliability [153]. Since MEMS has been such an unexplored field for the mictamict alloys, the use of Mo-Si-N films in real MEMS devices (described in the experimental part of this thesis) was a novelty.

Other applications of the mictamict alloys are just sporadic studies. Ta-Si-N films have been used for low stress x-ray masks [151], anti-corrosive coatings for wafer-level packaging [152], thin-film resistors [171], and conductive encapsulants of GaAs [172, 173]. Ti-Si-N films have been investigated for attenuated phase-shift masks [198, 199], W-Si-N films for annealing caps on GaAs [240], and Ti-Si-O films for optical coatings [283, 284].

4. Mo-N thin films

4.1 Introduction

Amorphous metals stand out with their mechanical properties; above all, they are highly elastic (Section 2.3). Such high elasticity would be a tempting feature also in MEMS. Surface micromachined MEMS devices are made up of thin films. However, elemental metal films take practically always a polycrystalline form [36]. To obtain an amorphous metal film, its crystalline structure should be disturbed by alloying.

Molybdenum (Mo) is a metal that is commonly found in IC fabs. It belongs to the transition metals, and is also classified as a refractory metal. In general, refractory metals have very strong interatomic bonding, which accounts for their extraordinarily high melting temperature, large elastic modulus, and high strength and hardness [62]. Nitrogen (N) is a non-metal. Under standard temperature and pressure (STP), it is a colourless, odourless and tasteless gas. Nitrogen is frequently found as a biatomic molecule with a strong triple bond. Because of the strength of this bond, gaseous N_2 is rather inert. Nevertheless, nitrogen forms binary compounds with almost any element in the periodic table, including all metals. The metallic nitrides are usually opaque, hard, chemically inert, refractory materials with metallic lustre and conductivity. [288] When Mo is combined with N, they end up molybdenum nitrides that can be synthesised easily as thin films [289-327]. Since the incorporation of nitrogen into polycrystalline molybdenum films turns the film structure more disordered (e.g. [289]), i.e. more amorphous by nature, Mo-N films became the first attempt towards the amorphous metal films for MEMS.

Chapter 4 begins with a literature review of the main features of Mo-N films. The experimental part describes the deposition and properties of Mo-N films, and eventually the reasons for the attractiveness of Mo-Si-N films. The thermal stability of Mo-N films is discussed here as well, although the motive for the study appeared only after Mo-Si-N films were synthesised and *they* were annealed.

4.2 Review

4.2.1 Process technology

Reactive sputtering is the most frequently used method to deposit Mo-N films [289-310]. When a molybdenum target is sputtered in the presence of nitrogen, nitrogen as a reactive gas binds itself into the depositing film. The nitrogen concentration in Mo-N films increases with the N_2 partial pressure prevailing during sputtering [30, 289, 293, 297, 301], sometimes even in a linear manner [297]. The surface of the molybdenum target nitrifies as well. DC biasing is still possible as molybdenum nitrides are conductive and do not bring on arcing. The deposition rate falls at high N_2 pressures, however, because of target poisoning [30, 289, 293]. Values between 10 and 45 nm/min have been reported for the deposition rate of Mo-N films [30, 289, 291, 293, 301], albeit the exact rate always depends on the particular deposition system and the parameters that are used. The general sputtering parameters, relevant also to the deposition of Mo-N films, were discussed in Section 2.2.1.

CVD methods are another way to synthesise Mo-N films [311-314]. The conformality of CVD films is better than that of sputter deposited ones, but CVD processes usually require a higher deposition temperature: 200°C at the least [311], and 400...700°C in a normal case [312-314]. $Mo(N(CH_3)_2)_4$ and NH_3 [311], MoF_6, NH_3 and H_2 [312], $MoCl_5$ and NH_3 [313, 314], and $Mo(CO)_6$ and NH_3 [314] are all possible combinations for the precursors. The deposition rate can be anything between 10 and 1000 nm/min [311, 314]. If the reaction rate is too high, one can end up with powdery Mo-N instead of a film [312]. CVD processed Mo-N films may contain a substantial amount of hydrogen as an impurity; at the worst a Mo/H atom ratio of 1.0 was reported [311]. The synthesis of Mo-N films is feasible also by ALD, which is a special case of CVD processes [315-317]. In general, ALD films are very conformal and uniform. As a drawback, their deposition rate is very low.

The direct synthesis of Mo-N by letting molybdenum react with gaseous nitrogen is regarded as rather difficult [328] but not impossible: He *et al.* prepared thin (20 nm) Mo_xN films by annealing sputter deposited Mo films in N_2 gas at 700°C [323]. The direct reaction is impeded by the low chemical affinity of molybdenum for nitrogen, lower than that of other transition metals [286, 297, 327, 328]. Still other methods for the deposition of Mo-N films are arc PVD [318-321], pulsed laser deposition (by ablating a molybdenum target in the presence of nitrogen) [322, 324, 325], and laser-promoted nitridation [327].

The data on the etching of Mo-N films are rather scarce. Fix *et al.* reported that their Mo-N films with a high hydrogen content were resistant to HCl but dissolved readily in HF [311]. Chuang *et al.* patterned Mo-N films in an etching solution of H_3PO_4:HNO_3 = 100:1 [293], and Kattelus *et al.* in a commercial wet aluminium etchant [30]. The last-mentioned found the amorphous compositions were etched the fastest, about 250 nm/min. The etching of Mo-N films by $CF_4/Cl_2/O_2$ plasma chemistry was possible as well [30].

4.2.2 Composition and structure

MN, M_2N and M_4N are general formulae for metallic nitrides [288]. The equilibrium phase diagram exhibits three solid phases for the Mo-N system at room temperature: pure Mo, Mo_2N and MoN [308]. In practice, Mo-N films are often non-stoichiometric, and so their composition can be expressed by MoN_x where *x* does not need to be an integer. In the case of sputter deposited Mo-N films, the nitrogen concentration in the films can be adjusted by the N_2 partial pressure prevailing during sputtering: the higher the N_2 pressure, the higher the nitrogen concentration [30, 289, 293, 297, 301]. Since oxygen is more reactive than nitrogen and the Mo-O bond is more stable than the Mo-N bond [291, 303], it is not uncommon that sputter deposited Mo-N films incorporate several atomic percents of oxygen as an impurity [289, 297, 303, 307]. Carbon impurity may be found as well [289].

In order to get amorphous films, the innate grain growth of elemental Mo films must be restrained somehow. One alternative is to incorporate nitrogen into them (Section 4.1). When this is done, the end result still varies. Regardless of the deposition method, both crystalline and amorphous Mo-N films may be encountered. A survey through a sample of sputter deposited Mo-N films indicated that most reported films were crystalline [30, 289, 291, 293, 294-300, 302, 303, 307-309] or mixtures of amorphous and crystalline phases [30, 290]. Amorphous films [30, 293, 301, 302, 308, 309] were rarer even if sputtering as a low temperature deposition method should work in favour of an amorphous microstructure [301]. The above finding reflects the fact that transition metal nitrides are much more difficult to make amorphous than their silicide or boride counterparts [142]. While Wang *et al.* managed to turn their sputter deposited Mo-N films amorphous by increasing the nitrogen content high enough (50 % of the sputtering gas) [308, 309], the others obtained amorphous films only in a certain range of nitrogen pressure [30, 293]. Shen *et al.* suggested nitrogen might act as a roadblock or a trap for diffusing Mo atoms, or serve as a nucleation site for lattice defects, each decreasing the mobility of Mo atoms, and thus preventing grain growth [303]. Chuang *et al.* concluded that nitrogen was located mainly in Mo grains and grain boundaries at low nitrogen contents, while the chemical reaction between Mo and N became significant only at higher nitrogen contents [293]. Oxygen, if incorporated into Mo-N films, tends to further decrease the grain size, i.e. to make the films more amorphous [289, 291, 294, 303]. The total sputtering pressure, with its clear relation to the microstructure [302], is yet another parameter to play with. For example, the same Wang *et al.* noticed their earlier crystalline Mo-N films turned amorphous when the total sputtering pressure was increased high enough (15 mTorr = 2.0 Pa) [309]. They explained the higher pressure induced a higher deposition rate which further induced the amorphisation as the atoms did not have time to organise themselves in a crystalline structure before another layer of atoms was landing. Finally, the microstructure may well depend on the film thickness, too [303].

There are a few studies reporting the mass density of sputter deposited Mo-N films, each with compositions close to Mo_2N [30, 301-303]. The reported mass densities varied from 7.4 to 9.5 g/cm^3. The nitrogen partial pressure [30] and the

sputtering pressure [302] made only a slight difference, while a heat treatment at 600°C induced an increase of 10… 20 % in the density [301, 302]. The densification can be easily explained by crystallisation, i.e. the enhanced ordering of the microstructure [303]. The above Mo-N films are heavier than the mictamict alloys reviewed in Section 3.2.

4.2.3 Thermal stability

Elemental molybdenum is prone to oxidation at high temperatures, and the reaction product, molybdenum trioxide MoO_3, is volatile (e.g. [329]). The stability of molybdenum nitrides under oxidative conditions, however, was not studied thoroughly until the early 2000s according to [320].

Depending on the atmosphere at issue, two different pictures of the thermal stability of Mo-N films are outlined. When Mo-N films are annealed in a vacuum (i.e. under very low pressure) or a protective gas (like Ar or N_2), their stability is moderate. Originally amorphous Mo-N films survived a heat treatment at 700°C without crystallisation; neither did they react with silicon at the same temperature. However, both crystallisation and the formation of silicides took place at 800°C. [293, 308, 309] For a comparison, elemental Mo reacted with silicon at 650°C forming Mo_5Si_3 [293]. The above temperatures are roughly comparable to the stability region of the mictamict alloys, discussed in Section 3.3. Some other Mo-N films, however, started to crystallise already at 450°C followed by a concurrent densification. The resulting Mo_2N structure was stable up to 750°C above which it started to lose nitrogen, converting to pure Mo. [301-303]

The picture gets worse when Mo-N films are heated in an oxidative atmosphere like air. Doing that, MoN films showed first signs of oxidation at no higher than 225°C [295], and Mo_2N films at 350°C [295, 307, 320]. Such temperatures are notably low. The oxidation was accompanied by the rapid decrease of the surface reflectivity of the films [295]. The oxidation of Mo_2N takes place through

$$Mo_2N + 2O_2 = 2MoO_2 + 1/2N_2 \qquad (7)$$

and

$$MoO_2 + 1/2O_2 = MoO_3 \qquad (8)$$

The developing oxide scale is not protective as the reaction product MoO_3 is volatile above 550°C. Furthermore, Mo_2N can decompose at 681°C and above by

$$Mo_2N = 2Mo + 1/2N_2 \qquad (9)$$

after which the resulting Mo can oxidise again to volatile MoO_3. [320] As a result, Mo-N films can be consumed eventually away as they are prone to lose both Mo and N when annealed under oxidising conditions. In conclusion, the oxidation resistance of Mo-N films is rather poor resembling that of pure Mo in respect of both reaction temperatures and reaction products [320].

The perceptions whether oxygen incorporation makes Mo-N films more or less stable are conflicting. Cunha *et al.* found the adhesion of their Mo-N coatings superior to that of the Mo-N-O coatings when annealed above 500°C [294]. Shen *et al.* instead regarded Mo-N-O as more stable, since their Mo_2N films started to convert to Mo at 800°C, while the Mo-N-O films were still stable at 850°C with no loss of nitrogen or oxygen [303]. All these experiments were conducted in a vacuum. The oxidation of Mo-N is not a disadvantage in all circumstances. The lubricious oxides of Mo-N may reduce the friction of hard coatings (used on cutting tools and machine parts); yet the onset of intense oxidation at 350°C and the formation of volatile MoO_3 above 500°C set the upper limit to the operating temperature [295, 307].

4.2.4 Mechanical properties

The residual stress of metal films depends on their microstructure. The microstructure of sputter deposited molybdebum films, in turn, depends strongly on the sputtering pressure like e.g. Shen *et al.* have proved [302]. Deposited under a low Ar pressure (2 mTorr), their Mo films had a dense crystalline structure and high compressive stress. After increasing the Ar pressure to 12 mTorr, Mo films with a very columnar structure and high tensile stress were obtained. A further pressure increase to 40 mTorr resulted in a dendritic-like microstructure and almost full stress relaxation. [302] Elemental metal films prepared by sputter deposition are often impaired by large internal stress variations, making them unsuitable for MEMS [30]. Nitrogen incorporation is a prospect of changing the fact.

Most reported values for the residual stress of as-deposited Mo-N films indicate a compressive stress, usually between -0.5 and -3.0 GPa in magnitude [30, 291, 294, 295, 297, 301-303, 305, 306, 319]. Tensile stress is rarer, even though possible [30, 297, 302]. The residual stress of sputter deposited Mo-N films is governed by the joint action of the nitrogen concentration and the total sputtering pressure [30, 302], the latter being influential because it governs the ion bombardment the film experiences during its growth (e.g. [302]). Kattelus *et al.* showed how a proper nitrogen concentration, inducing the amorphisation of Mo-N films, was able to eliminate lateral stress variations in the plane of the film surface. By selecting a suitable total pressure, the consequential laterally uniform stress could be tuned thereafter from compressive to tensile across the zero stress. A vertical stress gradient still remained. [30] If a stress gradient exists, it can prevail in either direction: the stress can turn more compressive or more tensile as the film gets thicker [30, 303]. Oxygen incorporation, along with amorphisation, was able to relax the compressive stress of Mo-N films as well [291, 303]. It also made the vertical stress gradient vanish [303]. In conclusion, in total three studies indicate a relationship between an amorphous microstructure and the diminution of internal stress variations [30, 301, 303].

As annealing can change the microstructure of Mo-N films, it is also capable of changing their stress state. Three studies of the topic (Gassner *et al.* [295], Shen *et al.* [301] and Stöber *et al.* [306]) have proved the same: when a threshold temperature is exceeded, the compressive stress of as-deposited Mo-N films turns steeply more tensile by nature. The onset of the stress change took place between 350°C

and 480°C depending on the composition [295, 301, 306]. The stress change was accompanied by crystallisation, and explained by concurrent volumetric shrinkage [301]. During the films were heated up to the threshold temperature and cooled back to room temperature, their stress behaviour followed linear thermoelasticity [295].

Values between 240 and 450 GPa have been reported for the elastic modulus of Mo-N films [30, 291, 294, 297, 319], with the highest values achieved for films deposited by arc PVD [319]. For the hardness, most reported values fall in the range of 18...28 GPa [30, 287, 291, 294, 297, 307, 322], albeit 4...5 GPa at the lower end [312] and 39...50 GPa at the upper end [318, 321] have been encountered as well. The softest films were deposited by CVD, and the hardest by arc PVD. For a comparison, the hardness of bulk γ-Mo_2N was 17 GPa [297]. The elastic modulus and the hardness of the mictamict alloys were roughly of the same order (Section 3.4). In general, high hardness is said to relate to a covalent bonding, a small crystallite size, low porosity and high compressive stress [287, 297]. If oxygen was incorporated, it induced a rapid decrease in both the elastic modulus and the hardness of sputter deposited Mo-N films [291].

Shen *et al.* measured the surface roughness of their 160 nm thick Mo-N films [301]. The root mean square (RMS) roughness of the as-deposited amorphous films was 0.6 nm but it increased to 2.0 nm as the films were crystallised upon annealing at 500°C. Similar to some mictamict alloys, the roughness of sputter deposited Mo-N films decreased with the increasing nitrogen content, along with their amorphisation [308].

4.2.5 Other properties

The electric resistivity of Mo-N films can vary from less than 50 µΩcm to above 10 mΩcm depending on their nitrogen concentration. Very consistently, an increase in the nitrogen concentration leads to an increase in the resistivity, just like for the mictamict alloys. [30, 289, 292, 293, 303, 308, 309, 311, 315, 322] This happens likely because nitrogen tends to decrease the grain size if not make the films amorphous, or it may act as an electron acceptor, binding free electrons provided by the metal atoms of the matrix [308, 309, 311, 322]. Similar to nitrogen, an increase in the oxygen content (i.e. the formation of molybdenum oxynitrides) makes the resistivity rise [303]. In addition, the resistivity of ALD deposited Mo-N films depended strongly on their deposition temperature [315]. The temperature coefficient of resistance (TCR) of Mo_2N films was negative at 30...300 K showing a temperature dependent activation energy [289]. When annealed, the resistivity of Mo-N films kept stable up to 700°C beyond which it declined [292, 308, 309]. The fall-off was accompanied by the crystallisation of the films [308, 309].

It has been predicted theoretically that the superconducting transition temperature of f.c.c. MoN is 29 K [289, 324]. In practice, tetragonal β-Mo_2N films proved to be superconductive below 5.2 K [324, 325], while the critical temperature for MoN is 12.8 K [330]. Apparently, there is a critical relation between the stoichiometry and the superconductivity of Mo-N films [324].

The typical appearance of Mo-N films is metallic and mirror-like (e.g. [315]). The measurement of Atuchin *et al.* showed the optical constants (the refractive index n and the extinction coefficient k) of sputter deposited Mo_2N films were wavelength dependent, and determined by the substrate temperature and the relative N_2 partial pressure prevailing during sputtering [290]. The complex index of refraction varied from $\tilde{n} = 2.55 + i1.71$ to $\tilde{n} = 3.29 + i2.69$ herein. The thickness of Mo-N films was measurable by laser ellipsometry up to 85 nm, beyond which optical absorption got too high [290].

4.2.6 Applications

The most important applications of Mo-N films, diffusion barriers [293, 298, 299, 304, 308, 309, 315, 323] and hard, wear-resistant or tribological coatings [295, 297, 307, 317, 318-321], are common to those of the mictamict alloys (see Section 3.7). Molybdenum nitrides have also been considered for corrosion-resistant coatings [321], catalysts [331-334], superconductors [324, 325], the gate electrode for metal-oxide-semiconductor (MOS) capacitors [292], interconnections in semiconductor devices [302], electrodes for high energy density electrochemical storage devices [313, 314] as well as nanotubes (to be used in catalysis) [316].

As diffusion barriers between silicon and copper, Mo-N films have consistently proved to stand a heat treatment at 600°C for 15...30 min without a failure [293, 298, 304, 315], showing an improvement on Mo films [293, 323]. This can be due to the amorphous microstructure of Mo-N films, or because the grain boundaries were stuffed by nitrogen atoms [293, 323]. Failures were attributed to diffusion along grain boundaries or defects [293, 298], which both are common failure mechanisms. As diffusion barriers between aluminium and gold, crystalline Mo_2N films were able to preclude the interdiffusion only below 500°C [299].

Apparently the first published work on Mo-N films for MEMS applications was the one by Kattelus *et al.* from 2002 [30]. It constituted the starting point with which this thesis went on. Besides the basic characterisation of the sputter deposited Mo-N films at issue, the study showed how to eliminate the lateral stress variations of Mo based films by way of their amorphisation (described in Section 4.2.4). It also demonstrated the first MEMS structures formed of Mo-N films: beams that curved upwards owing to their vertical stress gradient. No functional MEMS devices were yet presented. Also Stöber *et al.* [305, 306] have recently studied Mo-N films for MEMS applications, but without the demonstration of any micromechanical structures.

4.3 Experimental procedure

Three sputtering systems were used for the reactive sputter deposition of Mo-N films: Balzers LLS 801 for 100 mm substrates, updated Provac LLS 801 for 100 mm substrates, and further updated Provac LLS 801 for 150 mm substrates; however,

the systems were close counterparts of each other. The magnetron-type batch systems had a rotating sample holder carrying 100 mm wafers in three rows, or 150 mm wafers in two rows. As the cylindric sample holder drum rotated around its axis, wafers passed by a rectangular, vertically positioned molybdenum target sputtered in a gas mixture of argon and nitrogen. The electric power applied to the molybdenum target, the nitrogen flow rate (N_2 partial pressure) and the argon flow rate (Ar partial pressure) were adjustable. The chemical composition of Mo-N films was determined by the first two, while argon was used for controlling the total pressure besides its conventional role in sustaining sputtering discharge. Since molybdenum nitrides are conductive, DC biasing of the molybdenum target was possible. Prior to deposition, the target was always cleaned by pre-sputtering. No external heating was used. Film thickness was determined by the rotation speed and the number of revolutions of the sample holder; however, only the latter was varied herein.

The numerical values of the sputtering parameters are listed in Table 2. The 100 mm deposition process at Balzers was developed before the author joined the work, and has been reported in [6] and [30]. The 100 mm process at Provac was effectively a copy of the former. Most experimental results presented in this thesis were obtained with the 150 mm process at Provac that was characterised by the author; the cases for which this does not hold true will be specified separately. The parameters for the standard 150 mm process were picked on account of the favourable residual stress state of the resulting Mo-N films like described later in Section 4.4.

Table 2. The sputtering processes for the deposition of Mo-N films.

Parameter	**Standard 100 mm process at Balzers LLS 801 system [6]**	**Variable 150 mm process at Provac LLS 801 system**	**Standard 150 mm process at Provac LLS 801 system**
Base pressure (μbar)	$5.0 \cdot 10^{-4}$	$5.0 \cdot 10^{-4}$	$5.0 \cdot 10^{-4}$
Throttle setting (off/on)	Off	Off/on	Off
Ar flow rate (sccm)	-	50...250	250
Ar pressure (μbar)	4	3.2...6.4	4.0
N_2 flow rate (sccm)	-	10...70	50
N_2 pressure (μbar)	0.3	0.3...0.9	0.4
Total pressure (μbar)	4.3	3.5...6.9	~4.5
DC power on Mo target (W)	3000	3000	3000
Duration of a drum revolution (s)	200	200	200

The 150 mm substrates were polished, (100) oriented silicon wafers with details described in Table 3. Some wafers were covered with a silicon oxide layer of around 100 nm, and grown by wet oxidation at 850°C; the oxide thickness was measured

by reflectometry (NanoSpec AFT 4150, or FilmTek 2000M). Reflectometry is capable of determining the thickness of dielectric films with accuracy better than 1 nm, although not with films thinner than 10 nm [36]. It was not analysed whether the properties of Mo-N films were affected by the orientation of the silicon substrates, or the kind or the thickness of the oxide layer; instead, it was herein assumed the properties were mainly dependent on the deposition process, without a study of possible substrate effects.

Table 3. The substrates for the experiments on Mo-N films. All silicon wafers were (100) oriented, and 150 mm in diameter. SSP = single side polished, DSP = double side polished.

Sample #	**Thickness of silicon wafer (μm)**	**Polishing of silicon wafer**	**Type of substrate (blank/ oxidised)**	**Thickness of silicon oxide (nm)**
1...8	675 ± 15	SSP	Oxidised	105
26...33, 47…49	675 ± 15	SSP	Blank	-
74, 75	675 ± 15	SSP	Oxidised	97
76...82	675 ± 15	SSP	Oxidised	103
N26	330 ± 10	DSP	Blank	-

The first set of experiments determined the properties of as-deposited Mo-N films as the argon and nitrogen flow rates (the Ar and N_2 partial pressures) were varied (Table 4). The relationship between the gas flow rates and the resulting pressure was available as system-specific background information. Since this relationship was recorded prior to the actual experiments, the corresponding pressure values are cited as reference values in Table 4. Correspondingly, the pressure readings recorded during each deposition are cited as true values. The N_2 partial pressure as a percentage figure was computed by the reference values. The purpose of the deposition runs #1…8 was to find the optimal composition of Mo-N films, while the purpose of the runs #A1…A3 was to prepare samples for annealing experiments, and to solve whether the properties of Mo-N films are dependent on thickness. The two sets of deposition runs were temporally separated by almost three years, bringing on a chance of slightly differing outcomes.

The second set of experiments studied the thermal stability of Mo-N films (Table 5). Except for the first experiment, the Mo-N films were deposited with the standard 150 mm process described in Table 2. The annealing experiments were performed in a vacuum oven (Heraeus VT 5042 EKP) where the samples lay on quartz jigs when heated. One could select either nitrogen or air for the surrounding gas. The pressure in the oven was adjustable from the atmospheric pressure down to clearly less than 50 mbar. Similarly, the temperature could be adjusted from room temperature (22°C) up to 400°C. The samples were loaded into the oven at room temperature, after which the heating was turned on. The oven was slow in operation: heating from 22°C to 400°C took about 60 minutes, and cooling from 400°C back to room temperature several hours. The hold time in Table 5 refers to the time the

samples were kept at the set temperature; due to the slow heating and cooling, they spent a notably longer time at increased temperature.

Table 4. The variable sputtering parameters of the Mo-N depositions. The films were deposited with the 150 mm process at Provac LLS 801 sputtering system. The pressure values cited as (ref.) and (true) refer to reference and true measured values, respectively; see the text for more information. The number of revolutions refers to how many times the sample holder rotated around its axis during the deposition, dictating the thickness of the depositing Mo-N film.

Deposition run #	**Sample #**	**Throttle setting (off/ on)**	**Ar flow rate (sccm)**	**Ar pressure (ref.) (μbar)**	**N_2 flow rate (sccm)**	**N_2 pressure (ref.) (μbar)**	**Total pressure (ref.) (μbar)**	**N_2 partial pressure (%)**	**Total pressure (true) (μbar)**	**Number of revolutions**
1	1, 26	off	250	3.95	30	0.27	4.22	6.4	4.1	12
2	2, 27	off	250	3.95	50	0.43	4.38	9.8	4.2	12
3	3, 28	off	250	3.95	70	0.60	4.55	13.2	4.3	12
4	4, 29	off	190	3.18	30	0.27	3.45	7.8	3.3	12
5	5, 30	on	70	6.35	10	0.43	6.78	6.3	6.6	12
6	6, 31	off	190	3.18	60	0.52	3.70	14.1	3.5	12
7	7, 32	on	50	4.66	15	0.69	5.35	12.9	4.9	12
8	8, 33	on	65	5.94	20	0.94	6.88	13.7	6.3	12
A1	74, N26, a carbon button	off	250	3.95	50	0.43	4.38	9.8	4.5	6
A2	47, 48, 75...81	off	250	3.95	50	0.43	4.38	9.8	4.5	12
A3	49, 82	off	250	3.95	50	0.43	4.38	9.8	4.5	18

The thickness of conductive films must be measured by non-optical methods. If a film can be patterned, its thickness can be measured by contact profilometry. If the patterning is made by etching (instead of patterned deposition), the etch selectivity over the underlying substrate must be good. Alternatively, thickness can be determined by sheet resistance if the resistivity is known and independent from thickness, or by electron microscopy. The resistivity ρ of a conductive film is

$$\rho = R_S \cdot t_f \tag{10}$$

where R_S is the sheet resistance and t_f the thickness of the film. The sheet resistance is typically measured by four-point probing, with the conductive film lying on top of an insulator. In this case, the sheet resistance is [32]

$$R_S = \frac{\pi}{\ln 2} \cdot \frac{V}{I} \tag{11}$$

where V is the voltage, and I the current.

Table 5. The annealing parameters for studying the thermal stability of Mo-N films. The second column in the table identifies the deposition run from which the sample originated from.

Annealing experiment #	**Deposition run #**	**Sample #**	**Surrounding gas**	**Pressure (mbar)**	**Temperature (°C)**	**Hold time (min)**
5	1	1	Nitrogen	1000	400	95
6	3	3	Nitrogen	1000	400	95
11	A2	47	Air	1000	350	75
12	A2	48	Air	<< 50	250	75
13	A2	75	Air	1000	400	75
14	A2	76	Air	1000	300	75
15	A2	77	Air	1000	350	75
16	A2	78	Air	1000	325	75

To measure the thickness of Mo-N films, the as-deposited films were patterned by lithography with AZ 5214 photoresist and a Canon FPA-2500i3 wafer stepper. The Mo-N films were etched until the underlying silicon oxide layer with PS 70-10 aluminium wet etchant at room temperature. After resist stripping, the resulting step heights were measured by a profilometer (Veeco Dektak V200). The deposition and etch rates were calculated subsequently from the deposition and etch times, respectively. Alternatively, the thickness of Mo-N films was assessed by SEM which lends itself to the imaging of cross-sectional samples and provides concurrently a rough picture of the microstructure, too. The structural analysis with SEM was troubled by the sample preparation, however: manual cleaving by a diamond pen was a harsh method to prepare a cross-section of a thin film. The patterning method was used for the samples originating from the deposition runs #1...8, and SEM for the rest.

The sheet resistance was measured by a four-point probe at room temperature from samples that had a Mo-N film on top of a silicon oxide layer. Five measurements were run on each wafer, and the average was computed. The equations (10) and (11) were then used to calculate the resistivity. The residual stress was determined by measuring the substrate bow with and without a Mo-N film by stylus profilometry (Veeco Dektak V200). After the change in the substrate bow was recorded, the stress was valued by the Stoney equation (2) that can be written also as

$$\sigma_f = \frac{4E_S}{3(1-\nu_S)} \frac{t_S^2}{t_f} \frac{y}{L^2} \qquad (12)$$

where $E_s/(1-\nu_s)$ is the biaxial modulus of the silicon substrate, y the bending of the substrate (i.e. the change in the wafer bow due to the stressed film), and L the scan length of the profilometer stylus (e.g. [301]). Mo-N films were removed from silicon substrates with PS 70-10 aluminium wet etchant between the two curvature measurements. A value of 180 GPa was used for the biaxial modulus of the (100) silicon substrates; the above value is fairly accurate when the surface of a (100) silicon

wafer is scanned parallel or perpendicular to the main flat of the wafer [286]. The scan length L was 11 cm. The annealing induced stress change was determined by measuring the substrate bow before and after a heat treatment. The maximum error in the determination of the residual stress was valued by the total differential of the equation (12):

$$\Delta\sigma_f(t_s, t_f, y, L) = \left|\frac{\partial\sigma_f}{\partial t_s}\right|\Delta t_s + \left|\frac{\partial\sigma_f}{\partial t_f}\right|\Delta t_f + \left|\frac{\partial\sigma_f}{\partial y}\right|\Delta y + \left|\frac{\partial\sigma_f}{\partial L}\right|\Delta L \quad (13)$$

where Δt_s, Δt_f, Δy and ΔL are the measurement uncertainties of the substrate thickness, the film thickness, the substrate bending and the scan length, respectively.

The composition of a selected Mo-N film was analysed by RBS, in which the sample is bombarded by light, energetic ions (typically He ions of 1...3 MeV). The energy spectrum of the backscattered ions reveals the stoichiometry of the film, as well as the nature, amount and distribution of impurities [37]. RBS has limitations in detecting light elements in a heavier matrix [36]; in any case, the concentration must generally be about 1 at.% to be detectable [31]. The 250 nm thick Mo-N film for RBS was deposited on top of a carbon button by the standard 150 mm sputtering process described in Table 2. The sample was analysed herein with He beams of two energies: 3.05 MeV (the analysis A), and 2.00 MeV (the analysis B).

4.4 Properties of as-deposited films

The deposition and etch rates and the resistivity of Mo-N films are presented in Table 6. The deposition rate varied between 39 and 49 nm per one revolution of the sample holder, each taking 200 seconds (Figure 8). The deposition rate had a downward trend with the increasing N_2 partial pressure, common to [30, 289, 293], and explained by target poisoning. Assuming an equal relative N_2 partial pressure, a higher total sputtering pressure resulted in thicker Mo-N films, i.e. a higher deposition rate. The etch rate in PS 70-10 wet aluminium etchant at room temperature (RT) varied between 420 and 780 nm/min (Figure 9). It followed a roughly similar pattern to the deposition rate if plotted against the N_2 partial pressure: a Mo-N film with a high deposition rate tended to have a high etch rate, too.

The resistivity of Mo-N films at room temperature fell between 90 and 190 μΩcm. The resistivity rose with the increasing relative N_2 partial pressure during sputtering regardless of the total pressure (Figure 10). The trend was foreseeable as a high N_2 partial pressure relates to a high nitrogen concentration in Mo-N films (Section 4.2.1), which is known to relate to a high resistivity (Section 4.2.5).

Table 6. The deposition rate, the etch rate, and the resistivity of as-deposited Mo-N films. The pressure values refer to those that prevailed during deposition. The films were etched at room temperature with PS 70-10 which is a commercial etch mixture comprising phosphoric and nitric acids, and mainly used for aluminium wet etching. The thickness for the run #A2 is a nominal value (tagged with *).

Deposition run #	**Sample #**	**Total pressure (µbar)**	**N_2 partial pressure (%)**	**Thickness of Mo-N (nm)**	**Deposition rate (nm/ revolution)**	**Etching time (s)**	**Etch rate (nm/ min)**	**Resistivity (µΩcm)**
1	1	4.1	6.4	540	45	48	680	90
2	2	4.2	9.8	490	41	70	420	120
3	3	4.3	13.2	470	39	55	510	140
4	4	3.3	7.8	520	43	52	600	90
5	5	6.6	6.3	590	49	45	780	100
6	6	3.5	14.1	470	39	46	610	190
7	7	4.9	12.9	530	44	54	590	140
8	8	6.3	13.7	510	43	65	470	160
A1	74	4.5	9.8	250	42	-	-	120
A2	75	4.5	9.8	500*	-	-	-	120
A3	82	4.5	9.8	770	43	-	-	120

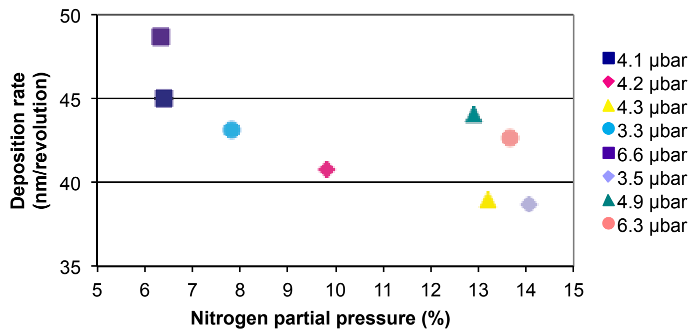

Figure 8. The relationship between the nitrogen partial pressure (%) and the deposition rate of Mo-N films. Each revolution of the sample holder took 200 seconds. Note that also the total sputtering pressure was varied, marked by the coloured labels.

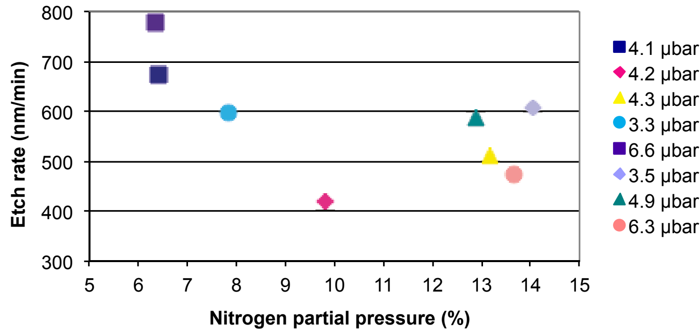

Figure 9. The relationship between the etch rate of Mo-N films and the nitrogen partial pressure (%) prevailing during sputtering. The films were etched with PS 70-10 aluminium wet etchant at room temperature. Note that also the total sputtering pressure was varied, marked by the coloured labels.

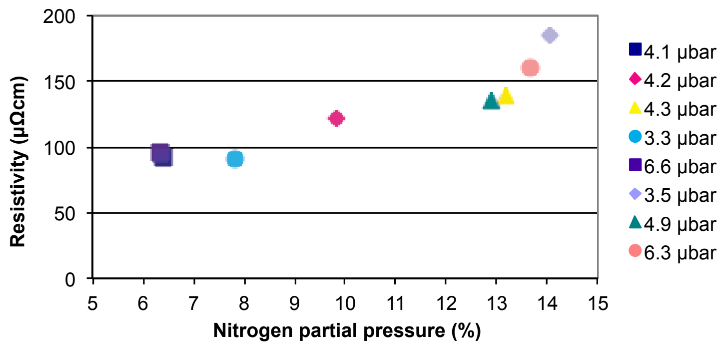

Figure 10. The resistivity of Mo-N films as a function of the nitrogen partial pressure (%) prevailing during sputtering. Note that also the total sputtering pressure was varied, marked by the coloured labels.

The residual stress of as-deposited Mo-N films was anticipated to depend on their nitrogen concentration and the total sputtering pressure [30, 302]. The contribution of the thermal stress σ_{th} was hardly considerable since the deposition temperature at sputtering is low. Being a strong function of the sputtering parameters, both tensile and compressive stress occurred (Table 7). There was no single trend when the residual stress was plotted against the relative N_2 partial pressure prevailing during sputtering (Figure 11). Instead, it was more useful to examine the stress against the total sputtering pressure while keeping the relative N_2 partial pressure roughly constant (Figure 12). Doing this, the graph with the N_2 partial pressure between 13 and 14 % revealed a familiar behaviour: a sharp stress reversal from compressive to tensile, similar to the famous trend identified by Hoffman and Thornton [56]. (Interestingly, a similar kind of sharp change was observed also for the reflectivity of sputter deposited metal films [56].) In their study in 2002, Kattelus *et al.*

showed how the lateral stress variation in the plane of the film was smallest for the Mo-N compositions with the most amorphous microstructure [30]. The samples originating from the runs #3 and #6 were the best in this sense. Unfortunately, they both were under compressive stress. As for the stress state, the best among this set was the sample from the run #2, since it had a low tensile residual stress (125 MPa on average) together with a moderate lateral stress variation (50 MPa). Therefore, the subsequent experiments were conducted with Mo-N films deposited by identical sputtering parameters, named the standard 150 mm process in Table 2. The magnitude of a possible vertical stress gradient was not studied. The relation between the smallest lateral stress variation and the fastest wet etch rate, both characteristic of the amorphous compositions according to Kattelus *et al.* [30], could not be confirmed by the data herein.

Table 7. The residual stress of as-deposited Mo-N films. The pressure values refer to those that prevailed during deposition. Stress X denotes the residual stress parallel to the main flat of the silicon substrate, stress Y the residual stress perpendicular to the main flat, and Δstress the difference between the two preceding as an absolute value, i.e. the lateral stress variation. The thickness for the run #A2 is a nominal value (tagged with *).

Deposition run #	**Sample #**	**Total pressure (μbar)**	**N_2 partial pressure (%)**	**Thickness of Mo-N (nm)**	**Stress X (MPa)**	**Stress Y (MPa)**	**Δstress (MPa)**
1	26	4.1	6.4	540	410	500	90
2	27	4.2	9.8	490	100	150	50
3	28	4.3	13.2	470	-180	-190	10
4	29	3.3	7.8	520	190	310	120
5	30	6.6	6.3	590	480	460	20
6	31	3.5	14.1	470	-280	-290	10
7	32	4.9	12.9	530	440	550	110
8	33	6.3	13.7	510	500	590	90
A1	N26	4.5	9.8	250	-20	10	30
A2	47	4.5	9.8	500*	160	210	50
A2	48	4.5	9.8	500*	180	210	30
A3	49	4.5	9.8	770	210	250	40

The structure and properties of thin films may depend on their thickness, or vary with depth (Section 2.2.2). Whether this held true for Mo-N films between 250 and 770 nm was studied briefly (Figure 13). The resistivity of Mo-N films proved rather independent from thickness: it was always 120 μΩcm. Instead, the residual stress turned more tensile with the increasing thickness: the stress of a 250 nm Mo-N film was close to zero (or even slightly compressive) whereas the stress of 500 and 770 nm films was around 200 MPa (tensile). The finding is consistent with Kattelus

et al. whose Mo-N films had their bottom sections under more compressive stress than the top sections [30]. One can speculate that the interaction with the underlying substrate may affect the stress state of the depositing Mo-N film. Janssen *et al.* [335] offered another aspect by stating the stress in CrN and other hard films consists of tensile stress generated at grain boundaries, compressive stress due to ion peening, and potential thermal stress if the deposition temperature was different from the temperature at which the stress was measured. In this model, only the first term was thickness dependent. [335]

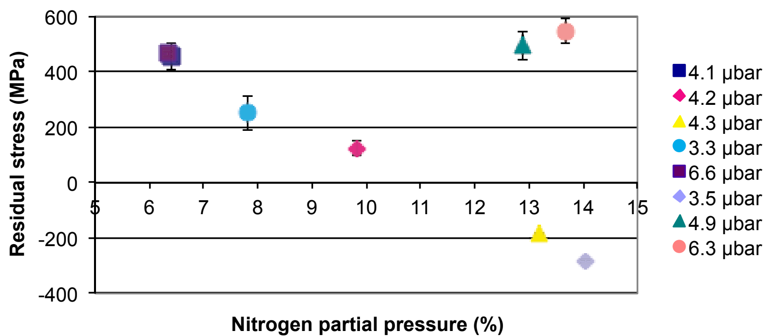

Figure 11. The relationship between the residual stress of Mo-N films and the nitrogen partial pressure (%) prevailing during sputtering. Note that also the total sputtering pressure was varied, marked by the coloured labels. The error bars indicate the difference between the stress measured parallel (X) and perpendicular (Y) to the main flat of the silicon substrates. The difference was invisible in some cases.

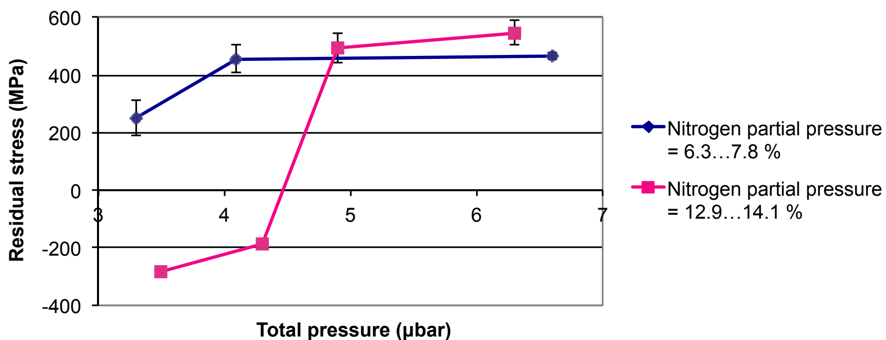

Figure 12. The residual stress of Mo-N films as a function of the total sputtering pressure. The blue graph illustrates a case where the N_2 partial pressure was between 6 and 8 % during sputtering, while the red graph refers to a case with the N_2 partial pressure between 13 and 14 %. The error bars indicate the difference between the stress measured parallel (X) and perpendicular (Y) to the main flat of the silicon substrates. The difference was invisible in some cases.

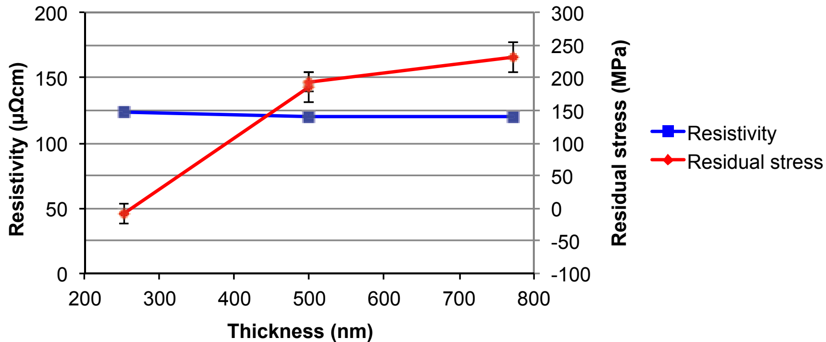

Figure 13. The resistivity and the residual stress of Mo-N films as functions of film thickness. The films were deposited with the total sputtering pressure of 4.5 μbar, and the N_2 partial pressure of 9.8 % (the standard 150 mm process outlined in Table 2). The error bars indicate the difference between the stress measured parallel (X) and perpendicular (Y) to the main flat of the silicon substrates.

The microstructures of 250 and 770 nm thick Mo-N films were imaged by SEM (Figure 14 and Figure 15). The cross-section of the latter revealed a changing look from the bottom to the top of the film. The bottom (roughly one third of the film) appeared to comprise vertically aligned columns, whereas the appearance of the top part was spongier. Also the ~250 nm thick Mo-N films by Kattelus *et al.* had a vertically aligned columnar structure; these films were amorphous by XRD but not by TEM [30]. The above finding is in tune with earlier discoveries: the residual stress (reflecting the microstructure) was not independent from thickness (Figure 13). Altogether, the findings support the understanding that the structure of these sputter deposited Mo-N films likely varied with depth.

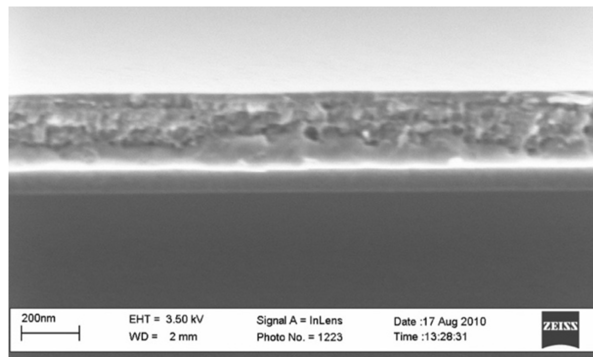

Figure 14. A SEM image of a 250 nm thick Mo-N film on top of a silicon oxide layer. The Mo-N film was deposited by the standard 150 mm sputtering process.

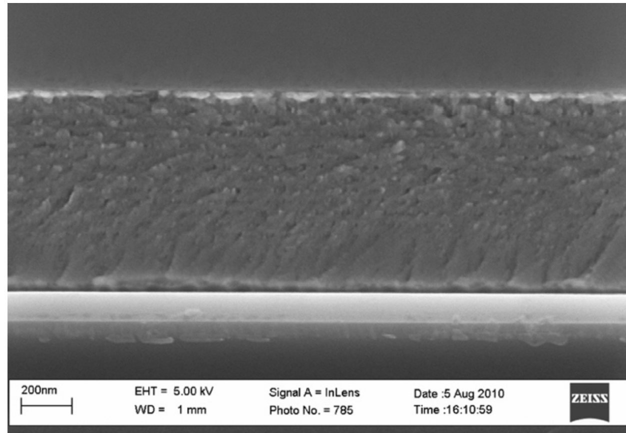

Figure 15. A SEM image of a 770 nm thick Mo-N film on top of a silicon oxide layer. The Mo-N film was deposited by the standard 150 mm sputtering process.

The reliability of the determination of the residual stress was estimated by means of the total differential according to (13). The equation (13) gives the maximum error that is possible, assuming all terms work in the same direction. Table 8 presents the contributions of each variable to the total measurement uncertainty. The numerical values were calculated with the sample #27 from the deposition run #2 as an example. The uncertainties due to the substrate thickness and the substrate bending proved to matter the most. Nevertheless, the total error remained moderate: it was less than 20 MPa. An error of this magnitude is acceptable to most MEMS device applications.

The rest of the experiments were conducted with Mo-N films deposited by the standard 150 mm sputtering process described in Table 2. The chemical composition of such Mo-N films was analysed by RBS with He beams of two energies: 3.05 MeV (the analysis A) and 2.00 MeV (the analysis B). The spectrum obtained with the 2.00 MeV beam was more reliable to solve a Mo-N composition on the whole because its yield (the number of counts) was higher. However, the 3.05 MeV beam was more reliable for the determination of a possible oxygen impurity content because of oxygen resonance. The analysis A proved the oxygen content in the as-deposited Mo-N film was less than 1 %, and the oxygen was concentrated on the surface of the film. The actual film composition was solved by the analysis B, and it was 80 at.% Mo and 20 at.% N. The Mo-N films were hence molybdenum-rich compared to the stoichiometric Mo-N compositions, MoN and Mo_2N.

Table 8. The evaluation of the measurement uncertainty of the residual stress. Stress Y of the sample #27 from the deposition run #2 was used as an example. The sample was deposited by the standard 150 mm sputtering process outlined in Table 2.

Variable	**Value of variable**	**Measurement uncertainty of variable**	**Partial differential**	**Contribution to measurement uncertainty of σ_f**
Substrate thickness	t_s = 675 μm	Δt_s = 15 μm	$\left\lvert\frac{\partial \sigma_f}{\partial t_s}\right\rvert = \left\lvert\frac{8E_s}{3(1-\nu_s)}\frac{t_s}{t_f}\frac{y}{L^2}\right\rvert$	$\Delta\sigma_{f1}$ = 6.6 MPa
Film thickness	t_f = 490 nm	Δt_f = 5 nm	$\left\lvert\frac{\partial \sigma_f}{\partial t_f}\right\rvert = \left\lvert\frac{-4E_s}{3(1-\nu_s)}\frac{t_s^2}{t_f^2}\frac{y}{L^2}\right\rvert$	$\Delta\sigma_{f2}$ = 1.5 MPa
Substrate bending	y = 8.1 μm	Δy = 0.4 μm	$\left\lvert\frac{\partial \sigma_f}{\partial y}\right\rvert = \left\lvert\frac{4E_s}{3(1-\nu_s)}\frac{t_s^2}{t_f \cdot L^2}\right\rvert$	$\Delta\sigma_{f3}$ = 7.4 MPa
Scan length	L = 11 cm	ΔL = 1 mm	$\left\lvert\frac{\partial \sigma_f}{\partial L}\right\rvert = \left\lvert\frac{-8E_s}{3(1-\nu_s)}\frac{t_s^2}{t_f}\frac{y}{L^3}\right\rvert$	$\Delta\sigma_{f4}$ = 2.7 MPa
Residual stress	σ_f = 149 MPa	$\Delta\sigma_f$ = 18.2 MPa	-	-

4.5 Thermal stability

The thermal stability of Mo-N films turned into a relevant topic after *Mo-Si-N* films were annealed with a somewhat unexpected outcome (see Section 5.5). On the grounds of the article survey (Section 4.2.3), the onset of the crystallisation of initially amorphous Mo-N films took place at 450°C at lowest [303]. In addition, Mo-N films started to oxidise below 400°C if heated in an oxidative atmosphere [295, 307, 320]. The purpose of this section was to verify whether our sputter deposited Mo-N films behave in a similar fashion; if yes, it would shed light on the findings on Mo-Si-N films.

The visual look, the resistivity and the residual stress of annealed Mo-N films were recorded while the surrounding gas, the pressure and the annealing temperature served as experimental variables (Table 9). The visual look, primarily the colour, is an inexact but easily perceivable attribute to show whether a metal-based film has undergone oxidation. If contemplated after a heat treatment, a change in the colour of a film does not reveal the exact temperature at which the oxidation started; neither does it indicate the composition or the thickness of the resultant oxide layer as such. In any case, the relation between the oxidation and the colour of metal-based thin films, i.e. the fact that oxidation manifests itself as a change in the colour, has been verified by thermogravimetry (TG) and SEM [185], Auger electron spectroscopy (AES) and SEM [202], as well as X-ray photoelectron spectroscopy (XPS) and secondary ion mass spectrometry (SIMS) [336]. The combination of TG and differential thermal analysis (DTA) [320], or merely TG [228, 238, 345], would have been a more informative method to study the oxidation of Mo-N films;

unfortunately, these quantitative methods were not available in our premises. Under the circumstances, a change in the visual look was considered a proof of oxidation despite the relating problems.

Table 9. The colour, the resistivity, and the residual stress of Mo-N films after annealing. The film thickness was around 500 nm. Note that the Mo-N films of the experiments #5 and #6 were not deposited with the standard 150 mm sputtering process, while the others were. The surrounding gas, the pressure and the temperature refer to those that prevailed during annealing; see Table 5 for other details. Stress X denotes the residual stress parallel to the main flat of the silicon substrate, and stress Y the residual stress perpendicular to the main flat. The measuring signal for the resistivity of one sample was slightly unstable (tagged with *).

Annealing experiment #	**Surrounding gas**	**Pressure (mbar)**	**Temperature (°C)**	**Colour**	**Resistivity (µΩcm)**	**Stress X (MPa)**	**Stress Y (MPa)**
5	Nitrogen	1000	400	Bright grey	70	-	-
6	Nitrogen	1000	400	Bright grey	140	-	-
11	Air	1000	350	Grey tinged with brown	-	520	580
12	Air	<< 50	250	Grey	-	360	410
13	Air	1000	400	Grey tinged with brown	100*	-	-
14	Air	1000	300	Grey	130	-	-
15	Air	1000	350	Grey tinged with brown	130	-	-
16	Air	1000	325	Grey	130	-	-

The first two experiments in Table 9 were conducted in a nitrogen gas at 400°C with non-standard Mo-N compositions. In their as-deposited state, all Mo-N films were bright grey, having a shiny metallic appearance. When annealed, the looks of the films stayed unaltered, while there was a smallish or no change in resistivity. If without an explicit proof, the outcome of the standard Mo-N composition ($Mo_{80}N_{20}$) would have been more than likely the same because the samples in question had nitrogen contents below and above the standard one, with other deposition parameters in common.

The rest of the experiments were conducted in ambient air at temperatures between 250 and 400°C. Up to 325°C, the colour of Mo-N films stayed grey with no noticeable difference from the as-deposited state. From 350°C upward, the initially grey colour of the films got a brown tint. The temperature region coincides perfectly with the reported onset temperature of the oxidation of Mo_2N films [295, 307, 320], although the composition of our Mo-N films was $Mo_{80}N_{20}$ by RBS. The resistivity of as-deposited Mo-N films was 120 µΩcm. After annealing, a resistivity of 130 µΩcm was gauged for each sample except for the one annealed at 400°C, whose resistivity decreased to 100 µΩcm together with a slightly unstable measuring signal of a

digital four-point probe (Figure 16). The latter may be a further support for the incipient oxidation: a thin surface oxide film could explain the difficulty in four-point probing. Also Wang *et al.* observed an annealing induced resistivity drop with their Mo-N films that was accompanied by the crystallisation of the films; however, this was reported to happen in a protective gas (N_2) only above 700°C [308, 309].

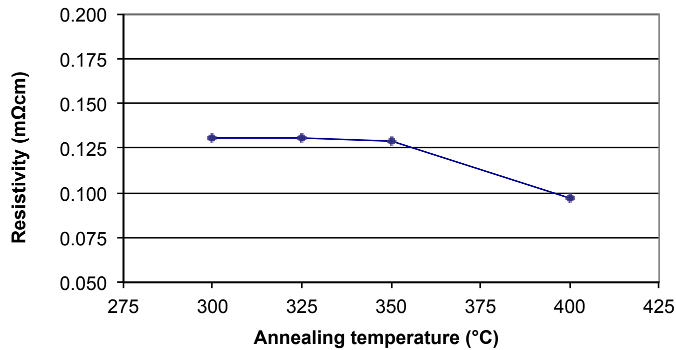

Figure 16. The resistivity of $Mo_{80}N_{20}$ films after annealing at the atmospheric pressure with air as the surrounding gas.

The residual stress of 500 nm thick $Mo_{80}N_{20}$ films was compared before and after annealing in ambient air (Table 10). In their as-deposited state, the samples had a low tensile stress of around 200 MPa. On the grounds of the article survey (Section 4.2.4), an annealing induced stress change was expected to come up between 350 and 480°C [295, 301, 306]. However, our Mo-N films demonstrated an increase in the tensile residual stress even at 250°C, being a considerably low temperature. When annealed at 350°C, the stress increased already by ~350 MPa. The lateral stress variation did not change significantly. The Mo-N films of the referenced articles differed from the Mo-N films herein in respect of the as-deposited stress state: the former were under compressive stress, while our films were tensile stressed. Because the stress measurements were conducted after the films were cooled back to room temperature, the changes in residual stress reflect changes in the microstructure; they are not due to the thermal expansion mismatch between the film and the substrate.

The microstructure of a $Mo_{80}N_{20}$ film annealed at 400°C in ambient air was imaged by SEM (Figure 17). The film was not shining grey in colour but tinged with brown. Its cross-section did not look smooth, but the impression was granular, possibly even lamellar. For the sake of comparison, the appearance of the underlying amorphous silicon oxide film was quite homogeneous even if it had undergone the same robust cleaving. The surface of the Mo-N film was notably rough as well; yet a separate surface oxide film could not be distinguished.

Table 10. The comparison of the residual stress of 500 nm thick $Mo_{80}N_{20}$ films before and after annealing in ambient air. Stress X denotes the residual stress parallel to the main flat of the silicon substrate, stress Y the residual stress perpendicular to the main flat, and Δstress the difference between the two preceding as an absolute value, i.e. the lateral stress variation. Both samples were deposited with the standard 150 mm sputtering process, even though their residual stresses before annealing differed slightly.

Annealing experiment #	**Temperature (°C)**	**Stress X before annealing (MPa)**	**Stress Y before annealing (MPa)**	**Δstress before annealing (MPa)**	**Stress X after annealing (MPa)**	**Stress Y after annealing (MPa)**	**Δstress after annealing (MPa)**
11	350	160	210	50	520	580	60
12	250	180	210	30	360	410	50

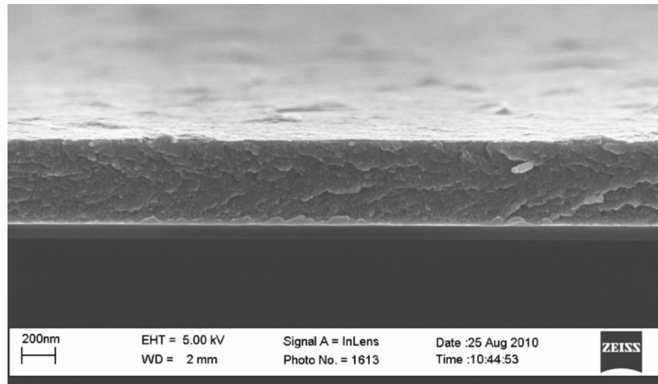

Figure 17. A SEM image of a 500 nm thick $Mo_{80}N_{20}$ film on top of a silicon oxide layer after annealing at 400°C and 1000 mbar for 75 minutes. The annealing atmosphere was of air.

In conclusion, the properties of sputter deposited Mo-N films with a composition of $Mo_{80}N_{20}$ were subject to change if annealed in ambient air at 400°C or even below. Changes in the visual look suggested the oxidation of these Mo-N films was likely to start at 350°C, which is exactly the reported onset temperature of the oxidation of Mo_2N films [295, 307, 320]. When $Mo_{80}N_{20}$ films were annealed in a protective N_2 gas, such changes were not observed. The crystallisation temperature of these Mo-N films was not determined in an explicit way; however, a heat treatment of as low as 250°C was enough to increase the tensile residual stress, and the SEM image of a sample annealed at 400°C revealed a film with an inhomogeneous look, both implicating microstructural changes have taken place. For the sake of comparison, Ti-N films crystallise at 400°C and may experience stress relaxation from

250°C upward [337]; in other words, the temperature range discussed here is common to other transition metal nitrides.

4.6 Conclusions

The purpose of this study was to synthesise Mo-N films, determine their properties most relevant to MEMS, and explore how they behave upon annealing. Reactive sputtering, which is the most common deposition method of Mo-N films, was used. The results have been compiled in Table 11. The created 150 mm deposition process was a close counterpart of the earlier 100 mm process reported in [6] and [30]; the old process could not be used as such because of a system update. After the system change, a repetitive characterisation was justified. However, the transformation of the crystallinity of Mo-N films along with the nitrogen content was not revisited by XRD or TEM, after such study was already presented in [30]. The existence of a strong stress gradient was not reverified either; it was proved only implicitly through the thickness dependent residual stress.

Table 11. A summary of the deposition parameters and the properties of Mo-N films of the selected standard composition. The deposition process was operated at Provac LLS 801 sputtering system with 150 mm substrates.

Sputter deposition	
Base pressure	$5.0 \cdot 10^{-4}$ μbar
Ar flow rate	250 sccm
Ar pressure	4.0 μbar
N_2 flow rate	50 sccm
N_2 pressure	0.4 μbar
Total pressure	~4.5 μbar
DC power on Mo target	3000 W
Duration of a drum revolution	200 s
Deposition rate	41 nm/revolution
Properties	
Composition	$Mo_{80}N_{20}$
Resistivity (as-deposited)	120 μΩcm
Residual stress of 500 nm thick films:	
As-deposited	160…210 MPa (tensile)
Annealed at 250°C in ambient air	360…410 MPa (tensile)
Annealed at 350°C in ambient air	520…580 MPa (tensile)
Etch rate in PS 70-10 wet etch mixture at 21°C (comprising H_3PO_4 and HNO_3)	420 nm/min

When the first paper on Mo-N films for MEMS was published, the thermal stability of Mo-N films was ignored [30]. At the time the author first encountered Mo-Si-N

films oxidating at unexpectedly low temperatures in the lab, an extensive study on the oxidating behaviour of Mo-N coatings was just being issued [320], offering an idea of what might explain the recent foundings. Because the role of this thesis is to confirm what has been already found regarding the thermal stability of Mo-N films, a restricted set of experiments was contented with. However, this work showed the residual stress of Mo-N films can change already at 250°C, which is lower than reported before [295, 301].

Set against elemental Mo films, Mo-N films are superior in regard to the homogeneity of the intrinsic stress [30], but inferior as regards the electrical conductivity. Even so, the conductivity of Mo-N films is much higher than that of even heavily doped polysilicon (e.g. [338]), and well sufficient for a multitude of MEMS applications. Compared to polysilicon, sputter deposited Mo-N films have another advantage: they can be deposited close to room temperature while the typical deposition temperature is 570…610°C for LPCVD silicon, and around 300°C for PECVD silicon [339, 340]; on the other hand, the low thermal stability of Mo-N films remains their weak spot. According to literature (Section 4.2.4), both the elastic modulus and the hardness of Mo-N films are higher than those of single crystal silicon.

All in all, amorphous Mo-N films are usable for MEMS applications with the proviso that they are not applied to self-supporting structures like beams (that will curve due to a stress gradient) or devices one intends to operate at elevated temperatures. From the standpoint of fabrication, both the deposition and the patterning of Mo-N films are convenient: the former by sputtering, the latter by standard photolithography and aluminium wet etchant with a practical etch rate. The superconductivity of Mo-N, though not studied here, might open interesting low temperature applications.

Eventually, the weak spots of Mo-N films turned the attention on Mo-Si-N films. If the amorphisation was more complete, one could anticipate a more uniform intrinsic stress (a lower stress gradient) and, as an extra benefit, a smoother surface. Mo-N-O films would have been another alternative since oxygen incorporation has been reported to make Mo-N films more amorphous in structure, giving rise to stress relaxation, a reduced stress gradient and increased resistivity (Sections 4.2.2, 4.2.4 and 4.2.5). At the time the choice was made, Mo-Si-N films were praised for their high structural metastability as a member of the mictamict family [140], as well as for “excellent oxidation resistance up to 800°C” of their own [222].

5. Mo-Si-N thin films

5.1 Introduction

Since the amorphisation of sputter deposited Mo-N films was incomplete, their properties were not optimal for MEMS. If Mo-N films were supplemented with silicon, it would lead to Mo-Si-N films belonging to the mictamict alloys (reviewed in Chapter 3). Since the mictamict alloys often possess an amorphous microstructure, the choice was inviting.

Molybdenum and silicon compose molybdenum silicides with three known stoichiometries: Mo_3Si, Mo_5Si_3 and $MoSi_2$ [341], among which $MoSi_2$ has possibly the most technological importance. $MoSi_2$ is a borderline compound with properties between those of ceramics and intermetallics [342]. It is used as a high-temperature structural material owing to its high melting point (2030°C) and excellent high-temperature oxidation resistance. However, it is brittle at room temperature, and suffers from poor creep resistance at high temperatures. [222, 225, 235, 341, 342] Silicon and nitrogen, in turn, compose Si_3N_4 or non-stoichiometric Si-N. In a bulk form, Si_3N_4 and its composites have been applied to high-temperature structural materials similar to $MoSi_2$ [227, 343, 344]. In microfabrication, Si_3N_4 (or Si-N) films are commonly used as electric insulators and chemical passivators. What molybdenum, silicon and nitrogen compose together is finally explored herein.

Like the previous chapter, the discussion on Mo-Si-N films is divided into two parts: the first is a review of the published research, while the second describes the experimental findings of this work. Mo-Si-N films share naturally a lot with other mictamict alloys; the role of Section 5.2 is to dwell deeper on the characteristics of Mo-Si-N as well as to compare them with other mictamict alloys and Mo-N films. The thermal stability of Mo-Si-N films is explored in particular since the experimental findings differed the most from the preliminary assumptions in relation to it.

5.2 Review

5.2.1 Process technology

Sputter deposition seems to be almost the sole method to produce Mo-Si-N films [142, 222-238, 296]; a rare exception is the study of Heo *et al.* who combined DC magnetron sputtering with arc ion plating (AIP) at 300°C [221]. The sputtering target can be a silicide compound target ($MoSi_2$ [222-224, 226, 228-230, 234, 235] or Mo_5Si_3 [142, 231-233, 296]) or, alternatively, molybdenum and silicon targets may be co-sputtered simultaneously [221, 227, 236-238]. In the latter case, the Mo/Si ratio in the films can be freely adjusted. Sputtering of Mo-Si-N films is reactive by nature, since nitrogen is introduced in gaseous form into the films. The deposition rate decreases with the increasing N_2 partial pressure, along with the change from the metallic to the compound sputtering mode [228, 230]. As usual, argon gas is used for maintaining the plasma discharge and controlling the sputtering pressure. If separate Mo and Si targets are settled on, one should remember DC biasing is not applicable to a silicon target since silicon develops an insulating surface nitride in N_2 gas, resulting in arcing. In addition, one should note the deposition rate of molybdenum nitride is higher than that of silicon nitride (assuming other things equal) [227].

Sputter deposition is usually performed at or close to room temperature, albeit few groups sputtered their Mo-Si-N films at 400...500°C [224, 227, 228, 237, 238]. The base pressure is typically in the range of $10^{-6}...10^{-4}$ Pa, and the sputtering pressure around 1 Pa or somewhat less. The reported deposition rates vary from 5 nm/min [2] to 0.9 μm/min [228] depending on the sputtering parameters. The composition can be controlled by the selection of the sputtering targets, the electrical power applied to them, the sputtering current, and the nitrogen flow rate. Oxygen [142, 230-232, 234, 235, 296], argon [231, 232, 234, 235] and carbon [234, 235] impurities are commonly found with concentrations typically of a few percents. A low deposition rate promotes the opportunity that the residual oxygen gas in the sputtering chamber incorporates into the depositing film.

To produce Mo-Si-N composites in a bulk form, hot pressing of pre-alloyed powders ($MoSi_2$ and Si_3N_4) with sintering aids has been used [343, 345]. Mo_5Si_3 – Si_3N_4 composites, in turn, have been prepared by infiltration in-situ synthesis where porous Si_3N_4 was infiltrated by a molybdenum solution, dried, and finally sintered [344].

The etching of Mo-Si-N films has been apparently studied very little, since only one of the referenced articles [142, 221-239, 296] contained data on it: Patel *et al.* patterned their Mo-Si-N films in CF_4/O_2 etch chemistry [230]. When Reid *et al.* needed to pattern their Mo-Si-N films for shallow junction diodes, they used lift-off [231, 232].

5.2.2 Composition and structure

The composition of sputter deposited Mo-Si-N films can be controlled by the selection of the sputtering targets, the sputtering current and power, and the nitrogen flow rate. Intuitively, the nitrogen content in Mo-Si-N films increased with the increasing N_2 partial pressure [142, 228, 230, 232], and the silicon content with the increasing sputtering current of the silicon source [221]. Hirvonen *et al.* proved the Mo:Si concentration ratio in their Mo-Si-N films corresponded well to that of the sputtering target ($MoSi_2$) [222, 223].

Strong Si-N bonds are commonly detected in Mo-Si-N films [222, 223, 227, 230, 234, 237]. In general, the chemical interaction between Si and N is much stronger than that between Mo and Si [223, 228] which, in turn, is stronger than that between Mo and N [228]. This makes understandable the preferential formation of Si_3N_4 before other possible compounds [221, 228], or that Si_3N_4 or SiN_x was the only detected state of silicon in Mo-Si-N films [227, 237].

The addition of nitrogen to Mo-Si films [228], or the addition of silicon to Mo-N films [221, 227, 236] turns the microstructure of the resultant films more amorphous by nature. Contrary to Mo-N films that were commonly crystalline, most Mo-Si-N films have proved to be amorphous [221-223, 225-228, 234-236, 296], albeit crystalline [224, 237, 238] and nanocomposite [221, 227, 228] films have also been encountered. In the latter case, fine Mo_2N [221, 227] or $MoSi_2$ [228] crystallites have been embedded in an amorphous matrix of Si_3N_4. When the microstructure is to be determined, one should remember TEM is a more reliable analysis method than XRD like the case of Kattelus *et al.* proved: the Mo-N films were amorphous according to X-ray diffraction, but a TEM analysis revealed elongated crystallites [30]. A few groups have managed to specify composition limits beyond which Mo-Si-N films are amorphous: Si > 15 at.% [221], Mo/Si ≤ 2 [227], or Si_3N_3 > 40 vol.% [228]. Alternatively, the limit can be expressed in terms of a deposition parameter, like the condition on the nitrogen partial pressure ($p_{N2} \geq 0.1$ Pa) in case of [228].

The mass density of Mo-Si-N films depends on their composition, ranging from 4.2 to 5.3 g/cm^3 [2, 235]. Slightly surprisingly, the mass density of bulk $MoSi_2$ – Si_3N_4 composites was somewhat lower, ranging from 3.3 to 4.5 g/cm^3 [343].

5.2.3 Thermal stability

Elemental molybdenum and Mo-N films are prone to oxidation (see Section 4.2.3), whereas the oxidation resistance of Si_3N_4 is excellent (e.g. [345]). Also $MoSi_2$ is said to possess excellent oxidation resistance at high temperatures [222, 223, 225, 226, 235, 341, 342, 345] but suffers from so called pest disintegration at moderate temperatures (400…600°C) [222, 226, 235, 341, 345]. Pesting means the structural disintegration of a continuous solid into a powder under oxidative conditions. The pesting of $MoSi_2$ takes place through

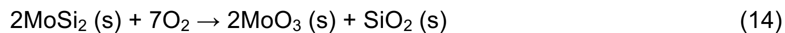

$$2MoSi_2\,(s) + 7O_2 \rightarrow 2MoO_3\,(s) + SiO_2\,(s) \qquad (14)$$

and is accompanied by a substantial volume expansion [341, 345]. In addition, MoO_3 starts to evaporate at temperatures above 550°C [320]. Mo_5Si_3, in turn, suffers from pesting at 700…800°C [344, 345]. At high temperatures (above 900°C), the surface of Mo-Si films is sealed by a protective SiO_2 layer, restraining further oxidation [345]. The thermal stability of Mo-Si-N films is finally discussed herein.

Published data on the thermal stability of Mo-Si-N films has been collected into Table 12. At their best, Mo-Si-N films have been reported to remain amorphous upon annealing at 1000°C, albeit some structural relaxation or phase separation was observed [222, 223, 225]. Some other Mo-Si-N films crystallised instead at 660…680°C [222] or, most commonly, at 800…900°C [142, 226, 232, 235, 296] with Mo_3Si and Mo_5Si_3 as the crystallisation products [142, 232]. For a comparison, initially amorphous Mo-Si films crystallise at 500…550°C [142, 222, 223, 225, 234, 235], i.e. at lower temperature than any Mo-Si-N films. The composition evidently affects the crystallisation temperature. Interestingly, all Mo-Si-N films in Table 12 sputtered from a Mo_5Si_3 target crystallised at 800°C [142, 232, 296] while each film remaining amorphous at 900…1000°C had been sputtered from a $MoSi_2$ target [222, 223, 225, 226]. Hirvonen *et al.* also proved how the crystallisation temperature increased hand in hand with the increasing nitrogen concentration in the films. They suggested the strong Si–N bonding inhibits the nucleation of molybdenum silicides, thus working in favour of the high metastability. [222] In conclusion, Mo-Si-N films are comparable to the other mictamict alloys in relation to their crystallisation temperatures.

Nitrogen tends to diffuse out from Mo-Si-N films when they are annealed in a vacuum at high temperatures [142, 232, 235, 296]. When Reid explored this phenomenon with $Mo_{35}Si_{17}N_{48}$ films he noticed the onset of the nitrogen loss occurred at 700°C, and at 1000°C virtually all nitrogen had been lost. Mo-Si-N films also liberated nitrogen more than any other mictamict alloys that were studied. [142] The nitrogen loss is possibly connected with the crystallisation in the sense the former acting as a driving force towards the latter [232].

The oxidation of Mo-Si-N thin films has been investigated by few groups only. The frequently referenced study of Hirvonen *et al.* from 1995 [222] states that the oxidation resistance of Mo-Si-N films is “excellent up to 800°C”. The study proved the oxidation resistance of Mo-Si-N films with 50 at.% N (~$Mo_{17}Si_{33}N_{50}$) was superior to that of pure $MoSi_2$ films but did not examined the role of the film composition in any more detail. The study of Musil *et al.* from 2005 [228], instead, pointed out the relevance of the phase (and elemental) composition (see Table 12 for the results). In general, an increase in the nitrogen content correlated with *decreased* oxidation resistance [228], contrary to the crystallisation temperature that *increased* with the increasing nitrogen content [222]. In any case, any Mo-Si-N films studied by Musil *et al.* did not oxidise significantly until 900°C, while the best compositions (e.g. $Mo_{19}Si_{37}N_{44}$) survived even 1300°C with “very low” oxidation [228]. A totally different picture of the oxidation resistance of Mo-Si-N films is given by Yuan *et al.* in 2010 whose Mo-Si-N films with a low silicon content (9 at.%) started to oxidise already at 400°C [238]. As an obscure topic, the oxidation of Mo-Si-N films will be discussed at length in Section 5.5.

Table 12. A summary of the published data on the thermal stability of sputter deposited Mo-Si-N films. The annealing conditions reported in the table do not necessarily represent the extreme conditions where the films would survive or fail, but only the conditions that were examined in a particular study. The table continues on the next page.

Reference	Samples and general annealing conditions	Specific annealing conditions where Mo-Si-N films survived	Specific annealing conditions where Mo-Si-N films failed
Giauque (1998) [296]	Blank $Mo_{25}Si_{17}N_{53}O_{12}$ film sputtered from a Mo_5Si_3 target. Vacuum of $7 \cdot 10^{-7}$ torr.	-	800°C, 30 min: The film lost 50 % of its nitrogen, and crystallised into Mo-N and Mo-Si.
Hirvonen (1994) [223]	Blank $Mo_{17}Si_{33}N_{50}$ films sputtered from a $MoSi_2$ target. Annealing conditions not specified.	1000°C: The films remained amorphous, albeit structural relaxation was observed.	800°C, 1 h: The nearest neighbour spacing decreased, suggesting densification.
Hirvonen (1995) [222]	Blank Mo-Si-N films with various compositions sputtered from a $MoSi_2$ target. Annealing conditions: not specified. Oxidation conditions: wet oxidation by bubbling pure O_2 gas through distilled water.	Annealing: $Mo_{17}Si_{33}N_{50}$ remained amorphous at 1000°C, albeit structural relaxation was observed. Oxidation of $Mo_{17}Si_{33}N_{50}$: “excellent oxidation resistance up to 800°C”, no nitrogen diffusion into a silicon substrate at 1000°C/2 h.	Annealing: $Mo_{27}Si_{53}N_{20}$ crystallised at 660...680°C, and $Mo_{22}Si_{43}N_{35}$ at 740...760°C. Oxidation of $Mo_{17}Si_{33}N_{50}$: nitrogen diffused into a steel substrate at 800°C/2 h.
Kung (1995) [225]	Blank $MoSi_2N_x$ (x=3–4) films sputtered apparently from a $MoSi_2$ target. Vacuum of 10^{-8} torr.	900°C, 1 h: $MoSi_2N_x$ worked as a diffusion barrier between Mo and $MoSi_2$. 1000°C, 1 h: $MoSi_2N_x$ remained amorphous.	800°C, 1 h: Phase separation (spinodal decomposition) was observed.
Kung (1996) [226]	Blank $MoSi_2N_x$ (x=0–4.2) films sputtered from a $MoSi_2$ target. Vacuum of 10^{-8} torr.	900°C, 3 hours: The films with x=2.95 and x=4.2 remained amorphous, albeit phase separation was observed.	900°C, 3 hours: The film with x=1.5 crystallised partly.
Musil (2005) [228]	Blank Mo-Si-N films with various compositions sputtered from a $MoSi_2$ target on top of silicon. Pure flowing air.	1300°C, 30 min: Films with a phase composition of Si_3N_4 + $MoSi_2$ + Mo or Si_3N_4 + Mo_2N + Mo exhibited a very low mass loss (Δm < -0.01 mg/cm^2) due to oxidation.	900...1300°C, 30 min: Films with a phase composition of Si_3N_4 + $MoN_{x>1}$ started to exhibit a mass loss at 900°C. The loss was -0.01 mg/cm^2 ≤ Δm < -0.05 mg/cm^2 at 1300°C. A porous surface oxide layer formed simultaneously.

Reference	Samples and general annealing conditions	Specific annealing conditions where Mo-Si-N films survived	Specific annealing conditions where Mo-Si-N films failed
Reid (1993) [232]	Blank Mo-Si-N films sputtered from a Mo_5Si_3 target, and with 36...48 at.% of nitrogen; n^+p shallow junction diodes with Mo-Si-N as a diffusion barrier. Vacuum of $4 \cdot 10^{-7}$ torr.	800°C, 30 min: Mo-Si-N worked as a diffusion barrier between Si and Cu. 850°C, 30 min: no reaction with copper.	800°C, 1 h: Amorphous Mo-Si-N crystallised into Mo_3Si and Mo_5Si_3, and lost 5...10 at.% of nitrogen.
Reid (1995) [142]	Blank Mo-Si-N films sputtered from a Mo_5Si_3 target, and with 10...50 at.% of nitrogen. Vacuum.	600°C, 1 h: no out-diffusion of nitrogen from $Mo_{35}Si_{17}N_{48}$ films. 700°C, 1 h: All Mo-Si-N films (with various compositions) remained amorphous.	700°C, 1 h: the onset of nitrogen out-diffusion from $Mo_{35}Si_{17}N_{48}$ films. 800°C, 1 h: All Mo-Si-N films (with various compositions) crystallised. 1000°C, 1 h: Virtually all nitrogen was lost from $Mo_{35}Si_{17}N_{48}$ films.
Reid (1996) [231]	Blank $Mo_{36}Si_{17}N_{47}$ films sputtered from a Mo_5Si_3 target; n^+p shallow junction diodes with $Mo_{36}Si_{17}N_{47}$ as a diffusion barrier. Vacuum better than 10^{-6} torr.	600°C, 2 h: no reaction with aluminium. 675°C, 10 min: $Mo_{36}Si_{17}N_{47}$ worked as a diffusion barrier between Si and Al. 700°C, 2 h: The films remained amorphous.	-
Sun (2001) [233]	p^+n diodes with Mo-Si-N as a diffusion barrier; the Mo-Si-N films were sputtered from a Mo_5Si_3 target with various N_2 flow rates. Vacuum.	750°C, 30 min: Mo-Si-N worked as a diffusion barrier between Si and Cu.	-
Torri (1999) [235]	Blank $MoSi_{2.2}N_{2.5}$ films sputtered from a $MoSi_2$ target. Annealing at ≤ 900°C: vacuum better than 10^{-6} Pa; annealing at 1050...1075°C: vacuum better than $5 \cdot 10^{-4}$ Pa.	500°C, 3 h: The films remained amorphous. 900°C, 3 h: no out-diffusion of nitrogen. 900°C, 16 h: Mo-Si-N worked as a diffusion barrier between $MoSi_2$ and SiC. 1075°C, 41 h: The thermal stability of the Mo-Si-N/SiC interface was good.	900°C, 3 h: The films crystallised partly (Mo_5Si_3 nanocrystals were embedded in an amorphous matrix). 1050°C: The film lost about 30 % of its nitrogen close to the surface (30 nm).
Torri (2000) [234]	Blank $MoSi_{2.2}N_{2.5}$ films sputtered from a $MoSi_2$ target. Vacuum better than $5 \cdot 10^{-4}$ Pa.	500°C, 3 h: The films remained amorphous.	-
Yuan (2010) [238]	Blank Mo-Si-N films with 9 at.% of silicon. Oxidation conditions not specified.	50…400°C: The weight change due to oxidation was ≤ 0.05 %.	400°C: the onset of oxidation (the weight change exceeded 0.05 %)

5.2.4 Mechanical properties

The mechanical properties of thin films are governed by their microstructure. The microstructure, in turn, is dictated by the composition, the deposition parameters, and the heat treatments the films have experienced. The residual stress of Mo-Si-N films, according to the references of Table 13, has usually been compressive. The only exception is the work of Kattelus *et al.*, who managed to turn the stress of sputter deposited Mo-Si-N films from compressive to tensile by changing the argon pressure. They also proved the residual stress of TEM amorphous Mo-Si-N films was more uniform than that of Mo-N films with only a partly amorphous microstructure, or elemental Mo films with a polycrystalline structure. [2] Musil *et al.*, in turn, recorded the relationship between the residual stress and the N_2 partial pressure (p_{N2}) during sputter deposition, given that the total pressure was constant: the stress got more compressive with the increasing N_2 pressure until a plateau of approximately -2 GPa at p_{N2} = 0.2 Pa was reached. When Mo-Si-N films were annealed at 350...500°C, their compressive stress decreased in magnitude, i.e. it became more tensile by nature. The stress change occurred during the first 15 minutes, and was dependent on the annealing temperature: the higher the temperature, the larger the change. [235]

Table 13. A summary of the mechanical properties of as-deposited Mo-Si-N films. In several cases, a range of values is reported instead of a single figure. The ranges do not refer to measurement uncertainty, but to the variation due to the composition or the structure. The sign convention for residual stress is: (+) = tensile, (-) = compressive.

Reference	**Residual stress (MPa)**	**Elastic modulus (GPa)**	**Hardness (GPa)**	**Elastic recovery (%)**	**Friction coefficient**
Heo (2006) [221]	-	-	24...37	-	0.40…0.60
Hirvonen (1994) [223]	-	257	18.8	-	-
Jung (2007) [224]	-2000...-2300	-	28...32	-	-
Kattelus (2003) [2]	-100…+200	-	-	-	-
Kung (1996) [226]	-	201...213	12.9...17.8	-	-
Liu (2006) [227]	-	150...366	10…30	30…40	0.22…0.28
Musil (2005) [228]	-500…-2500	200…270	15…27	50…70	-
Reid (1995) [142]	-560	-	-	-	-
Torri (1999) [235]	-1300	215	19	-	-
Yuan (2010) [238]	-	320	24	-	-
Yuan (2011) [237]	-	-	22	-	0.24

Table 13 contains a summary of the mechanical properties of as-deposited Mo-Si-N films. The elastic modulus ranges from 150 to 370 GPa, and the hardness from 10 to 37 GPa, i.e. both vary a lot. The elastic modulus was rather independent from the nitrogen content [226]; instead, it increased with the increasing Mo/Si ratio in the films, just like the hardness also did [227]. In general, the hardness varied with the composition but the relationship remained ambiguous, differing from case to case [221, 226-228]. The findings were consistent with, however, that both the elastic modulus and the hardness increase upon annealing [223, 226, 235], likely due to densification or crystallisation [226]. The elastic recovery of Mo-Si-N films ranged between 30 and 70 %, and was found to increase together with the hardness [228]. The friction coefficient was 0.22 at its best, appearing to decrease with the increasing silicon content in the films [221, 227]. Amorphous films under small compressive stress were most resistant to cracking [229].

5.2.5 Other properties

The typical resistivities of Mo-Si-N films range from 250 to 1800 μΩcm [142, 231-233], i.e. they are at the same or lower level than those of heavily doped polysilicon films. For a comparison, the resistivity of Mo-Si films deposited from a Mo_5Si_3 target has been around 200 μΩcm [231-233]. Not surprising, a rise in the N_2 gas flow during sputter deposition results in Mo-Si-N films with increased resistivity [142, 230, 232, 233]. Since high nitrogen content promotes a small grain size or even the amorphisation of the films, the resistivity rise has been explained by the reduced mobility of charge carriers due to the increased grain boundary scattering [233]. When Mo-Si-N films were annealed in vacuum at 900°C for 1 hour their resistivity dropped even by 90 % [142].

Kattelus *et al.* [2] have been the only ones measuring the temperature coefficient of resistance for Mo-Si-N films. The TCR at room temperature was negative varying from -480 to -1900 ppm/K depending on the composition. The reason for the negative TCR was not explained.

Patel *et al.* [230] and Wen *et al.* [236] have determined the work function of Mo-Si-N films when evaluating them for CMOS metal gate electrodes. The former found the work function decreased with the increasing nitrogen content in the films, ranging from 4.4 to 4.7 eV [230]. The latter found, in turn, the work function decreased with the increasing silicon content, falling between 4.3 and 4.5 eV after a rapid anneal at 1000°C [236].

5.2.6 Applications

Mo-Si-N films have been studied most for diffusion barriers [142, 225, 226, 231-233, 235] and surface coatings for various purposes [221, 222-224, 227, 228, 234], just like the mictamict alloys in general. Mo-Si-N films were able to prevent the diffusion between silicon and copper at 750…800°C for 30 min [232, 233], and between silicon and aluminium at 675°C for 10 min [231] (see Table 12). Mo-Si-N films so beat

both Mo-Si [231, 232] and Mo-N films [233] in performance. The failure was associated with the crystallisation of the films together with resultant grain boundary diffusion [232]. Besides diffusion barriers, Mo-Si-N films have been evaluated for CMOS metal gate electrodes [230, 236].

In a bulk form, Mo-Si-N composites have been explored for use as structural materials, similar to $MoSi_2$ and Si_3N_4 [343, 344]. Mo-Si-N films have also been incorporated into some nanolayered composites as second-phase reinforcements [225, 226, 235]. In the above applications, the high-temperature behaviour of Mo-Si-N is often essential.

To the best of the author's knowledge, Mo-Si-N films have not been applied to MEMS outside VTT.

5.3 Experimental procedure

5.3.1 Analysis of as-deposited films

The experimental procedure to study Mo-Si-N films followed that to study Mo-N films (see Section 4.3) and is not repeated in detail wherein identical. Mo-Si-N films were deposited by reactive sputtering in the presence of N_2 gas by using either separate Mo and Si targets (in Balzers/Provac LLS 801 sputtering system) or a Mo_5Si_3 compound target (in Von Ardenne CS 730 S sputtering system). Like earlier, the Balzers/Provac LLS 801 system carried sputtering processes for both 100 and 150 mm substrates (Table 14). The 100 mm process was developed before the author fully joined the work [2], whereas the 150 mm process was picked and characterised by the author. The use of separate sputtering targets in the Balzers/Provac system involved a risk of inhomogeneity in the film composition as films formed layer upon layer; on the other hand, it enabled independent control of each constituent of the films. Because of the former, the rotation speed of the sample holder was set at its maximum to keep the distinct layers as thin as possible. Unlike in the case of a molybdenum target, DC biasing is not applicable to a silicon target since silicon develops an insulating surface nitride in N_2 gas resulting in arcing; in consequence, pulsed DC power was used. Prior to deposition, the targets were always cleaned by pre-sputtering. No external heating or cooling was used. At Balzers/Provac, film thickness was determined by the rotation speed and the number of revolutions of the sample holder; at Von Ardenne, thickness was determined by the sputtering time. The 150 mm substrates for the experiments are detailed in Table 15.

The first major set of experiments aimed to deposit Mo-Si-N films from separate Mo and Si targets (Table 16). Again, the pressure values provided as system-specific background information are cited as reference values, and the actual pressure readings as true values. There was a systematic discrepancy between the above values, the true ones being always 8…11 % lower than the reference ones, which was possibly due to the time elapsed between the measurements. The deposition runs #1…8 studied the effects of the Ar and N_2 flow rates on the film properties, while the runs #B1…B9 provided samples for the experiments on thermal stability

Table 14. The sputtering processes for the deposition of Mo-Si-N films by using separate Mo and Si targets.

Parameter	**Standard 100 mm process at Balzers LLS 801 system [6]**	**Variable 150 mm process at Provac LLS 801 system**	**Standard 150 mm process at Provac LLS 801 system**
Base pressure (µbar)	$6.0 \cdot 10^{-4}$	$5.0 \cdot 10^{-4}$	$5.0 \cdot 10^{-4}$
Throttle setting (off/on)	-	On	On
Ar flow rate (sccm)	-	40…70	50
Ar pressure (µbar)	4.45	3.8…6.4	~4.2
N_2 flow rate (sccm)	-	20…35	25
N_2 pressure (µbar)	0.85	0.9…1.6	~1.1
Total pressure (µbar)	5.3	4.3…7.3	5.3
DC power on Mo target (W)	600	600	600
Pulsed DC power on Si target (W)	1000	1000	1000
Duration of a drum revolution (s)	20	20	20

Table 15. The 150 mm silicon substrates for the experiments on Mo-Si-N films. All wafers were (100) oriented. SSP = single side polished, DSP = double side polished.

Sample #	**Thickness of silicon wafer (µm)**	**Polishing of silicon wafer**	**Type of substrate (blank/ oxidised)**	**Thickness of silicon oxide (nm)**
9…24	675 ± 15	SSP	Oxidised	105
36…39, 41	675 ± 15	SSP	Oxidised	103
42…46	675 ± 15	SSP	Blank	-
51, 52, 54…63, 65…73	675 ± 15	SSP	Oxidised	97
83…86	675 ± 15	SSP	Oxidised	103
E1…E10, E16…E23	675 ± 15	SSP	Oxidised	360
J2…J12	400 ± 5	DSP	Blank	-
J13…J17	400 ± 5	DSP	Oxidised	103
N25	330 ± 10	DSP	Blank	-

Table 16. The variable sputtering parameters of the Mo-Si-N depositions with the 150 mm process at Provac LLS 801 sputtering system by using separate Mo and Si targets. The pressure values cited as (ref.) and (true) refer to reference and true measured values, respectively. The number of revolutions refers to how many times the sample holder rotated around its axis during the deposition, dictating the thickness of the depositing Mo-Si-N film. In the run #B9, a 10 nm silicon film was sputter deposited both beneath and on top of the Mo-Si-N film.

Deposition run #	Sample #	Base pressure (µbar)	Ar flow rate (sccm)	Ar pressure (ref.) (µbar)	N_2 flow rate (sccm)	N_2 pressure (ref.) (µbar)	Total pressure (ref.) (µbar)	N_2 partial pressure (%)	Total pressure (true) (µbar)	Number of revolutions
1	9	$5.0 \cdot 10^{-4}$	50	4.66	25	1.16	5.82	19.9	5.3	200
2	10…15	$5.0 \cdot 10^{-4}$	50	4.66	25	1.16	5.82	19.9	5.3	140
3	16, 17	$5.0 \cdot 10^{-4}$	40	3.80	20	0.94	4.74	19.8	4.3	200
4	18, 19	$5.0 \cdot 10^{-4}$	60	5.52	30	1.38	6.90	20.0	6.3	200
5	20, 21	$5.0 \cdot 10^{-4}$	70	6.35	35	1.60	7.95	20.1	7.3	200
6	22, 23	$5.0 \cdot 10^{-4}$	40	3.80	25	1.16	4.96	23.4	4.4	200
7	51, 52	$5.0 \cdot 10^{-4}$	60	5.52	25	1.16	6.68	17.4	6.1	200
8	24, E1…E10	$5.0 \cdot 10^{-4}$	50	4.66	25	1.16	5.82	19.9	5.3	200
B1	63, 65, J11	$5.0 \cdot 10^{-4}$	50	4.66	25	1.16	5.82	19.9	5.2	350
B2	42, E16	$5.0 \cdot 10^{-3}$	50	4.66	25	1.16	5.82	19.9	5.1	150
B3	43, E17…E19	$5.0 \cdot 10^{-4}$	50	4.66	25	1.16	5.82	19.9	5.1	300
B4	44, 66	$5.0 \cdot 10^{-3}$	50	4.66	25	1.16	5.82	19.9	5.2	150
B5	67…72	$5.0 \cdot 10^{-4}$	50	4.66	25	1.16	5.82	19.9	-	300
B6	41, J13	$5.0 \cdot 10^{-4}$	50	4.66	25	1.16	5.82	19.9	5.2	450
B7	73, E20…E23, J14…J16	$5.0 \cdot 10^{-4}$	50	4.66	25	1.16	5.82	19.9	5.2	300
B8	83, J17, a carbon button	$5.0 \cdot 10^{-4}$	50	4.66	25	1.16	5.82	19.9	5.2	150
B9	84…86	$5.0 \cdot 10^{-4}$	50	4.66	25	1.16	5.82	19.9	5.2	300

and thickness dependency. The base pressure at #B2 and #B4 was impaired on purpose so as to figure out whether a higher impurity content would make any difference. The Mo-Si-N films of #B9 had a 10 nm silicon film both beneath and on top of them; these silicon capping layers were sputter deposited by the parameters of Table 17. The silicon depositions were conducted immediately before and after the Mo-Si-N deposition without breaking the vacuum in between.

Table 17. The parameters to deposit 10 nm of silicon with Provac LLS 801 sputtering system. No external heating was used.

Parameter	Value
Base pressure	$5.0 \cdot 10^{-4}$ µbar
Throttle setting	Off
Ar flow rate	195 sccm
Ar pressure	3.25 µbar
Pulsed DC power on Si target	1000 W
Duration of a drum revolution	51 s
Number of revolutions	4

The second major set of experiments involved the deposition of Mo-Si-N films from a Mo_5Si_3 compound target (Table 18) in order to find out if the film properties were dependent on the choice of the sputtering target. Since introducing a compound target into Provac LLS 801 sputtering system was not practicable, the new deposition process was built up with Von Ardenne CS 730 S system described in [346]. Because the composition of the Mo-Si-N films deposited by the standard 100 mm process was $Mo_{31}Si_{18}N_{45}O_6$ [6], a Mo_5Si_3 target was selected rather than $MoSi_2$ or Mo_3Si targets, the former having a Mo/Si ratio quite close to the reported one. The relationship between a flow rate and the resulting pressure was available only for argon, not for nitrogen. Once again, the deposition runs #1..6 aimed to study the effects of the Ar and N_2 flow rates, while the runs #C1…C4 provided samples for subsequent experiments.

Mo-Si-N films were analysed mainly by similar methods to Mo-N films (see Section 4.3). To measure the thickness of Mo-Si-N films, they were patterned by lithography with SPR 700 photoresist and Süss Microtec mask aligner. The Mo-Si-N films were etched until the underlying silicon oxide layer with LAM Research Rainbow 4420 plasma etcher by using processes based on SF_6 and He, or Cl_2 and HBr. The photoresist was removed by a low temperature plasma process at GaSonics Aura A-1000 microwave asher. The resulting step heights were measured by profilometry. Because the fluorine-based plasma etching was capable of erasing silicon oxide, the amount of the consumed silicon oxide was determined by measuring its original thickness (before the Mo-Si-N deposition) and the thickness after the Mo-Si-N etching, both by reflectometry. Alternatively, the thickness of Mo-Si-N films was evaluated by SEM.

The resistivity of Mo-Si-N films was measured completely similarly to Mo-N films. The procedure to measure the residual stress was also alike except for the removal of Mo-Si-N films, which was done by AOE n/o 37743 oxide ICP etcher with a process based on SF_6, C_4F_8 and O_2, or by a wet etch mixture comprising H_2O, NH_4F and HNO_3 (polysilicon wet etchant). The underlying silicon oxide was removed by liquid HF. In the case of the Mo-Si-N films sputtered from a compound target the films did not need to be removed at all, because the first curvature measurement

was performed already before the deposition; this was not possible for the samples sputtered from separate targets because of a cleanliness-related lab policy.

Table 18. The variable sputtering parameters of the Mo-Si-N depositions with the 150 mm process at Von Ardenne CS 730 S sputtering system by using a Mo_5Si_3 target. The base pressure was $5.0 \cdot 10^{-4}$ µbar, and the sputtering power 500 W. No external heating or cooling was used.

Deposition run #	Sample #	Ar flow (sccm)	N_2 flow (sccm)	Throttle setting	Ar pressure (ref.) (µbar)	Sputtering time (s)
1	54, J2	60	10	Open	4.0	900
2	55, J3	60	10	Closed	13.2	900
3	56, J4	100	5	Open	6.5	900
4	57, J5	100	10	Open	6.5	900
5	58, J6	90	10	Open	5.9	900
6	59, J7	50	5	Closed	11.2	900
C1	60, 61, J8, J9	90	10	Open	5.9	900
C2	36, 46	90	10	Open	5.9	1460
C3	62, J10, a carbon button	90	10	Open	5.9	485
C4	37…39, 45, J12, N25	90	10	Open	5.9	975

The microstructures of selected Mo-Si-N films were analysed by XRD, and the compositions by RBS with a He beam of 2.00 MeV. XRD makes use of the fact that X-rays obey the Bragg condition for constructive interference from an array made by atoms in a crystal, and is therefore used for the study of the crystal structure, or vice versa, the lack of crystallinity. For the RBS analyses, 200…250 nm thick Mo-Si-N films were deposited on top of carbon buttons.

The Mo-Si-N samples for the surface roughness measurements were deposited by 100 mm sputtering processes at Balzers LLS 801 system (Table 14). The substrates were polished, (100) oriented silicon wafers coated by silicon oxide. The oxide layers were grown by wet oxidation at 950°C, and were either 100 or 300 nm thick. Three Mo-Si-N compositions were studied; the compositions were accordant with [2]. The roughness was measured by AFM with Digital Instruments Dimension 3100 AFM system and a measurement area of $1 \cdot 1$ µm^2. In AFM, the sample is scanned by a sharp tip mounted to a cantilever, and the force between the probe and the specimen is sensed.

The mechanical properties of Mo-Si-N films were investigated by nanoindentation. The 500 nm thick films were deposited with the standard 100 mm sputtering process of Table 14. For a comparison, elemental molybdenum films of the same thickness were analysed as well. Both types of samples were deposited on polished, (100) oriented, 525 µm thick silicon substrates coated with thermal silicon oxide of 100 nm. The molybdenum deposition was conducted at Balzers LLS 801 sputtering

system with argon pressure of 0.19 Pa, and DC target power of 3.0 kW. No heating was used. The molybdenum films had 10 nm Ti-W films beneath and 4 nm silicon films on top of them; the former served as adhesion layers, while the latter are normally included for improving thermal stability. Prior to indentation, the wafers were diced and the sample chips glued to the sample holder. The nanoindentation itself was performed with an upgraded NanoTest 550 instrument (Micro Materials Ltd., Wrexham, UK). The displacement of a pyramidal Berkovich diamond indenter and the corresponding load were recorded. Three different load forces were applied: 1, 10 and 50 mN. The measurements were repeated a statistically significant number of times. The hardness and the elastic modulus were computed from the load–displacement data by the Oliver–Pharr analysis method [347]. A Poisson's ratio of 0.3 was assumed for the samples. After the indentation, the plastic deformation profiles were analysed by AFM.

The Mo-Si-N films for the optical measurements were deposited by the standard 150 mm sputtering process of Table 14. The substrates were polished, (100) oriented, phosphorus-doped, 675 µm thick silicon wafers that were cleaned with standard clean SC-1 and rinsed in deionised (DI) water before the deposition. Some substrates were coated with thermal silicon oxide of 100 nm grown by wet oxidation at 850°C. The dispersions of the refractive indices were determined based on reflectance measurements conducted with spectroscopic reflectometry (FilmTek 4000), gonioreflectometry [348], and double-beam transfer standard spectrometry (Perkin-Elmer). The wavelength regions for the measurements were 190...1650 nm (spectroscopic reflectometry), 1000...1650 nm (gonioreflectometry), and 400...2400 nm (transfer standard spectrometry). The spectroscopic reflectometer operated with two fixed angles (0° and 70°). The gonioreflectometer employed a silicon detector on the visible spectral range, and an InGaAs detector on the near-infrared (NIR) range being capable of measuring up to 1650 nm. A measuring interval of 50 nm was used. The transfer standard spectrometer, for one, measures regular spectral reflectance. The instrument in question employed halogen-tungsten and deuterium-arc light sources. The size of the incident beam was roughly 5 mm × 10 mm, and its angle relative to the sample normal 6°. The regular reflectance was determined twice for both orthogonal polarisation states (p and s), and with wavelength intervals of 5.0 nm. An aluminium mirror served as a reference.

5.3.2 High and low temperature experiments

The thermal stability of Mo-Si-N films was first studied with Tencor FLX-2320 thin film stress measurement instrument. The Mo-Si-N films for these experiments were deposited by the standard 100 mm sputtering process (Table 14) except for one molybdenum-rich sample whose composition was $Mo_{34}Si_{20}N_{41}O_5$ [2], and one sample that had a low deposition rate, achieved by halving the sputtering powers on Mo and Si targets compared to the standard process. Consequently, the thickness and the composition of the latter were not known precisely. The substrates were polished, (100) oriented silicon wafers coated with thermal silicon oxide of 100 or

300 nm. The Tencor FLX-2320 stress measurement instrument used laser interferometry (with two solid-state lasers operating at wavelengths of 670 and 750 nm) to measure changes in the radius of curvature of the sample wafer. The scan length was 8.0 cm. A value of 180 GPa was assumed for the biaxial modulus of the silicon substrates. The instrument incorporated a hot plate that could be heated up to 500°C; thus stress measurements as a function of time and temperature were possible. The heating and cooling rates were 2°C/min. The surrounding gas during the experiments was a mixture of nitrogen and residual air. Two samples were annealed by RTA (rapid thermal annealing) in N_2 gas before the measurements, and one sample was heated twice to the related maximum temperature (200°C).

The Mo-Si-N films for RTA annealing tests were deposited by the standard 100 mm sputtering process (Table 14). The film thickness was 325 nm. Half of the substrates were polished, (100) oriented silicon wafers coated with thermal silicon oxide of 100 nm, while the other half of the substrates were of fused silica (SiO_2). The samples were RTA annealed in N_2 gas for 1 minute, after which the resistivity of Mo-Si-N films was measured by four-point probing.

Similar to above, the Mo-Si-N films for longer-term annealing tests were deposited by the standard 100 mm sputtering process on top of polished, (100) oriented silicon wafers coated with thermal silicon oxide of 100 nm. The thickness of the Mo-Si-N films was 300 nm. The films were annealed for 30 or 60 min at temperatures between 400 and 700°C in an annealing tube. The surrounding gas was either O_2 or N_2. In the case of nitrogen annealing, the samples were exposed to ambient air (and oxygen) at slightly increased temperatures upon loading and unloading when the tube was not pumped out of residual air. After annealing, the Mo-Si-N films were studied for their looks and composition by microscope imaging, SEM and EDX.

The composition of a Mo-Si-N sample heated in a Tencor FLX-2320 stress measurement instrument was measured by RBS on top of an oxidised silicon substrate. In addition, the compositions of a few annealed Mo-Si-N samples were analysed with energy dispersive X-ray spectroscopy (EDX), which was combined to the SEM tool. In EDX, the sample is bombarded by electrons, and the resulting X-ray emission is detected. Since the energies of the X-rays are characteristic to the elements they originate from, EDX is suitable for the identification of elements. The use of EDX is limited by its poor sensitivity (elemental concentrations below 1 % are difficult to observe [36]), and problems in detecting carbon, oxygen and nitrogen [37].

In the search for passivation against oxidation, some Mo-Si-N films were underlaid and capped with 10 nm silicon films beneath and on top of them. The Mo-Si-N films for these experiments were deposited by the standard 100 mm process at Provac LLS 801 sputtering system (Table 14) on top of polished, (100) oriented, 380 µm thick silicon wafers coated with thermal silicon oxide of 200 nm. The thickness of the Mo-Si-N films was 300 nm. The silicon films were deposited in the same sputtering system immediately before and after the Mo-Si-N films without breaking the vacuum in between. After the deposition, the samples were heated at temperatures between 100 and 400°C; the heat treatments at 100 and 150°C were performed on a hot plate in ambient air, while the heat treatments at 200…400°C were performed in an annealing tube with N_2 gas. The annealing time was 30 min except

Table 19. The annealing parameters for studying the thermal stability of Mo-Si-N films. The second column in the table identifies the deposition run from which the sample originated from. The samples for the experiment #2 were sputtered from a Mo_5Si_3 target (tagged with *); see Table 18. The base pressure of the deposition runs #B2 and #B4 was impaired on purpose to $5.0 \cdot 10^{-3}$ µbar (tagged with **).

Annealing experi-ment #	Deposi-tion run #	Sample #	Surround-ing gas	Pressure (mbar)	Tempera-ture (°C)	Hold time (min)
1	C1	60, J8	Nitrogen	< 50	400	75
2	3*	56, J4	Nitrogen	< 50	400	75
3	B1	65, J11	Nitrogen	< 50	400	75
4	B1	65, J11	Nitrogen	1000	400	75
7	B2**	E16	Oxygen plasma	1300	220…260	< 1.5
8	B2**	42	Nitrogen	1000	400	75
9	B1	J11	Air	1000	400	75
10	B2**	42	Air	1000	400	75
17	B4**	44, 66	Air	1000	400	75
18	B5	67	Air	1000	400	75
19	B5	68	Air	1000	300	75
20	B5	69	Air	1000	350	75
21	B5	70	Air	1000	325	75
22	B7	73	Air	1000	375	75
23	B7	J14	Air	1000	350	75
24	B7	J15	Air	1000	250	75
25	B9	84	Air	1000	400	75
26	B9	85	Air	1000	350	75
27	C1	61, J9	Air	1000	400	75
28	C4	37	Air	1000	300	75
29	C4	38	Air	1000	350	75
30	C4	39	Air	1000	375	75
31	C4	J12	Air	1000	350	75
32	C4	N25	Air	1000	250	75

for one sample heated twice at 400°C for 2 × 30 min. The samples were measured for their resistivity and residual stress after the heat treatments. Between the curvature measurements, the sputtered films were removed by RIE with SF_6/O_2 plasma chemistry, and the underlying silicon oxide by liquid HF.

A major set of experiments investigated the dependence of the thermal stability on the sputtering targets (Table 19). Like in the case of Mo-N films, the samples

were annealed in the Heraeus VT 5042 EKP vacuum oven except for the experiment #7, which was conducted with GaSonics Aura A-1000 microwave asher normally used for photoresist stripping. In the GaSonics asher, the sample was exposed to oxygen plasma for about 90 seconds. During such a treatment, the temperature in the plasma chamber rose to 220…260°C. With the Heraeus oven, the surrounding gas (N_2 or air), the pressure and the annealing temperature were varied. The hold time was always 75 minutes.

The Mo-Si-N films for low temperature experiments were deposited by the standard 100 mm process at Balzers LLS 801 sputtering system onto polished, (100) oriented silicon wafers coated with thermal silicon oxide of 100 nm. The film thickness was 25 nm for nanoscale wires, and between 5 and 325 nm for other samples. The nanoscale patterns were defined into a 140 nm polymethyl methacrylate (PMMA) film by electron beam lithography (EBL). The Mo-Si-N films were etched in SF_6/He plasma chemistry with an etch rate of 200 nm/min. As the final step, contact pads were defined by ultraviolet (UV) lithography and lift-off into a 300 nm thick sputtered copper film. The width of the nanowires at their narrowest isthmus was either 20 or 85 nm. As a reference, 25 μm wide and 24100 μm long Mo-Si-N bars were patterned beside the nanostructures. The sheet resistance of 50 nm thick Mo-Si-N films was measured by an alternating current (AC) resistance bridge with the lowest possible excitation voltage (3−30 μV) in order to avoid the current-induced self-heating of the films. In the temperature range from 80 mK to 4.2 K, a He^3/He^4 dilution refrigerator was used. Above 4.2 K, the measurements were carried out in a helium container in the temperature gradient above liquid helium. The sample was fixed on a copper sample holder. The temperature was recorded by calibrated ruthenium oxide (below 4.2 K) or rhodium−iron (above 4.2 K) thermometers. The maximum current endurance was measured at room temperature from a resistor of length 20 μm, width 10 μm and thickness 100 nm.

5.4 Properties of as-deposited films

The 100 mm sputtering process to deposit Mo-Si-N films at Balzers LLS 801 system was developed before the author fully joined the work [2], and is summarised in Table 20 to serve as a reference. The table contains also specific data on the 100 mm process at the updated Provac LLS 801 system wherein it differed from the previous; this data was acquired by the author. All in all, the latter was effectively a copy of the former. The summary of Table 20 is presented because several experiments performed by the author and reported as a part of this thesis were conducted with Mo-Si-N films deposited by the 100 mm process.

Table 20. A summary of the properties of Mo-Si-N films deposited by the standard 100 mm process at Balzers/Provac LLS 801 sputtering system.

Property	Value
Deposition rate:	
Balzers LLS 801	1.8 nm/revolution [2]
Provac LLS 801	1.5 nm/revolution
Composition:	
Balzers LLS 801	$Mo_{31}Si_{18}N_{45}O_6$ [2]
Provac LLS 801	$Mo_{31}Si_{20}N_{45}O_4$
Microstructure	Amorphous (verified by TEM and electron diffraction) [2]
Mass density	5.1 g/cm^3 [2]
Resistivity [2]:	
As-deposited	1.1 mΩcm
RTA annealed at 700°C for 1 min	1.0 mΩcm
RTA annealed at 1100°C for 1 min	0.4 mΩcm
Temperature coefficient of resistance (near *T*=300 K)	-840 ppm/K [2]
Residual stress (as-deposited)	~200 MPa (tensile)
Plasma etching	SF_6/He, or SF_6/O_2 [4]

The 150 mm deposition process for Mo-Si-N films at Provac LLS 801 sputtering system by using separate Mo and Si targets was built up by the author, and is described in more detail. The electric powers on molybdenum and silicon targets were fixed, and only argon and nitrogen flow rates (Ar and N_2 partial pressures) were varied. The deposition rate, the etch rate and the resistivity of the resulting films are presented in Table 21. The deposition rate of all samples fell between 1.3 and 1.4 nm per one revolution of the sample holder, each taking 20 seconds, which is slightly less than for the former 100 mm deposition process at Balzers LLS 801 system [2]. A low deposition rate increases the risk that any residual oxygen gas in the sputtering chamber incorporates into the depositing films. An unambiguous downward trend in the deposition rate with the increasing N_2 partial pressure was not observed. The etch rate by SF_6/He plasma varied between 160 and 240 nm/min (see Section 6.1.1 for more information on the etch properties of Mo-Si-N films). Plotted against the total deposition pressure, the etch rate had a local drop at 5.3 µbar, verified by a double measurement (Figure 18). The physical or chemical origin of the drop was not known.

Table 21. The deposition rate, the etch rate, and the resistivity of Mo-Si-N films deposited from separate Mo and Si targets with a 150 mm process at Provac LLS 801 sputtering system. The pressure values refer to those that prevailed during deposition. The films were plasma etched by SF_6 and He. SM = system monitor. It was assumed the thickness of the run #1 was identical to the thickness of the run #8 (tagged with *). It was also assumed the deposition rates of #B1…B9 were identical to each other (tagged with **); only the thickness of #B6 was really measured, and the rest were calculated consequentially. In the run #B9, a 10 nm silicon film was sputter deposited both beneath and on top of the Mo-Si-N film.

Deposition run #	**Sample #**	**Total pressure (µbar)**	**N_2 partial pressure (%)**	**Thickness of Mo-Si-N (nm)**	**Deposition rate (nm/ revolution)**	**End-point time (s)**	**Etch rate (nm/ min)**	**Resistivity (mΩcm)**
1	9	5.3	19.9	270*	-	-	-	1.2
2	10	5.3	19.9	190	1.4	-	-	-
3	16, 17	4.3	19.8	270	1.4	90	180	0.8
4	18, 19	6.3	20.0	260	1.3	75	210	1.7
5	20, 21	7.3	20.1	270	1.3	68	240	2.3
6	22, 23	4.4	23.4	280	1.4	85	200	1.1
7	51, 52	6.1	17.4	280	1.4	81	200	1.3
8	24, E8, E10	5.3	19.9	270	1.3	104	160	1.2
B1	63	5.2	19.9	510**	-	-	-	1.0
B3	SM	5.1	19.9	430**	-	-	-	1.0
B4	SM	5.2	19.9	210**	-	-	-	1.0
B5	67	-	19.9	430**	-	-	-	1.0
B6	41	5.2	19.9	640	1.4	-	-	1.1
B7	73	5.2	19.9	430**	-	-	-	1.1
B8	83	5.2	19.9	210**	-	-	-	1.0
B9	84	5.2	19.9	10+430** +10	-	-	-	1.1

The resistivity of Mo-Si-N films varied from 0.8 to 2.3 mΩcm depending on the deposition parameters. The trend was upward with the total deposition pressure (Figure 19). However, the rise was much steeper for a constant Ar/N_2 gas flow ratio than for a fixed N_2 flow, pointing out the significance of the nitrogen content. There was no evidence the resistivity would depend on film thickness.

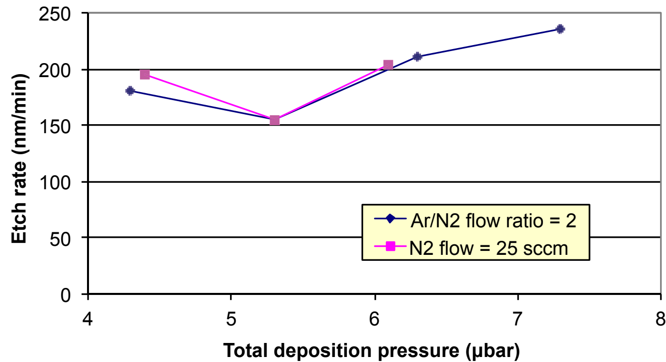

Figure 18. The SF_6/He plasma etch rate of Mo-Si-N films deposited from separate Mo and Si targets. The blue graph illustrates a case with a constant Ar/N_2 gas flow ratio, while the red graph refers to a case with a fixed N_2 flow but a variable Ar flow.

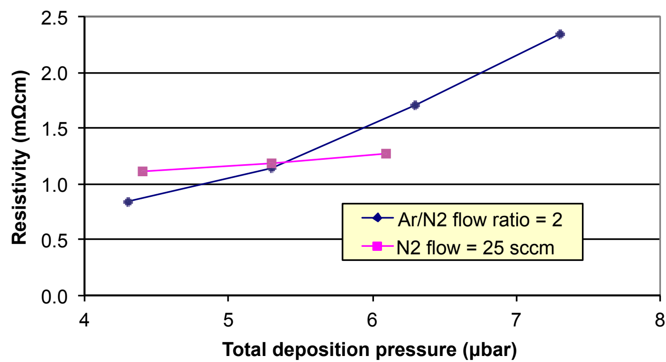

Figure 19. The resistivity of Mo-Si-N films deposited from separate Mo and Si targets. The blue graph illustrates a case with a constant Ar/N_2 gas flow ratio, while the red graph refers to a case with a fixed N_2 flow but a variable Ar flow.

Similarly to Mo-N films, the residual stress of Mo-Si-N films was expected to depend on the total sputtering pressure together with the nitrogen content (Section 5.2.4). It turned out the stress went down with the increasing total pressure, turning eventually from tensile into compressive (Table 22, Figure 20). The trend was totally opposite to that of Kattelus *et al.* [2] although the pressure range was roughly the same; the number of samples was fewer in [2] than herein. According to the preliminary assumption, a more complete amorphisation than achieved in Mo-N films should bring about the diminution of internal stress variations. Based on the below data, this held true: independent from the Mo-Si-N composition, the lateral stress variation was small or very small. Putting this and [2] together, one can only conclude the residual stress of as-deposited Mo-Si-N films is a strong function of

the sputtering pressure but the relation may be ambiguous; the stress must be confirmed experimentally, if a certain stress value needs to be achieved. However, once attained, the repeatability of the residual stress of similarly deposited films was rather good like the runs #1, #8, #B6 and #B7 (with two samples) proved; the sample from #B8 was the only one whose stress did not fall between 90 and 110 MPa.

Table 22. The residual stress of Mo-Si-N films deposited from separate Mo and Si targets with a 150 mm process at Provac LLS 801 sputtering system. The pressure values refer to those that prevailed during deposition. Stress X denotes the residual stress parallel to the main flat of the silicon substrate, stress Y the residual stress perpendicular to the main flat, and Δstress the difference between the two preceding as an absolute value, i.e. the lateral stress variation. It was assumed the thickness of the run #1 was identical to the thickness of the run #8 (tagged with *). It was also assumed the deposition rates of #B1…B8 were identical to each other (tagged with **); only the thickness of #B6 was really measured, and the rest were calculated consequentially. The residual stress values of #B1, #B2 and #B4 are only approximate because Mo-Si-N films were removed from top of silicon substrates by polysilicon wet etchant (tagged with ***).

Deposition run #	**Sample #**	**Total pressure (μbar)**	**N_2 partial pressure (%)**	**Thickness of Mo-Si-N (nm)**	**Stress X (MPa)**	**Stress Y (MPa)**	**Δstress (MPa)**
1	9	5.3	19.9	270*	110	110	0
3	16	4.3	19.8	270	120	130	10
4	18	6.3	20.0	260	-110	-110	0
5	20	7.3	20.1	270	-190	-230	40
6	22	4.4	23.4	280	160	160	0
7	52	6.1	17.4	280	50	90	40
8	24	5.3	19.9	270	100	90	10
B1***	J11	5.2	19.9	510**	100	110	10
B2***	42	5.1	19.9	210**	60	60	0
B4***	44	5.2	19.9	210**	0	0	0
B6	J13	5.2	19.9	640	90	100	10
B7	J14	5.2	19.9	430**	110	110	0
B7	J15	5.2	19.9	430**	100	100	0
B8	J17	5.2	19.9	210**	-210	70	280

The deposition parameters of the mutually alike runs #1, #2 and #8 were picked for the standard 150 mm process (see Table 14) on the grounds of the favourable stress state (low tensile stress of 90…110 MPa with a lateral variation of only 0…10 MPa) and resistivity (similar to the former 100 mm process [2]). It was an interesting detail that the Mo-Si-N composition with the most beneficial stress state happened to possess the lowest etch rate, too, resembling the case of the Mo-N films (Section 4.4). The amorphous microstructure of the films was not verified here.

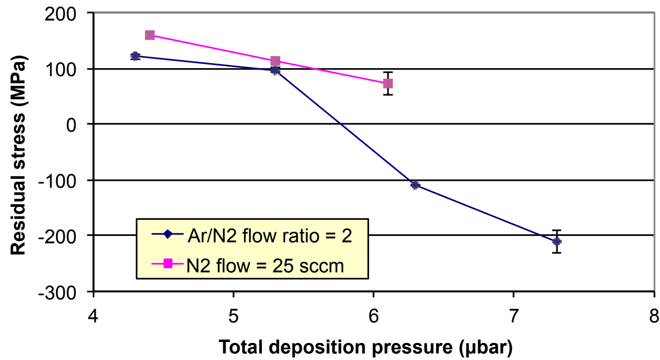

Figure 20. The residual stress of Mo-Si-N films deposited from separate Mo and Si targets. The blue graph illustrates a case with a constant Ar/N_2 gas flow ratio, while the red graph refers to a case with a fixed N_2 flow but a variable Ar flow. The error bars indicate the difference between the stress measured parallel (X) and perpendicular (Y) to the main flat of the silicon substrates. The difference was invisible in most cases.

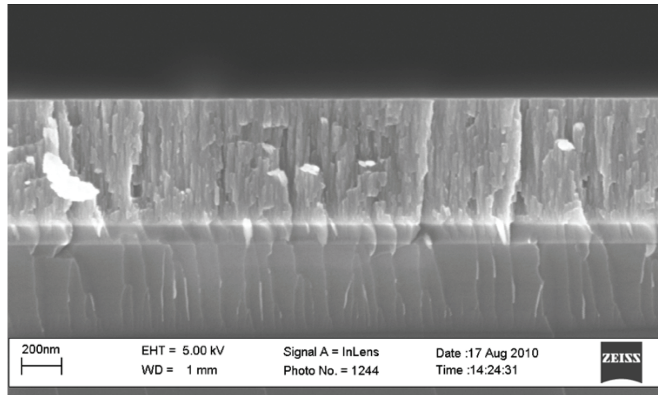

Figure 21. A SEM image of a 640 nm thick $Mo_{35}Si_{22}N_{39}O_4$ film on top of a silicon oxide layer. The Mo-Si-N film was deposited by the standard 150 mm sputtering process from separate Mo and Si targets.

The appearance was columnar in a SEM image (Figure 21) but one cannot say for sure if this ensued from the cleaving method or was a real character of the film. The composition was determined by RBS, and was 35 at.% Mo, 22 at.% Si, 39 at.% N and 4 at.% O ($Mo_{35}Si_{22}N_{39}O_4$). Oxygen was found throughout the film, not only on its surface. The rather high oxygen content is a likely result of the low deposition rate, albeit fairly usual among sputter deposited Mo-Si-N films (Section 5.2.1). The

above composition fulfils the conditions under which Mo-Si-N films have been reported to be amorphous: Si > 15 at.% [221] and Mo/Si ≤ 2 [227]. Compared to the former 100 mm process [2], the present films have slightly higher molybdenum and silicon contents but lower nitrogen content.

There was a question if the thermal stability of Mo-Si-N films depends remarkably on whether the films have been sputtered from separate Mo and Si, or a molybdenum silicide target. To find it out, a 150 mm deposition process with a Mo_5Si_3 sputtering target was built up. Once again, the deposition rate, the resistivity and the residual stress of Mo-Si-N films were determined (Table 23). Because the relationships between the Ar and N_2 flow rates and the resulting Ar and N_2 partial pressures were not readily available, a deeper study on the effects of the deposition parameters was not carried out. The deposition rate varied between 18 and 35 nm/min, and the resistivity between 1.2 and 39.1 mΩcm. As regards the residual stress, both tensile and compressive values were encountered. The deposition parameters of the run #5 were selected for the standard process, having a moderate resistivity (2.1 mΩcm), low tensile residual stress (140…150 MPa), and a small lateral stress variation (10 MPa). Although a SEM image showed a film with an inhomogeneous structure (Figure 22), an XRD analysis proved the films were amorphous (Figure 23). The only peak detected in the XRD scan was that of silicon, coming more than likely from the silicon substrate underneath. The composition, measured by RBS, was 29.5 at.% Mo, 14.5 at.% Si and 56 at.% N ($Mo_{29.5}Si_{14.5}N_{56}$). The Mo/Si concentration ratio in the films (2.0) was thus larger than the Mo/Si ratio in the sputtering target (1.7). Oxygen was concentrated on the surface of the Mo-Si-N film; if there was any inside the film, its concentration was a few percents maximum.

Whether the properties of Mo-Si-N films depend on their thickness can be extracted from Table 21, Table 22 and Table 23; only the films deposited by the standard 150 mm processes were considered here. In regard to resistivity, no signs of thickness dependence appeared. The data on the residual stress was plotted in Figure 24, including a comparison between the Mo-Si-N films deposited from separate Mo and Si targets ($Mo_{35}Si_{22}N_{39}O_4$), and a Mo_5Si_3 silicide target ($Mo_{29.5}Si_{14.5}N_{56}$). Based on the data, the stress proved rather independent from film thickness when the latter ranged between 250 and 760 nm. If some variation existed, it was not larger than the variation within samples of identical thickness. The findings are opposite to Mo-N films, whose residual stress *did* depend on film thickness (Figure 13). One may speculate the Mo-Si-N films may well owe their improved stress uniformity to the silicon incorporation, resulting in a more amorphous microstructure.

Table 23. The deposition rate, the resistivity, and the residual stress of Mo-Si-N films deposited from a Mo_5Si_3 target at Von Ardenne CS 730 S sputtering system. The throttle setting and the gas flow rates refer to those that prevailed during deposition. Stress X denotes the residual stress parallel to the main flat of the silicon substrate, stress Y the residual stress perpendicular to the main flat, and Δstress the difference between the two preceding as an absolute value, i.e. the lateral stress variation. It was assumed the deposition rates of #C1…C4 were identical to each other (tagged with *); only the thickness of #C2 was really measured.

Deposition run #	**Sample #**	**Throttle setting**	**Ar flow (sccm)**	**N_2 flow (sccm)**	**Thickness of Mo-Si-N (nm)**	**Deposition rate (nm/ min)**	**Resistivity (mΩ· cm)**	**Stress X (MPa)**	**Stress Y (MPa)**	**Δstress (MPa)**
1	54, J2	Open	60	10	390	26	2.1	-190	-180	10
2	55, J3	Closed	60	10	270	18	39.1	90	90	0
3	56, J4	Open	100	5	530	35	1.2	-250	-320	70
4	57, J5	Open	100	10	480	32	2.3	180	190	10
5	58, J6	Open	90	10	460	31	2.1	140	150	10
6	59, J7	Closed	50	5	490	33	8.5	90	80	10
C1	60, J8	Open	90	10	460*	-	2.2	170	140	30
C1	61, J9	Open	90	10	460*	-	2.2	150	130	20
C2	36, 46	Open	90	10	760	31	2.2	140	170	30
C3	62, J10	Open	90	10	250*	-	2.2	100	130	30
C4	37, 45	Open	90	10	500*	-	2.2	70	110	40
C4	J12	Open	90	10	500*	-	-	120	130	10
C4	N25	Open	90	10	500*	-	-	30	70	40

The surface roughness of Mo-Si-N films was measured by AFM (Table 24). In general, the films were rather smooth: their roughness remained at or below 0.3 % of the film thickness except for the thinnest sample (25 nm) whose roughness as an absolute value, for one, was only slightly above that of a polished silicon wafer. This compares favourably with other mictamict films (Section 3.4). Among the three compositions studied here, the standard one (labelled with A) turned out the best with the smoothest surface. This limited data set could not confirm a trend of decreasing surface roughness with increasing nitrogen content like anticipated by Section 3.4; if anything, the roughness and the silicon content increased hand in hand. As expected, the roughness decreased with decreasing film thickness. What sticks out are the unequal roughness values of two samples with a similar composition and thickness, but prepared and measured at different times. As a ready explanation for this is lacking, the results must be regarded with caution: as noticed with other mictamict films (Section 3.4), surface roughness data of thin films may be inconsistent.

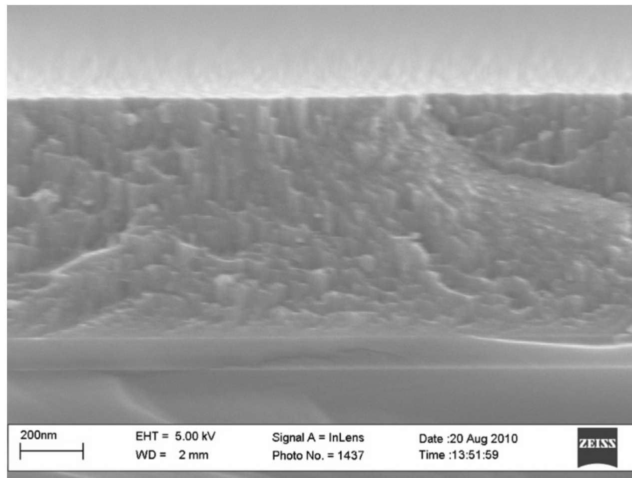

Figure 22. A SEM image of a 760 nm thick $Mo_{29.5}Si_{14.5}N_{56}$ film on top of a silicon oxide layer. The Mo-Si-N film was deposited by the standard 150 mm sputtering process from a Mo_5Si_3 compound target (corresponding to the run #5 in Table 23).

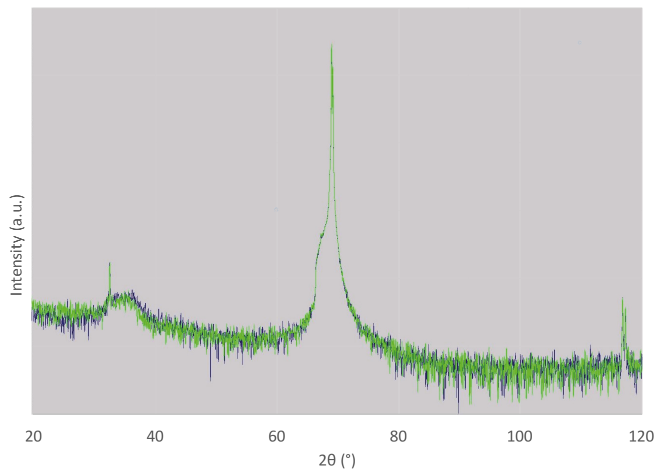

Figure 23. An XRD scan of a 460 nm thick $Mo_{29.5}Si_{14.5}N_{56}$ film on top of an amorphous silicon oxide layer. The Mo-Si-N film was deposited by the standard 150 mm sputtering process from a Mo_5Si_3 compound target (corresponding to the run #5 in Table 23). The substrate was of silicon.

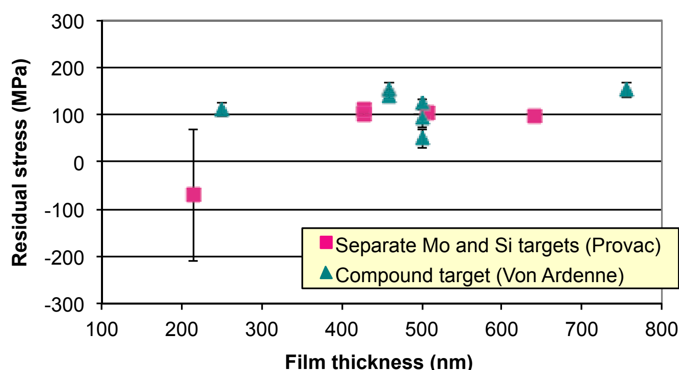

Figure 24. The residual stress of Mo-Si-N films as a function of film thickness. A comparison was made between samples deposited from dissimilar sputtering targets. The error bars indicate the difference between the stress measured parallel (X) and perpendicular (Y) to the main flat of the silicon substrates. Except for one sample, the difference was small.

Table 24. The surface roughness of Mo-Si-N films deposited by 100 mm sputtering processes at Balzers LLS 801 system. The composition A was accordant with the standard 100 mm process described in Table 14 and Table 20.

Composition	**Film thickness t_f (nm)**	**Average roughness R_a (nm)**	**R_a/t_f (%)**	**Root mean square roughness R_q (nm)**	**R_q/t_f (%)**
A ($Mo_{31}Si_{18}N_{45}O_6$)	400	0.56	0.14	0.71	0.18
B ($Mo_{19}Si_{26}N_{49}O_6$)	400	0.92	0.23	1.14	0.29
C ($Mo_{34}Si_{20}N_{41}O_5$)	400	0.64	0.16	0.82	0.21
A ($Mo_{31}Si_{18}N_{45}O_6$)	25	0.19	0.76	0.24	0.96
A ($Mo_{31}Si_{18}N_{45}O_6$)	170	0.30	0.18	0.38	0.22
A ($Mo_{31}Si_{18}N_{45}O_6$)	400	1.02	0.26	1.26	0.32

The mechanical properties of molybdenum and Mo-Si-N films were investigated by nanoindentation. In a nanoindentation test, force and displacement are recorded while the indenter tip is pressed into the sample, resulting in a load−displacement curve like in Figure 25. During the loading phase, both elastic and plastic deformation occurs. The unloading phase is usually dominated by elastic displacement. [349-351] A load−displacement curve indicates three specific points on the displacement axis: h_{MAX} that is the maximum displacement at the peak load, h_C that is the contact depth, and h_F that is the final displacement after the complete withdrawal of the load [350, 352, 353]. The concept of elastic recovery ER is defined by way of these magnitudes [238, 353, 354]:

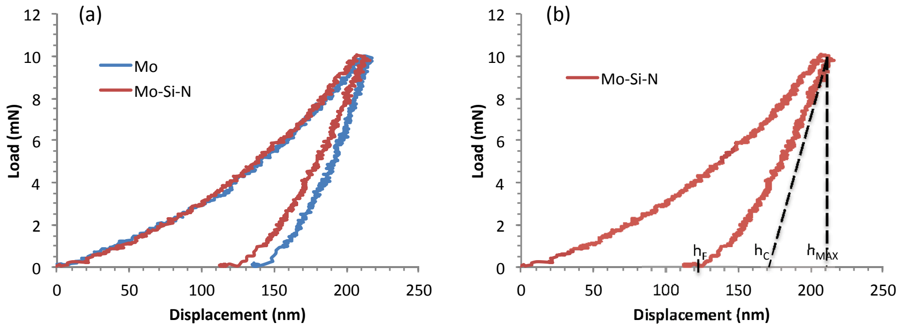

Figure 25. Examples of nanoindentation load−displacement curves of molybdenum and $Mo_{31}Si_{18}N_{45}O_6$ films of 500 nm. The maximum load was 10 mN. h_{MAX} = the maximum displacement at the peak load, h_C = the contact depth, and h_F = the final displacement after complete unloading.

$$ER = \frac{h_{MAX} - h_F}{h_{MAX}} \cdot 100\% \tag{15}$$

The mechanical properties of molybdenum and $Mo_{31}Si_{18}N_{45}O_6$ films are presented in Table 25. As a basic rule, it is recommended the maximum indentation depth should not exceed 10 % [228, 237, 355, 356] or 10…20 % [31, 352, 353, 357] of the film thickness in order to avoid the effect of the substrate on the measurement. For a soft film on a hard substrate, the substrate effect may be negligible even up to 50 % of the film thickness [356, 357] but the assumption is not valid for the Mo/Si and Mo-Si-N/Si systems considered here. On the other hand, also surface effects are possible and should be avoided as well [205, 349, 358]. Based on above, the results obtained with the indentation load of 1 mN are likely to be the most reliable as the related penetration depths were around 10 % of the film thickness, compared to around 40 and 100 % for the indentation loads of 10 and 50 mN, respectively. However, surface effects cannot be ruled out completely for the molybdenum films with a silicon cap of 4 nm. In conclusion, the figures presented here should be regarded as approximate.

The elastic modulus and the hardness obtained with an indentation load of 1 mN were 180 and 8 GPa for molybdenum films, and 170 and 15 GPa for Mo-Si-N films. Compared to each other, the elastic moduli of Mo and Mo-Si-N films coincided rather closely, whereas the hardness of Mo-Si-N films was almost twice that of Mo films. Compared to the findings of other research groups (Table 13), both the elastic modulus and the hardness of these Mo-Si-N films fell on the range of the earlier findings, albeit the elastic modulus was lower than the average. The nanoindentation was followed by an AFM study that provided indentation-induced surface deformation profiles supplementing the displacement data obtained by indentation. The combined data was used for calculating the elastic recoveries of Mo

Table 25. The mechanical properties of 500 nm thick Mo and $Mo_{31}Si_{18}N_{45}O_6$ films. h_{MAX} and h_C were measured by nanoindentation, and h_F by AFM; the elastic modulus and the hardness were computed from the indentation data. The indentation load forces were 1, 10 and 50 mN. The errors relating to the elastic modulus and the hardness of molybdenum at 1 mN were not evaluated (tagged with *). The figures in the table are averages of multiple measurements.

Property	**Mo**			**$Mo_{31}Si_{18}N_{45}O_6$**		
	1 mN	**10 mN**	**50 mN**	**1 mN**	**10 mN**	**50 mN**
h_{MAX} (nm)	59	222	509	49	206	500
h_C (nm)	49	190	430	34	166	406
h_F (nm)	58	158	326	37	115	262
$(h_{MAX} – h_C)/h_{MAX}$ (%)	17	14	16	31	19	19
$(h_{MAX} – h_F)/h_{MAX}$ (%)	2	29	36	25	44	47
Elastic modulus (GPa)	180.7*	220.1 ± 7.5	210.0 ± 6.1	171.5 ± 13.7	189.7 ± 8.3	182.5 ± 1.2
Hardness (GPa)	8.3*	9.5 ± 0.5	10.4 ± 0.4	15.0 ± 1.6	12.1 ± 0.4	11.6 ± 0.4

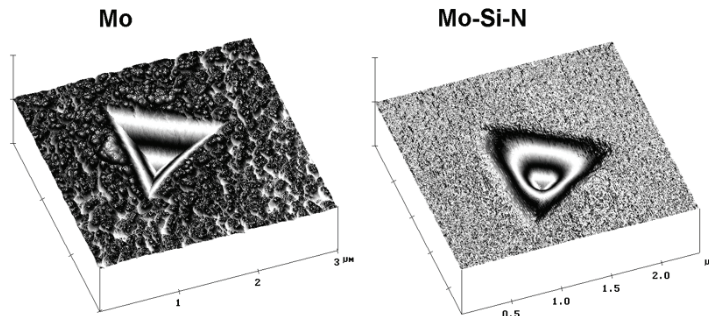

Figure 26. The traces of the nanoindenter tip in Mo and $Mo_{31}Si_{18}N_{45}O_6$ films imaged by AFM. The thickness of both films was 500 nm, while the indentation load force was 10 mN. Published previously in [6].

and Mo-Si-N films (Table 25). The elastic recovery of Mo films was 2 % at an indentation load of 1 mN and 29 % at a load of 10 mN. The corresponding figures for Mo-Si-N films were 25 % (1 mN) and 44 % (10 mN). The elastic recovery of Mo-Si-N films matched well the results of Liu *et al.* who reported elastic recoveries of 30 and 40 % for their amorphous and nanostructured Mo-Si-N films, respectively [227]. The elastic recoveries of nanostructured Ti-Si-N [204, 205] and nanocomposite W-Si-N films [249] were though higher: 70…76 % at their best. Figure 26 shows the traces of the nanoindenter tip on the surfaces of molybdenum and Mo-Si-N films imaged by AFM. The figure highlights the difference between the surface morphology of the

crystalline Mo and the amorphous Mo-Si-N films: the surface and the perimeter of the indenter trace were smoother as well as the pit was shallower for the latter. Altogether, the results illustrate how the ability of amorphous Mo-Si-N films to recover after deformation was better than that of crystalline Mo films.

The dispersion of the complex refractive index of Mo-Si-N films was determined by reflectance measurements performed with gonioreflectometry (1000...1650 nm), double-beam transfer standard spectrometry (400...2400 nm) and spectroscopic reflectometry (190...1650 nm). With the use of these three sets of overlapping measuring data, the complex refractive index of a $Mo_{35}Si_{22}N_{39}O_4$ film on top of a silicon substrate was modelled (Figure 27a). The thickness of the Mo-Si-N film was 33 nm. The measuring data and the modelling result fitted quite well. Both the refractive index n and the extinction coefficient k increased with increasing wavelength λ, resembling the findings of Atuchin *et al.* with their Mo_2N films [359]. The increasing trend is opposite to common dielectric materials such as SiO_2, Si_3N_4 or Al_2O_3, which have $dn/d\lambda < 0$ (normal dispersion) and $k \cong 0$ at visible and near-infrared wavelengths [360, 361]. Instead, elemental metals may show increasing n and k with wavelength, though with notably higher values of k, which represents the attenuation [362-364].

For a reference, the reflectance of a 33 nm thick $Mo_{35}Si_{22}N_{39}O_4$ film on top of an oxidised silicon substrate was measured, too. The thickness of the thermal oxide film was 100 nm. The measurement was made with spectroscopic reflectometry at wavelengths of 230…1650 nm, and the complex refractive index was modelled based on the data (Figure 27b). The result was not fully identical to the earlier one (Figure 27a) although the two graphs resemble each other. The reason for the difference or whether it has any physical origin (instead of being a measuring artifact) is not known for sure. The result of the first sample is possibly more reliable, because the related reflectance data was obtained by three separate measurement methods with their wavelength ranges overlapping each other. Additional information could be sought e.g. through determining the refractive index of Mo-Si-N films with different thicknesses. To the best of the author’s knowledge, there are no other published studies reporting the dispersion of the refractive index of sputter-deposited Mo-Si-N thin films.

The above results can be compared to what has been reported on the optical properties of other mictamict films. Amorphous $Ta_{42}Si_{13}N_{45}$ films were described as metal-like: the reflectivity was high, free electrons were present, and the optical penetration depth was only 9 nm [171]. Another Ta-Si-N composition, amorphous-like $Ta_{53}Si_7N_{40}$, experienced a strong photoluminescence process on visible wavelengths with the peak at 554 nm [148]. In general, the optical properties of TM-Si-N films reflect their composition. The refractive index (n) and the extinction coefficient (k) of $TiSi_xN_y$ films were adjustable by the N_2 flow rate and the sputtering powers applied to Si and Ti targets, e.g. the increase in the nitrogen content of $TiSi_xN_y$ led to a higher n and a lower k [198, 199]. Thermal annealing is capable of changing the optical properties as well. When W-Si-N films were annealed at 800°C, their

surface reflectance in the infrared (IR) region increased and transmittance decreased as a result of nitrogen loss from the films. It made the films more metallic by nature. [243]

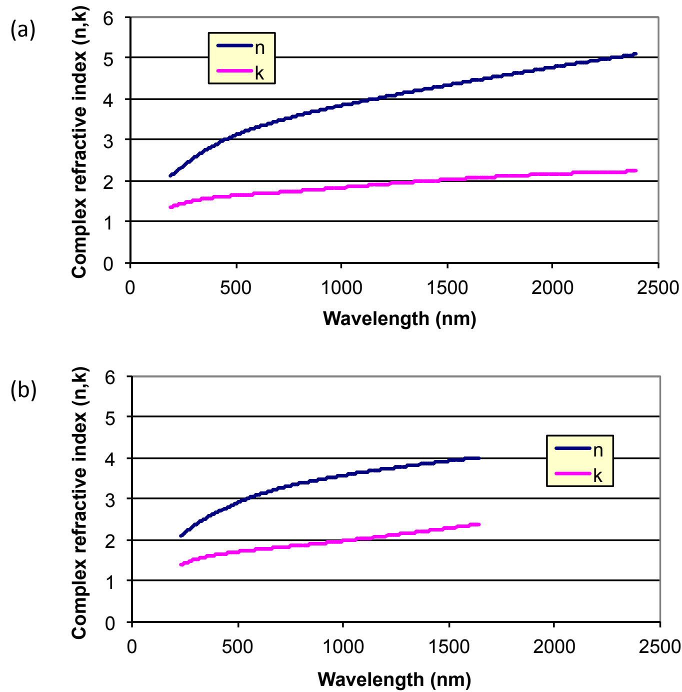

Figure 27. (a) The dispersion of the complex refractive index (*n*, *k*) of a $Mo_{35}Si_{22}N_{39}O_4$ film deposited on top of a silicon substrate. The measurements were made with gonioreflectometry, double-beam transfer standard spectrometry and spectroscopic reflectometry. (b) The dispersion of the complex refractive index (*n*, *k*) of a $Mo_{35}Si_{22}N_{39}O_4$ film deposited on top of an oxidised silicon substrate. The measurements were made with spectroscopic reflectometry. Published previously in [14] and [15].

5.5 Thermal stability

The study of the thermal stability of Mo-Si-N films originated from an aim to demonstrate their stress relaxation at moderate temperatures (up to 500°C) in a similar way like Reid had done with his Ta-Si-N and W-Si-N films [142], Lin *et al.* with Ti-Si-N films [198], and later also Gassner *et al.* with Mo-N films [295]. It was wished to find a specific temperature at which the as-deposited residual stress of Mo-Si-N films would relax close to zero, preferably even without the crystallisation of the initially amorphous films.

For the above purpose, Mo-Si-N films were heated in a Tencor FLX-2320 stress measurement instrument, which allowed of recording the residual stress together with the prevailing temperature (Table 26). Each annealing cycle started at an “initial temperature” (usually room temperature), from which the temperature was ramped up to a “hold temperature” (originally 500°C) and back down to an ”end temperature”. The planned hold time was 60 minutes maximum. What happened, however, was that the first three measurements stopped unintentionally at temperatures between 362…377°C (the ”stop temperature”) because the reflected laser beam was lost. Two different Mo-Si-N compositions, $Mo_{31}Si_{18}N_{45}O_6$ and $Mo_{34}Si_{20}N_{41}O_5$, experienced the same. When the maximum temperature was limited at 350°C the reflected signal was still lost, albeit after spending 12 minutes at the hold temperature (the experiment #F4). Before the measurements stopped, the samples exhibited stress vs. temperature curves like in Figure 28a, resembling the first part of the curves of Reid and others, and including a ”turn temperature” at which $d\sigma/dT$ turned from negative to positive. During the heating, the appearance of the Mo-Si-N films always turned from shiny grey to richly coloured, suggesting oxidation had taken place. The observation contradicted the best knowledge of that time, stating that the oxidation resistance of Mo-Si-N films was ”excellent up to 800°C” [222].

Only when the maximum temperature was limited at 300°C, a stress vs. temperature curve fully similar to Reid [142] was obtained (the experiment #F5, Figure 28b). Even then, the Mo-Si-N film turned dark yellow in colour. From the start until the turn temperature, and again from the hold temperature down to the end, the stress behaviour of the Mo-Si-N film followed linear thermoelasticity, reflecting changes in the thermal stress that result from the thermal expansion mismatch between the film and the substrate. The observed turn temperature (between 80 and 100°C for the standard composition) matched well the presumed sputter deposition temperature. The onset of the structural relaxation took place after this temperature was exceeded, coming up as a deviation from the linear thermoelastic behaviour. One should note, however, that the stress change into the tensile direction above the turn temperature was not really stress relaxation: the term ‘relaxation’ would be accurate only if the film was originally under compressive stress (like the films of Reid [142] and Lin *et al.* [198]). As the film had originally tensile stress, the term ‘restructuring’ might be more exact.

Table 26. The outcomes of the annealing experiments with a Tencor FLX-2320 stress measurement instrument. The Mo-Si-N films were deposited by the standard 100 mm sputtering process (Table 14, $Mo_{31}Si_{18}N_{45}O_6$) except for the sample of #F1 whose composition was $Mo_{34}Si_{20}N_{41}O_5$ [2], and the sample of #F12 that had a low deposition rate, achieved by halving the sputtering powers on Mo and Si targets compared to the standard process. Consequently, the thickness and the composition of the latter were not known precisely. The heating and cooling rates were 2°C/min. The samples of #F8 and #F10 experienced RTA pre-annealing in N_2 gas, and the sample of #F13 was heated twice to the maximum temperature. The ”turn T” denotes the temperature at which d*σ*/d*T* turned from negative to positive during heating, and the ”stop T” the temperature at which the optical measurement sometimes stopped unintentionally (see e.g. Figure 28a). R^2 refers to the coefficient of determination in relation to the evaluation of Δ*σ*/Δ*T* by linear regression. The colour (if reported) was recorded after annealing. The samples of #F6 and #F11 were analysed afterwards by RBS and XRD, respectively.

Experiment #	**F1**	**F2**	**F3**	**F4**	**F5**	**F6**	**F7**	**F8**	**F9**	**F10**	**F11**	**F12**	**F13**
Film thickness (nm)	400	325	325	325	325	325	325	400	170	170	325	~300	325
Initial T (°C)	38	21	22	22	22	22	22	21	21	21	22	22	23
Turn T (°C)	110	90	90	80	90	90	90	-	80	-	100	-	100
Stop T (°C)	362	369	377	350	-	350	-	-	350	350	-	-	-
Hold T (°C)	-	-	-	350	300	350	300	350	350	350	200	300	200
End T (°C)	-	-	-	-	57	-	57	56	-	-	56	62	58
Hold time (min)	-	-	-	12	30	12	30	60	12	26	60	30	30+30
Initial σ (MPa)	-	-	210	170	170	-	-	-	-	-	-	-	-
Δσ during hold (MPa)	-	-	-	-	7	-	6	-9	-	-	12	-2	5 and -7
Δσ/ΔT (MPa/°C)	-	-	-	-	-0.315	-	-0.307	-0.327	-	-	-0.301	-0.376	-0.276
Coefficient of determination R^2	-	-	-	-	0.9843	-	0.9833	0.9913	-	-	0.9766	0.9549	0.9057
Colour	-	-	-	-	Dark yellow	Blue	Dark yellow - brown	Bright grey - a little bit of blue	Blue	Blue - a little bit of yellow	-	-	-
Initial ρ (mΩcm)	-	-	-	-	-	1.12	1.12	0.99	1.19	1.19	1.12	1.12	-
End ρ (mΩcm)	-	-	-	-	-	1.25	1.08	0.96	1.61	1.41	1.12	1.15	-
Remarks	Composition C	-	-	-	-	RBS	-	RTA pre-annealing (500°C, 1 min)	-	As-deposited ρ = 0.99 mΩcm. HF dip (30 s) and RTA pre-annealing (600°C, 1 min)	XRD	Low deposition rate	Two temperature ramps

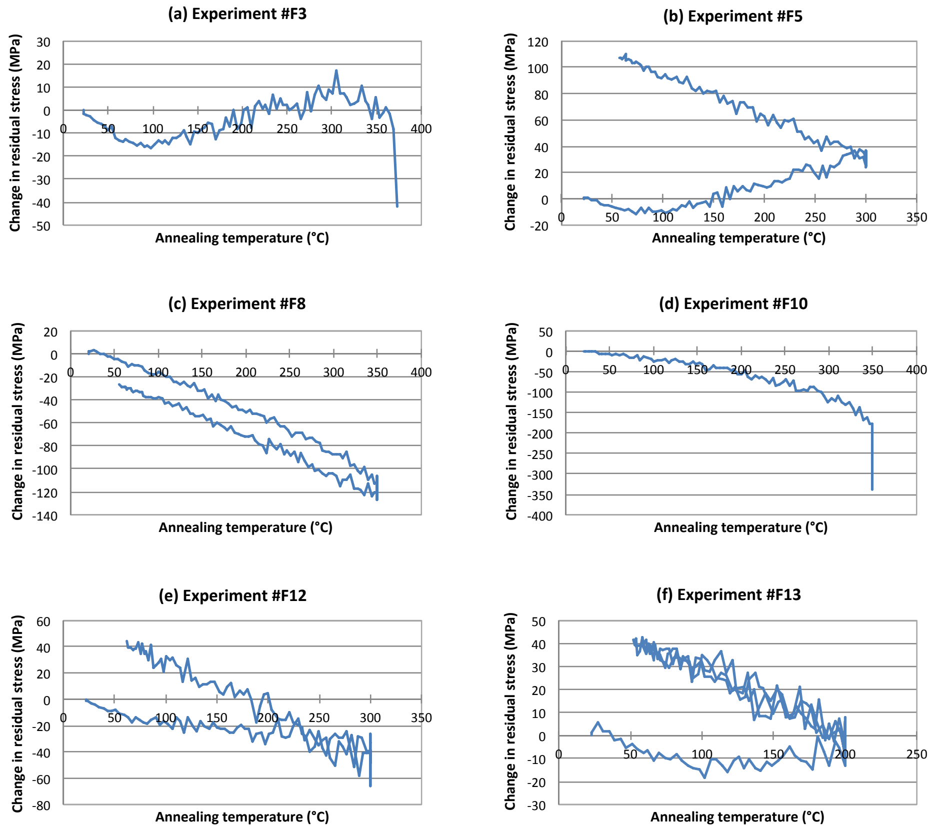

Figure 28. The change in the residual stress of Mo-Si-N films compared to their stress state at room temperature. See Table 26 for the experimental details. (a) The optical measurement stopped unintentionally at 377°C. (b) The maximum temperature was limited to 300°C. Mo-Si-N samples (c) with RTA pre-annealing, (d) with a HF dip and RTA pre-annealing, (e) with a low deposition rate, and (f) heated twice to the maximum temperature (200°C).

A Mo-Si-N sample ramped up to 350°C was analysed by RBS (the experiment #F6, Figure 29). The RBS analysis proved a surface oxide layer had formed on top of the Mo-Si-N film. The composition of the surface oxide was $Mo_{15}Si_8N_{18}O_{59}$, while the composition of the underlying Mo-Si-N film was $Mo_{32}Si_{18}N_{50}$, which was rather close to the original $Mo_{31}Si_{18}N_{45}O_6$ of an as-deposited film [2]. The surface oxide layer thus contained rather much of both molybdenum and nitrogen instead of being mere silicon dioxide. To study potential changes in the microstructure, another $Mo_{31}Si_{18}N_{45}O_6$ sample was heated up to 200°C and analysed thereafter by XRD (the experiment #F11, Figure 30). Although the heating temperature was this low, a peak of Mo_2N was detected. If the film had remained amorphous, no peak should

have been observed. As-deposited Mo-Si-N films of a similar kind were proved amorphous by TEM [2]. The analyses hence suggested that not only oxidation, but also microstructural changes can take place already at 200…350°C in these Mo-Si-N films sputtered from separate Mo and Si targets. The latter contradicted the widespread understanding of the high structural metastability of mictamict alloys (e.g. [140]).

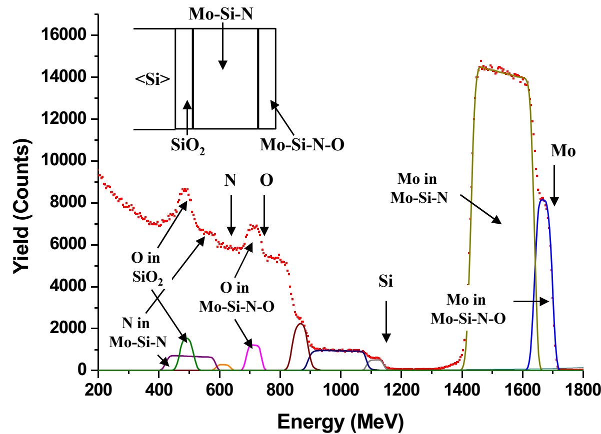

Figure 29. An RBS spectrum of a Mo-Si-N film annealed at 350°C in a gas mixture of nitrogen and air, together with selected parts from the simulated spectrum at the bottom of the plot. (See the experiment #F6 in Table 26 for more information.) An oxide film had formed on top of the Mo-Si-N film. The graph was created from the measurement data by H. Kattelus, and published previously in [4].

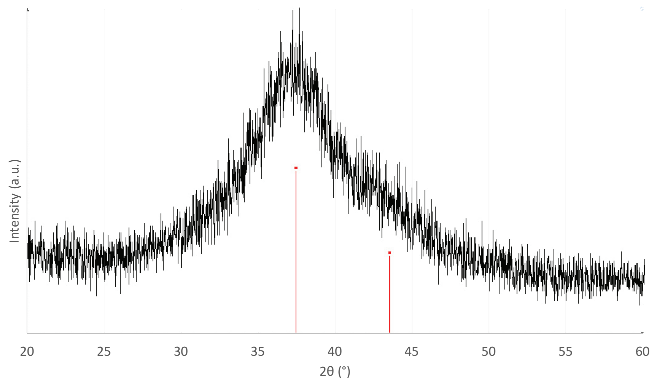

Figure 30. An XRD scan of a 325 nm thick $Mo_{31}Si_{18}N_{45}O_6$ film annealed at 200°C in a gas mixture of nitrogen and air. (See the experiment #F11 in Table 26 for more information.) A peak of Mo_2N was detected. The substrate was of silicon.

Faced with the above unexpected observations, a few attempts were made to stabilise Mo-Si-N films against low temperature oxidation and structural changes. First, a Mo-Si-N film was annealed by RTA in N_2 gas at 500°C for 1 minute prior to the actual experiment (#F8). Second, another Mo-Si-N film was exposed to a HF dip of 30 seconds and RTA annealing of 600°C and 1 min in N_2 gas (the experiment #F10). Third, a Mo-Si-N sample was prepared with a low deposition rate, achieved by halving the sputtering powers on Mo and Si targets compared to the standard process (the experiment #F12). The purpose was to suppress the formation of a nanolayered film, composed of thin Mo-N and Si-N layers. None of these exercises, however, stabilised the Mo-Si-N films in an unambiguous and complete manner. During the heat treatments at 300 or 350°C in the Tencor FLX-2320 instrument, the visual appearance of each Mo-Si-N film was changed. The sample of #F8 was the stablest in this sense as it remained bright grey with metallic shine for the most part. The other two samples turned coloured, indicating the formation of surface oxide. The stress vs. temperature curves of these three samples were different from the earlier though (Figure 28c-e). All samples missed now the turning points at which $d\sigma/dT$ turned from negative to positive. This was comprehensible for the samples of #F8 and #F10 that had been pre-annealed at temperatures higher than the maximum temperature of the Tencor FLX-2320 tests: the pre-annealing might have already induced the stress relaxation possible at these temperatures. The experiment #F8 exhibited a stress behaviour with linear thermoelasticity both upon heating and cooling. Amongst these three exercises, the RTA pre-annealing prior to the actual long-time heat treatment appeared to stabilise the Mo-Si-N films best, albeit not completely. The experiment #F13 with double ramping up to the maximum temperature supported the understanding that a subsequent heat treatment at or below the maximum temperature the Mo-Si-N film has earlier experienced does not induce significant further relaxation of the residual stress; the second ramping of #F13 followed the thermoelastic stress behaviour of the cooling phase of the first ramping.

Closer scrutiny of Table 26 shows the initial (as-deposited) stress of Mo-Si-N films was 170…210 MPa tensile, matching well the previous measurements [2]. The stress change during the hold at the maximum temperature was always low: 12 MPa at the most. Neither did the resistivity change much; when changes occurred, one cannot state whether they resulted from the measurement instability due to the four-point probing through the surface oxide layer. In the case of heavy oxidation, the sheet resistance could not be measured at all.

The coefficient of thermal expansion of Mo-Si-N films was extracted from the stress vs. temperature data obtained by the Tencor FLX-2320 stress measurement instrument. When a thin film is heated on a substrate with a known coefficient of thermal expansion α_S, the coefficient of thermal expansion of the film is

$$\alpha_F = \alpha_S - \frac{d\sigma/dT}{[E/(1-\nu)]_F} \tag{16}$$

where E is the elastic modulus and v the Poisson's ratio for the film (e.g. [335]). To calculate $\alpha_{Mo\text{-}Si\text{-}N}$, the slopes $\Delta\sigma/\Delta T$ related to the regions of linear thermoelasticity

were determined from several σ-T curves (Table 27). The table shows also the respective coefficients of determination (R^2), indicating the reliability of the extracted figures obtained by linear regression. Assuming that α_{Si} = 2.56 ppm/K at room temperature [52], $E_{Mo\text{-}Si\text{-}N}$ = 171.5 GPa (from Table 25) and $\nu_{Mo\text{-}Si\text{-}N}$ = 0.3 (the accurate value was not available), the values for $\alpha_{Mo\text{-}Si\text{-}N}$ varied between 3.7 and 4.1 ppm/K. Since the experiment #F8 had both the largest R^2 and the best thermal stability (see above), its result was considered the most reliable, that is, $\alpha_{Mo\text{-}Si\text{-}N}$ = 3.9 ppm/K near room temperature.

Table 27. The calculation of the coefficient of thermal expansion of $Mo_{31}Si_{18}N_{45}O_6$ films. The data for the calculation was taken from Table 26. R^2 refers to the coefficient of determination in relation to the evaluation of $\Delta\sigma/\Delta T$ by linear regression.

Experiment #	$\Delta\sigma/\Delta T$ (MPa/K)	Coefficient of determination R^2	Coefficient of thermal expansion of Mo-Si-N films (10^{-6}/K)
F5	-0.315	0.9843	3.85
F7	-0.307	0.9833	3.81
F8	-0.327	0.9913	3.89
F11	-0.301	0.9766	3.79
F12	-0.376	0.9549	4.09
F13	-0.276	0.9057	3.69

The $\alpha_{Mo\text{-}Si\text{-}N}$ can be compared to the reported data on the thermal expansion of a few Ta-Si-N, Ti-Si-N and W-Si-N compositions. A value of 5 ppm/°C was obtained for the thermal expansion coefficients of both $Ta_{36}Si_{14}N_{50}$ and $W_{36}Si_{14}N_{50}$ films at room temperature [142], and 3.2 ppm/°C for $Ti_{0.95}Si_{0.05}N_{1.02}$ films [214]. The thermal expansion can be dependent on the ambient temperature: at 500°C the thermal expansion coefficient of the above Ta-Si-N films was already 8 ppm/°C [142].

The above findings about the poor thermal stability of Mo-Si-N films at relatively low temperatures (T < 400°C) were in conflict not only with the published research of that time (see Section 5.2.3), but also with our own experience. The difference between our previous work [2] and the above experiments was that Mo-Si-N films had been previously annealed by RTA in an inert atmosphere, whereas the present experiments were long-time heat treatments with the surrounding gas containing air. To exclude the possibility of Mo-Si-N samples being somehow different from the previous, a set of Mo-Si-N films were RTA annealed in N_2 gas (Table 28). All Mo-Si-N films lying on top of silicon substrates survived the annealing without a visible sign of oxidation, whereas the Mo-Si-N films on top of fused silica substrates turned dark and matt from the annealing temperature of 800°C upwards, indicating the film surface had oxidised or even burnt. For such films, the measurement of sheet resistance came to nought. The dissimilar thermal conductivities of silicon and SiO_2 substrates may explain the difference. The resistivities of annealed Mo-Si-N films followed those obtained previously [2], decreasing with the increasing RTA

temperature (Figure 31). This confirmed the previous measurements of [2] were repeatable, and the observed low stability of Mo-Si-N films had to relate to the heating conditions of the Tencor FLX-2320 stress measurements.

Table 28. The resistivity of $Mo_{31}Si_{18}N_{45}O_6$ films after RTA annealing in N_2 gas for 1 minute. Half of the Mo-Si-N samples were deposited on SiO_2 coated silicon substrates, and the other half on silica (SiO_2) substrates. The as-deposited resistivity was 1.13 mΩcm.

Experiment #	Annealing temperature (°C)	Resistivity on a SiO_2 coated silicon substrate (mΩcm)	Resistivity on a silica (SiO_2) substrate (mΩcm)
R1	500	1.12	1.12
R2	600	1.09	1.09
R3	700	1.06	1.07
R4	800	0.94	1.00
R5	900	0.82	-
R6	1000	0.43	-
R7	1100	0.23	-

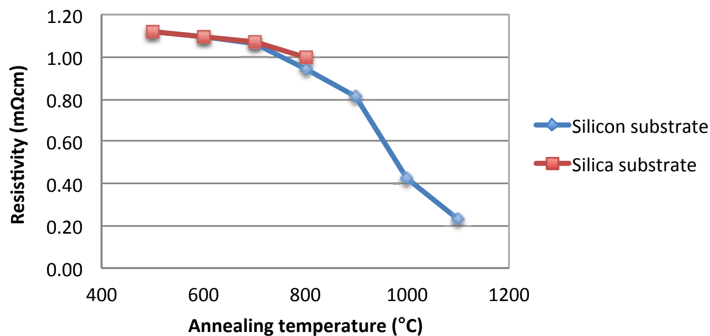

Figure 31. The resistivity of $Mo_{31}Si_{18}N_{45}O_6$ films after RTA annealing in N_2 gas for 1 minute.

To get further clarification of the case, Mo-Si-N films were next annealed for at least 30 minutes at temperatures between 400 and 700°C with either O_2 or N_2 as the surrounding gas (Table 29). The microscope images of Figure 32 reveal how the originally regular and shiny looks of Mo-Si-N films has turned grainy and speckled during annealing in O_2 gas. Due to the rough surface, the thickness of the developed surface oxide scales could not be measured by reflectometry. Along with the increasing annealing temperature, the tiny spots of the Mo-Si-N films annealed at 400°C changed into the richly coloured blotches of the Mo-Si-N films annealed at

700°C. The change of the annealing gas from oxygen to nitrogen did not make a considerable difference: the films still looked coarse and coloured when annealed (Figure 33).

Table 29. A summary of the microscope imaging, SEM and EDX analyses of Mo-Si-N films annealed in O_2 and N_2 gases at temperatures between 400 and 700°C.

Experiment #	Surrounding gas during anneal	Annealing temperature (°C)	Annealing time (min)	Microscope image	SEM image	EDX spectrum
H1	O_2	400	30	Figure 32a	Figure 34	Figure 36a
H2	O_2	500	30	Figure 32b	-	-
H3	O_2	600	30	Figure 32c	-	-
H4	O_2	700	30	Figure 32d	Figure 35	Figure 36b
H5	N_2	500	60	Figure 33a	-	-
H6	N_2	700	30	Figure 33b	-	-

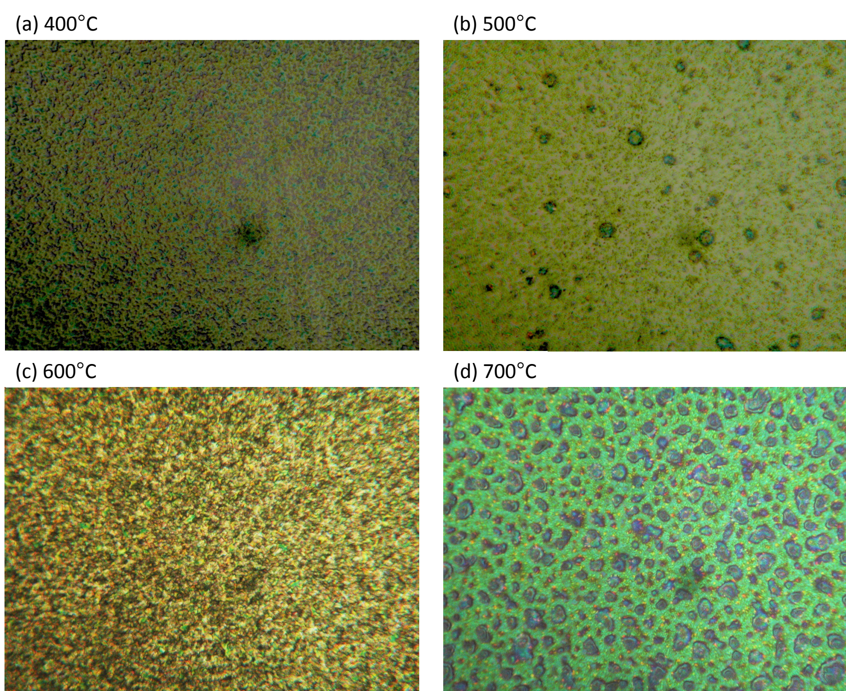

Figure 32. Microscope images of Mo-Si-N films annealed in O_2 gas for 30 min at temperatures between 400 and 700°C. The magnification of the microscope was 60X for all images. The diameter of the largest patterns in (d) is several microns.

(a) 500°C, 60 min

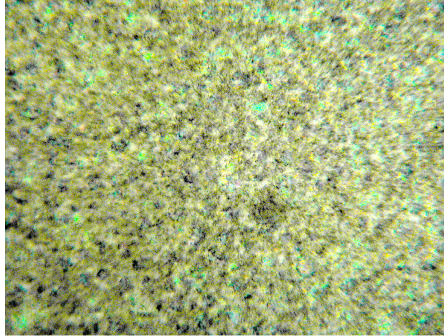

(b) 700°C, 30 min

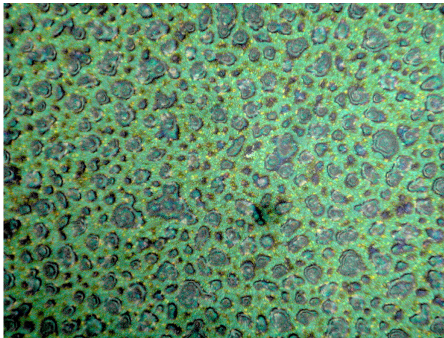

Figure 33. Microscope images of Mo-Si-N films annealed in N_2 gas at 500 and 700°C. The magnification of the microscope was 60X for both images. The diameter of the largest patterns in (b) is several microns.

More information was gained through SEM imaging of the samples. The SEM image of a Mo-Si-N film annealed at 400°C in O_2 gas revealed an irregular and lamellar film surface, suggesting the film had crystallised (Figure 34). The contents of the small, light spots were not known. The SEM image of a Mo-Si-N film annealed at 700°C in O_2 gas was different (Figure 35). Unlike for the preceding sample, the majority of the film surface looked rather smooth. However, there were also cracks of several microns in length, and 100…200 nm in width.

The EDX analyses of the above samples were even more interesting (Figure 36). The position resolution of the EDX instrument was not high enough to solve the light spots of Figure 34, being much below 1 μm in diameter. Hence the films had to be analysed without information on possible composition variations in the plane of the film surface. By EDX, the Mo-Si-N film annealed at 400°C contained a large amount of oxygen besides molybdenum and silicon, which could be anticipated already by the RBS analysis of Figure 29. (Nitrogen was not found because EDX is not capable of detecting it.) However, the EDX spectrum of the Mo-Si-N film annealed at 700°C had peaks only for silicon and oxygen while the peak for molybdenum was missing or very weak, i.e. the film did not seemingly contain molybdenum anymore.

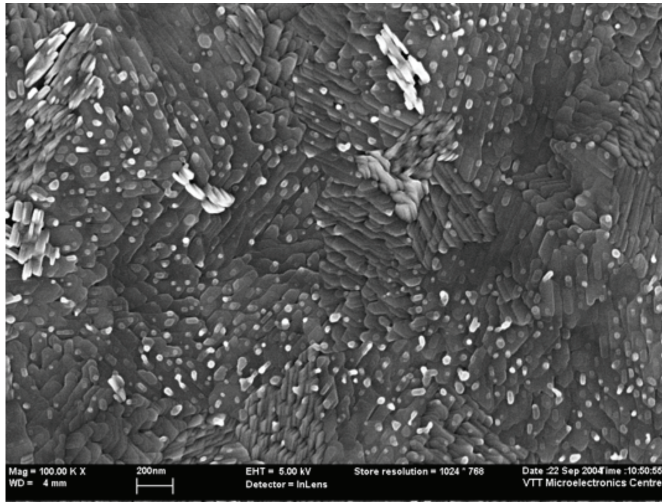

Figure 34. A SEM image of a Mo-Si-N film annealed in O_2 gas at 400°C for 30 minutes.

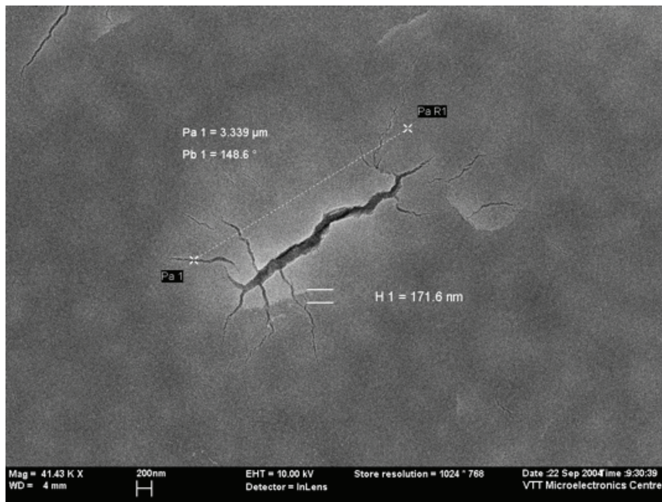

Figure 35. A SEM image of a Mo-Si-N film annealed in O_2 gas at 700°C for 30 minutes.

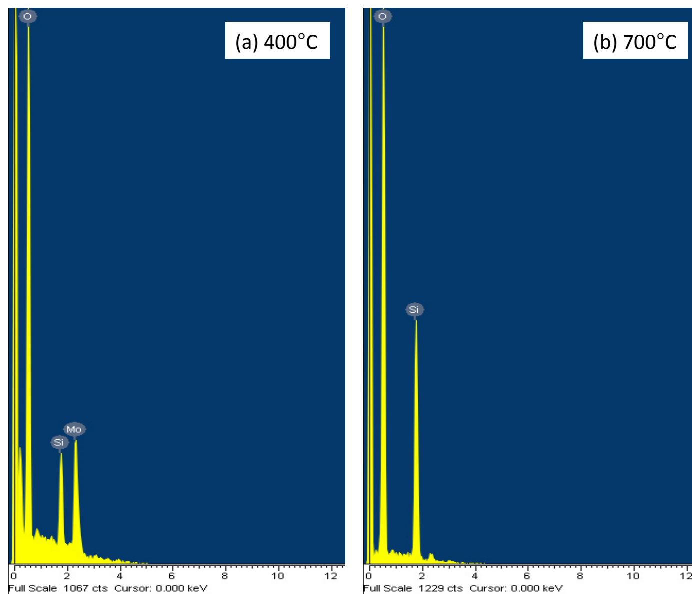

Figure 36. The EDX spectra of Mo-Si-N films annealed at (a) 400°C and (b) 700°C in O_2 gas for 30 minutes.

The above findings together with a recently issued article on the oxidation behaviour of Mo-N films [320] led to a hypothesis that our Mo-Si-N films sputter deposited from separate Mo and Si targets were actually nanolaminates consisting of thin Mo-N and Si-N films. Before dwelling upon this idea, a pragmatic solution to the low temperature oxidation of Mo-Si-N films was searched. For the purpose, some $Mo_{31}Si_{20}N_{45}O_4$ films were underlaid and capped with 10 nm silicon films beneath and on top of them. The samples were heated at 100…400°C, inspected, and measured for their resistivity and residual stress (Table 30). The looks of the Mo-Si-N films remained metallic, suggesting oxidation had not happened. The resistivity reduced during annealing (Figure 37), but the decline was moderate, only 2.5 % compared to the as-deposited value of 1.41 mΩcm. The resistivity change due to repeating annealing at 400°C was minor. The residual stress exhibited a consistent increase with the increasing annealing temperature except for a dip at 250°C, which possibly was a measurement anomaly only (Figure 38). The double annealing at 400°C induced a decrease in the residual stress also for the second annealing time. In conclusion, the 10 nm silicon cap on top of the Mo-Si-N films suppressed the formation of visible surface oxide, but not the structural changes (observed by a change in residual stress). The former is comprehensible by the thin protective layer of SiO_2 that seals a silicon surface, restraining any further oxidation. Controlled heat treatments could possibly be used for the tuning of the residual stress of Mo-Si-N films as long as the subsequent service temperatures stay below the tuning temperature.

Table 30. The resistivity and the residual stress of silicon capped $Mo_{31}Si_{20}N_{45}O_4$ films after annealing at temperatures between 100 and 400°C for 30 min. There was a 10 nm thick silicon film both beneath and on top of Mo-Si-N films. Stress X denotes the residual stress parallel to the main flat of the silicon substrate, stress Y the residual stress perpendicular to the main flat, and Δstress the difference between the two preceding as an absolute value, i.e. the lateral stress variation. The sample of #S8 was heated twice to 400°C.

Experiment #	**Annealing temperature (°C)**	**Surrounding gas during anneal**	**Resistivity (mΩcm)**	**Stress X (MPa)**	**Stress Y (MPa)**	**Δstress (MPa)**
S1	100	Air	1.42	220	240	20
S2	150	Air	1.43	260	290	30
S3	200	N_2	1.44	270	340	70
S4	250	N_2	1.44	280	320	40
S5	300	N_2	1.42	360	360	0
S6	350	N_2	1.40	360	410	50
S7	400	N_2	1.38	420	420	0
S8	2 × 400	N_2	1.37	360	360	0

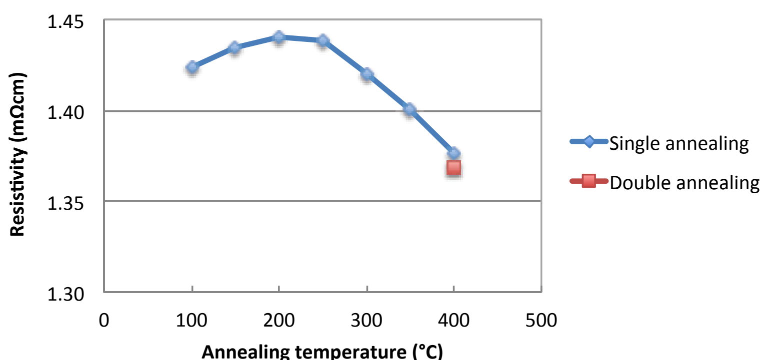

Figure 37. The resistivity of silicon capped $Mo_{31}Si_{20}N_{45}O_4$ films after annealing at temperatures between 100 and 400°C for 30 min. There was a 10 nm thick silicon film both beneath and on top of Mo-Si-N films.

Although the thin silicon cap prevented the surface oxidation of Mo-Si-N films, the fundamental reason for the inconsistency between the publications and the above observations was still unresolved. According to the best knowledge of that time, Mo-Si-N films were expected to crystallise from 660°C upwards and oxidise only above 800°C [222] (see Section 5.2.3). On the other hand, Mo_2N films had been proved to oxidise from 350°C upwards [320] (see Section 4.2.3). The winning

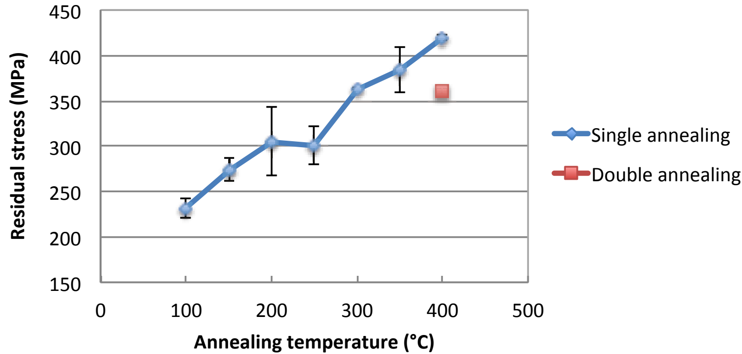

Figure 38. The residual stress of silicon capped $Mo_{31}Si_{20}N_{45}O_4$ films after annealing at temperatures between 100 and 400°C for 30 min. There was a 10 nm thick silicon film both beneath and on top of Mo-Si-N films. The error bars indicate the difference between the stress measured parallel (X) and perpendicular (Y) to the main flat of the silicon substrates.

hypothesis at this stage was the Mo-Si-N films sputtered from separate Mo and Si targets were not homogeneous but consisted of nanolayered Mo-N and Si-N despite the fact such Mo-N/Si-N layering was not observed by TEM [2]. If this was the case, the nanophases of Mo-N might oxidise separately from Si-N. Furthermore, it is known the reaction product MoO_3 is volatile above 550°C (Section 4.2.3). This could explain why molybdenum was not detected by EDX from the Mo-Si-N sample annealed at 700°C in O_2 gas.

To confirm or reject the above hypothesis, Mo-Si-N films were sputter deposited from a Mo_5Si_3 compound target for a comparison (Section 5.4). The films were annealed under inert and oxidising atmospheres, inspected, and measured for their resistivity and residual stress (Table 31). Like in the case of Mo-N films, a change in the visual look (primarily the colour) was considered a proof of oxidation despite the relating problems (Section 4.5). Annealing at 400°C in N_2 gas did not alter the looks of any Mo-Si-N samples regardless of the choice of the sputtering target, the sputtering base pressure (affecting the impurity content), the film composition, or the annealing pressure (the experiments #1…4 and #8). On the contrary, even a short O_2 plasma treatment at 220…260°C resulted in heavy oxidation (the experiment #7). The rest of the experiments were performed at 1000 mbar in ambient air. Now when the surrounding gas was of air (instead of N_2), both kinds of standard Mo-Si-N films oxidised at 400°C, no matter whether they had been deposited from separate or a compound target. Interestingly, the colour of the Mo-Si-N films with purposely impaired sputtering base pressure turned only light brown or brownish at 400°C, compared to the rich colours of the standard Mo-Si-N films. In their as-deposited state, all Mo-Si-N films were grey.

Table 31. The colour, the resistivity, and the residual stress of Mo-Si-N films after annealing. The films were deposited by the 150 mm sputtering processes, and the film thickness varied between 210 and 530 nm. The surrounding gas, the pressure and the temperature refer to those that prevailed during annealing; see Table 19 for other details. Stress X denotes the residual stress parallel to the main flat of the silicon substrate, and stress Y the residual stress perpendicular to the main flat. Note that the Mo-Si-N films of the experiment #2 (tagged with *) were not deposited with either of the standard 150 mm sputtering processes, while the others were. The sputtering base pressure of the samples originating from the deposition runs #B2 and #B4 was impaired on purpose to $5.0 \cdot 10^{-3}$ µbar (tagged with **). The Mo-Si-N films of the experiments #25 and #26 had a 10 nm silicon film both beneath and on top of them (tagged with ***).

Annealing experiment #	**Sputtering target**	**Surrounding gas**	**Pressure (mbar)**	**Temperature (°C)**	**Colour**	**Resistivity (µΩcm)**	**Stress X (MPa)**	**Stress Y (MPa)**
1	Mo_5Si_3	N_2	< 50	400	Grey	2.2	210	180
2*	Mo_5Si_3	N_2	< 50	400	Grey	1.1	-190	-170
3	Mo, Si	N_2	< 50	400	Grey	1.1	240	250
4	Mo, Si	N_2	1000	400	Grey	1.0	240	250
7**	Mo, Si	O_2 plasma	1300	220…260	Colourful, blotchy	-	-	-
8**	Mo, Si	N_2	1000	400	Grey	-	290	270
9	Mo, Si	Air	1000	400	Dark blue - violet	-	230	230
10**	Mo, Si	Air	1000	400	Light brown	-	260	220
17**	Mo, Si	Air	1000	400	Brownish	1.1	180	200
18	Mo, Si	Air	1000	400	Dark blue - violet	1.1	-	-
19	Mo, Si	Air	1000	300	Grey	1.0	-	-
20	Mo, Si	Air	1000	350	Brownish	1.0	-	-
21	Mo, Si	Air	1000	325	Grey	1.0	-	-
22	Mo, Si	Air	1000	375	Brown	1.1	-	-
23	Mo, Si	Air	1000	350	Brownish	-	190	180
24	Mo, Si	Air	1000	250	Grey	-	130	130
25***	Mo, Si	Air	1000	400	Grey tinged with blue	1.1	-	-
26***	Mo, Si	Air	1000	350	Grey tinged with blue	1.1	-	-
27	Mo_5Si_3	Air	1000	400	Dark blue - purple - yellowish	-	150	150
28	Mo_5Si_3	Air	1000	300	Grey tinged with brown	2.2	-	-
29	Mo_5Si_3	Air	1000	350	Brownish	2.2	-	-
30	Mo_5Si_3	Air	1000	375	Brown - a little bit of purple	2.4	-	-
31	Mo_5Si_3	Air	1000	350	Brownish	-	120	130
32	Mo_5Si_3	Air	1000	250	Grey	-	20	70

Table 32 encompasses a summary of the colours of Mo-N and Mo-Si-N films after annealing in ambient air at temperatures between 250 and 400°C. It was used for the evaluation of the onset temperature of oxidation for three kinds of Mo-Si-N films and, for the sake of comparison, for Mo-N films. It was assumed the lowest annealing temperature resulting in a visible change in the colour of the film coincided the oxidation onset temperature of the film at issue. According to this simple criterion, the Mo-Si-N films sputtered from separate Mo and Si targets started to oxidise at 350°C, repeating the behaviour of the Mo-N films studied earlier (see Section 4.5). The Mo-Si-N films sputtered from a Mo_5Si_3 compound target showed the first signs of oxidation already at 300°C, meaning the initial hypothesis was wrong: the Mo-Si-N films sputtered from a compound target were not stabler than those sputtered from separate Mo and Si targets. At 400°C, both films experienced heavy oxidation with richly coloured surface oxide layers. Adding a 10 nm silicon cap on top of Mo-Si-N films prevented their oxidation, repeating the observations made by the Tencor FLX-2320 stress measurement instrument; the capped Mo-Si-N films had a slight tinge of blue due to the 10 nm silicon film already in their as-deposited state.

Table 32. A summary of the colours of Mo-N and Mo-Si-N films after annealing in ambient air at temperatures between 250 and 400°C. The silicon capped Mo-Si-N films had a 10 nm silicon film both beneath and on top of them.

Annealing temperature (°C)	**Mo-N films**	**Mo-Si-N films sputtered from separate Mo and Si targets**	**Silicon capped Mo-Si-N films sputtered from separate Mo and Si targets**	**Mo-Si-N films sputtered from a Mo_5Si_3 target**
400	Grey tinged with brown	Dark blue - violet	Grey tinged with blue	Dark blue - purple - yellowish
375	-	Brown	-	Brown - a little bit of purple
350	Grey tinged with brown	Brownish	Grey tinged with blue	Brownish
325	Grey	Grey	-	-
300	Grey	Grey	-	Grey tinged with brown
250	Grey	Grey	-	Grey

SEM analyses of two Mo-Si-N samples sputtered from separate Mo and Si targets confirmed the above. Figure 39 shows the cross-section of a Mo-Si-N film annealed at 300°C in ambient air, and being grey in colour. The cross-section looked grainy but there was no sign of a surface layer. The other Mo-Si-N sample had been

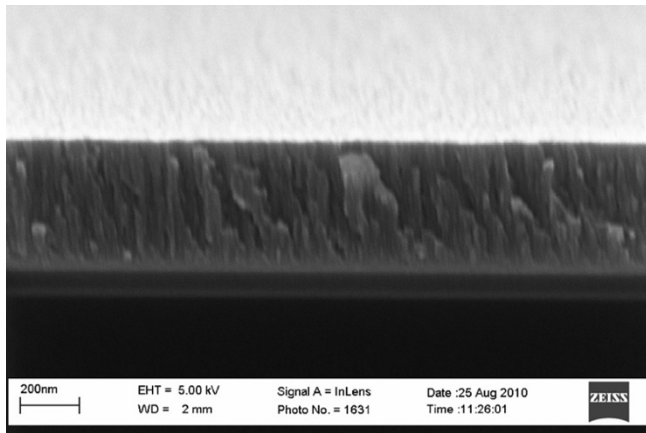

Figure 39. A SEM image of a ~430 nm thick Mo-Si-N film after annealing in ambient air at 300°C for 75 minutes. The $Mo_{35}Si_{22}N_{39}O_4$ film was deposited by the standard 150 mm sputtering process from separate Mo and Si targets on top of a silicon oxide layer, and had no silicon cap.

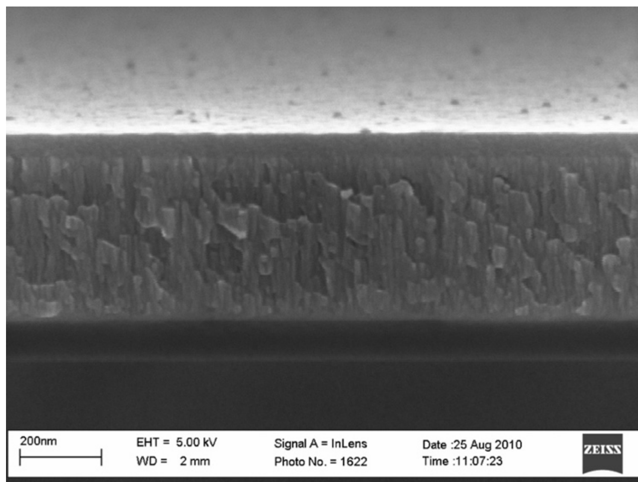

Figure 40. A SEM image of a ~430 nm thick Mo-Si-N film after annealing in ambient air at 400°C for 75 minutes. The $Mo_{35}Si_{22}N_{39}O_4$ film was deposited by the standard 150 mm sputtering process from separate Mo and Si targets on top of a silicon oxide layer, and had no silicon cap. One can see a surface layer of 50…60 nm on top of the Mo-Si-N film, formed during the annealing.

annealed in ambient air at 400°C (Figure 40). The film was richly coloured, suggesting oxidation had taken place. Again, the SEM cross-section looked grainy but, in-

terestingly, there was a clearly distinguishable surface layer, 50…60 nm in thickness, on top of the Mo-Si-N film. The observation hence confirmed the assumption about the colour change indicating the formation of a surface oxide layer.

Regardless of the surrounding gas, annealing at temperatures between 250 and 400°C was capable of inducing only a marginal (if any) change in the resistivity of Mo-Si-N films. The only sample whose resistivity after annealing did not fall into the resistivity range of the corresponding as-deposited films was that of the experiment #30; however, the related measurement signal was unstable due to the four-point probing through the surface oxide layer, casting doubt on the reliability of the particular measurement.

Figure 41 shows the annealing-induced change in the residual stress of Mo-Si-N films. The as-deposited films were under low tensile stress. The residual stress of Mo-Si-N films sputtered from separate Mo and Si targets increased with the increasing annealing temperature, i.e. became more tensile by nature. Due to annealing at 400°C, the stress change was slightly below 200 MPa. This repeated the behaviour of Mo-N films, except that the stress change of Mo-N films was somewhat higher (Section 4.5). Contrary to this, the annealing-induced stress change for Mo-Si-N films sputtered from a Mo_5Si_3 compound target was practically zero. That is, both kinds of Mo-Si-N films developed a surface oxide layer during annealing at 350…400°C, but only the films sputtered from separate targets exhibited a stress change indicating changes also in the microstructure. In conclusion, Mo-Si-N films sputtered from a compound target *and* capped with a thin silicon film should be quite stable at least up to 400°C, which was the highest temperature studied herein. Based on hands-on experience, a silicon cap need not be 10 nm thick but 4 nm is usually sufficient.

The Mo-Si-N films of this study oxidised in a repeatable and indisputable manner at temperatures below 400°C. On the other hand, Hirvonen *et al.* (in 1995) [222] and Musil *et al.* (in 2005) [228] stated their Mo-Si-N films were resistant to oxidation up to 800…900°C. For example, Hirvonen *et al.* measured a surface concentration of $\sim 1 \cdot 10^{16}$ oxygen atoms/cm^2 for a 1 µm thick Mo-Si-N sample after oxidation at 500°C for 30 min, corresponding to a volume concentration of $\sim 1 \cdot 10^{20}$ oxygen atoms/cm^3 if a uniform distribution of the oxygen atoms was assumed. For the sake of comparison, a volume concentration of $\sim 4 \cdot 10^{21}$ oxygen atoms/cm^3 was estimated for our as-deposited Mo-Si-N films sputtered by the standard 100 mm process at Balzers LLS 801 system, taking that their composition was $Mo_{0.31}Si_{0.18}N_{0.45}O_{0.06}$ (leading to the assumption of 42.06 g/mol for the molar mass) and the mass density 5.1 g/cm^3 [2]. In other words, even if Hirvonen *et al.* detected oxygen on their samples, the amounts were rather low. Both Hirvonen *et al.* and Musil *et al.* prepared the Mo-Si-N films by sputter deposition, the films were amorphous by XRD, and they were annealed for at least 30 min in flowing air or under wet oxidation conditions. All this was common to this study. In principle, one could conceive an amorphous microstructure would retard or suppress the oxidation of a film if the voids of a columnar microstructure, providing direct paths through the film, were eliminated [228]. However, this did not hold true for the Mo-Si-N films studied here.

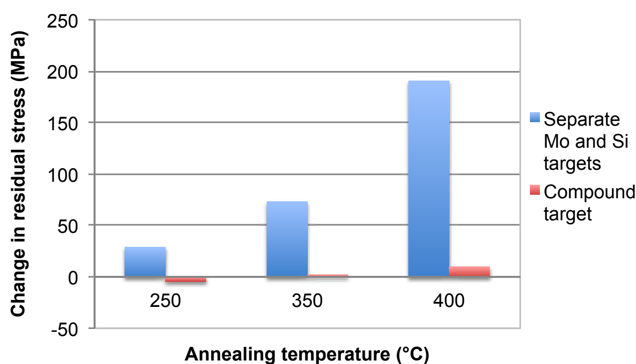

Figure 41. The change in the residual stress of Mo-Si-N films due to annealing in ambient air for 75 minutes. The Mo-Si-N films were deposited by the standard 150 mm sputtering processes, with the composition of $Mo_{35}Si_{22}N_{39}O_4$ for separate Mo and Si targets, and $Mo_{29.5}Si_{14.5}N_{56}$ for the compound target. The chart plots the averages of the residual stress before and after annealing; the lateral stress variations (the difference between the stress measured parallel (X) and perpendicular (Y) to the main flat of the silicon substrates) were excluded because they were small.

Only the article of Yuan *et al.* in 2010 [238] reported that crystalline, sputter deposited Mo-Si-N films had oxidised from 400°C upwards, presenting something similar to what was found herein. The difference between Hirvonen's and Musil's films on the one hand, and Yuan's and our films on the other was their composition: it was ~$Mo_{17}Si_{33}N_{50}$ for Hirvonen [222], in the range of $Mo_{19}Si_{37}N_{44}$…$Mo_{12}Si_{24}N_{64}$ for Musil [228], and $Mo_{31}Si_{18}N_{45}O_6$, $Mo_{35}Si_{22}N_{39}O_4$ or $Mo_{29.5}Si_{14.5}N_{56}$ for us, whereas the silicon content was 9 at.% for Yuan (the exact composition was not given) [238]. In other words, the Mo/Si ratio for Hirvonen and Musil was about 1:2, while Yuan's and our films contained more molybdenum than silicon. Natesan *et al.* state the oxidation behaviour of molybdenum silicide alloys is determined by two competing reactions: the formation of a protective SiO_2 scale, and the formation of non-protective molybdenum oxides [345]. If this was the case also for Mo-Si-N films, the difference in the relative contents of Mo and Si might explain the dissimilar oxidation behaviours of the above films. The experimental results on Mo-N films (Section 4.5), sharing the onset temperature for visible oxidation with Mo-Si-N films, supported the idea that the oxidation of our Mo-Si-N films stemmed from the oxidation of a Mo-N phase. It seems possible that Hirvonen's and Musil's Mo-Si-N films were not prone to oxidation due to their higher silicon content, sealing the film surface by a protective SiO_2 layer. This conclusion is also in agreement with the observations about other mictamict alloys, stating that an increase in the silicon concentration was able to improve the oxidation resistance of Ta-Si-N, Ti-Si-N and Zr-Si-N films (Section 3.3).

The highly stable Mo-Si-N films of Hirvonen and Musil were sputtered from $MoSi_2$ compound targets [222, 228]. The Mo-Si-N films of this study were sputtered from

separate Mo and Si targets, and later from a Mo_5Si_3 compound target. The former enabled the free adjustment of the Mo/Si ratio in the films, while the latter was selected so as to reproduce the composition of the former kind of films, having a favourable residual stress state. In addition, Mo_5Si_3 suffers from pesting at 700…800°C while $MoSi_2$ already at 400…600°C (Section 5.2.3), which prefers the former. At the time these choices were made, there were no studies warning about the poor thermal stability of Mo-Si-N films, nor its link with the composition. Quite the contrary, the famous review article by Prof. M.-A. Nicolet, a pioneer of the field, defined the mictamict alloys as *highly metastable amorphous or near-amorphous ternary films of the generic composition (early transition metal)–Si–(nitrogen or oxygen)*, and regarded Mo-Si-N films as their express representatives [140]. (Note that also near-amorphous films are included in this definition.) However, this study showed the amorphous microstructure of such a ternary film did not guarantee the film was thermally stable at 200…700°C. In other words, the mictamict alloys do not always possess high thermal stability, or – alternatively – amorphous Mo-Si-N films do not always belong to the mictamict alloys. Consequently, this study suggests the definition of the mictamict alloys could be clarified or revised. Lastly, this study did not conclude anything about the thermal stability of other mictamict films than Mo-Si-N as such, neither did it concern other aspects of thermal stability such as phase equilibrium, metal, nitrogen and impurity diffusion, phase separation, and interfacial reactions [337].

In summary, the Mo-Si-N films sputtered from separate Mo and Si targets showed the first signs of crystallisation at 200°C, oxidised from 350°C upwards when heated in air, changed their residual stress at the same temperature, and finally lost their molybdenum at 700°C. The Mo-Si-N films sputtered from a Mo_5Si_3 compound target oxidised at temperatures above 300°C but did not change their residual stress up to 400°C (the highest temperature studied herein). The resistivity of either films did not change significantly at 400°C or below; neither did they react if heated in N_2 gas. The formation of a surface oxide layer on top of Mo-Si-N films could be suppressed by a thin (4…10 nm) silicon cap, and a short RTA annealing in an inert gas may stabilise Mo-Si-N films against a further stress change. In addition, it might be possible to tune the residual stress of Mo-Si-N films by the proper selection of the above annealing temperature.

5.6 Low temperature behaviour

The electrical properties of Mo-Si-N films were investigated over a wide temperature range, reaching from cryogenic up to room temperatures. First, the resistivity of 50 nm thick films was measured from 90 mK up to 300 K, with the results plotted in Figure 42. The temperature coefficient of resistance was negative, being about −800 ppm/K close to room temperature. This result is in accordance with many other mictamict materials also having a negative temperature coefficient (Section 3.5). The negative temperature coefficient demonstrates that the conduction mechanism is not primarily metallic. Figure 43 shows the conductivity σ_c on a logarithmic scale

as a function of $1/T$ through the temperature range 4.2…300 K, in order to find out whether the conductivity followed the Arrhenius behaviour with the thermal activation term $\exp(-E_a/k_B T)$ typical for semiconductors, where E_a is the activation energy. The resulting curve resembled indeed that which is often encountered with semiconductors. At temperatures 90 mK < T < 4.2 K (0.25 K^{-1} < $1/T$ < 11 K^{-1}) the values on the y-axis, i.e. $\ln(\sigma_c(10^4$ S/m)), remained between 11.15 and 11.17, which was excluded from the plot.

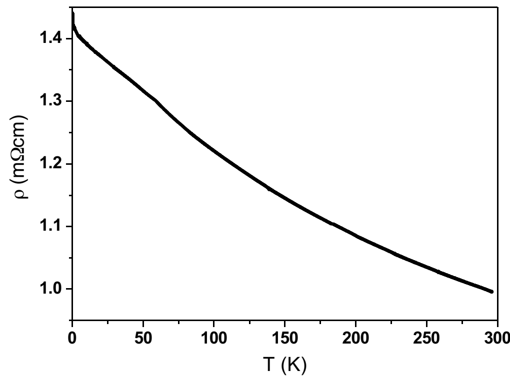

Figure 42. The resistivity of $Mo_{31}Si_{18}N_{45}O_6$ films at temperatures from 90 mK to 300 K. Published previously in [3].

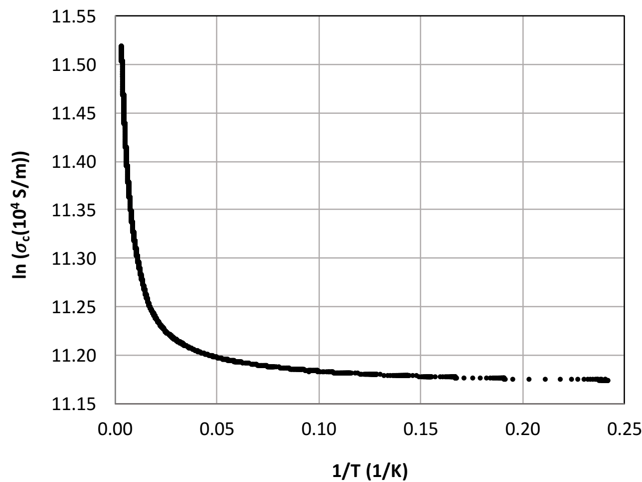

Figure 43. The conductivity σ_c of $Mo_{31}Si_{18}N_{45}O_6$ films plotted on a logarithmic scale as a function of $1/T$ through the temperature range 4.2…300 K.

Second, a characteristic *I−V* curve was measured at 80 mK and is presented in Figure 44. The curve follows a linear ohmic behaviour and confirms that no transition into a superconductive state takes place at this or higher temperatures. The critical temperatures of Mo (0.915 K), $MoSi_{0.7}$ (1.30 K) and MoN (12.8 K) [330] are all higher than what was measured for Mo-Si-N. Finally, the current endurance of a resistor was determined by ramping the current and measuring the voltage over it. The maximum current density before failure was 60 mA/μm^2.

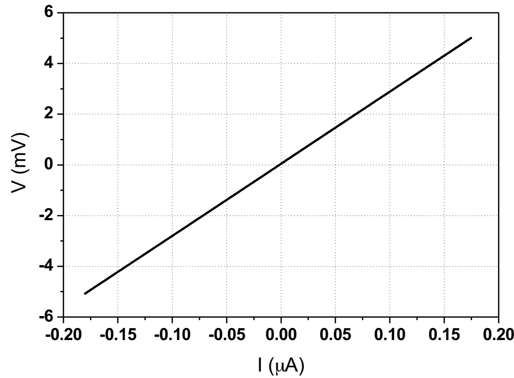

Figure 44. The characteristic *I−V* curve at temperature *T* = 80 mK. Published previously in [3].

In order to scale Mo-Si-N structures down in size, their resistivity was measured as a function of decreasing film thickness (Table 33). The resistivity remained in the vicinity of its original value even if the film thickness went down to 6 nm, showing no monotonic trend. The amorphous microstructure of Mo-Si-N films suggests an advantage in narrow linewidth devices because crystallites, grain boundaries and edge irregularities are absent. In addition, the surface roughness of Mo-Si-N films was low (see Section 5.4). Backed by the above, 25 nm thick nanoscale wires with a varying isthmus width were fabricated by electron beam lithography (Figure 45). The resistances of these wires were measured in the temperature range 80 mK−300 K and normalised relative to the resistance at temperature *T* = 273 K. The temperature dependence of the normalised resistances of 20 and 85 nm wide nanowires and a 25 μm wide long bar resembled very closely the temperature dependence of resistivity shown in Figure 42. The normalised resistances of these three samples also coincided very well, indicating no detectable dependence on the dimensions. This facilitates the use of Mo-Si-N films in nanoscale structures as the scale effects can be neglected, at least with designs having dimensions comparable to those investigated in this study. In general, metallic nanowires have applications in e.g. catalysis, microelectronics and high-density magnetic memories [316]. Since the resistivity of Mo-Si-N films is higher than those of metals, they could be used as resistors.

Table 33. The resistivity of $Mo_{31}Si_{18}N_{45}O_6$ films as a function of decreasing film thickness.

Thickness (nm)	Resistivity (mΩcm)
325	1.17
167	1.17
26	1.01
6	1.27

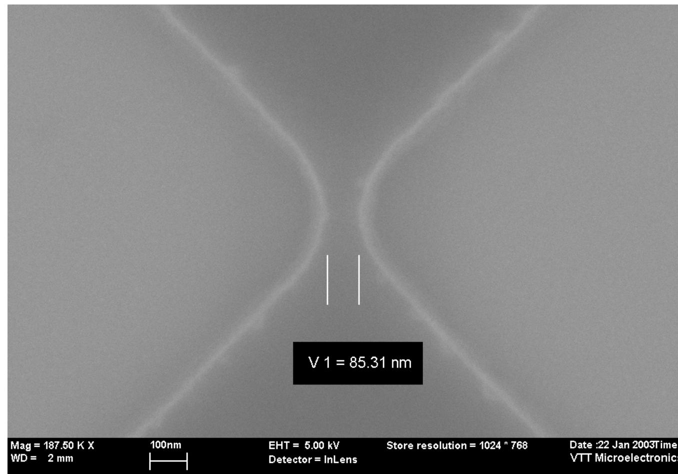

Figure 45. A SEM image of a Mo-Si-N wire with the isthmus width of 85 nm. The film thickness was 25 nm.

5.7 Conclusions

The purpose of this study was to deposit amorphous Mo-Si-N films from separate Mo and Si targets and a Mo_5Si_3 compound target by sputtering, determine their most relevant properties from the perspective of MEMS, and investigate their behaviour over a wide temperature range (from 80 mK up to 1373 K to the utmost). The deposition parameters and the key properties have been compiled in Table 34. The created 150 mm deposition process at Provac LLS 801 sputtering system resembled the earlier 100 mm process (see Table 20) in many ways; where not proved explicitly, the resultant material properties are also likely to resemble each other.

Table 34. A summary of the deposition parameters and the properties of Mo-Si-N films of the selected standard compositions. The deposition processes were operated with 150 mm substrates at Provac LLS 801 sputtering system with separate Mo and Si targets, and at Von Ardenne CS 730 S sputtering system with a Mo_5Si_3 compound target. The elastic modulus, the hardness, the coefficient of thermal expansion and the temperature coefficient of resistance were measured for Mo-Si-N films sputtered by the standard 100 mm process at Balzers/Provac LLS 801 system (tagged with *).

SPUTTER DEPOSITION		
Parameter	**Provac LLS 801**	**Von Ardenne CS 730 S**
Base pressure	$5.0 \cdot 10^{-4}$ µbar	$5.0 \cdot 10^{-4}$ µbar
Throttle setting	On	Open
Ar flow rate	50 sccm	90 sccm
Ar pressure	~4.2 µbar	5.9 µbar
N_2 flow rate	25 sccm	10 sccm
N_2 pressure	~1.1 µbar	-
Total pressure	5.3 µbar	-
DC power on Mo target	600 W	-
Pulsed DC power on Si target	1000 W	-
Power on Mo_5Si_3 target	-	500 W
Duration of a drum revolution	20 s	-
Deposition rate	1.3…1.4 nm/revolution	31 nm/min
PROPERTIES		
Property	**Provac LLS 801**	**Von Ardenne CS 730 S**
Composition	$Mo_{35}Si_{22}N_{39}O_4$	$Mo_{29.5}Si_{14.5}N_{56}$
Resistivity	1.0…1.2 mΩcm	2.1 mΩcm
Residual stress (as-deposited)	90…110 MPa (tensile)	140…150 MPa (tensile)
Change in residual stress due to annealing at 400°C	~200 MPa (more tensile)	~0 MPa
Onset temperature of oxidation	~350°C	~300°C
Elastic modulus*	170 GPa	-
Hardness*	15 GPa	-
Coefficient of thermal expansion (near T=300 K)*	3.9 ppm/K	-
Temperature coefficient of resistance (near T=300 K)*	~ −800 ppm/K	-
Complex refractive index (n,k)	See Figure 27	-
Etch rates in various etch chemistries	See Section 6.1.1	

The interest in Mo-Si-N films originated from the fact the amorphisation of sputter deposited Mo-N films was incomplete, bringing on a vertical stress gradient across

the films (Chapter 4). It was wished the addition of silicon to Mo-N films would lead to more complete amorphisation similar to the case of Ti-N and Ti-Si-N films [140]. This anticipation materialised indeed like proved in [2], which shows the structural transformation from crystalline Mo films to amorphous Mo-Si-N films by TEM. A systematic set of XRD and TEM studies through the entire ternary system might have provided interesting data, though excluded from the current study. Based on the best knowledge of that time, Mo-Si-N films were also anticipated to have high structural stability upon thermal annealing as well as good oxidation resistance up to 800°C (see [140, 222] and Sections 3.3 and 5.2.3).

Along with their amorphous microstructure, the residual stress of Mo-Si-N films proved very suitable for MEMS: it could be tuned to low tensile values by selecting a proper sputtering pressure, it was laterally uniform, and the thickness dependence of Mo-N films had mostly disappeared. The latter indicated the Mo-Si-N films did not suffer from a vertical stress gradient similar to Mo-N films. The resistivity of Mo-Si-N films was at the level of highly doped polysilicon films: higher than the resistivity of elemental metals or Mo-N, but adequate for many MEMS devices. The deposition rate related to the separate Mo and Si targets was low (~5 nm/min) in order to avoid the layering of separate Mo-N and Si-N phases; consequently, the practical film thickness was limited to about 1 micron. The surface roughness, elastic modulus, hardness, elastic recovery, coefficient of thermal expansion, temperature coefficient of resistance (TCR) and complex refractive index of Mo-Si-N films were determined in order to facilitate their application to MEMS devices (see Table 34). No transition into a superconductive state was observed down to 80 mK. Thin Mo-Si-N films were characterised with nanoscale structures in mind; the nanoscale wires fabricated by EBL showed no non-linear size dependence down to a width of 20 nm and thickness of 25 nm. The design of Mo-Si-N structures with sub-100 nm dimensions is hence possible.

The extensive study of the thermal stability of Mo-Si-N films started half by chance as the formation of an anti-reflective surface oxide layer stopped the measurements whose purpose was to demonstrate the stress relaxation of Mo-Si-N films. It turned out that Mo-Si-N films started to oxidise at around 350°C when heated in air, and showed the first signs of crystallisation at no higher than 200°C. These observations were significantly inconsistent with the contemporary research papers. In addition, the residual stress of the Mo-Si-N films sputtered from separate Mo and Si targets changed due to post-deposition heat treatments, so that the stress increased with the increasing annealing temperature, i.e. became more tensile by nature. Therefore, in principle, controlled heat treatments could be used for the tuning of the residual stress of Mo-Si-N films as long as the subsequent service temperatures stay below the tuning temperature.

At first the above-mentioned oxidation was thought to stem from the nanolayering of the Mo-Si-N films sputtered from separate Mo and Si targets. If so, nanophases of Mo-N might oxidise separately from Si-N. To test this hypothesis, the thermal stability of Mo-N films was studied (Section 4.5) as well as Mo-Si-N films were sputter deposited from a Mo_5Si_3 compound target, assuming the latter films would not

oxidise. The initial hypothesis turned out wrong since also these Mo-Si-N films oxidised at temperatures above 300°C, albeit they were more resistant against annealing-induced change in residual stress. After comparing the above findings with few other research papers available on the topic, it was concluded it was possibly the low silicon content that lay behind the unexpected low thermal stability of our Mo-Si-N films. Consequently, the stability might improve if Mo-Si-N films were deposited from a $MoSi_2$ target with higher silicon content. However, also a thin silicon cap on top of Mo-Si-N proved to prevent the surface oxidation of the films.

In conclusion, the Mo-Si-N films of this study are well suitable for several kinds of MEMS devices on condition they are not exposed to increased temperatures in an oxidising atmosphere without a thin protective silicon cap. The inclusion of the silicon cap in a MEMS process is rather easy as silicon can be deposited by sputtering just like Mo-Si-N, and its patterning is feasible by SF_6 based plasma chemistries, again similar to Mo-Si-N. If photoresist is used as the sacrificial layer (see Section 2.1.2), it is the photoresist, not Mo-Si-N, that limits the maximum temperature the wafers can stand during their processing. After the sacrificial photoresist is removed, it depends entirely on the application what temperatures the MEMS devices should tolerate, and whether the service temperature is acceptable for Mo-Si-N films. These restrictions in mind, it was possible to create a MEMS process technology employing Mo-Si-N films as the structural layer, and fabricate functional MEMS devices with it. The results will be covered in the next chapter.

6. MEMS devices

The chapter 6 deals with the application of amorphous metal films to MEMS devices. It starts with a description of the available process technology: the way in which the patterning of Mo-N and Mo-Si-N films was possible, and the presentation of the feasible micromechanical structures. The chapter continues with the demonstration of RF MEMS devices and thin film absorbers that were realised with the use of these films.

6.1 Process technology

6.1.1 Patterning

Mo-N and Mo-Si-N films can be patterned by standard photolithography processes used in microfabrication and MEMS. Examples of such processes are given in Table 35. As sputter deposition is a low temperature process, the sacrificial layer underneath a Mo-N or Mo-Si-N structural layer can be of photoresist. When photoresist was used for the sacrificial layer, it was first patterned in a usual way, including hexamethyldisilazane (HMDS) vapour prime, spin coating, soft bake, exposure, development and post-exposure bake (PEB). A typical thickness for the sacrificial photoresist was 1.5 µm. Before sputtering the structural layer, however, the sacrificial photoresist needed to be ”bled” and hardened so as to stabilise it. The former was performed by an extra postbake at 145°C, the latter by a supplementary UV exposure without a mask. Besides the stabilisation, the procedure rendered the corners of the sacrificial photoresist rounder and the edge slopes gentler, thus enhancing the step coverage of sputter deposition. The photoresist near the edges of the wafer, outside the patterned area, had better be removed in order to avoid wrinkling of large, unpatterned metal and resist layers, one on top of the other.

Table 35. Examples of photolithography processes Mo-N and Mo-Si-N films are compatible with.

	Lithography process #1	**Lithography process #2**	**Lithography process #3**
Purpose	Patterning of a Mo-N or Mo-Si-N film	Patterning of a Mo-N or Mo-Si-N film	Formation of a sacrificial layer
Photoresist	SPR 700 (positive)	AZ 5214 E (positive)	AZ 5214 E (positive)
Priming	Vapour prime with HMDS (150°C, 20 min)	Vapour prime with HMDS (150°C, 20 min)	Vapour prime with HMDS (150°C, 20 min)
Soft bake	90°C, 60 s	90°C, 60 s	90°C, 60 s
Exposure	According to the photoresist and mask specifications	According to the photoresist and mask specifications	According to the photoresist and mask specifications
Developer	AZ 726 MIF	AZ 726 MIF	AZ 726 MIF
Post-exposure bake	110°C, 60 s	110°C, 60 s	110°C, 60 s
Photoresist bleeding	-	-	145°C, 20 min
Photoresist hardening	-	-	UV exposure (100 mJ/cm^2)

The masking photoresist on top of a Mo-N or Mo-Si-N film was usually removed by Posistrip® EKC830™, which is a commercial photoresist remover in a liquid form, typically used at 80ºC. Like any metal, Mo-N and Mo-Si-N films cannot be cleaned with standard RCA clean. The release etching (the removal of the sacrificial photoresist) was performed in low-temperature oxygen plasma in a barrel-type O_2 plasma stripper (PRS 800/801), resulting in isotropic etching suitable for release. The etch rate was about 80 nm/min, meaning the maximum practical etch distance in a lateral direction was limited to 10…15 µm. The operating temperature was not allowed to exceed 140ºC in order to maintain the photoresist stability. Photoresist stripping in high-temperature O_2 plasma was out of question also because of the susceptibility of Mo-N and Mo-Si-N films to oxidation at 300ºC and above. If the films were capped with silicon (see Section 5.5), such restriction did not hold, albeit a change in the residual stress could still occur. The release etching in low-temperature O_2 plasma is gentle to most materials used in MEMS, unlike hydrofluoric acid (HF) that is conventionally used for the removal of silicon oxide sacrificial layers. Another advantage of the plasma release etching is that stiction problems are usually avoided.

Mo-N films can be patterned both by plasma and wet etching (Table 36). If the former is preferred, $CF_4/Cl_2/O_2$ chemistry (usually intended for molybdenum etching) is a choice. If the latter is favoured, an etch mixture containing H_3PO_4 and HNO_3 is practical. In the case aluminium films should be etched selectively against Mo-N, one can use phosphoric acid (H_3PO_4) alone, since it proved not to etch Mo-N films at any measurable rate.

Table 36. A summary of the etch properties of Mo-N films. $Mo_{76}N_{24}$ films were deposited with the standard 100 mm sputtering process (Table 2), and $Mo_{80}N_{20}$ films with the standard 150 mm process (Table 11).

#	Composition	Type of etching	Etch chemistry	Temperature (°C)	Etch rate (nm/min)	Remarks
1	$Mo_{76}N_{24}$	Plasma	$CF_4/Cl_2/O_2$	-	280	Ref. [30]. Primarily intended for Mo etching.
2	$Mo_{76}N_{24}$	Wet	85% H_3PO_4 (phosphoric acid)	60	Slow (not measurable)	Suitable for Al etching
3	$Mo_{80}N_{20}$	Wet	PS 70-10 etch mixture (H_3PO_4 + HNO_3)	21	420	Primarily indended for Al etching

Mo-Si-N films can be etched by several SF_6 based plasma chemistries, with the etch rates varying with the other parameters involved (Table 37). The standard polysilicon wet etch (also known as the isotropic silicon etchant [365, 366]) etched Mo-Si-N films at a rate of 150…220 nm. Similar to Mo-N films, phosphoric acid did not attack Mo-Si-N films at any measurable rate. PES 80-16-04, a commercial wet etch mixture designed for aluminium etching, did not etch Mo-Si-N films either. The effect of concentrated HF was ambiguous: it evidently damaged Mo-Si-N films but did not remove them in a neat way. Something similar was encountered with HF vapour: it did not result in any measurable etch rate when analysed by SEM but produced little peculiar rolls on top of Mo-Si-N films (Figure 46). The rolls looked like they had peeled off from the surface of Mo-Si-N. Also light little spots were found all over the samples. A possible explanation for the observations was if a few topmost Si-N layers of the Mo-Si-N film reacted with HF vapour while the rest of the film remained intact. This might be possible as the Mo-Si-N films in question had been deposited from separate Mo and Si targets, and Si-N is generally known to react with HF vapour. The light spots might thus be of non-volatile etch residue of silicon nitride. It was not experimented whether a thin silicon cap or the use of a silicide compound target would have affected the etch behaviour.

If a metallic mask is needed for Mo-Si-N (if, for some reason, photoresist is not applicable), Table 37 suggests Ti-W is a choice. An etch rate of 16 nm/min was measured for a sputtered Ti-W film in the polysilicon wet etch, compared to the 150…220 nm/min of Mo-Si-N. This means a selectivity of 1:9 at least.

Due to their susceptibility to oxidation, the use of a thin silicon cap on top of Mo-Si-N films is advisable. The inclusion of the silicon cap in a MEMS process does not complicate it, because the silicon cap can be deposited by sputtering just like the Mo-Si-N film (even without breaking the vacuum in between). In addition, its etching is straightforward in SF_6 plasma or by the polysilicon wet etch, again similar to Mo-Si-N.

Table 37. A summary of the etch properties of Mo-Si-N films. $Mo_{31}Si_{18}N_{45}O_6$ films were deposited with the standard 100 mm sputtering process (Table 14), and $Mo_{35}Si_{22}N_{39}O_4$ films with the standard 150 mm process (Table 34). *p* = pressure, *P* = power, RT = room temperature, LF = light field, DF = dark field.

#	Composition	Type of etching	Etch chemistry	Temperature (°C)	Other parameters	Etch rate (nm/min)	Remarks
1	$Mo_{31}Si_{18}N_{45}O_6$	Plasma	SF_6/He	-	p = 375 mtorr, P = 228 W	200	Intended for Si-N etching
2	$Mo_{31}Si_{18}N_{45}O_6$	Plasma	SF_6/O_2	-	p = 300 mtorr, P = 122 W	200	Intended for Si-N etching
3	$Mo_{31}Si_{18}N_{45}O_6$	Wet	Polysilicon etch (HNO_3 + H_2O + NH_4F)	Not known (near RT)	-	220	-
4	$Mo_{31}Si_{18}N_{45}O_6$	Wet	85% H_3PO_4 (phosphoric acid)	60	-	Slow (< 2)	Suitable for Al etching
5	$Mo_{31}Si_{18}N_{45}O_6$	Wet	Concentrated HF (49%)	21	-	Not well measurable	Mo-Si-N is attacked partly, resulting in a damaged film.
6	$Mo_{35}Si_{22}N_{39}O_4$	Plasma	SF_6/CF_4/He	-	p = 250 mtorr, P = 300 W	140	Intended for Si-N etching
7	$Mo_{35}Si_{22}N_{39}O_4$	Plasma	SF_6/HBr	-	p = 750 mtorr, P = 190 W	30…40	Intended for Si-N etching
8	$Mo_{35}Si_{22}N_{39}O_4$	Plasma	SF_6/He	-	p = 400 mtorr, P = 315 W	160…300	The etch rate depends on the mask polarity (LF/DF).
9	$Mo_{35}Si_{22}N_{39}O_4$	Plasma	Cl_2/HBr	-	p = 300 mtorr, P = 300 W	10	Intended for polysilicon etching
10	$Mo_{35}Si_{22}N_{39}O_4$	ICP	SF_6 (optionally complemented with C_4F_8 and/or O_2)	-	p = 30 mtorr, P = 1000 W at the coil generator, P = 10 W at the platen generator	~ 200	A cleaning step with O_2 is needed after each wafer.
11	$Mo_{35}Si_{22}N_{39}O_4$	Wet	Polysilicon etch (HNO_3 + H_2O + NH_4F)	21	-	150	-
12	$Mo_{35}Si_{22}N_{39}O_4$	Wet	PES 80-16-04 etch mixture (H_3PO_4 + CH_3COOH + HNO_3)	40	-	Slow (not measurable)	Intended for Al etching
13	$Mo_{35}Si_{22}N_{39}O_4$	Vapour	HF vapour	45	p = 150 torr, HF flow = 500 sccm, ethanol flow = 400 sccm, N_2 flow = 1200 sccm	Slow (not measurable)	See Figure 46. Intended for sacrificial Si-O etching.

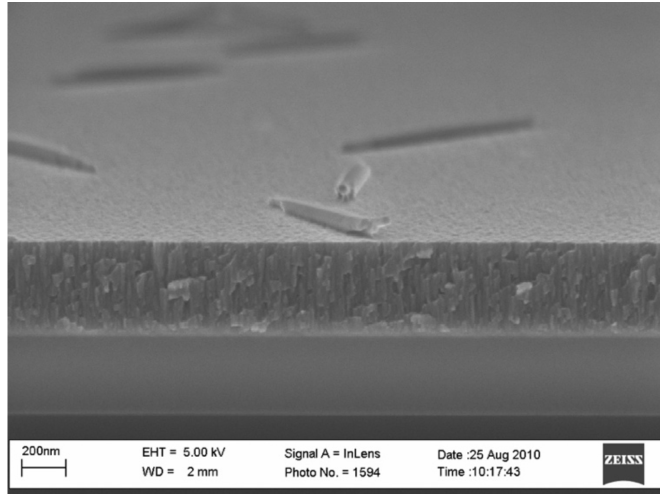

Figure 46. A SEM image of a 430 nm thick Mo-Si-N film after HF vapour etching of 45 min. See Table 37 for other parameters.

Since the published data on the etch properties of Mo-Si-N films proved very scarce (see Section 5.2.1), this is likely the first time an extensive set of the etch rates of Mo-Si-N films is reported in public.

6.1.2 MEMS structures

Capacitive structures are widely used in MEMS. The maximum tuning range of a parallel plate capacitor is only 1/3 of the gap height before the pull-in phenomenon takes place. It is too low for many RF MEMS applications. To increase the tuning range of voltage-controlled capacitive devices, a stepped membrane structure was designed (Figure 47a). At the same time, the fabricability of a corrugated membrane was tested (Figure 47b). The stepped membrane structure is capable of increasing the tuning range if the lower electrodes of capacitors are divided in two: one for electrostatic position control, the other for read-out. In the Design A of Figure 47, the control electrode should situate at the rim (with a larger gap), while the read-out electrode would be placed in the centre (with a narrower gap).

The fabrication of the Design A was possible with a stepped sacrificial layer which was formed by spinning two photoresist layers one upon the other. The bottom one was patterned with the usual lithography process detailed in Table 35 (the process #3). The upper one was patterned in a similar way, except that the HMDS vapour prime was omitted. One should use such designs that the upper sacrificial layer always covers the bottom one, and any single-layer structures are formed from the upper one.

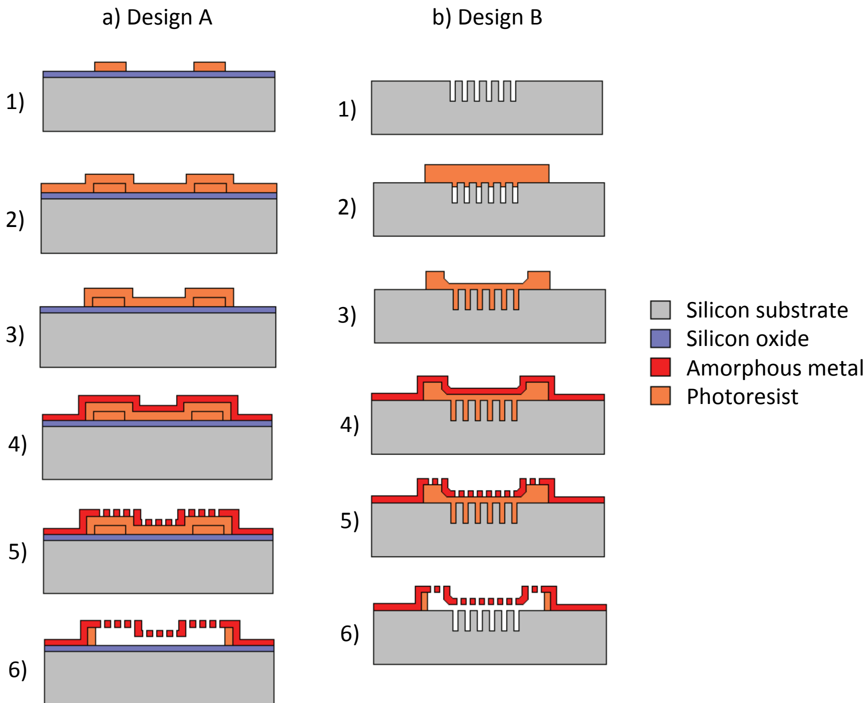

Figure 47. Two designs to verify the fabricability of (a) stepped and (b) corrugated membranes. The film thickness was 100 nm for thermal silicon oxide, 1.5 µm for each layer of sacrificial photoresist, and 260 nm for Mo-N. The depth of the grooves in the silicon substrate in Design B varied between 0.5 and 1.5 µm.

The sputter deposited 260 nm thick Mo-N films proved to have good step coverage, resulting in an almost 100% yield of stepped membranes (Figure 48a). Also the yield of corrugated membranes was very high (Figure 48b). If an aluminium layer is deposited on top of the amorphous metal (see Section 6.2.2), supporting aluminium rims can be patterned on the steps in order to reinforce the structures further. Like described later, stepped membranes similar to Design A were applied to capacitive RF MEMS devices in practice to increase their tuning range.

A simple way of supporting free-standing MEMS structures is to leave a rim of the sacrificial layer (here: photoresist) at the anchors for reinforcement (see e.g. Figure 47). If the devices are used at room temperature, a photoresist rim does not harm. However, the maximum temperature the usual photoresists stand is around 150ºC; in addition, their long-term stability may be questionable. It would be beneficial therefore to be rid of supporting photoresist rims. In the case of sputter deposited Mo-N, Mo-Si-N and aluminium films the free-standing structures proved to take in one piece without a photoresist rim if the nominal thickness of the metal layer at the anchor steps was 1200 nm. (The actual film thickness must have been lower because the step coverage of sputter deposited films is moderate or poor.) If the

nominal thickness was 300 nm, the structures tended to collapse. In other words, the supporting photoresist rims can be etched completely away if the anchor steps are reinforced in another way, such as with a thick aluminium film. The structural layer itself can be naturally thinner.

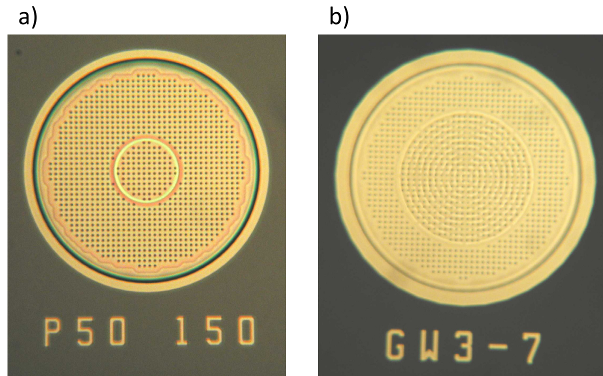

Figure 48. Microscope images of (a) a stepped and (b) a corrugated membrane fabricated of 260 nm thick Mo-N films deposited at the Balzers LLS 801 system. The diameter of the circular membranes was 300 μm.

The hermetic sealing of free-standing amorphous metal membranes would be a significant capability since it would enable e.g. the realisation of pressure sensors and ultrasonic transducers. The first and simplest attempt to achieve it was to define small holes into a Mo-Si-N membrane and try to seal them by a thick aluminium layer. The smallest hole diameter that was easily achievable by the in-house lithography process of that time was 600 nm. However, such holes were too large to be sealed with sputter deposited aluminium of 1.0 μm like Figure 49 indicates. It shows the open holes on the underside of the Mo-Si-N membrane as well as the aluminium lumps deposited onto the floor of the cavity. The conclusion was that the hermetic sealing of free-standing Mo-N or Mo-Si-N membranes would require an ancillary thin semipermeable film similar to that used in the so-called ”plug-up” concept [367]. The concept utilises a thin polysilicon film with a controlled density of nanometer-scale pinholes through which the sacrificial release etching can be done. After the release, the cavities are sealed with another polysilicon film, but now non-permeable. The semipermeable polysilicon film of the original plug-up concept cannot be applied to the low temperature metal micromachining, however, because its deposition temperature is close to 600°C.

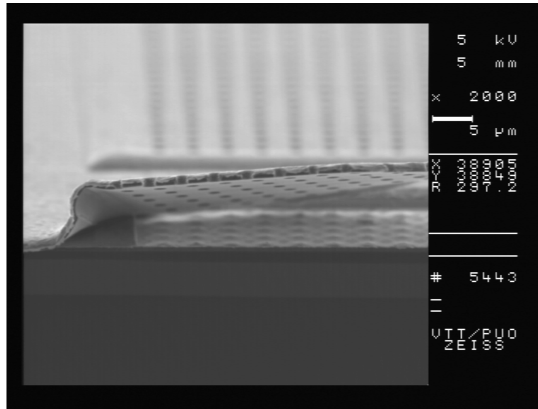

Figure 49. A SEM image of a test device with an air gap of 1.5 µm, a perforated Mo-Si-N membrane of 400 nm, and an aluminium layer of 1.0 µm. The aluminium was not able to seal the holes with a diameter of 600 nm. The sputter depositions were performed at the Balzers LLS 801 system.

The search for a suitable semipermeable film began with porous silica aerogels but the approach was not successful due to unintentional particle generation and the low adhesion on metal surfaces [368]. The search continued with thin Ti-W films sputter deposited at the Balzers LLS 801 system. The adhesion of 50 nm thick highly stressed Ti-W films on top of sacrificial photoresist was poor as long as the argon flow during the deposition was 580 sccm, corresponding to sputtering pressure of 2.9 µbar (Figure 50a). The adhesion improved when the argon flow was increased to 990 sccm, relaxing the residual stress (Figure 50b). The Ti-W films were exposed to concentrated HF (49%) for 20 seconds so as to make them porous (titanium is attacked by HF while tungsten is not [365]). Subsequent sacrificial etching in low temperature oxygen plasma through the Ti-W films rendered the looks wrinkly, suggesting the underlying photoresist would have been etched (Figure 50c); however, a tape test revealed the etching was not complete (Figure 50d).

Another material candidate for the semipermeable thin films was molybdenum. Mo films sputtered under a low argon pressure are dense and crystalline but the microstructure turns first columnar and then dendritic-like as the pressure is increased [302]. This was aimed to be utilised in obtaining semipermeable Mo films. 50 and 15 nm thick Mo films were deposited on top of sacrificial photoresist at the Balzers LLS 801 system under the highest achievable argon pressure. After a low temperature O_2 plasma treatment, the surface of the 50 nm thick Mo film was mostly smooth (Figure 51a) while the surface of the 15 nm thick film was very wrinkly (Figure 51b), indicating the latter had permitted the sacrificial etching of the underlying photoresist through it. On the latter kind of samples, a tape test revealed photoresist residues only by the wrinkles (Figure 51c). To experiment the use of thin Mo films as semipermeable films, test structures of Figure 52 were prepared. However, the sputter deposition of a 15 nm thick molybdenum film on top of a perforated metal

membrane produced a high number of particles. The reason was that the underlying sacrificial photoresist had got very coarse at the open holes of the membrane during the patterning in $CF_4/Cl_2/O_2$ plasma. A thin sputtered film was not able to adhere to such a surface but peeled off, resulting in unwanted particle generation.

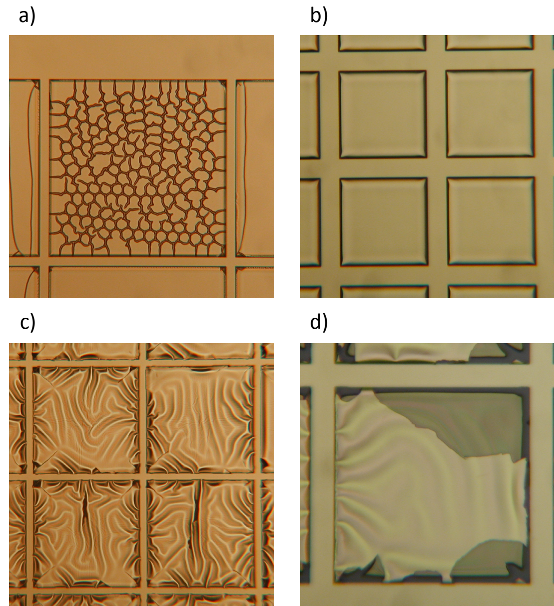

Figure 50. Sputter deposited 50 nm thick Ti-W films on top of sacrificial photoresist in the search for semipermeable thin films. The depositions were performed at the Balzers LLS 801 system. The diameter of the square cells varied between 50 and 210 μm. a) A Ti-W film deposited with an argon flow of 580 sccm corresponding to sputtering pressure of 2.9 μbar, b) a Ti-W film deposited with an argon flow of 990 sccm, c) a sample similar to (b) but exposed to concentrated HF and low temperature oxygen plasma, d) a sample similar to (c) after a tape test.

The problem of hermetic sealing remained unsolved since any of the above approaches did not work well. Despite the failure herein, the results should not be considered definitive. In the opinion of the author, thin metal films might eventually be a viable solution for semipermeable films if one was able to develop a more sophisticated total process, possibly involving wet etching for the perforation of the structural membrane. At the time when the above experiments were made it was not yet known that the polysilicon wet etch (HNO_3+H_2O+NH_4F) is capable of etching Mo-Si-N, for example.

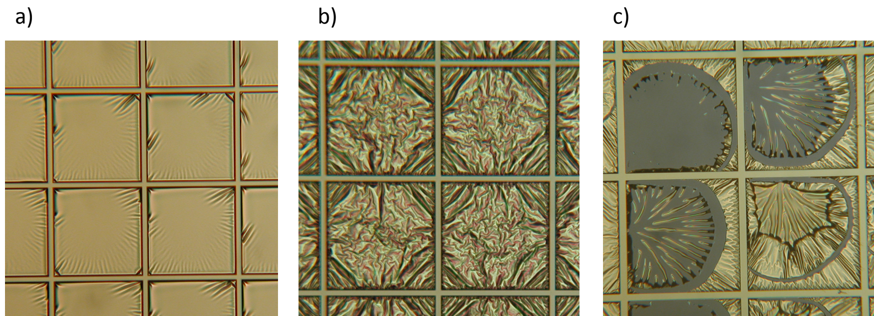

Figure 51. Sputter deposited molybdenum films on top of sacrificial photoresist in the search for semipermeable thin films. The depositions were performed at the Balzers LLS 801 system. The diameter of the square cells varied between 50 and 210 μm. a) A 50 nm thick Mo film and b) a 15 nm thick Mo film after sacrificial etching in low temperature oxygen plasma, c) a sample similar to (b) after a tape test.

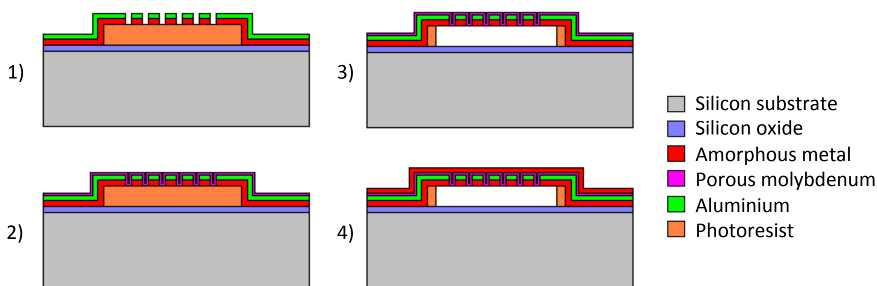

Figure 52. A scheme to experiment the hermetic sealing of free-standing metal membranes. The membrane consisting of Mo-N and aluminium was deposited on top of sacrificial photoresist, and patterned with phosphoric acid (aluminium) and $CF_4/Cl_2/O_2$ plasma (Mo-N). The patterning photoresist was removed in between the etchings. Porous molybdenum was deposited for the thin semipermeable film, while another Mo-N film was intended for sealing. The structure was supposed to be released in low temperature oxygen plasma. In the original design, the film thickness was 1.5 µm for the sacrificial photoresist, 260 nm for Mo-N, 150 nm for aluminium, and 15 or 30 nm for the porous molybdenum.

6.2 RF MEMS

6.2.1 Introduction

RF and microwave engineering encompass the frequencies between 300 kHz and 300 GHz, corresponding to the free-space wavelengths between 1 mm and 1 km [369]. This is also the frequency range in which RF MEMS devices typically operate. The most important RF MEMS components are switches, variable capacitors (varactors), variable inductors, non-radiating transmission lines, and antennas [370].

Also high-Q micromechanical resonators and filters as well as thin film bulk acoustic wave (BAW) resonators are often included [48, 371, 372].

As a part of this thesis, a CMOS compatible, surface micromechanical MEMS fabrication process utilising Mo-Si-N films as the structural layer was developed. While it was clear that the resistivity of Mo-Si-N films far exceeds those of elemental metals, it was conceived its mechanical properties might be useful for RF MEMS devices such as switches that are mechanically actuated millions of times between their up- and down-states during their life. For that reason, the newly developed process was used for the fabrication of variable and switched capacitors for microwave and millimeter wave frequencies. The fabrication process is emphasised in this thesis over the RF design and measurements because of the distribution of work between the author and the other research team members.

6.2.2 Fabrication

When this work on applying amorphous metal films to RF MEMS (or any MEMS devices) was started, there was available only one simple test device that had been fabricated for demonstration purposes at VTT [6]. The device was a variable capacitor (varactor) with the lower electrode made of aluminium or molybdenum, the sacrificial layer of photoresist, and a circular Mo-N membrane as the upper electrode. DC biasing from 0 to 19 V (the latter being a typical pull-in voltage) changed its capacitance from 2.1 to 3.2 pF. No RF measurements or lifetime testing (repetitious cycling between the up- and down-states) had been carried out. From this initial stage of work, the author gained a process of applying photoresist to a sacrificial layer, and a method for patterning Mo-N films (the wet and dry etch rates were also given in [30]).

The RF MEMS devices presented in this thesis were fabricated with the surface micromachining processes of Figure 53 and Figure 54. Fused silica (SiO_2) wafers were used for the substrates owing to their low electrical losses. Both process variations applied high-resistivity polysilicon to bias lines, molybdenum to the first metal layer (signal lines), photoresist to the sacrificial layer, and Mo-Si-N and aluminium to the structural and shunt layers. The material layers are detailed in Table 38.

The fused silica substrates were single side polished. They were coated with low temperature oxide (LTO) to improve the adhesion of the rest of thin films. Either doped LPCVD polysilicon or sputter deposited aluminium were used on the backside of the wafers to enable their passage through such process equipment whose automated wafer handling systems were based on capacitive detection.

The high-resistivity bias lines were made of LPCVD polysilicon doped with B^+ ion implantation. The sheet resistance of the 120 nm polysilicon films was about 1000 Ω. The bias lines were incorporated into the process in order to prevent the electrical coupling between the millimeter-wave signal and control (biasing) circuits.

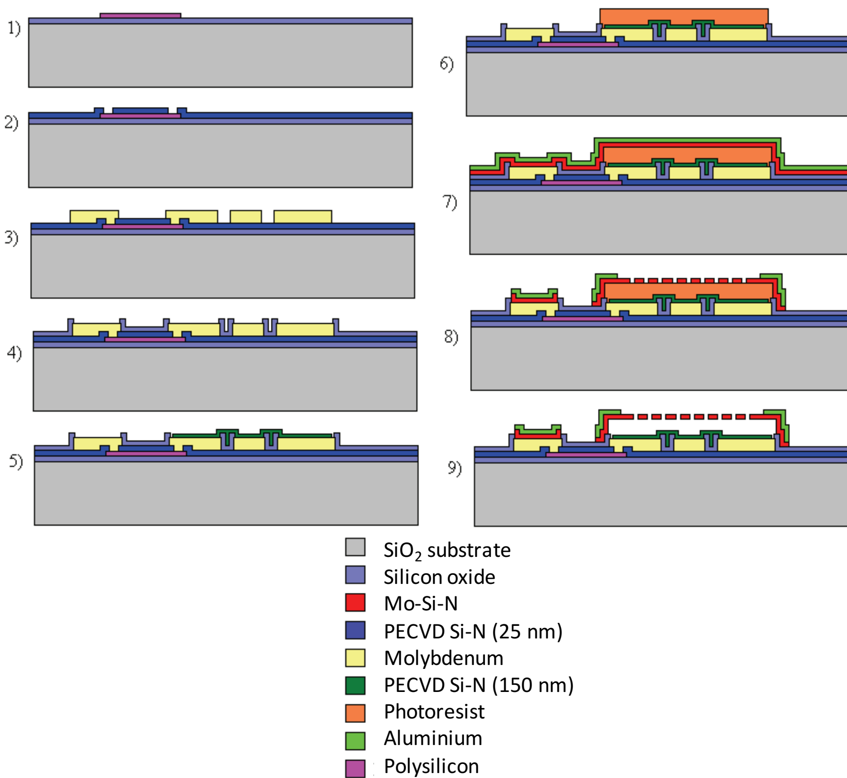

Figure 53. The device fabrication process A. 1) Polysilicon bias lines are processed on a fused silica substrate coated with low temperature oxide (LTO). 2) Bias contacts are opened via a thin PECVD Si-N film. 3) Molybdenum signal lines are processed. 4) The contacts to the signal lines are opened via a PECVD Si-O film. 5) A PECVD Si-N film is deposited and patterned for the dielectric layer. 6) The sacrificial layer is formed of photoresist. 7-8) Mo-Si-N and aluminium are sputter deposited and patterned for the structural and shunt layers. 9) Devices are released in oxygen plasma.

The purpose of the polysilicon stoppers in the device process B was to prevent ohmic contact between the electrodes in the down-state of capacitive devices without a dielectric layer. Typical stoppers were 2 µm in diameter and 600 nm in height. Concurrently, they served as anti-stiction structures. By means of the stoppers, the capacitors could be actuated beyond their pull-in point without yet touching. The stoppers made it possible to realise switched capacitors whose down-state capacitance as well as capacitance ratio were determined by the height of the stoppers. The bias lines and the stoppers can be made of one and the same polysilicon film if its thickness and resistivity are tuned suitable for both.

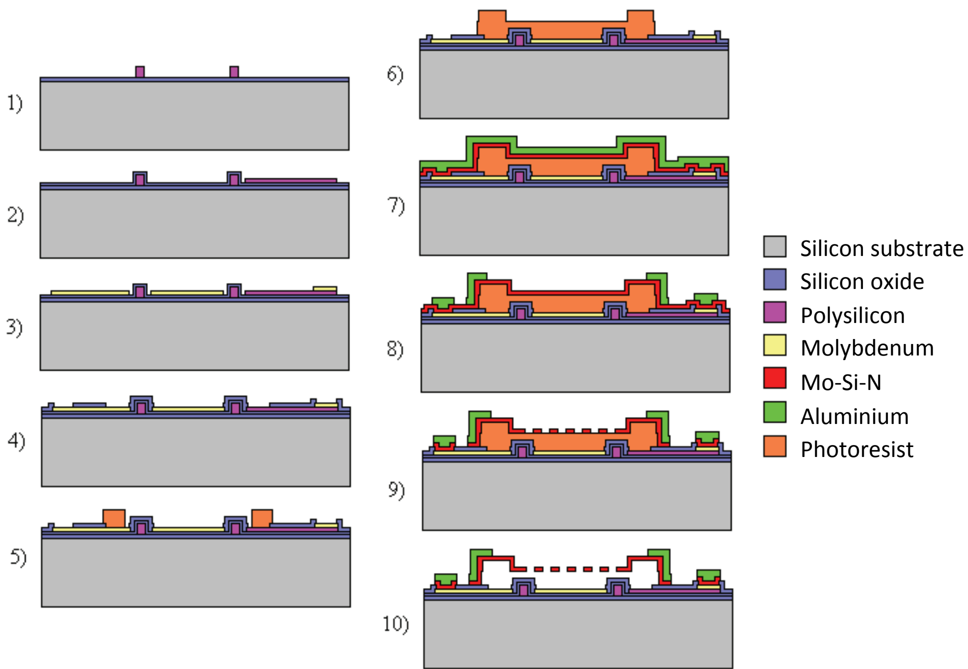

Figure 54. The device fabrication process B. 1) Polysilicon stoppers are processed on a fused silica substrate coated with LTO. 2) The stoppers are covered by another LTO film, on top of which polysilicon bias lines are processed. 3) Molybdenum signal lines are deposited and patterned. 4) The contacts to the signal lines are opened via a PECVD Si-O film serving also as the dielectric layer where needed. 5-6) A stepped sacrificial layer is formed of two photoresist coatings processed one on top of the other. 7) Mo-Si-N and aluminium are sputter deposited for the structural and shunt layers. 8) The aluminium film is patterned. 9) The Mo-Si-N film is patterned. 10) Devices are released in oxygen plasma.

The first metal layer (the signal lines) were made of molybdenum, that has a low resistivity as an elemental metal. The thickness was 300 nm. Molybdenum was preferred to aluminium because the latter tends to form hillocks even at 150°C. Optimally, RF MEMS devices would have highly conductive signal lines, requiring the use of thick metal films. The incorporation of such thick patterned coatings into a surface micromachining process may be challenging due to the resulting topography. These problems could be circumvented if the thick metal signal lines were buried in the substrate, accompanied by surface planarisation with chemical mechanical polishing (CMP). Because the emphasis was on the feasibility proof of Mo-Si-N films in MEMS, however, such buried signal lines were finally not realised in this initiative.

Table 38. The material layers of the device fabrication processes A and B (see Figure 53 and Figure 54 for graphical presentations).

Layer #	Device fabrication process A	Device fabrication process B
1	Fused silica (SiO_2) substrate (520 µm)	Fused silica (SiO_2) substrate (520 µm)
2	LTO (100 nm)	LTO (750 nm)
3	LPCVD polysilicon (120 nm)	LPCVD polysilicon (600 nm)
4	PECVD Si-N (25 nm)	LTO (100 nm)
5	Molybdenum (300 nm)	LPCVD polysilicon (120 nm)
6	PECVD Si-O (300 nm)	Molybdenum (300 nm)
7	PECVD Si-N (150 nm)	PECVD Si-O (200 nm)
8	Photoresist (1200 nm)	Photoresist #1 (1200 nm)
9	Mo-Si-N (450 nm)	Photoresist #2 (1200 nm)
10	Aluminium (1000 nm)	Mo-Si-N (400 nm)
11	-	Aluminium (1200 nm)

The dielectric layer was either a PECVD silicon nitride film of 150 nm, or a PECVD silicon oxide film of 200 nm. Capacitive devices with a dielectric layer between their electrodes can reach high capacitance ratios between the up- and down-states; on the other hand, dielectric layers often suffer from charging that may have a notable influence on the stability of the devices. Because of the latter, the above described polysilicon stoppers were included in the device process B, enabling the fabrication of dielectric-less capacitive devices with no ohmic contact in their down-state.

Because the deposition temperature of sputtered metal films is low, it was possible to have a polymeric sacrificial layer made of photoresist. In the case of the device process B, the capacitive tuning range was increased by the use of a stepped sacrificial layer like described in Section 6.1.2. The devices were released in low temperature oxygen plasma through the holes in the structural layer. Because such plasma release was not vulnerable to stiction, there was no need for supercritical drying. A further advantage of the plasma release was that the wafers could be diced prior to their release, avoiding the chance that fragile released MEMS structures would break during saw dicing.

Finally, Mo-Si-N films served as the structural layer. In most cases, they were accompanied by shunting aluminium films of higher conductivity. Mo-Si-N and aluminium could be deposited in the same sputtering system, one immediately after the other without breaking the vacuum in between. To pattern them separately, a selective etch chemistry was needed. The solution was to use 85% phosphoric acid (H_3PO_4) at 60ºC to etch aluminium on top of Mo-Si-N, since phosphoric acid etched Mo-Si-N slower than 2 nm/min. Mo-Si-N films were patterned in SF_6/O_2 plasma. Because the aluminium films contained 1% of silicon, some silicon residue remained on top of Mo-Si-N after etching the former in H_3PO_4. This residue did not seem to harm the devices. The silicon residue could not be removed by the Freckle etch (a

commercial etchant intended for the removal of residual silicon nodules after Al-Si etching) because it damaged the Mo-Si-N films. To pattern the aluminium films with holes being 2…3 μm in diameter, a short (1 minute) oxygen plasma treatment was needed prior to etching so as to start the wet etching in a reliable and repeatable manner. To reduce the underetching of aluminium films, it was tried to combine $BCl_3/Cl_2/CHCl_3/N_2$ plasma etching and H_3PO_4 wet etching. The approach was not successful, however, because the wet etching of small holes started very unevenly after the chlorine-based plasma. H_3PO_4 wet etching was needed as the final stage in order to have a good etch selectivity over the underlying Mo-Si-N films. The figures 55-57 below show MEMS bridges and devices fabricated by the above device processes and imaged through a microscope or by SEM.

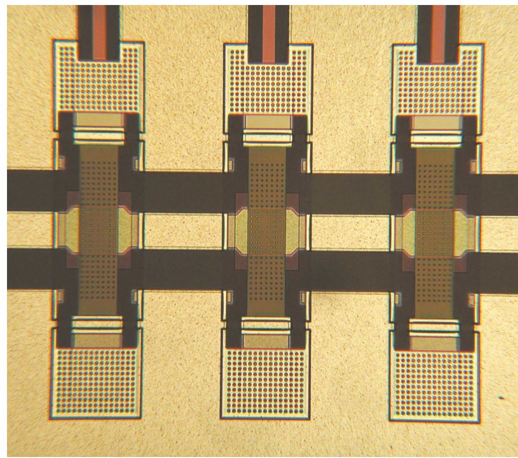

Figure 55. A microscope image of MEMS bridges made of Mo-Si-N (fabricated by the device process A). The width of the MEMS bridges was 60 μm.

If the above processes would be optimised for the needs of RF MEMS, they could be improved in the following terms: 1) lower electrical losses for the transmission lines and the structural layer, 2) a higher capacitance ratio for the digital varactors, 3) a technology for metal-to-metal contact switches, and 4) a technology for wafer level packaging. However, these objectives went beyond the main goal of this dissertation (to study the feasibility of Mo-N and Mo-Si-N films for MEMS) and were thus excluded.

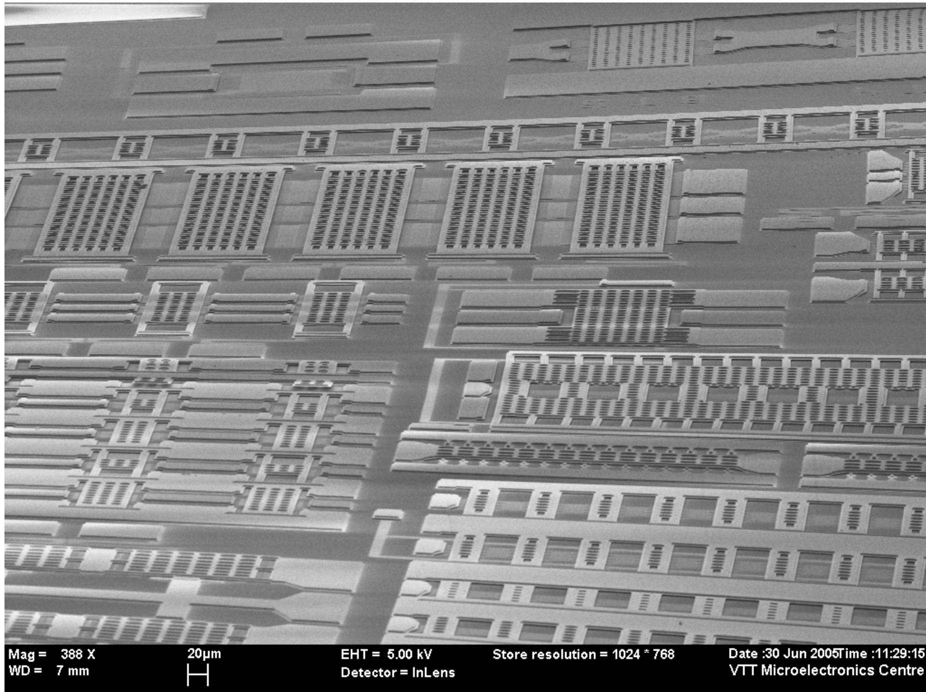

Figure 56. A SEM panorama of MEMS devices fabricated by the device process B.

In conclusion, amorphous metal micromachining is a low temperature process technology when actualised as above. As regards the device fabrication processes A and B, the LPCVD polysilicon bias lines and the polysilicon stoppers were the only parts fabricated above 450ºC. If needed, they both could be replaced with other materials deposited either by sputtering or PECVD. Further, they both were included so as to fabricate well functioning *RF MEMS* devices, not as intrinsic constituents of the amorphous metal micromachining itself. Owing to their low process temperature, amorphous metal MEMS devices could be integrated on top of IC (the MEMS post-processing approach [36]) in principal.

6.2.3 Performance

The performance of the RF MEMS devices fabricated with the above described processes is presented only in a limited manner because neither the RF design nor the device measurements were performed by the author. Few selected results are yet included in this thesis so as to provide a concrete proof of the feasibility of amorphous metal films in real MEMS devices.

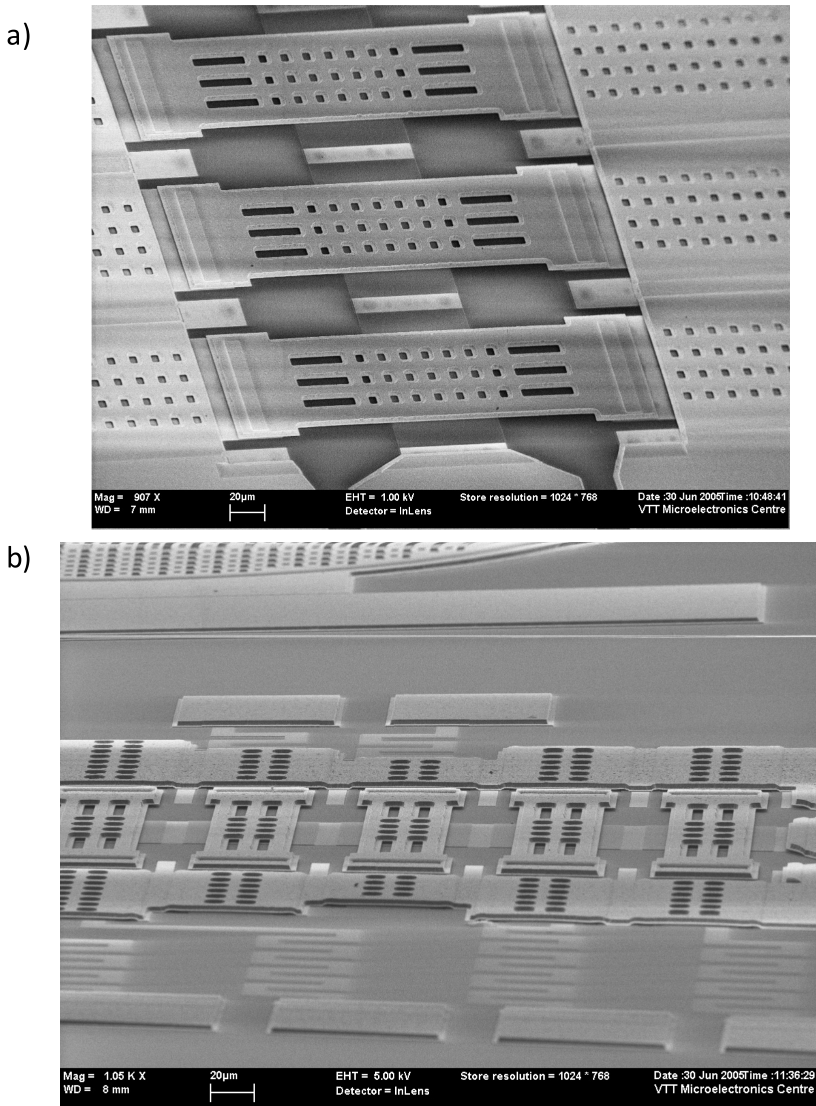

Figure 57. Two SEM images of MEMS devices fabricated by the device process B.

The first device was a varactor that comprised two MEMS bridges and a coplanar waveguide (CPW) as a transmission line (Figure 58). It was fabricated with the device process A (Figure 53). The associated physical measures and the circuit model parameters are listed in Table 39. The free-standing bridges connecting the ground planes functioned as a varactor between the RF signal and the ground. The bridges were matched inductively by using a distributed inductive matching technique similar to that used in distributed MEMS transmission lines (DMTL) [373]. The inductive

matching was realised with a high impedance transmission line having a characteristic impedance of 94 Ω.

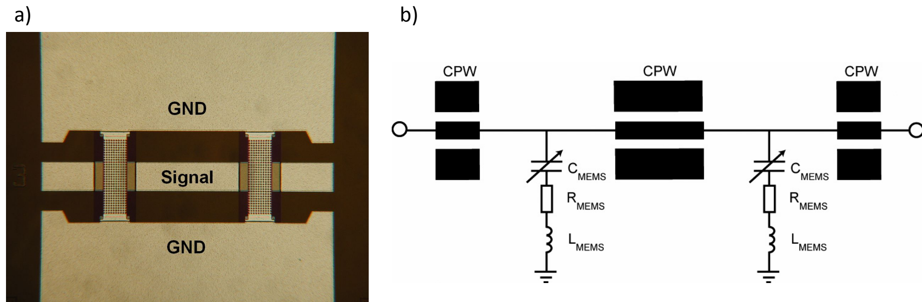

Figure 58. a) A microscope image of a fabricated bridge-type varactor. b) The circuit model for the bridge-type varactor (drawn up by Dr. Tauno Vähä-Heikkilä). C_{MEMS} = capacitance, R_{MEMS} = resistance, and L_{MEMS} = inductance of a MEMS bridge. Published previously in [8].

Table 39. A summary of the physical measures and the electrical parameters of the bridge-type varactor.

Physical measures	
Width of the centre conductor	100 µm
Distance between the centre conductor and the ground planes	100 µm
Total length of the device	960 µm
Structural layer	450 nm of Mo-Si-N + 1000 nm of Al
Dielectric layer	150 nm of PECVD silicon nitride
Height of the air gap	1.2 µm
Circuit model parameters of Figure 58b	
C_{MEMS}	60 fF
L_{MEMS}	9 pH
R_{MEMS}	0.9 Ω

On-wafer measurements up to 50 GHz were carried out for the device. The capacitance could be tuned about 30% in the analogue mode before pull-in. The devices with a structural layer of 450 nm Mo-Si-N had a pull-in voltage of 18 V, whereas the devices with a structural layer of 450 nm Mo-Si-N and 1000 nm aluminium had a pull-in voltage of 24 V. This indicates the stiffness and the spring constant of the bridges were mostly defined by Mo-Si-N. In the digital mode, the device had a capacitance ratio of 1:3 (120–360 fF) between the up- and down-states, which is a suitable range for tuneable RF MEMS circuits [374, 375]. Figure 59 shows the measured scattering (*S*-) parameters for the device between 0 and

50 GHz. The matching (S_{11}) in the up-state was better than -20 dB. The loss in the up-state was less than 0.2 dB up to 20 GHz, and less than 0.6 dB up to 50 GHz, including the loss from the contact resistance between the probe tip and the aluminium contact pads. The results are comparable to other CMOS compatible varactors and switches of that time operating at similar frequencies [48].

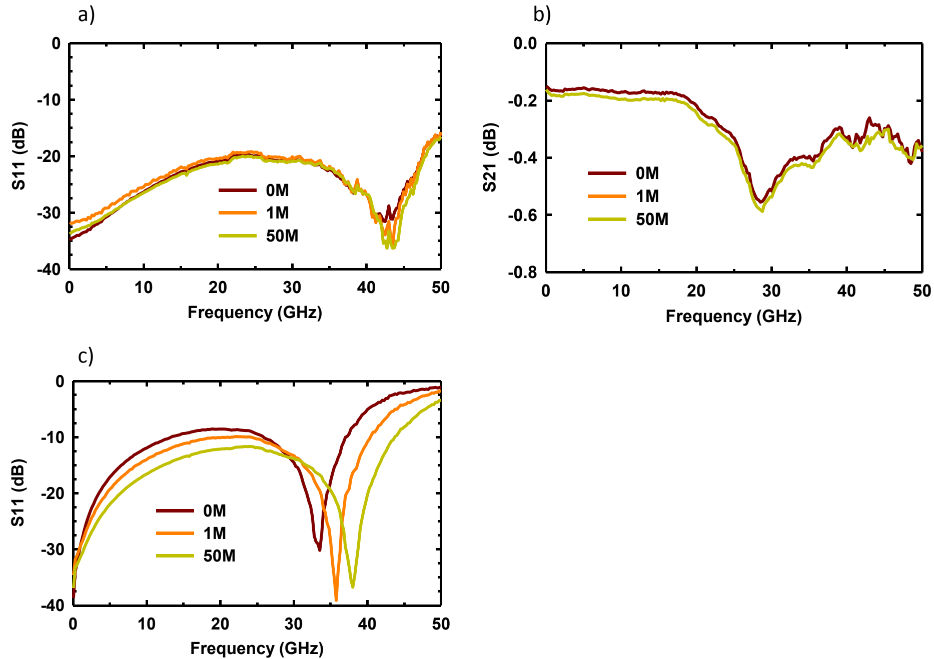

Figure 59. a) The measured S_{11} of the bridge-type varactor in the up-state at the beginning and after 1 million and 50 million up- and down-cycles. b) The measured S_{21} of the bridge-type varactor in the up-state at the beginning and after 1 million and 50 million up- and down-cycles. c) The measured S_{11} of the bridge-type varactor in the down-state at the beginning and after 1 million and 50 million up- and down-cycles. The measurements were performed by Dr. Tauno Vähä-Heikkilä. Published previously in [8].

Even if the measured capacitance ratio of 1:3 is suitable for many applications, it is rather low for digital-type RF MEMS devices [48]. The low capacitance ratio was probably mostly due to the roughness of the dielectric film and the layers underneath. In order to increase the ratio, either a surface treatment of the PECVD silicon nitride film or a choice of another high permittivity dielectric material should have been considered.

To investigate reliability, the bridge-type varactors were cycled between the up- and down-states at 100 Hz frequency. The *S*-parameters were measured at the beginning and after 1 million and 50 million cycles (Figure 59). The measurements were performed in a laboratory environment (not in a clean room) for non-packaged

devices with a standard probe station. The devices were fully operational after the test. No change in performance was observed in the up-state, meaning that the mechanical properties of the bridges were unchanged. The down-state capacitance decreased slightly during the cycling, which was mostly due to the charging of the PECVD silicon nitride film or impurities in the environment. The difference in the results included the differences in on-wafer calibration carried out between the measurements. The results show the robustness of the technology, and are comparable to other capacitive varactors and switches of that time [376].

The second device was designed for millimetre wave applications (Figure 60 and Table 40), and fabricated with the device process B (Figure 54). It can be used as a varactor or a phase shifter. In the design, the DMTL technique was applied. The device consisted of MEMS cantilevers anchored to the centre conductor of the CPW. By applying a voltage between the centre conductor and the ground planes, the capacitance between the RF signal and ground could be changed. The pull-in voltage of a MEMS cantilever was 45 V. Up to 110 GHz, the up-state matching (S_{11}) of this cantilever-type varactor was better than -25 dB, and the loss less than 1.2 dB (Figure 61). The up- and down-state capacitances for one cantilever were 6 fF and 20.5 fF, respectively. This resulted in a 90° phase shift at 86 GHz between the up- and down-states, showing that the device can be used as a phase shifting element in W-band (75–110 GHz) phased array antennas.

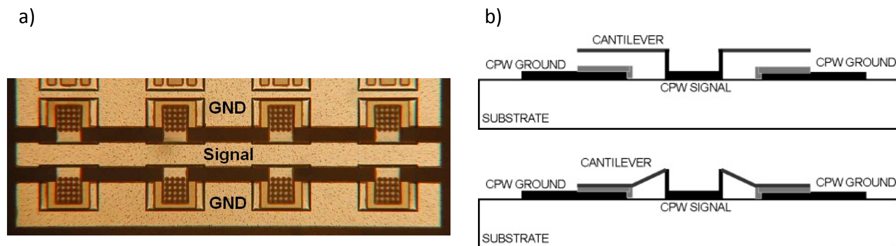

Figure 60. a) A photograph of a fabricated cantilever-type varactor. b) The schematic cross-section of the cantilever-type varactor in a CPW configuration in the up- and down-state positions (drawn by Dr. Tauno Vähä-Heikkilä). Published previously in [8].

Table 40. A summary of the physical measures of the cantilever-type varactor.

Physical measures	
Width of the centre conductor	40 µm
Distance between the centre conductor and the ground planes	20 µm
Number of cantilevers per device	8 (= 4 elements, each having 2 cantilevers)
Dimensions of a cantilever	40 µm × 55 µm
Overlapping area between a cantilever and the CPW ground	40 µm × 35 µm
Total length of the device	640 µm
Structural layer	400 nm of Mo-Si-N + 1200 nm of Al
Dielectric layer	200 nm of PECVD silicon oxide
Height of the air gap	2.4 µm

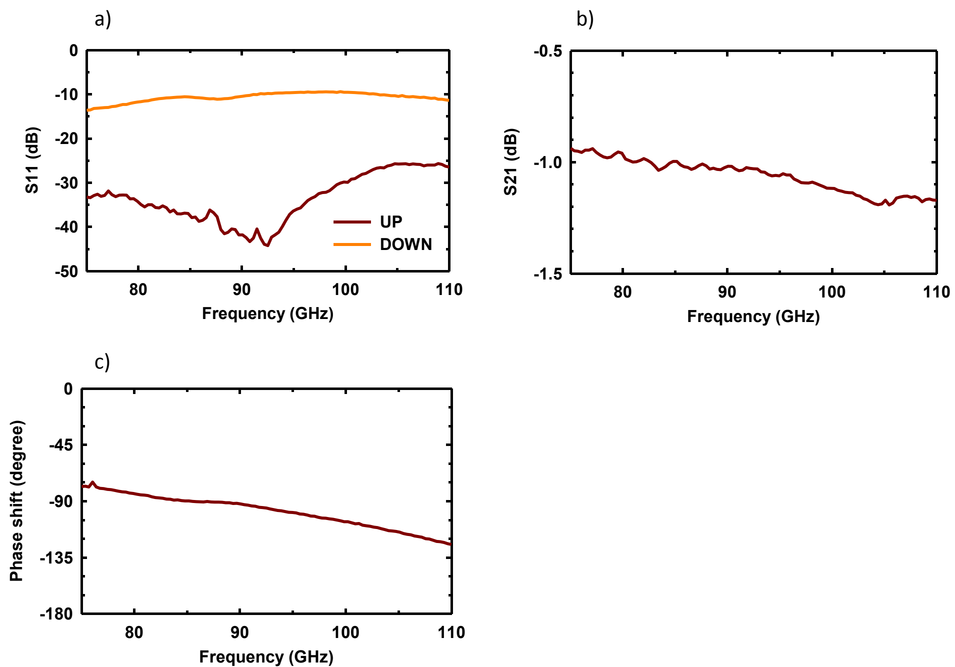

Figure 61. a) The measured S_{11} of the cantilever-type varactor in the up- and down-states. b) The measured S_{21} of the cantilever-type varactor in the up-state. c) The measured phase shift of the cantilever-type varactor between the up- and down-states. The measurements were performed by Dr. Tauno Vähä-Heikkilä. Published previously in [8].

The third device was a wideband distributed MEMS transmission line (DMTL) based on four switched MEMS capacitors (Figure 62 and Table 41) and operating at G-band (140–220 GHz). It was fabricated with almost the same process as the cantilever-type varactor above (the device process B) but *without* Mo-Si-N in the structural layer. Each of the four elements was equipped with separate bias control. The bias lines were made of high-resistivity polysilicon, and had a total series resistance of 20 kΩ at the least. Because each switched capacitor had two states (up and down), in total 16 different impedances could be established ($2^4 = 16$). The measured pull-in voltages of the switched capacitors varied between 4 and 5 V, while the capacitance ratio between the up- and down-states was about 1:3. The measured and fitted S_{11} for the four-element DMTL with switched capacitors in the up- and down-states as well as for an unloaded transmission line of an equal length are shown in Figure 63.

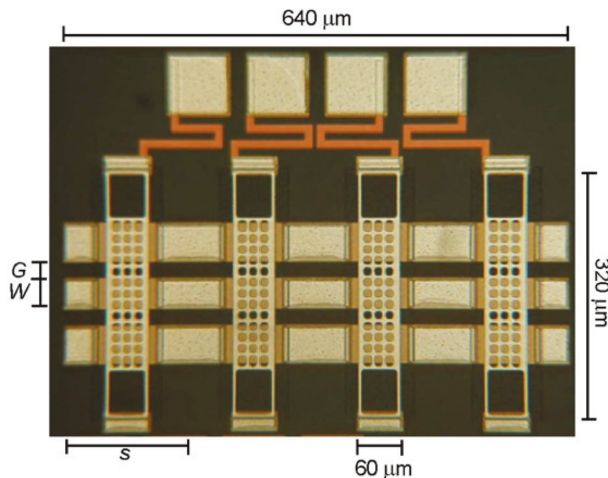

Figure 62. A photograph of a four-element DMTL based on switched MEMS capacitors. Published previously in [13] ©2008 IEEE.

At the time this four-element DMTL was demonstrated in 2008, it was apparently (as far as was known) the first electrically controllable MEMS device that was presented in public for frequencies above 110 GHz (between 140 and 220 GHz) [13]. This accomplishment was beaten in 2015 when Shah *et al.* reported on their MEMS phase shifter that operated between 500 and 600 GHz, citing our work as the preceding state-of-the-art [377, 378]. In general, this type of devices could be applied to millimeter-wave imaging systems involving electrically steerable phased- and reflect-array antennas. However, the case also pointed out how RF MEMS was not finally the optimal application field for the feasibility proof of amorphous Mo-N or Mo-Si-N films for MEMS: remarkable results were obtained even without them, al-

beit without a specific reliability study. The references [5, 9-12] are other publications presenting RF MEMS devices fabricated by the author with the above described processes.

Table 41. A summary of the physical measures of the DMTL based on four switched MEMS capacitors, and the fitted electrical parameters of a single MEMS capacitor. Q = quality factor. The RF design and the fitting were performed by Dr. Tauno Vähä-Heikkilä.

Physical measures of the four-element DMTL	
CPW conductor width (W in Figure 62)	40 µm
CPW gap width (G in Figure 62)	20 µm
Dimensions of a single capacitor	60 µm × 320 µm
Length of a single element	160 µm
Total length	640 µm
Structural layer	1200 nm of Al
Dielectric layer	200 nm of PECVD silicon oxide
Height of the air gap	1.2 µm
Fitted electrical parameters of a single MEMS capacitor	
C_{MEMS} in the up-state	9.5 fF
C_{MEMS} in the down-state	30 fF
L_{MEMS}	2 pH
R_{MEMS}	1.1 Ω
R_{BIAS}	> 20 kΩ
Q_{MEMS} in the up-state at 170 GHz	90
Q_{MEMS} in the down-state at 170 GHz	28

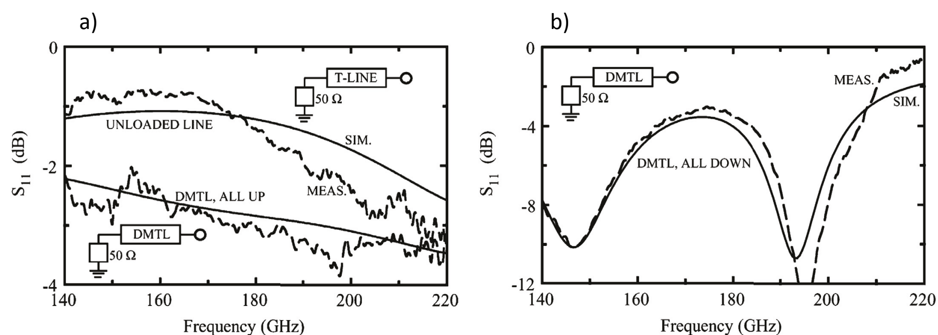

Figure 63. a) The measured and fitted S_{11} for the four-element DMTL with all switched MEMS capacitors in the up-state, and for an unloaded transmission line of an equal length (640 µm). b) The measured and fitted S_{11} for the four-element DMTL with all switched MEMS capacitors in the down-state. The one-port measurements were performed by Tauno Vähä-Heikkilä. Published previously in [13] ©2008 IEEE.

6.3 Thin film absorber for optical MEMS

6.3.1 Introduction

Optical spectrometers are widely used when the composition of a gas or a fluid must be measured. Such measurements are needed in industry, science, medicine, pharmacy, agriculture and biology with a wide range of applications [379]. Conventional spectrometers are bulky laboratory equipment with high performance and high cost. The demand for small-sized spectrometers for portable measuring devices and system integrated sensors has resulted in increasing interest in microspectrometers. A thermal infrared (IR) detector with sufficient absorption efficiency is a central part of many spectrometers. The operational principle of such detector is simple. First, incident radiation is absorbed. Second, the energy of the absorbed radiation is transformed into heat. Third, the consequent temperature change is measured. In order to achieve high sensitivity, high absorption efficiency combined with a small thermal mass is needed [380].

In general, infrared radiation absorbers can be divided into three groups: thin metallic films, porous metal blacks and thin film stacks [380]. Thin metallic films act as IR absorbers over a wide spectral range. Absorption of 50 % can be achieved [381, 382]. If a metal film is deposited on a solid substrate, however, its absorbing properties may be strongly dependent on the dielectric function of the substrate [382]. The metal black coatings are of e.g. gold or platinum. They are low-density deposits with a very porous structure. The metal blacks have been demonstrated to work as IR absorbers at wavelengths up to 50 µm, and they have a low thermal mass [383]. Due to their fragile nature, however, they may get easily crushed or displaced by any touch [384]. Hence, they cannot be patterned with lithography and etching. The metal black absorbers have also been reported to be sensitive to baking or changes in relative humidity, and to suffer from aging phenomena [383]. There are several studies on the third absorber group, the thin film stacks. The reported approaches include e.g. the use of the passivation layers of a CMOS process for an integrated absorber [385, 386], thin metals with a dielectric spacer [381, 387], and a blackbody structure consisting of thin Si-N, Mo and amorphous silicon films [388]. Also IR absorbers based on highly boron doped silicon slabs have been proposed [389]. The silicon slabs work simultaneously as heat spreaders but, on the other hand, their thermal mass is large resulting in low response time.

The absorbers realised here were based on thin film stacks because of their high performance together with feasible integration into MEMS. Two absorber structures are presented: one for visible and near-infrared (NIR) wavelengths (350…1000 nm), the other for the short-wavelength infrared (SWIR) spectrum (1200…2000 nm). Besides Mo-Si-N films, the absorbers employed Al_2O_3 films fabricated by ALD, which is a CVD technique suitable for the fabrication of inorganic thin films at rather low temperatures. It is based on the sequential use of self-terminating gas-solid reactions which result in material layers with thickness down to a fraction of a monolayer

[390]. The advantages include precise thickness control as well as very high uniformity and conformity of the deposited films [391]. The dispersion of the refractive index of amorphous Mo-Si-N films, essential for designing absorbers, was reported already in Section 5.4.

6.3.2 Experimental procedure

The Mo-Si-N films were deposited by the standard 150 mm sputtering process at Provac LLS 801 sputtering system (described in Table 34). The Al_2O_3 films were prepared in a SUNALE^{TM} R150 ALD reactor manufactured by Picosun. It was a showerhead-type reactor where the reactant gases enter the reaction space from above the substrate. A trimethylaluminium/water ($AlMe_3/H_2O$) process at 300ºC was used for the deposition. Nitrogen served both as the purging gas and the carrier gas for the $AlMe_3$ and H_2O reactants. After loading a sample, the reactor was purged with nitrogen by three refilling – evacuation cycles. Before starting a process run, the chamber and the wafer were allowed to stabilise at the process temperature for about 20 minutes. A deposition process of 5000 cycles resulted in a film whose thickness was 473 nm. Each reaction cycle consisted of a trimethylaluminium pulse, nitrogen purge, a water pulse, and another nitrogen purge.

Two kinds of absorber structures were fabricated, one for the wavelength range of 350…1000 nm (Absorber VIS/NIR), the other for 1200…2000 nm (Absorber SWIR). Polished silicon wafers served as substrates. The wafers were cleaned with SC-1 before their use. The absorbers were based on thin film stacks of four different layers like defined by Table 42. Besides the Al_2O_3 and Mo-Si-N films, they included conventional Mo and Si-N films. The molybdenum films were deposited by sputtering, and the Si-N films by PECVD. The appropriate value for the thickness of each film was calculated with TFCalc thin film design software (a product of Software Spectra, Inc.).

Table 42. The specification of the thin film stacks that composed the absorbers. The absorber VIS/NIR was designed for wavelengths of 350…1000 nm, and the absorber SWIR for wavelengths of 1200…2000 nm.

Layer #	**Absorber VIS/NIR**			**Absorber SWIR**		
	Material	**Thickness (nm)**	**Deposition method**	**Material**	**Thickness (nm)**	**Deposition method**
1	Mo	275	Sputtering	Mo	100	Sputtering
2	Al_2O_3	38	ALD	Si-N	40	PECVD
3	Mo-Si-N	14	Sputtering	Mo-Si-N	42	Sputtering
4	Al_2O_3	60	ALD	Si-N	169	PECVD

The reflectance measurements of the thin film absorbers were made with spectroscopic reflectometry and transfer standard spectrometry. The wavelength regions

for the measurements were 350...1650 nm (spectroscopic reflectometry), and 400...2000 nm (transfer standard spectrometry).

The thin film stack of Absorber SWIR can be patterned with plasma etching by the use of SF_6/He chemistry for the Si-N and Mo-Si-N films, and $CF_4/Cl_2/O_2$ chemistry for the Mo film.

6.3.3 Results

On the basis of the known refractive indices, the structures of two absorbers were optimised with the help of a simulation software (TFCalc). After the absorbers were fabricated, their reflectance spectra were measured (Figure 64). The absorption on the *y* axes of the graphs was calculated assuming $A(\lambda) = 1 - R(\lambda)$ where $A(\lambda)$ is the absorption and $R(\lambda)$ the reflection as functions of the wavelength λ. It was assumed that no transmission through the structures occurred because the molybdenum films at the bottom of the structures were fairly thick.

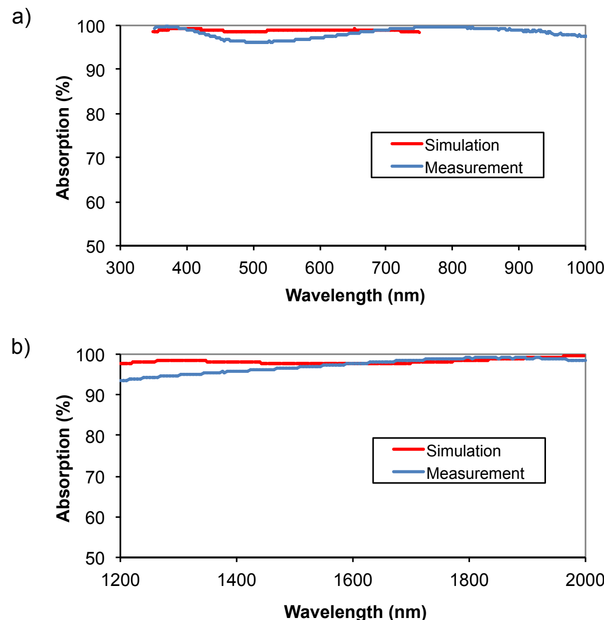

Figure 64. The simulated and measured absorption spectra of (a) Absorber VIS/NIR designed to work at wavelengths of 350…1000 nm, and (b) Absorber SWIR designed to work at wavelengths of 1200…2000 nm. Published previously in [14] and [15].

The graphs of Figure 64 show that both absorbers were broadband. The absorption was higher than 96 % for Absorber VIS/NIR, and higher than 93 % for Absorber

SWIR over the whole spectra of interest. For Absorber VIS/NIR, the absorption fluctuated between few local minima and maxima at wavelengths below 350 nm, while it decreased smoothly and slowly at wavelengths above 1000 nm. For example, the absorption was still 89.9 % at 1200 nm. For Absorber SWIR, a small deviation of the measured data from the simulated one occurred at the lower end of the spectrum but the absorption yet remained well above 90 % even at its worst. For understanding the reason behind the small deviation, the roughness of a Mo-Si-N film of about 40 nm (the same thickness as in the absorber structure) was measured by AFM. The AFM scan proved, however, that the film was very smooth with the root mean square (RMS) value of just few ångströms. Thus the surface roughness of Mo-Si-N films could not be the reason for the deviation. Instead, simulations revealed that the absorption is rather sensitive to the thickness tolerances of thin film depositions. In conclusion, the deviations between the simulated and measured data in Figure 64 are likely a consequence of thickness inaccuracy of one or more of the constituent films.

In conclusion, both absorbers were broadband with absorptions well above 90 % over the whole spectra of interest. The absorbers may find practical use in MEMS thermopiles, bolometers and pyranometers.

7. Conclusions and outlook

The interest in the amorphous metal films for the structural MEMS material originated from the exceptionally high elasticity of bulk amorphous metals. Such high elasticity would be an attractive feature to many MEMS applications if the process integration was feasible. In short, the purpose of this thesis was to introduce amorphous molybdenum-based thin films as an alternative material choice to surface micromachining, which is still often based on silicon technology.

Elemental metal films are practically always polycrystalline and may suffer from anisotropic residual stresses, which is disadvantageous to MEMS applications. To obtain an amorphous microstructure, metals must be alloyed. The elemental molybdenum films were amorphised first by nitrogen, leading to Mo-N films. Since their amorphisation was incomplete, silicon was added, leading to Mo-Si-N films. The latter belong to the so called *mictamict* alloys, which are ternary thin films of the generic composition (early transition metal)–Si–(nitrogen or oxygen). To constitute the necessary background for the experimental part of this work and, additionally, to provide a more generic reference supporting their use in MEMS, the thesis reviewed both mictamict, Mo-N and Mo-Si-N films in detail.

The Mo-N and Mo-Si-N films were deposited by reactive sputtering. Sputtering is a common deposition method in IC and MEMS fabs, and benefits from low deposition temperature. The deposition of the structural layer close to room temperature enables the use of a polymeric sacrificial layer which, in turn, enables the release etching of MEMS structures in oxygen plasma. The low temperature O_2 plasma is gentle to almost any MEMS material, allowing a broad material selection during the release phase, unlike the aggressive HF based chemistries that are conventionally used for the removal of silicon oxide sacrificial layers. Another advantage of the plasma release is that stiction problems are usually avoided.

Both Mo-N and Mo-Si-N films were characterised for their deposition and etch rates, composition, resistivity and residual stress. In addition, the Mo-Si-N films were characterised for their microstructure, surface roughness, elastic modulus, hardness, elastic recovery, coefficient of thermal expansion, temperature coefficient of resistance and complex refractive index. The deposition and patterning of both films are mastered well, being crucial to their use in MEMS. It was found that these amorphous Mo-Si-N films have resistivity of 1…2 mΩcm, and their residual stress can be tuned to low tensile values (around 100 MPa) by the sputtering pressure.

The thermal stability of the above films was studied in particular. The first signs of oxidation were observed at 350°C, and structural changes even below. These findings contradicted the initial assumptions and prevailing knowledge of that time, stating that Mo-Si-N films, as a member of the mictamict alloys, would have high structural metastability upon thermal annealing as well as good oxidation resistance up to 800°C. It was concluded that the unexpectedly low thermal stability of our Mo-Si-N films probably stems from their low silicon content. However, it is possible to prevent the unsealing surface oxidation of Mo-N and Mo-Si-N films by a thin protective silicon cap on top of them. The residual stress of the Mo-Si-N films sputtered from separate Mo and Si targets depends on the post-deposition annealing temperature, while the Mo-Si-N films sputtered from a Mo_5Si_3 compound target are more resistant to annealing-induced structural changes, experiencing only a minor (if any) change in the residual stress up to 400°C, which was the highest temperature studied herein.

The Mo-Si-N films were studied also at low (cryogenic) temperatures. No transition into a superconductive state was observed down to 80 mK. The nanoscale Mo-Si-N wires did not exhibit non-linear size dependence down to a width of 20 nm and thickness of 25 nm, indicating that they could be used in nanoelectronic structures.

Although the materials characterisation constituted a substantial part of this work, a key objective was to move forward to MEMS process integration and real MEMS devices. By the end of this study, surface micromachined MEMS devices with amorphous Mo-Si-N films as their structural layer were demonstrated. The capacitive RF MEMS devices operated at frequencies up to 110 GHz, and were fully functional after the actuation of 50 million cycles between the up- and down-states of their MEMS bridges. The fabrication of stepped and corrugated membranes was demonstrated concurrently. Mo-Si-N films were also applied to thin film absorbers that were designed for the visible and near-infrared wavelengths (350…2000 nm), and that can be easily integrated into MEMS devices. The absorption was measured to be higher than 93 % over the whole spectrum of interest.

Although this study was inspired by the bulk amorphous metals, neither Mo-N nor Mo-Si-N belongs to the BMGs as such. The sputter deposition of Mo-N and Mo-Si-N films is somewhat simpler than that of TFMGs, because Mo, Si, $MoSi_2$ and Mo_5Si_3 sputtering targets are readily available, and the control of the chemical composition of Mo-N and Mo-Si-N films is relatively easy. In addition, these molybdenum-based films are IC compatible, unlike the common metallic glasses. The MEMS process integration of Mo-N and Mo-Si-N films is straightforward since they can be patterned by the standard photolithography and the etch chemistries commonly found in IC and MEMS fabs. This is contrary to the metallic glasses that are formed into micro- and nanostructures by more specialised methods such as thermoplastic forming and nanoimprinting lithography. The upper limits for the service temperature are comparable, as the glass transition temperatures of many BMGs fall between 200 and 450°C [42], coinciding by chance the onset temperatures of the structural changes and surface oxidation of the Mo-N and Mo-Si-N synthesised here.

The conventional and well-established polysilicon technology is an obvious and nearly overwhelming competitor of the Mo-N and Mo-Si-N films but, nonetheless, these amorphous metal films could challenge polysilicon in some MEMS applications. The deposition temperature is a primary difference: while Mo-N and Mo-Si-N can be sputter deposited close to room temperature, LPCVD silicon usually requires 570…610°C and PECVD silicon around 300°C for deposition. In addition, the dopant activation of silicon films needs even higher temperatures, 800°C or above. On the other hand, polysilicon films are stable at notably higher temperatures than Mo-N and Mo-Si-N. The conductivity of even heavily doped polysilicon can only just reach that of Mo-Si-N films (1…2 mΩcm in this study) but not that of Mo-N films (here 120 μΩcm). The residual stress of both polysilicon and Mo-Si-N films can be tuned suitable for MEMS, i.e. to have homogeneous tensile stress of a desired value, but they both are also highly dependent on the deposition and annealing parameters. In surface micromachining, polysilicon structural layers are paired with silicon oxide as the sacrificial layer, whereas the use of polymeric sacrificial layers is possible in the case of Mo-N and Mo-Si-N films. The advantages of the latter were discussed already above.

Aluminium, gold, copper and nickel are metals that are frequently used as the structural layer in MEMS. Amongst them, only aluminium is considered IC compatible similar to Mo-N and Mo-Si-N. However, aluminium films suffer e.g. from poor mechanical stability as well as hillock formation already around 100°C. In consequence, even though the Mo-N and Mo-Si-N films are prone to structural changes and surface oxidation below 400°C, their thermal stability is still superior to aluminium.

All things considered, the Ti-Al alloys used in Texas Instruments' digital micromirrors and Fraunhofer's CMUTs are probably the closest counterpart of the Mo-N and Mo-Si-N films, sharing a considerable number of similarities with each other. The Ti-Al films are amorphous and deposited by sputtering, their residual stress can be controlled, and they are used together with polymeric sacrificial layers [20, 119, 125]. All this is common to Mo-N and Mo-Si-N. Moreover, Elsaesser *et al.* have reported that annealing above 170°C induced an irreversible stress shift in Ti-Al films [125], indicating structural changes at similar temperatures to Mo-N and Mo-Si-N.

Regarding the materials characterisation, the current study could be still extended to properties such as the elastic strain limit and tensile strength, or the investigation of a possible short- or medium-range structural order similar to BMGs. A highly systematic chemical and structural characterisation of our Mo-Si-N films throughout the whole ternary system could still enhance the understanding of these films. The study of the thermal stability of Mo-Si-N films could be completed by producing a set of Mo-Si-N films with different elemental contents, extending again throughout the ternary system, and by experimenting these samples preferably by means of thermogravimetry. This would finally confirm (or reject) the prevailing conclusion that the unexpectedly low thermal stability of our Mo-Si-N films was caused by their low silicon content. The original definition of the mictamict alloys encompassed "ternary thin films of the generic composition (early transition metal)–Si–

(nitrogen or oxygen) that have an amorphous or near-amorphous structure and are highly resistant to crystallisation upon thermal annealing", and regarded Mo-Si-N films as their express representatives [140]. This definition could be clarified with a remark that an amorphous microstructure of such a ternary film does not guarantee the film possesses high thermal stability, as this study proved.

Regarding the applications in MEMS and nanotechnology, Mo-N films could be studied for their superconductivity and potential low temperature applications, bearing in mind that the critical temperature may be strongly dependent on the stoichiometry. Although the hermetic sealing of Mo-N and Mo-Si-N membranes remained undemonstrated here, there is no fundamental reason why a practical solution could not be found, broadening the range of MEMS applications that could benefit from these materials. The concrete demonstration of the monolithic integration of the amorphous metal MEMS and IC was also excluded but it is readily conceivable due to the low process temperatures, with the approach of MEMS post-processing on top of IC electronics. RF MEMS was not finally an optimal application field for the feasibility demonstration of amorphous metal films in MEMS, even though fully functional devices with well satisfactory performance were fabricated. Because the resistivity of Mo-Si-N films was too high for RF applications to be used as such, they were always combined with more conductive materials like aluminium. Although the mechanical properties of Mo-Si-N films were most likely superior to those of aluminium, also aluminium structures survived repetitive mechanical switching in a sufficient manner. To fully exploit the best features of Mo-N or Mo-Si-N films, they should serve as the structural layer of such MEMS devices that necessitate a low processing temperature and excellent mechanical properties. These amorphous molybdenum-based films are thus still lacking their "killer application" to break through in the MEMS market, similar to the Ti-Al alloy used in digital micromirrors.

While this thesis was written as a monograph, a major part of this work has been already published in [1-16]. This gives an opportunity to review how the findings have been utilised or cited by others so far. Schmidt *et al.* recognise Mo-Si-N films as an option for the structural material for the monolithic integration of MEMS on CMOS while advancing their Ti-Al films for the same purpose [392, 393]. Also Lin *et al.* refer to our work when suggesting amorphous metals for a mechanical material in MEMS [394], and Atuchin *et al.* [359] and Liu *et al.* [227] regarding the material properties of Mo-N and Mo-Si-N films. The journal article on the multilayer IR absorbers [15] has been cited by Heo *et al.* [395], Ma *et al.* [396, 397] and Oishi *et al.* [398] in their reviews of infrared detection. However, most citations relate to the work on the RF MEMS devices [377, 378, 399-411]. Debogovic *et al.* [400], Malmqvist *et al.* [407], Ouacha *et al.* [408] and Perruisseau-Carrier *et al.* [409, 410] used the metal micromachining process developed within this work to realise their RF MEMS designs in practice. Citations [377, 378, 401, 405, 406] recognise the work on the G-band (140…220 GHz) MEMS devices, while [404] and [411] refer to the availability of the CMOS compatible fabrication process suitable for RF MEMS. These citations, however, do not have interest in Mo-Si-N films but the RF MEMS designs the micromachining process has enabled, often without much consideration to the fabrication details. Besides the above, the findings on Mo-N and Mo-Si-N films

have been utilised within some in-house R&D projects, but without public references.

This thesis, together with the publications [1-16], has presented a wide-ranging characterisation of sputter-deposited Mo-N and Mo-Si-N films to facilitate their use in MEMS. It has elaborated the understanding of the thermal stability of Mo-Si-N films, which has been discussed previously only by a limited number of studies. To the best of the author's knowledge, there are no other reports presenting the dispersion of the complex refractive index of Mo-Si-N films, or providing an extensive set of their etch rates in public. This is apparently the first time a functioning MEMS process based on Mo-Si-N films as the structural layer has been presented. Furthermore, when the four-element G-band distributed MEMS transmission line (DMTL) component utilising the metal micromachining process of this work was published in 2008, it was apparently the first electrically controllable MEMS device working at frequencies above 110 GHz (between 140 and 220 GHz) [13]. Shah *et al.* reported they beat this accomplishment only in 2015, citing our work as the preceding state-of-the-art [377, 378].

In conclusion, the amorphous Mo-N and Mo-Si-N films of this study are suitable for several kinds of MEMS devices on condition that they are not exposed to increased temperatures in an oxidising atmosphere without a protective silicon cap. Their integration with conventional MEMS processes is convenient, as they can be deposited by sputtering and patterned with common dry and wet etch chemistries. The demonstrated MEMS fabrication process was CMOS compatible. The low process temperature enables the use of a polymeric sacrificial layer and provides an opportunity for the monolithic integration of MEMS and CMOS.

References

1 Kattelus, H., Heikkinen, H., Häärä, A., Ylönen, M. & Tolkki, A. A batch process to deposit amorphous metallic Mo-Si-N films. Proceedings of 4th International Conference on Materials for Microelectronics and Nanoengineering, MFMN 2002. 10-12 June 2002, Espoo, Finland. IOM Communications Ltd. (2002) 125-128.

2 Kattelus, H., Heikkinen, H., Häärä, A., Ylönen, M. & Tolkki, A. A batch process to deposit amorphous metallic Mo-Si-N films. Journal of Materials Science: Materials in Electronics 14 (5) (2003) 427-430.

3 Ylönen, M., Kattelus, H., Savin, A., Kivinen, P., Haatainen, T. & Ahopelto, J. Potential of amorphous Mo-Si-N films for nanoelectronic applications. Microelectronic Engineering 70 (2-4) (2003) 337-340.

4 Kattelus, H., Ylönen, M. & Blomberg, M. Characterization of amorphous electrically conductive Mo-Si-N films for micromechanical applications. Proceedings of the International Conference on Advanced Technology in Experimental Mechanics 2003 (ATEM'03). 10-12 September 2003, Nagoya, Japan. The Japan Society of Mechanical Engineers (JSME-MMD) (2003) 5 pp.

5 Kattelus, H., Ylönen, M. & Vähä-Heikkilä, T. Amorphous metals for RF MEMS. VTT Symposium 235, URSI/IEEE XXIX Convention on Radio Science. 1-2 November 2004, Espoo, Finland. VTT (2004).

6 Kattelus, H., Ylönen, M. & Blomberg, M. Amorphous Mo-N and Mo-Si-N films in microelectromechanical systems. Fatigue & Fracture of Engineering Materials & Structures 28 (2005) 743-749.

7 Ylönen, M., Vähä-Heikkilä, T. & Kattelus, H. Amorphous metal alloy based MEMS for RF applications. Proceedings of the Eurosensors XIX conference. 11-14 September 2005, Barcelona, Spain (2005) TC22.

8 Ylönen, M., Vähä-Heikkilä, T. & Kattelus, H. Amorphous metal alloy based MEMS for RF applications. Sensors and Actuators A 132 (1) (2006) 283-288.

9 Vähä-Heikkilä, T., Ylönen, M. & Kattelus, H. CMOS compatible MEMS varactors for millimeter waves. Proceedings of The 4th ESA Workshop on Millimetre Wave Technology and Applications, The 8th Topical Symposium

on Millimeter Waves – TSMMW2006, The 7th MINT Millimeter-Wave International Symposium – MINT-MIS2006. 15-17 February 2006, Espoo, Finland. ESA, Millilab, NiCT, MINT (2006) 527-531.

10 Vähä-Heikkilä, T. & Ylönen, M. Highly reliable wideband switched MEMS capacitors. Proceedings of The MEMSWAVE 2006. The 7th International Conference on RF MEMS and RF Microsystems. 27-30 June 2006, Orvieto, Italy (2006) 172-174.

11 Vähä-Heikkilä, T. & Ylönen, M. CMOS compatible switched MEMS capacitors up to 220 GHz applications. Proceedings of The 36th European Microwave Conference, EuMC 2006. 10-15 September 2006, Manchester, UK. Institute of Electrical and Electronics Engineers Computer Society (2006) 1060-1063.

12 Vähä-Heikkilä, T., Ylönen, M. & Kattelus, H. Microwave and millimeter wave MEMS components and circuits based on CMOS compatible fabrication. Proceedings of The Mediterranean Microwave Symposium 2006. 18-21 September 2006, Genova, Italy (2006) 1798-1801.

13 Vähä-Heikkilä, T. & Ylönen, M. G-band distributed microelectromechanical components based on CMOS compatible fabrication. IEEE Transactions on Microwave Theory and Techniques 56 (3) (2008) 720-728.

14 Laamanen, M., Blomberg, M., Puurunen, R., Miranto, A. & Kattelus, H. Thin film absorbers for visible, near-infrared, and short-wavelength infrared spectra. Proceedings of the Eurosensors XXIII conference. Procedia Chemistry 1 (1) (2009) 393-396.

15 Laamanen, M., Blomberg, M., Puurunen, R., Miranto, A. & Kattelus, H. Thin film absorbers for visible, near-infrared, and short-wavelength infrared spectra. Sensors and Actuators A 162 (2) (2010) 210-214.

16 Kiihamäki, J., Kattelus, H., Blomberg, M., Puurunen, R., Laamanen, M., Pekko, P., Saarilahti, J., Ritala, H. & Rissanen, A. Low-temperature processes for MEMS device fabrication. In: Gusev, E., Garfunkel, E. & Dideikin, A. (ed.). Advanced Materials and Technologies for Micro/Nano-Devices, Sensors and Actuators. Springer Netherlands (2010) 167-178.

17 Ryhänen, T. Impact of silicon MEMS – 30 years after. In: Lindroos, V., Tilli, M., Lehto, A. & Motooka, T. (ed.). Handbook of silicon based MEMS materials and technologies. United Kingdom: Elsevier, 2010. 1st edition. 636 p. ISBN 978-0-8155-1594-4.

18 Mounier, E. Future of MEMS: A market & technologies perspective. SEMI MEMS Tech Seminar. 23 September 2014, Milan, Italy (2014). Available: http://www.semi.org/eu/node/8791 (6.8.2015).

19 Stasiak, J., Richards, S. & Angelos, S. Hewlett Packard's inkjet MEMS technology: past, present, and future. In: George, T., Saif Islam, M. & Dutta, A.K. (ed.) Micro- and nanotechnology sensors, systems, and applications. Proceedings of SPIE 7318, 73180U (2009).

20 Tregilgas, J. Amorphous hinge material. Advanced Materials & Processes (January 2005) 46-49.

21 Kaajakari, V. Practical MEMS. USA: Small Gear Publishing, 2009. 465 p. ISBN 978-0-9822991-0-4.

22 mstnews, International newsletter on MICROSYSTEMS and MEMS. No. 4/02, September 2002. Main topic: Technologies and markets forecasts. Publisher: VDI/VDE – Technologiezentrum Informationstechnik GmbH (VDI/VDE-IT) (2002) 48 p.

23 Salomon, P. Microsensors and microsystems – World wide markets and economic impact. Proceedings of 20th Eurosensors Conference. 17-20 September 2006, Göteborg, Sweden (2006) 30-31.

24 Bouchaud, J. High value MEMS market overview. Symposium on Design, Test, Integration & Packaging of MEMS/MOEMS (DTIP). 11-13 May 2011, Aix-en-Provence, France (2011).

25 Manners, D. MEMS market grew 17% in 2011, says Yole. Electronics-Weekly.com, 27 March 2012. Available: http://www.electronicsweekly.com/news/ manufacturing/mems-market-grew-17-in-2011-says-yole-2012-03/ (6.8.2015).

26 Yole Développement (publisher). Challenged by newcomers proposing low-cost solutions, established MEMS companies must develop new strategies. Press release 30.7.2014. Available: http://www.yole.fr/MEMS-Market-MIS.aspx#. VcMUM3jB6fS (6.8.2015).

27 Amorphous metals. Materials Research Science and Engineering Center, University of Wisconsin, Madison, USA. Available: http://education.mrsec.wisc.edu/141.htm (6.8.2015)

28 Inoue, A. & Takeuchi, A. Recent developments and application products of bulk glassy alloys. Acta Materialia 59 (2011) 2243-2267.

29 Nicolet, M.-A., Suni, I. & Finetti, M. Amorphous metallic alloys in semiconductor contact metallizations. Solid State Technology 26 (12) (1983) 129-133.

30 Kattelus, H., Koskenala, J., Nurmela, A. & Niskanen, A. Stress control of sputter-deposited Mo-N films for micromechanical applications. Microelectronic Engineering 60 (2002) 97-105.

31 Ohring, M. Materials science of thin films – Deposition and structure. USA: Academic Press, 2002. 2nd edition. 794 p. ISBN 0-12-524975-6.

32 Wolf, S. & Tauber, R.N. Silicon processing for the VLSI era. Volume 1: Process technology. USA: Lattice Press, 2000. 2nd edition. ISBN 0-9616721-6-1.

33 Madou, M.J. Fundamentals of microfabrication and nanotechnology. Volume I: Solid-state physics, fluidics, and analytical techniques in micro- and nanotechnology. USA: CRC Press, Taylor & Francis Group, 2011. 3rd edition. 641 p. ISBN 978-1-4200-5511-5.

34 Madou, M.J. Fundamentals of microfabrication and nanotechnology. Volume II: Manufacturing techniques for microfabrication and nanotechnology. USA: CRC Press, Taylor & Francis Group, 2011. 3rd edition. 656 p. ISBN 978-1-4200-5519-1.

35 Madou, M.J. Fundamentals of microfabrication and nanotechnology. Volume III: From MEMS to bio-MEMS and bio-NEMS – Manufacturing techniques and applications. USA: CRC Press, Taylor & Francis Group, 2011. 3rd edition. 636 p. ISBN 978-1-4200-5516-0.

36 Franssila, S. Introduction to microfabrication. United Kingdom: John Wiley & Sons, Ltd., 2010. 2nd edition. 518 p. ISBN 978-0-470-74983-8.

37 Schroder, D.K. Semiconductor material and device characterization. USA: John Wiley & Sons, Inc., 2006. 3rd edition. 779 p. ISBN-13: 978-0-471-73906-7, ISBN-10: 0-471-73906-5.

38 Schneider, S. Bulk metallic glasses. Journal of Physics: Condensed Matter 13 (2001) 7723-7736.

39 Johnson, W.L. Bulk amorphous metal – An emerging engineering material. JOM 54 (3) (2002) 40-43.

40 Löffler, J.F. Bulk metallic glasses. Intermetallics 11 (2003) 529-540.

41 Telford, M. The case for bulk metallic glasses. Materials Today 7 (3) (2004) 36-43.

42 Wang, W.H., Dong, C. & Shek, C.H. Bulk metallic glasses. Materials Science and Engineering R 44 (2004) 45-89.

43 Greer, A.L. & Ma, E. Bulk metallic glasses: At the cutting edge of metals research. MRS Bulletin 32 (8) (2007) 611-619.

44 Schuh, C.A., Hufnagel, T.C. & Ramamurty, U. Mechanical behaviour of amorphous alloys. Acta Materialia 55 (12) (2007) 4067-4109.

45 Sharma, P. & Inoue, A. Metallic glass. In: Lindroos, V., Tilli, M., Lehto, A. & Motooka, T. (ed.). Handbook of silicon based MEMS materials and technologies. United Kingdom: Elsevier, 2010. 1st edition. 636 p. ISBN 978-0-8155-1594-4.

46 Chen, M. A brief overview of bulk metallic glasses. NPG Asia Materials 3 (9) (2011) 82-90.

47 Axinte, E. Metallic glasses from “alchemy” to pure science: Present and future of design, processing and applications of glassy metals. Materials and Design 35 (2012) 518-556.

48 Rebeiz, G.M. RF MEMS – Theory, design, and technology. USA: John Wiley & Sons, Inc., 2003. 1st edition. 483 p. ISBN 0-471-20169-3.

49 Baltes, H., Brand, O., Fedder, G.K., Hierold, C., Korvink, J. & Tabata, O. (ed.) Advanced micro and nanosystems. Volume 2: CMOS – MEMS. Germany: Wiley-VCH Verlag GmbH & Co. KGaA, 2005. 1st edition. 608 p. ISBN 3-527-31080-0.

50 Leinenbach, C., Kattelus, H. & Knechtel, R. Surface micromachining. In: Lindroos, V., Tilli, M., Lehto, A. & Motooka, T. (ed.). Handbook of silicon based MEMS materials and technologies. United Kingdom: Elsevier, 2010. 1st edition. 636 p. ISBN 978-0-8155-1594-4.

51 Fischer, A.C., Forsberg, F., Lapisa, M., Bleiker, S.J., Stemme, G., Roxhed, N. & Niklaus, F. Integrating MEMS and ICs. Microsystems & Nanoengineering 1, Article number: 15005 (2015) 1-16.

52 Tilli, M. & Haapalinna, A. Properties of silicon. In: Lindroos, V., Tilli, M., Lehto, A. & Motooka, T. (ed.). Handbook of silicon based MEMS materials and technologies. United Kingdom: Elsevier, 2010. 1st edition. 636 p. ISBN 978-0-8155-1594-4.

53 Madou, M.J. Fundamentals of microfabrication. USA: CRC Press, 1997. 1st edition. 589 p. ISBN 0-8493-9451-1.

54 Rossnagel, S. Sputtering and sputter deposition. In: Seshan, K. (ed.). Handbook of thin film deposition processes and techniques. USA: Noyes Publications – William Andrew Publishing, 2002. 2nd edition. 629 p. ISBN 0-8155-1442-5.

55 Chen, K.-S. & Ou, K.-S. MEMS residual stress characterization: methodology and perspective. In: Lindroos, V., Tilli, M., Lehto, A. & Motooka, T. (ed.). Handbook of silicon based MEMS materials and technologies. United Kingdom: Elsevier, 2010. 1st edition. 636 p. ISBN 978-0-8155-1594-4.

56 Hoffman, D.W. Perspective on stresses in magnetron-sputtered thin films. Journal of Vacuum Science & Technology A 12 (4) (1994) 953-961.

57 Janssen, G.C.A.M. Stress and strain in polycrystalline thin films. Thin Solid Films 515 (2007) 6654-6664.

58 Kendig, L.P., Rek, Z.U., Yalisove, S.M. & Bilello, J.C. The role of impurities and microstructure on residual stress in nanoscale Mo films. Surface and Coatings Technology 132 (2000) 124-129.

59 Windt, D.L. Stress, microstructure, and stability of Mo/Si, W/Si, and Mo/C multilayer films. Journal of Vacuum Science & Technology A 18 (3) (2000) 980-991.

60 Guckel, H., Burns, D.W., Visser, C.C.G., Tilmans, H.A.C. & Deroo, D. Fine-grained polysilicon films with built-in tensile strain. IEEE Transactions on Electron Devices 35 (6) (1988) 800-801.

61 Airaksinen, V.-M. Introduction to measuring MEMS. In: Lindroos, V., Tilli, M., Lehto, A. & Motooka, T. (ed.). Handbook of silicon based MEMS materials and technologies. United Kingdom: Elsevier, 2010. 1st edition. 636 p. ISBN 978-0-8155-1594-4.

62 Callister, W.D., Jr. Materials science and engineering – An introduction. USA: John Wiley & Sons, Inc., 2000. 5th edition. 871 p. ISBN 0-471-32013-7.

63 Elliott, S.R. Physics of amorphous materials. United Kingdom: Longman Scientific & Technical, Longman Group UK Limited, 1990. 2nd edition. 481 p. ISBN 0-582-02160-X.

64 Kovalenko, N.P., Krasny, Y.P. & Krey, U. Physics of amorphous metals. Berlin: Wiley-VCH Verlag Berlin GmbH, 2001. 296 p. ISBN 978-3-527-40315-8.

65 Inoue, A. Stabilization of metallic supercooled liquid and bulk amorphous alloys. Acta Materialia 48 (1) (2000) 279-306.

66 Inoue, A. Bulk amorphous and nanocrystalline alloys with high functional properties. Materials Science and Engineering: A 304-306 (2001) 1-10.

67 Nicolet, M.-A., Kolawa, E. & Molarius, J. Issues in metal/semiconductor contact design and implementation. Solar Cells 27 (1989) 177-189.

68 Takayama, S. Review: Amorphous structures and their formation and stability. Journal of Materials Science 11 (1976) 164-185.

69 Klement, W., Willens, R.H. & Duwez, P. Non-crystalline structure in solidified gold-silicon alloys. Nature 187 (4740) (1960) 869-870.

70 Weber, T.A. & Stillinger, F.H. Local order and structural transitions in amorphous metal-metalloid systems. Physical Review B 31 (4) (1985) 1954-1963.

71 DeCristofaro N. Amorphous metals in electric-power distribution applications. MRS Bulletin 23 (5) (1998) 50-56.

72 Kui, H.W., Greer, A.L. & Turnbull, D. Formation of bulk metallic glass by fluxing. Applied Physics Letters 45 (6) (1984) 615-616.

73 Inoue, A. High strength bulk amorphous alloys with low critical cooling rates (overview). Materials Transactions, JIM 36 (7) (1995) 866-875.

74 Peker, A. & Johnson, W.L. A highly processable metallic glass: Zr41.2Ti13.8Cu12.5Ni10.0Be22.5. Applied Physics Letters 63 (1993) 2342-2344.

75 Nishiyama, N. & Inoue, A. Stability and nucleation behavior of glass-forming Pd-Cu-Ni-P alloy with a critical cooling rate of 0.067 K/s. Intermetallics 10 (11) (2002) 1141-1147.

76 Nishiyama, N., Takenaka, K., Miura, H., Saidoh, N., Zeng, Y. & Inoue, A. The world's biggest glassy alloy ever made. Intermetallics 30 (2012) 19-24.

77 Lu, Z.P., Liu, C.T., Thompson, J.R. & Porter, W.D. Structural amorphous steels. Physical Review Letters 92 (24) (2004) 245503.

78 Babilas, R. & Nowosielski, R. Iron-based bulk amorphous alloys. Archives of Materials Science and Engineering 44 (1) (2010) 5-27.

79 Suryanarayana, C. & Inoue, A. Iron-based bulk metallic glasses. International Materials Reviews 58 (3) (2013) 131-166.

80 Schroers, J. Processing of bulk metallic glass. Advanced Materials 22 (14) (2010) 1566-1597.

81 Soinila, E., Antin, K., Bossuyt, S. & Hänninen, H. Bulk metallic glass tube casting. Journal of Alloys and Compounds 509 (2011) S210-S213.

82 Schroers, J. The superplastic forming of bulk metallic glasses. JOM 57 (5) (2005) 35-39.

83 Kawamura, Y., Shoji, T. & Ohno, Y. Welding technologies of bulk metallic glasses. Journal of Non-Crystalline Solids 317 (1) (2003) 152-157.

84 Kim, H.J., Lim, K.M., Seong, B.G. & Park, C.G. Amorphous phase formation of Zr-based alloy coating by HVOF spraying process. Journal of Materials Science 36 (1) (2001) 49-54.

85 Ni, H.S., Liu, X.H., Chang, X.C., Hou, W.L., Liu, W. & Wang, J.Q. High performance amorphous steel coating prepared by HVOF thermal spraying. Journal of Alloys and Compounds 467 (1) (2009) 163-167.

86 Zhang, C., Liu, L., Chan, K.C., Chen, Q. & Tang, C.Y. Wear behavior of HVOF-sprayed Fe-based amorphous coatings. Intermetallics 29 (2012) 80-85.

87 Zhou, Z., Wang, L., Wang, F.C., Zhang, H.F., Liu, Y.B. & Xu, S.H. Formation and corrosion behavior of Fe-based amorphous metallic coatings by HVOF thermal spraying. Surface and Coatings Technology 204 (5) (2009) 563-570.

88 Chu, J.P., Huang, J.C., Jang, J.S.C., Wang, Y.C. & Liaw, P.K. Thin film metallic glasses: Preparations, properties, and applications. JOM 62 (4) (2010) 19-24.

89 Chu, J.P., Jang, J.S.C., Huang, J.C., Chou, H.S., Yang, Y., Ye, J.C., Wang, Y.C., Lee, J.W., Liu, F.X., Liaw, P.K., Chen, Y.C., Lee, C.M., Li, C.L. & Rullyani, C. Thin film metallic glasses: Unique properties and potential applications. Thin Solid Films 520 (16) (2012) 5097-5122.

90 Hata, S., Sakurai, J. & Shimokohbe, A. Thin film metallic glasses as new MEMS materials. Proceedings of MEMS 2005. 18th IEEE International Conference on Micro Electro Mechanical Systems (2005) 479-482.

91 Jeong, H.-W., Hata, S. & Shimokohbe, A. Microforming of three-dimensional microstructures from thin-film metallic glass. Journal of Microelectromechanical Systems 12 (1) (2003) 42-52.

92 Liu, Y., Hata, S., Wada, K. & Shimokohbe, A. Thermal, mechanical and electrical properties of Pd-based thin-film metallic glass. Japanese Journal of Applied Physics 40 (2001) 5382-5388.

93 Liu, Y., Hata, S., Wada, K. & Shimokohbe, A. Thin film metallic glasses: Fabrication and property test. Proceedings of MEMS 2001. 14th IEEE International Conference on Micro Electro Mechanical Systems (2001) 102-105.

94 Liu, Y.H., Fujita, T., Hirata, A., Li, S., Liu, H.W., Zhang, W., Inoue, A. & Chen, M.W. Deposition of multicomponent metallic glass films by single-target magnetron sputtering. Intermetallics 21 (1) (2012) 105-114.

95 Porter, J.R., DeNatale, J., Gluck, N. & Branagan, D. Incorporation of amorphous metals into MEMS for high performance and reliability. Thousand Oaks, CA 91360, USA: Rockwell Scientific Company, 2003. 40 p. Report number GO 71189.

96 Sambandam, S.N., Bhansali, S. & Bhethanabotla, V.R. Synthesis and characterization of amorphous metallic alloy thin films for MEMS applications. Proceedings of Amorphous and Nanocrystalline Metals. Materials Research Society Symposium 806 (2004) 177-182.

97 Sharma, P., Kaushik, N., Kimura, H., Saotome, Y. & Inoue, A. Nano-fabrication with metallic glass – an exotic material for nano-electromechanical systems. Nanotechnology 18 (3) (2007) 035302.

98 Wang, S., Sun, D., Hata, S., Sakurai, J. & Shimokohbe, A. Fabrication of thin film metallic glass (TFMG) pipe for a cylindrical ultrasonic linear microactuator. Sensors and Actuators A: Physical 153 (1) (2009) 120-126.

99 Salmon, P.S. Amorphous metals – Order within disorder. Nature Materials 1 (2002) 87-88.

100 Miracle, D.B. A structural model for metallic glasses. Nature Materials 3 (2004) 697-702.

101 Yavari, A.R. A new order for metallic glasses. Nature 439 (2006) 405-406.

102 Sheng, H.W., Luo, W.K., Alamgir, F.M., Bai, J.M. & Ma, E. Atomic packing and short-to-medium-range order in metallic glasses. Nature 439 (2006) 419-425.

103 Cheng, Y.Q., Ma, E. & Sheng, H.W. Atomic level structure in multicomponent bulk metallic glass. Physical Review Letters 102 (24) (2009) 245501.

104 Cheng, Y.Q. & Ma, E. Atomic-level structure and structure–property relationship in metallic glasses. Progress in Materials Science 56 (4) (2011) 379-473.

105 Hirata, A. Guan, P., Fujita, T., Hirotsu, Y., Inoue, A., Yavari, A.R., Sakurai, T. & Chen, M. Direct observation of local atomic order in a metallic glass. Nature Materials 10 (1) (2011) 28-33.

106 Sheng, H.W., Liu, H.Z., Cheng, Y.Q., Wen, J., Lee, P.L., Luo, W.K., Shastri, S.D. & Ma, E. Polyamorphism in a metallic glass. Nature Materials 6 (2007) 192-197.

107 Yavari, A.R. Metallic glasses – The changing faces of disorder. Nature Materials 6 (2007) 181-182.

108 Greer, A.L., Cheng, Y.Q. & Ma, E. Shear bands in metallic glasses. Materials Science and Engineering R 74 (4) (2013) 71-132.

109 Hofmann, D.C. Bulk metallic glasses and their composites: a brief history of diverging fields. Journal of Materials (2013), article ID 517904.

110 Arora, N. Apple locks in Liquidmetal for two more years. Forbes, 22 June 2012. Available: http://www.forbes.com/sites/greatspeculations/2012/06/22/apple-locks-in-liquidmetal-for-two-more-years (24.7.2016).

111 Campbell, M. Apple continuing work on Liquidmetal casting techniques, patents show. Available: http://appleinsider.com/articles/15/08/11/apple-continuing-work-on-liquidmetal-casting-techniques-patents-show (24.7.2016)

112 Mohri, K. Review on recent advances in the field of amorphous-metal sensors and transducers. IEEE Transactions on Magnetics 20 (5) (1984) 942-947.

113 Schroers, J., Kumar, G., Hodges, T.M., Chan, S. & Kyriakides, T.R. Bulk metallic glasses for biomedical applications. JOM 61 (9) (2009) 21-29.

114 Axinte, E. & Chirileanu, M.P.I. Recent progress in the industrialization of metallic glasses. Recent Patents on Materials Science 5 (2012) 213-221.

115 Carmo, M., Sekol, R.C., Ding, S., Kumar, G., Schroers, J. & Taylor, A.D. Bulk metallic glass nanowire architecture for electrochemical applications. Acs Nano 5 (4) (2011) 2979-2983.

116 Sekol, R.C., Kumar, G., Carmo, M., Gittleson, F., Hardesty-Dyck, N., Mukherjee, S., Schroers, J. & Taylor, A.D. Bulk metallic glass micro fuel cell. Small 9 (12) (2013) 2081-2085.

117 Yang, Y., Ye, J., Lu, J., Gao, Y. & Liaw, P.K. Metallic glasses: Gaining plasticity for microsystems. JOM 62 (2) (2010) 93-98.

118 Kumar, G., Desai, A. & Schroers, J. Bulk metallic glasses: The smaller the better. Advanced Materials 23 (4) (2011) 461-476.

119 Van Kessel, P.F., Hornbeck, L.J., Meier, R.E. & Douglass, M.R. A MEMS-based projection display. Proceedings of the IEEE 86 (8) (1998) 1687-1704.

120 Douglass, M.R. DMD reliability: a MEMS success story. In: Micromachining and Microfabrication. SPIE International Society for Optics and Photonics (2003) 1-11.

121 DLP® products & MEMS. Texas instruments. Available: http://www.ti.com/lsds/ti/analog/dlp/how-dlp-works.page (12.8.2015)

122 Friedrichs, M., Schmidt, J., Duerr, P. & Bakke, T. One megapixel SLM with high optical fill factor and low creep actuators. Proceedings of IEEE/LEOS International Conference on Optical MEMS and Their Applications (2006) 23-24.

123 Friedrichs, M., List, M. & Mueller, M. Integration of multi-level MOEMS structure on CMOS for spatial light modulators. Proceedings of SSI 2013: International Conference & Exhibition on Integration Issues of Miniaturized Systems – MEMS, NEMS, ICs and Electronic Components. 13-14 March 2013, Amsterdam, The Netherlands (2013) 8 pp.

124 Fraunhofer IPMS (publisher). Acoustics with MEMS: Capacitive micromachined ultrasonic transducer (CMUT) from research to commercial products. MEMS Report 2/2013. Available: http://www.ipms.fraunhofer.de/content/dam/ipms/common/documents/MEMSReport_CMUT-e.pdf (18.8.2015).

125 Elsaesser, L., Friedrichs, M., Klemm, M. & Unamono, A. Stress controlled CMUT fabrication based on a CMOS compatible sacrificial release process. 2015 Symposium on Design, Test, Integration and Packaging of MEMS and MOEMS (DTIP). IEEE (2015) 1-4.

126 Fukushige, T., Yokoyama, Y., Hata, S., Masu, K. & Shimokohbe, A. Fabrication and evaluation of an on-chip micro-variable inductor. Microelectronic Engineering 67-68 (2003) 582-587.

127 Fukushige, T. & Hata, S. A MEMS conical spring actuator array. Journal of Microelectromechanical Systems 14 (2) (2005) 243-253.

128 Saotome, Y. & Inoue, A. New amorphous alloys as micromaterials and the processing technologies. Proceedings of MEMS 2000. 13th IEEE International Conference on Micro Electro Mechanical Systems (2000) 288-293.

129 Saotome, Y. Superplastic nano/microforming of bulk metallic glasses and the application to micromachines. Proceedings of 2003 International Symposium on Micromechatronics and Human Science (IEEE) (2003) 11-16.

130 Schroers, J., Nguyen, T. & Desai, A. Superplastic forming of bulk metallic glass – A technology for MEMS and microstructure fabrication. Proceedings of MEMS 2006. 19th IEEE International Conference on Micro Electro Mechanical Systems (2006) 298-301.

131 Schroers, J., Pham, Q. & Desai, A. Thermoplastic forming of bulk metallic glass – A technology for MEMS and microstructure fabrication. Journal of Microelectromechanical Systems 16 (2) (2007) 240-247.

132 Bardt, J.A., Bourne, G.R., Schmitz, T.L., Ziegert, J.C. & Sawyer, W.G. Micromolding three-dimensional amorphous metal structures. Journal of Materials Research 22 (2) (2007) 339-343.

133 Kumar, G., Tang, H.X. & Schroers, J. Nanomoulding with amorphous metals. Nature 457 (7231) (2009) 868-872.

134 Zhang, N., Chu, J.S., Byrne, C.J., Browne, D.J. & Gilchrist, M.D. Replication of micro/nano scale features by micro injection molding with bulk metallic glass (BMG) mold insert. Journal of Micromechanics and Microengineering 22 (6) (2012) 065019.

135 Zhang, N., Byrne, C.J., Browne, D.J. & Gilchrist, M.D. Towards nano-injection molding. Materials Today 15 (5) (2012) 216-221.

136 Nicolet, M.-A. A case for mictamict alloys. Proceedings of Microtechnique Meeting. 30 September – 1 October 1999, Buchs, Switzerland (1999).

137 Nicolet, M.-A. Amorphous thin films for diffusion barriers in microelectronic devices. In: Jain, H. & Gupta, D. Diffusion in amorphous materials. Proceedings of an international symposium sponsored by the Atomic Transport Activity Committee of American Society for Materials and The Minerals, Metals & Materials Society. 18-19 October 1993, Pittsburgh, Pennsylvania, USA (1993) 225-234.

138 Nicolet, M.-A. Ternary amorphous metallic thin films as diffusion barriers for Cu metallization. Applied Surface Science 91 (1995) 269-276.

139 Nicolet, M.-A. Diffusion barriers in semiconductor contact technology. Defect and Diffusion Forum 143-147 (1997) 1271-1284.

140 Nicolet, M.-A. & Giauque, P.H. Highly metastable amorphous or near-amorphous ternary films (mictamict alloys). Microelectronic Engineering 55 (2001) 357-367.

141 Nicolet, M.-A. Reactively sputtered ternary films of the type TM-Si-N and their properties (TM = early transition metal). Vacuum 59 (2000) 716-720.

142 Reid, J.S. Amorphous ternary diffusion barriers for silicon metallizations. Dissertation. USA: Califormia Institute of Technology, 1995.

143 Angyal, M.S., Shacham-Diamand, Y., Reid, J.S. & Nicolet, M.-A. Performance of tantalum-silicon-nitride diffusion barriers between copper and silicon dioxide. Applied Physics Letters 67 (15) (1995) 2152-2154.

144 Aouadi, S.M., Zhang, Y., Bohnhoff, A., Lee, J. & Williams, M. Real-time spectroscopic ellipsometry study of Ta-Si-N ultrathin diffusion barriers. Journal of Vacuum Science & Technology A 23 (5) (2005) 1359-1369.

145 Bicker, M., Pinnow, C.-U., Geyer, U., Schneider, S. & Seibt, M. Nanocrystallization of amorphous-$Ta_{40}Si_{14}N_{46}$ diffusion barrier thin films. Applied Physics Letters 78 (23) (2001) 3618-3620.

146 Chen, Y.I., Lin K.Y., Wang H.H. & Cheng, Y.R. Characterization of Ta-Si-N coatings prepared using direct current magnetron co-sputtering. Applied Surface Science 305 (2014) 805-816.

147 Chung, C.K., Chang, Y.L., Wu, J.C., Jhu, J.J. & Chen, T.S. Characterization and patterning of novel high-TCR Ta-Si-N thin films for sensor application. Sensors and Actuators A: Physical 156 (2) (2009) 323-327.

148 Chung, C.K. & Chen, T.S. Effect of microstructures on the electrical and optoelectronic properties of nanocrystalline Ta-Si-N thin films by reactive magnetron sputtering. Scripta Materialia 57 (2007) 611-614.

149 Chung, C.K. & Chen, T.S. Effect of Si/Ta and nitrogen ratios on the thermal stability of Ta-Si-N thin films. Microelectronic Engineering 87 (2) (2010) 129-134.

150 Chung, C.K., Chen, T.S., Peng, C.C. & Wu, B.H. Thermal stability of Ta-Si-N nanocomposite thin films at different nitrogen flow ratios. Surface and Coatings Technology 201 (7) (2006) 3947-3952.

151 Dauksher, W.J., Resnick, D.J., Cummings, K.D., Baker, J., Gregory, R.B., Theodore, N.D., Chan, J.A., Johnson, W.A., Mogab, J., Nicolet, M.-A. & Reid, J.S. Method for fabricating a low stress x-ray mask using annealable amorphous refractory compounds. Journal of Vacuum Science & Technology B 13 (6) (1995) 3103-3108.

152 de Reus, R., Christensen, C., Weichel, S., Bouwstra, S., Janting, J., Friis Eriksen, G., Dyrbye, K., Romedahl Brown, T., Krog, J.P., Søndergård Jensen, O. & Gravesen, P. Reliability of industrial packaging for microsystems. Microelectronics Reliability 38 (1998) 1251-1260.

153 Dubois, Ph., Guldimann, B., Grétillat, M.-A. & de Rooij, N.F. Electrostatically actuated gas microvalve based on a Ta-Si-N membrane. Proceedings of MEMS 2001. 14th IEEE International Conference on Micro Electro Mechanical Systems (2001) 535-538.

154 Fischer, D., Scherg, T., Bauer, J.G., Schulze, H.-J. & Wenzel, C. Study of Ta-Si-N thin films for use as barrier layer in copper metallizations. Microelectronic Engineering 50 (2000) 459-464.

155 Grétillat, M.-A., Linder, C., Dommann, A., Staufert, G., de Rooij, N.F. & Nicolet, M.-A. Surface-micromachined Ta-Si-N beams for use in micromechanics. Journal of Micromechanics and Microengineering 8 (1998) 88-90.

156 Halperin, L.E., Bartur, M., Kolawa, E. & Nicolet, M.-A. Silicon Schottky barriers and p-n junctions with highly stable aluminum contact metallization. IEEE Electron Device Letters 12 (6) (1991) 309-311.

157 Hübner, R., Hecker, M., Mattern, N., Voss, A., Acker, J., Hoffmann, V., Wetzig, K., Engelmann, H.-J., Zschech, E., Heuer, H. & Wenzel, Ch. Influence of nitrogen content on the crystallization behavior of thin Ta-Si-N diffusion barriers. Thin Solid Films 468 (2004) 183-192.

158 Ivanov, E. Evaluation of tantalum silicide sputtering target materials for amorphous Ta-Si-N diffusion barrier for Cu metallization. Thin Solid Films 332 (1998) 325-328.

159 Kacsich, T., Kolawa, E., Fleurial, J.P., Caillat, T. & Nicolet, M.-A. Films of Ni-7 at% V, Pd, Pt and Ta-Si-N as diffusion barriers for copper on Bi_2Te_3. Journal of Physics D: Applied Physics 31 (1998) 2406-2411.

160 Kolawa, E., Pokela, P.J., Reid, J.S., Chen, J.S. & Nicolet, M.-A. Amorphous Ta-Si-N diffusion barriers in Si/Al and SI/Cu metallizations. Applied Surface Science 53 (1991) 373-376.

161 Kolawa, E., Molarius, J.M., Nieh, C.W. & Nicolet, M.-A. Amorphous Ta-Si-N thin-film alloys as diffusion barrier in Al/Si metallizations. Journal of Vacuum Science & Technology A 8 (3) (1990) 3006-3010.

162 Kolawa, E., Pokela, P., Halperin, L.E., Vu, Q. & Nicolet, M.-A. Amorphous ternary thin-film alloys as diffusion barriers in silicon metallizations. Proceedings of ASM International's 3rd Electronic Materials & Processing Congress. 20-23 August 1990, San Francisco, California, USA (1990) 243-247.

163 Kolawa, E., Pokela, P.J., Reid, J.S., Chen, J.S., Ruiz, R.P. & Nicolet, M.-A. Sputtered Ta-Si-N diffusion barriers in Cu metallizations for Si. IEEE Electron Device Letters 12 (6) (1991) 321-323.

164 Kolawa, E., Chen, J.S., Reid, J.S., Pokela, P.J. & Nicolet, M.-A. Tantalum-based diffusion barriers in Si/Cu VLSI metallizations. Journal of Applied Physics 70 (3) (1991) 1369-1373.

165 Kuchuk, A., Kaminska, E., Piotrowska, A., Golaszewska, K., Dynowska, E., Lytvyn, O.S., Nowicki, L. & Ratajczak, R. Amorphous Ta-Si-N diffusion barriers on GaAs. Thin Solid Films 459 (2004) 292-296.

166 Lee, Y.-J., Suh, B.-S., Rha, S.-K. & Park, C.-O. Structural and chemical stability of Ta-Si-N thin film between Si and Cu. Thin Solid Films 320 (1998) 141-146.

167 Linder, C., Dommann, A., Staufert, G. & Nicolet, M.-A. Ternary Ta-Si-N films for sensors and actuators. Sensors and Actuators A 61 (1997) 387-391.

168 McLane, G.F., Casas, L., Reid, J.S., Kolawa, E. & Nicolet, M.-A. Dry etching of Ta-Si-N diffusion barrier material in CF_4 + O_2 gas mixtures. Proceedings of Materials Research Society Symposium 337 (1994) 669-674.

169 McLane, G.F., Casas, L., Reid, J.S., Kolawa, E. & Nicolet, M.-A. Reactive ion etching of Ta-Si-N diffusion barriers in CF_4 + O_2. Journal of Vacuum Science & Technology B 12 (4) (1994) 2352-2355.

170 McLane, G.F., Casas, L., Reid, J.S. & Nicolet, M.-A. Reactive ion etching of Ta-Si-N diffusion barriers in CHF_3 + O_2. Electronics Letters 31 (7) (1995) 591-592.

171 Meier, M., Bertsch, D., Onda, N., Etter, M., Gutsche, M., Dommann, A., Romano, V. & Nicolet, M.-A. Laser trimming of amorphous $Ta_{42}Si_{13}N_{45}$ thin films with ultrashort pulses. Microelectronic Engineering 83 (2006) 2234-2237.

172 Molarius, J.M., Morishita, K., Kolawa, E. & Nicolet, M.-A. Encapsulation of GaAs and GaAs–Pd in furnace annealing. Vacuum 41 (4-6) (1990) 1029-1032.

173 Molarius, J.M., Kolawa, E., Morishita, K., Nicolet, M.-A., Tandon, J.L., Leavitt, J.A. & McIntyre, Jr., L.C. Tantalum-based encapsulants for thermal annealing of GaAs. Journal of The Electrochemical Society 138 (3) (1991) 834-837.

174 Oizumi, M., Aoki, K., Hashimoto, S., Nemoto, S. & Fukuda, Y. Control of crystalline structure and electrical properties of TaSiN thin film formed by reactive RF-sputtering. Japanese Journal of Applied Physics 39 (2000) 1291-1294.

175 Oizumi, M., Aoki, K. & Fukuda, Y. Temperature dependence of TaSiN thin film resistivity from room temperature to 900°C. Japanese Journal of Applied Physics 40 (2001) L603-L605.

176 Olowolafe, J.O., Rau, I., Unruh, K.M., Swann, C.P., Jawad Z.S. & Alford, T. Effect of composition on thermal stability and electrical resistivity of Ta-Si-N films. Thin Solid Films 365 (2000) 19-21.

177 Pokela, P.J., Kolawa, E., Nicolet, M.-A. & Ruiz, R. Amorphous ternary Ta-Si-N diffusion barrier between Si and Au. Journal of The Electrochemical Society 138 (7) (1991) 2125-2129.

178 Pokela, P.J., Kolawa, E., Ruiz, R. & Nicolet, M.-A. Characterization of the Al/Ta-Si-N/Au metallization. Thin Solid Films 203 (1991) 259-266.

179 Pokela, P.J., Reid, J.S., Kwok, C.-K., Kolawa, E. & Nicolet, M.-A. Thermal oxidation of amorphous ternary $Ta_{36}Si_{14}N_{50}$ thin films. Journal of Applied Physics 70 (5) (1991) 2828-2832.

180 Romano, V., Meier, M., Theodore, N.D., Marble, D.K. & Nicolet, M.-A. Irradiation of amorphous $Ta_{42}Si_{13}N_{45}$ film with a femtosecond laser pulse. Applied Physics A 104 (1) (2011) 357-364.

181 Shalish, I., Gasser, S., Kolawa, E. & Nicolet, M.-A. Stability of Schottky contacts with Ta-Si-N amorphous diffusion barriers and Au overlayers on 6H-SiC. Transactions of 3rd International High Temperature Electronics Conference. 9-14 June 1996, Albuquerque, New Mexico, USA (1996) VII-21 – VII-26.

182 Sun, X., Kolawa, E., Reid, J.S., Ruiz, R. & Nicolet, M.-A. Effect of Al grain growth in Al/$Ta_{36}Si_{14}N_{50}$/Au metallization. Conference Proceedings of ULSI-IX. Materials Research Society (1994) 575-581.

183 Tsuji, Y., Gasser, S.M., Kolawa, E. & Nicolet, M.-A. Texture of copper films on $Ta_{35}Si_{18}N_{47}$ and $Ti_{33}Si_{23}N_{44}$ underlayers. Thin Solid Films 350 (1999) 1-4.

184 Zahn, W., Hildebrand, D., Menzel, S., Oswald, S. & Heuer, H. Characterization of thin Ta-Si-N_x layers of different nitrogen content using XPS, UPS and STM. Applied Surface Science 252 (2005) 89-93.

185 Zeman, P., Musil, J. & Daniel, R. High-temperature oxidation resistance of Ta-Si-N films with a high Si content. Surface & Coatings Technology 200 (2006) 4091-4096.

186 Chawla, V., Jayaganthan, R. & Chandra, R. A study of structural and mechanical properties of sputter deposited nanocomposite Ti-Si-N thin films. Surface and Coatings Technology 204 (9) (2010) 1582-1589.

187 Choi, J.B., Cho, K., Lee, M.-H. & Kim, K.H. Effects of Si content and free Si on oxidation behaviour of Ti-Si-N coating layer. Thin Solid Films 447-448 (2004) 365-370.

188 Choi, S.R., Park, I.-W., Kim, S.H. & Kim, K.H. Effects of bias voltage and temperature on mechanical properties of Ti-Si-N coatings deposited by a hybrid system of arc ion plating and sputtering techniques. Thin Solid Films 447-448 (2004) 371-376.

189 Eisenbraun, E., Upham, A., Dash, R., Zeng, W., Hoefnagels, J., Lane, S., Anjum, D., Dovidenko, K. & Kaloyeros, A., Arkles, B. & Sullivan, J.J. Low temperature inorganic chemical vapor deposition of Ti-Si-N diffusion barrier liners for gigascale copper interconnect applications. Journal of Vacuum Science & Technology B 18 (4) (2000) 2011-2015.

190 Fleming, J.G., Smith, P.M., Custer, J.S., Roherty-Osmun, E., Cohn, M., Jones, R.V., Roberts, D.A., Norman, J.A.T., Hochberg, A.K., Reid, J.S., Kim, Y.-D., Kacsich, T. & Nicolet, M.-A. Characteristics of CVD ternary refractory nitride diffusion barriers. Conference Proceedings of ULSI XII. Materials Research Society (1997) 245-251.

191 Gottlieb, U., Sun, X., Kolawa, E. & Nicolet, M.-A. Temperature dependence of resistivity for TiN and Ti-Si-N films. Proceedings of Materials Research Society Symposium 427 (1996) 361-364.

192 Jiang, N., Shen, Y.G., Mai, Y.-W., Chan, T. & Tung, S.C. Nanocomposite Ti-Si-N films deposited by reactive unbalanced magnetron sputtering at room temperature. Materials Science and Engineering B 106 (2) (2004) 163-171.

193 Kacsich, T. & Nicolet, M.-A. Moving species in $Ti_{34}Si_{23}N_{43}$ oxidation. Thin Solid Films 349 (1999) 1-3.

194 Kacsich, T., Gasser, S., Tsuji, Y., Dommann, A. & Nicolet, M.-A. Wet oxidation of $Ti_{34}Si_{23}N_{43}$. Journal of Applied Physics 85 (3) (1999) 1871-1875.

195 Kacsich, T., Gasser, S.M., Garland, C. & Nicolet, M.-A. Wet oxidation of $Ti_{34}Si_{23}N_{43}$ thin films with and without pre-annealing. Surface and Coatings Technology 124 (2000) 162-168.

196 Kondo, H., Furumai, K., Sakashita, M., Sakai, A. & Zaima, S. Thermal stability and scalability of mictamict Ti-Si-N metal-oxide-semiconductor gate electrodes. Japanese Journal of Applied Physics 48 (4S) (2009) 04C012.

197 Li, Z.G., Mori, M., Miyake, S., Kumagai, M., Saito, H. & Muramatsu, Y. Structure and properties of Ti-Si-N films prepared by ICP assisted magnetron sputtering. Surface & Coatings Technology 193 (2005) 345-349.

198 Lin, C.-M. & Loong, W.-A. $TiSi_xN_y$ and $TiSi_xO_yN_z$ as embedded materials for attenuated phase-shifting mask in 193 nm. Microelectronic Engineering 46 (1999) 93-96.

199 Loong, W.-A., Lin, C.-M., Tseng, S.-P. & Yeh, W.-L. The correlation between the chemical compositions and optical properties of $TiSi_xN_y$ as an embedded layer for AttPSM in 193 nm. Microelectronic Engineering 57-58 (2001) 481-487.

200 Meng, W.J., Zhang, X.D., Shi, B., Jiang, J.C., Rehn, L.E., Baldo, P.M. & Tittsworth, R.C. Structure and mechanical properties of Ti-Si-N ceramic nanocomposite coatings. Surface and Coatings Technology 163-164 (2003) 251-259.

201 Nose, M., Deguchi, Y., Mae, T., Honbo, E., Nagae, T. & Nogi, K. Influence of sputtering conditions on the structure and properties of Ti-Si-N thin films

prepared by r.f.-reactive sputtering. Surface and Coatings Technology 174-175 (2003) 261-265.

202 Park, I.-W. & Kim, K.H. Coating materials of TiN, Ti-Al-N, and Ti-Si-N by plasma-enhanced chemical vapor deposition for mechanical applications. Journal of Materials Processing Technology 130-131 (2002) 254-259.

203 Reid, J.S., Sun, X., Kolawa, E. & Nicolet, M.-A. Ti-Si-N diffusion barriers between silicon and copper. IEEE Electron Device Letters 15 (8) (1994) 298-300.

204 Shtansky, D.V., Lyasotsky, I.V., D'yakonova, N.B., Kiryukhantsev-Korneev, F.V., Kulinich, S.A., Levashov, E.A. & Moore, J.J. Comparative investigation of Ti-Si-N films magnetron sputtered using Ti_5Si_3 + Ti and Ti_5Si_3 + TiN targets. Surface and Coatings Technology 182 (2004) 204-214.

205 Shtansky, D.V., Kulinich, S.A., Levashov, E.A., Sheveiko, A.N., Kiri-uhancev, F.V. & Moore, J.J. Localised deformation of multicomponent thin films. Thin Solid Films 420-421 (2002) 330-337.

206 Sun, X., Kolawa, E., Im, S., Garland, C. & Nicolet, M.-A. Effect of Si in reactively sputtered Ti-Si-N films on structure and diffusion barrier performance. Applied Physics A: Materials Science & Processing 65 (1997) 43-45.

207 Sun, X., Reid, J.S., Kolawa, E. & Nicolet, M.-A. Reactively sputtered Ti-Si-N diffusion barriers. Conference Proceedings of ULSI XI. Materials Research Society (1996) 401-408.

208 Sun, X., Reid, J.S., Kolawa, E. & Nicolet, M.-A. Reactively sputtered Ti-Si-N films I. Physical properties. Journal of Applied Physics 81 (2) (1997) 656-663.

209 Sun, X., Reid, J.S., Kolawa, E. & Nicolet, M.-A. Reactively sputtered Ti-Si-N films II. Diffusion barriers for Al and Cu metallizations on Si. Journal of Applied Physics 81 (2) (1997) 664-671.

210 Tang, F., Gault, B., Ringer, S.P., Martin, P., Bendavid, A. & Cairney, J.M. Microstructural investigation of Ti-Si-N hard coatings. Scripta Materialia 63 (2) (2010) 192-195.

211 Vaz, F., Rebouta, L., Goudeau, P., Pacaud, J., Garem, H., Riviére, J.P., Cavaleiro, A. & Alves, E. Characterisation of $Ti_{1-x}Si_xN_y$ nanocomposite films. Surface and Coatings Technology 133-134 (2000) 307-313.

212 Vaz, F., Rebouta, L., Andritschky, M., da Silva, M.F. & Soares, J.C. Oxidation resistance of (Ti, Al, Si)N coatings in air. Surface and Coatings Technology 98 (1998) 912-917.

213 Vaz, F., Rebouta, L., Ramos, S., Cavaleiro, A., da Silva, M.F. & Soares, J.C. Physical and mechanical properties of $Ti_{1-x}Si_xN$ films. Surface and Coatings Technology 100-101 (1998) 110-115.

214 Vaz, F., Rebouta, L., Goudeau, Ph., Rivière, J.P., Schäffer, E., Kleer, G. & Bodmann, M. Residual stress states in sputtered $Ti_{1-x}Si_xN_y$ films. Thin Solid Films 402 (2002) 195-202.

215 Vaz, F., Carvalho, S., Rebouta, L., Silva, M.Z., Paúl, A. & Schneider, D. Young's modulus of (Ti,Si)N films by surface acoustic waves and indentation techniques. Thin Solid Films 408 (2002) 160-168.

216 Yazdi, M.A.P., Lomello, F., Wang, J., Sanchette, F., Dong, Z., White, T., Wouters, Y., Schuster, F. & Billard, A. Properties of TiSiN coatings deposited by hybrid HiPIMS and pulsed-DC magnetron co-sputtering. Vacuum 109 (2014) 43-51.

217 Zhang, P., Cai, Z. & Xiong, W. Influence of Si content and growth condition on the microstructure and mechanical properties of Ti-Si-N nanocomposite films. Surface & Coatings Technology 201 (2007) 6819-6823.

218 Zhang, S., Sun, D., Fu, Y. & Du, H. Effect of sputtering target power on microstructure and mechanical properties of nanocomposite nc-TiN/a-SiN_x thin films. Thin Solid Films 447-448 (2004) 462-467.

219 Zhang, X.D., Meng, W.J., Wang, W., Rehn, L.E., Baldo, P.M. & Evans, R.D. Temperature dependence of structure and mechanical properties of Ti-Si-N coatings. Surface and Coatings Technology 177-178 (2004) 325-333.

220 Zou, C.W., Wang, H.J., Li, M., Yu, Y.F., Liu, C.S., Guo, L.P. & Fu, D.J. Characterization and properties of TiN-containing amorphous Ti-Si-N nanocomposite coatings prepared by arc assisted middle frequency magnetron sputtering. Vacuum 84 (6) (2010) 817-822.

221 Heo, S.J., Kim, K.H., Kang, M.C., Suh, J.H. & Park, C.-G. Syntheses and mechanical properties of Mo-Si-N coatings by a hybrid coating system. Surface and Coatings Technology 201 (2006) 4180-4184.

222 Hirvonen, J.-P., Suni, I., Kattelus, H., Lappalainen, R., Torri, P., Kung, H., Jervis, T.R., Nastasi, M. & Tesmer, J.R. Crystallization and oxidation behaviour of Mo-Si-N coatings. Surface and Coatings Technology 74-75 (1995) 981-985.

223 Hirvonen, J.-P., Suni, I., Kattelus, H., Lappalainen, R., Torri, P., Kung, H., Jervis, T.R. & Nastasi, M. Microstructure and mechanical properties of nitrided molybdenum silicide coatings. Proceedings of High Temperature Silicides and Refractory Alloys. Materials Research Society Symposium 322 (1994) 279-284.

224 Jung, C.-K., Jeong, S.H., Chung, Y.-M., Han, J.-G. & Boo, J.-H. Comparative study on mechanical properties of MoSiN multilayer films deposited on Si(100) and Ti-covered Si(100) substrates. Metals and Materials International 13 (6) (2007) 463-468.

225 Kung, H., Jervis, T.R., Hirvonen, J.-P., Mitchell, T.E. & Nastasi, M. High-temperature structural stability of $MoSi_2$-based nanolayer composites. Journal of Vacuum Science & Technology B 13 (3) (1995) 1126-1129.

226 Kung, H., Jervis, T.R., Hirvonen, J.-P., Mitchell, T.E. & Nastasi, M. Synthesis, structure and mechanical properties of nanostructured $MoSi_2N_x$. NanoStructured Materials 7 (1-2) (1996) 81-88.

227 Liu, Q., Fang, Q.F., Liang, F.J., Wang, J.X., Yang, J.F. & Li, C. Synthesis and properties of nanocomposite MoSiN hard coatings. Surface and Coatings Technology 201 (2006) 1894-1898.

228 Musil, J., Dohnal, P. & Zeman, P. Physical properties and high-temperature oxidation resistance of sputtered Si_3N_4/MoN_x nanocomposite coatings. Journal of Vacuum Science & Technology B 23 (4) (2005) 1568-1575.

229 Musil, J. & Jirout, M. Toughness of hard nanostructured ceramic thin films. Surface and Coatings Technology 201 (2007) 5148-5152.

230 Patel, P., Nadesalingam, M., Wallace, R.M. & Buchanan, D.A. Physical and optoelectronic characterization of reactively sputtered molybdenum-silicon-nitride alloy metal gate electrodes. Journal of Applied Physics 105, 024517 (2009) 1-7.

231 Reid, J.S., Kolawa, E., Garland, C.M. & Nicolet, M.-A. Amorphous (Mo, Ta, or W)-Si-N diffusion barriers for Al metallizations. Journal of Applied Physics 79 (2) (1996) 1109-1115.

232 Reid, J.S., Kolawa, E., Ruiz, R.P. & Nicolet, M.-A. Evaluation of amorphous (Mo, Ta, W)-Si-N diffusion barriers for <Si>|Cu metallizations. Thin Solid Films 236 (1993) 319-324.

233 Sun, S.C., Yap, H.K., Chen, C.A. & Lin, P. Evaluation of amorphous (Ta, W, Mo)-Si-N diffusion barriers between Cu and Si. Proceedings of 6th International Conference on Solid-State and Integrated Circuit Technology 1 (2001) 379-399.

234 Torri, P., Mahiout, A., Koskinen, J., Hirvonen, J.-P. & Johansson, L.-S. Corrosion properties of amorphous Mo-Si-N and nanolayered Mo-Si-N/SiC coatings. Scripta Materialia 42 (6) (2000) 609-613.

235 Torri, P., Hirvonen, J.-P., Kung, H., Lu, Y.-C., Nastasi, M. & Gibson, P.N. Mechanical properties, stress evolution and high-temperature thermal stability of nanolayered Mo-Si-N/SiC coatings. Journal of Vacuum Science & Technology B 17 (4) (1999) 1329-1335.

236 Wen, H.C., Alshareef, H.N., Luan, H., Choi, K., Lysaght, P., Harris, H.R., Huffman, C., Brown, G.A., Bersuker, G., Zeitzoff, P., Huff, H., Majhi, P. & Lee, B.H. Systematic investigation of amorphous transition-metal-silicon-nitride electrodes for metal gate CMOS applications. Proceedings of Symposium on VLSI Technology (IEEE) (2005) 46-47.

237 Yuan, Z.G., Yang, J.F., Wang, X.P., Cheng, Z.J. & Fang, Q.F. Characterization and properties of quaternary Mo-Si-C-N coatings synthesized by magnetron sputtering technique. Surface & Coatings Technology 205 (2011) 3307-3312.

238 Yuan, Z.G., Yang, J.F., Wang, X.P. & Fang, Q.F. Effect of Al content on the microstructure and mechanical properties of Mo-Al-Si-N films synthesized by DC magnetron sputtering. Surface & Coatings Technology 204 (2010) 3371-3375.

239 Zhang, G., Fan, T., Wang, T. & Chen, H. Microstructure, mechanical and tribological behavior of MoN_x/SiN_x multilayer coatings prepared by magnetron sputtering. Applied Surface Science 274 (2013) 231-236.

240 Asai, K., Sugahara, H., Matsuoka, Y. & Tokumitsu, M. Reactively sputtered WSiN film suppresses As and Ga outdiffusion. Journal of Vacuum Science & Technology B 6 (5) (1988) 1526-1529.

241 Fu, T., Zhou, Z.F., Li, K.Y. & Shen, Y.G. Characterization of sputter deposited W-Si-N coatings based on α-W structure. Materials Letters 59 (2005) 618-623.

242 Fu, T., Zhou, Z.F., Li, K.Y. & Shen, Y.G. Structure, stress and hardness of sputter deposited nanocomposite W-Si-N coatings. Surface & Coatings Technology 200 (2005) 2325-2530.

243 Gocke, O.H., Amin, S., Ravindra, N.M., Szostak, D.J., Paff, R.J., Fleming, J.G., Galewski, C.J., Schallenberger, J. & Eby, R. Effects of annealing on X-ray-amorphous CVD W-Si-N barrier layer materials. Thin Solid Films 353 (1999) 149-156.

244 Louro, C., Cavaleiro, A. & Montemor, F. How is the chemical bonding of W-Si-N sputtered coatings? Surface and Coatings Technology 142-144 (2001) 964-970.

245 Louro, C. & Cavaleiro, A. Mechanical behaviour of amorphous W-Si-N sputtered films after thermal annealing at increasing temperatures. Surface and Coatings Technology 123 (2000) 192-198.

246 Louro, C., Cavaleiro, A., Dub, S., Smid, P., Musil, J. & Vlcek, J. The depth profile analysis of W-Si-N coatings after thermal annealing. Surface and Coatings Technology 161 (2002) 111-119.

247 Louro, C., & Cavaleiro, A. The oxidation behaviour of mixed tungsten silicon sputtered coatings. Thin Solid Films 343-344 (1999) 51-56.

248 Marques, A.P. & Cavaleiro, A. Structural and mechanical properties of amorphous W-Si-N sputtered films after thermal annealing. Thin Solid Films 441 (2003) 150-160.

249 Musil, J., Daniel, R., Soldán, J. & Zeman, P. Properties of reactively sputtered W-Si-N films. Surface & Coatings Technology 200 (2006) 3886-3895.

250 Benkahoul, M., Robin, P., Gujrathi, S.C., Martinu, L. & Klemberg-Sapieha, J.E. Microstructure and mechanical properties of Cr-Si-N coatings prepared by pulsed reactive dual magnetron sputtering. Surface & Coatings Technology 202 (2008) 3975-3980.

251 Castaldi, L., Kurapov, D., Reiter, A., Shklover, V., Schwaller, P. & Patscheider, J. High temperature phase changes and oxidation behavior of Cr-Si-N coatings. Surface & Coatings Technology 202 (2007) 781-785.

252 Lee, J.-W. & Chang, Y.-C. A study on the microstructures and mechanical properties of pulsed DC reactive magnetron sputtered Cr-Si-N nanocomposite coatings. Surface & Coatings Technology 202 (2007) 831-836.

253 Mercs, D., Bonasso, N., Naamane, S., Bordes, J.-M. & Coddet, C. Mechanical and tribological properties of Cr-N and Cr-Si-N coatings reactively sputter deposited. Surface & Coatings Technology 200 (2005) 403-407.

254 Sandu, C.S., Sanjinés, R., Benkahoul, M., Medjani, F. & Lévy, F. Formation of composite ternary nitride thin films by magnetron sputtering co-deposition. Surface & Coatings Technology 201 (2006) 4083-4089.

255 Shin, S.H., Kim, M.W., Kang, M.C., Kim, K.H., Kwon, D.H. & Kim, J.S. Cutting performance of CrN and Cr-Si-N coated end-mill deposited by hybrid coating system for ultra-high speed micro machining. Surface & Coatings Technology 202 (2008) 5613-5616.

256 Miyamoto, K., Furumai, K., Urban, B.E., Kondo, H. & Zaima, S. Nitrogen-content dependence of crystalline structures and resistivity of Hf-Si-N gate electrodes for metal-oxide-semiconductor field-effect transistors. Japanese Journal of Applied Physics 48 (2009) 045505.

257 Dong, Y., Liu, Y., Dai, J. & Li, G. Superhard Nb-Si-N composite films synthesized by reactive magnetron sputtering. Applied Surface Science 252 (2006) 5215-5219.

258 Sandu, C.S., Benkahoul, M., Sanjinés, R. & Lévy, F. Model for the evolution of Nb-Si-N thin films as a function of Si content relating the nanostructure to electrical and mechanical properties. Surface & Coatings Technology 201 (2006) 2897-2903.

259 Song, Z.X., Wang, Y., Wang, C.J.F., Liu, C.L. & Xu, K.W. The effect of N_2 partial pressure on the properties of Nb-Si-N films by RF reactive magnetron sputtering. Surface & Coatings Technology 201 (2007) 5412-5415.

260 Wang, J., Song, Z. & Xu, K. Influence of sputtering bias on the microstructure and properties of Nb-Si-N films. Surface & Coatings Technology 201 (2007) 4931-4934.

261 Ge, F., Zhu, P., Wang, H., Meng, F., Li, S. & Huang, F. Friction and wear behavior of magnetron co-sputtered V-Si-N coatings. Wear 315 (2014) 17-24.

262 Huang, F., Ge, F., Zhu, P., Wang, H., Meng, F. & Li, S. Superhard V-Si-N coatings (> 50 GPa) with cell-like nanostructure. Surface & Coatings Technology 232 (2013) 600-605.

263 Cui, X., Jin, G., Hao, J., Li, J. & Guo, T. The influences of Si content on biocompatibility and corrosion resistance of Zr-Si-N films. Surface and Coatings Technology 228 (2013) S524-S528.

264 Daniel, R., Musil, J., Zeman, P. & Mitterer, C. Thermal stability of magnetron sputtered Zr-Si-N films. Surface & Coatings Technology 201 (2006) 3368-3376.

265 Dong, Y., Zhao, W., Li, Y. & Li, G. Influence of silicon on the microstructure and mechanical properties of Zr-Si-N composite films. Applied Surface Science 252 (2006) 5057-5062.

266 Nose, M., Zhou, M., Nagae, T., Mae, T., Yokota, M. & Saji, S. Properties of Zr-Si-N coatings prepared by RF reactive sputtering. Surface and Coatings Technology 132 (2000) 163-168.

267 Martin, P.J., Bendavid, A., Cairney, J.M. & Hoffman, M. Nanocomposite Ti-Si-N, Zr-Si-N, Ti-Al-Si-N, Ti-Al-V-Si-N thin film coatings deposited by vacuum arc deposition. Surface & Coatings Technology 200 (2005) 2228-2235.

268 Musil, J., Daniel, R., Zeman, P. & Takai, O. Structure and properties of magnetron sputtered Zr-Si-N films with a high (≥25 at.%) Si content. Thin Solid Films 478 (1) (2005) 238-247.

269 Pilloud, D., Pierson, J.F., Marco de Lucas, M.C. & Alnot, M. Stabilisation of tetragonal zirconia in oxidised Zr-Si-N nanocomposite coatings. Applied Surface Science 229 (2004) 132-139.

270 Pilloud, D., Pierson, J.F., Marques, A.P. & Cavaleiro, A. Structural changes in Zr-Si-N films vs. their silicon content. Surface & Coatings Technology 180-181 (2004) 352-356.

271 Pilloud, D., Pierson, J.F. & Takadoum, J. Structure and tribological properties of reactively sputtered Zr-Si-N films. Thin Solid Films 496 (2006) 445-449.

272 Sandu, C.S., Medjani, F. & Sanjinés, R. Optical and electrical properties of sputtered Zr-Si-N thin films: From solid solution to nanocomposite. Reviews on Advanced Materials Science 15 (2007) 173-178.

273 Sandu, C.S., Sanjinés, R. & Medjani, F. Control of morphology (ZrN crystallite size and SiN_x layer thickness) in Zr-Si-N nanocomposite thin films. Surface & Coatings Technology 202 (2008) 2278-2281.

274 Song, Z.X., Xu, K.W. & Chen, H. The effect of nitrogen partial pressure on Zr-Si-N diffusion barrier. Microelectronic Engineering 71 (2004) 28-33.

275 Winkelmann, A., Cairney, J.M., Hoffman, M.J., Martin, P.J. & Bendavid, A. Zr-Si-N films fabricated using hybrid cathodic arc and chemical vapour deposition: Structure vs. properties. Surface & Coatings Technology 200 (2006) 4213-4219.

276 Wang, Y., Zhu, C., Song, Z. & Li, Y. High temperature stability of Zr-Si-N diffusion barrier in Cu/Si contact system. Microelectronic Engineering 71 (2004) 69-75.

277 Zeman, P. & Musil, J. Difference in high-temperature oxidation resistance of amorphous Zr-Si-N and W-Si-N films with a high Si content. Applied Surface Science 252 (2006) 8319-8325.

278 Giauque, P.H., Cherry, H.B., Nicolet, M.-A., Bernard, C. & Pisch, A. Annealing of amorphous $Ir_{18}Si_{15}O_{67}$ films in dry oxygen. Thin Solid Films 406 (2002) 299-301.

279 Gottlieb, U., Laborde, O., Giauque, P.H., Nicolet, M.-A. & Madar, R. Electronic transport in Ru-Si-O and Ir-Si-O amorphous thin films. Microelectronic Engineering 60 (2002) 107-111.

280 Cherry, H.B., Giauque, P.H. & Nicolet, M.-A. Stability of conducting amorphous Ru-Si-O thin films under oxygen annealing. Microelectronic Engineering 55 (2001) 403-408.

281 Gasser, S.M., Ruiz, R., Kolawa, E. & Nicolet, M.-A. Instability of amorphous Ru-Si-O thin films under thermal oxidation. Journal of The Electrochemical Society 146 (4) (1999) 1546-1548.

282 Gasser, S.M., Kolawa, E. & Nicolet, M.-A. Reactively sputtered Ru-Si-O films. Journal of Applied Physics 86 (4) (1999) 1974-1981.

283 Giauque, P.H., Cherry, H.B. & Nicolet, M.-A. Thermal stability of amorphous thin films: $Ti_3Si_1O_8$ vs. TiO_2 and mictamict compounds. Thin Solid Films 394 (2001) 136-141.

284 Giauque, P.H., Cherry, H.B. & Nicolet, M.-A. Thermal stability of amorphous $Ti_3Si_1O_8$ thin films. Microelectronic Engineering 55 (2001) 183-188.

285 Reid, J.S., Liu, R.Y., Smith, P.M., Ruiz, R.P. & Nicolet, M.-A. W-B-N diffusion barriers for Si/Cu metallizations. Thin Solid Films 262 (1995) 218-223.

286 Hopcroft, M.A., Nix, W.D. & Kenny, T.W. What is the Young's modulus of silicon? Journal of Microelectromechanical Systems 19 (2) (2010) 229-238.

287 Lévy, F., Hones, P., Schmid, P.E., Sanjinés, R., Diserens, M. & Wiemer, C. Electronic states and mechanical properties in transition metal nitrides. Surface and Coatings Technology 120-121 (1999) 284-290.

288 Greenwood, N.N. & Earnshaw, A. Chemistry of the elements. Great Britain: Butterworth-Heinemann, 1998. 2nd edition. 1341 p. ISBN 0-7506-3365-4.

289 Anitha, V.P., Major, S., Chandrashekharam, D. & Bhatnagar, M. Deposition of molybdenum nitride thin films by r.f. reactive magnetron sputtering. Surface and Coatings Technology 79 (1996) 50-54.

290 Atuchin, V.V., Khasanov, T., Kochubey, V.A., Pokrovsky, L.D. & Gavrilova, T.A. Structural and optical properties of γ-Mo_2N thin films deposited by DC reactive magnetron sputtering. International Journal of Modern Physics B 23 (23) (2009) 4817-4823.

291 Barbosa, J., Cunha, L., Rebouta, L., Moura, C., Vaz, F., Carvalho, S., Alves, E., Le Bourhis, E., Goudeau, Ph. & Rivière, J.P. Properties of MoN_xO_y thin films as a function of the N/O ratio. Thin Solid Films 494 (2006) 201-206.

292 Chatterjee, S., Kuo, Y. & Lu, J. Thermal annealing effect on electrical properties of metal nitride gate electrodes with hafnium oxide gate dielectrics in nano-metric MOS devices. Microelectric Engineering 85 (2008) 202-209.

293 Chuang, J.-C., Tu, S.-L. & Chen, M.-C. Sputter-deposited Mo and reactively sputter-deposited Mo-N films as barrier layers against Cu diffusion. Thin Solid Films 346 (1999) 299-306.

294 Cunha, L., Rebouta, L., Vaz, F., Staszuk, M., Malara, S., Barbosa, J., Carvalho, P., Alves, E., Le Bourhis, E., Goudeau, Ph. & Rivière, J.P. Effect of thermal treatments on the structure of MoN_xO_y thin film. Vacuum 82 (2008) 1428-1432.

295 Gassner, G., Mayrhofer, P.H., Kutschej, K., Mitterer, C. & Kathrein, M. Magnéli phase formation of PVD Mo-N and W-N coatings. Surface & Coatings Technology 201 (2006) 3335-3341

296 Giauque, P.H., Gasser, S., Nicolet, M.A. & Kolawa, E. Diamond metallization for Mo electroplating. Proceedings of 1998 Fourth International High Temperature Electronics Conference. HITEC (1998) 269-273.

297 Hones, P., Martin, N., Regula, M. & Lévy, F. Structural and mechanical properties of chromium nitride, molybdenum nitride, and tungsten nitride thin films. Journal of Physics D: Applied Physics 36 (2003) 1023-1029.

298 Lee, J.-Y. & Park, J.-W. Diffusion barrier property of molybdenum nitride films for copper metallization. Japanese Journal of Applied Physics 35 (1996) 4280-4284.

299 Lin, K.-L. & Ho, Y.-J. The interactions among the Al/Mo-N/Au multilayer. Thin Solid Films 260 (1995) 93-97.

300 Sanjinés, R., Wiemer, C., Almeida, J. & Lévy, F. Valence band photoemission study of the Ti-Mo-N system. Thin Solid Films 290-291 (1996) 334-338.

301 Shen, Y.G. & Mai, Y.-W. Crystallization-induced stress in reactively sputter-deposited molybdenum nitride thin films. Philosophical Magazine Letters 83 (2) (2003) 125-133.

302 Shen, Y.G. Effect of deposition conditions on mechanical stresses and microstructure of sputter-deposited molybdenum and reactively sputter-deposited molybdenum nitride films. Materials Science and Engineering A 359 (2003) 158-167.

303 Shen, Y.G. & Mai, Y.-W. Reactively sputter-deposited $Mo-O_x-N_y$ thin films. Materials Science and Engineering B 95 (2002) 222-229.

304 Song, S., Liu, Y., Mao, D., Ling, H. & Li, M. Diffusion barrier performances of thin Mo, Mo-N and Mo/Mo-N films between Cu and Si. Thin Solid Films 476 (2005) 142-147.

305 Stöber, L., Konrath, J.P., Krivec, S., Patocka, F., Schwarz, S., Bittner, A., Schneider, M. & Schmid, U. Impact of sputter deposition parameters on molybdenum nitride thin film properties. Journal of Micromechanics and Microengineering 25 (7) (2015) 074001.

306 Stöber, L., Konrath, J.P., Haberl, V., Patocka, F., Schneider, M. & Schmid, U. Nitrogen incorporation in sputter deposited molybdenum nitride thin films. Journal of Vacuum Science & Technology A 34 (2) (2016) 021513.

307 Suszko, T., Gulbínski, W. & Jagielski, J. The role of surface oxidation in friction processes on molybdenum nitride thin films. Surface & Coatings Technology 194 (2005) 319-324.

308 Wang, Y. & Lin, R.Y. Amorphous molybdenum nitride thin films prepared by reactive sputter deposition. Materials Science and Engineering B 112 (2004) 42-49.

309 Wang, Y., Seok, J.W. & Lin, R.Y. Properties of molybdenum nitride thin film deposited by reactive sputter deposition. Proceedings of Surface Engineering 2002 – Synthesis, Characterization and Applications. Materials Research Society Symposium 750 (2003) 307-312.

310 Wiemer, C., Sanjinés, R. & Lévy, F. Deposition and characterization of refractory ternary phases: the transition metal nitride $Ti_{1-x}Mo_xN_y$. Surface and Coatings Technology 86-87 (1996) 372-376.

311 Fix, R., Gordon, R.G. & Hoffman, D.M. Low-temperature atmospheric-pressure metal-organic chemical vapor deposition of molybdenum nitride thin films. Thin Solid Films 288 (1996) 116-119.

312 Nakajima, T. & Shirasaki, T. Chemical vapor deposition of tungsten carbide, molybdenum carbide nitride, and molybdenum nitride films. Journal of The Electrochemical Society 144 (6) (1997) 2096-2100.

313 Roberson, S.L., Finello, D. & Davis, R.F. Growth of Mo_xN films via chemical vapor deposition of $MoCl_5$ and NH_3. Surface and Coatings Technology 102 (1998) 256-259.

314 Roberson, S.L., Finello, D. & Davis, R.F. Phase control of Mo_xN films via chemical vapor deposition. Thin Solid Films 324 (1998) 30-36.

315 Alén, P., Ritala, M., Arstila, K., Keinonen, J. & Leskelä, M. Atomic layer deposition of molybdenum nitride thin films for Cu metallizations. Journal of The Electrochemical Society 152 (5) (2005) G361-G366.

316 Miikkulainen, V., Suvanto, M. & Pakkanen, T.A. Molybdenum nitride nanotubes. Thin Solid Films 516 (2008) 6041-6047.

317 Miikkulainen, V., Suvanto, M., Pakkanen, T.A., Siitonen, S., Karvinen, P., Kuittinen, M. & Kisonen, H. Thin films of MoN, WN, and perfluorinated silane deposited from dimethylamido precursors as contamination resistant coatings on micro-injection mold inserts. Surface & Coatings Technology 202 (2008) 5103-5109.

318 Kazmanli, M.K., Ürgen, M. & Cakir, A.F. Effect of nitrogen pressure, bias voltage and substrate temperature on the phase structure of Mo-N coatings produced by cathodic arc PVD. Surface and Coatings Technology 167 (2003) 77-82.

319 Sarioglu, C., Demirler, U., Kazmanli, M.K. & Ürgen, M. Measurement of residual stresses by X-ray diffraction techniques in MoN and Mo_2N coatings deposited by arc PVD on high-speed steel substrate. Surface and Coatings Technology 190 (2005) 238-243.

320 Solak, N., Ustel, F., Ürgen, M., Aydin, S. & Cakir, A.F. Oxidation behaviour of molybdenum nitride coatings. Surface and Coatings Technology 174-175 (2003) 713-719.

321 Ürgen, M., Eryilmaz, O.L., Cakir, A.F., Kayali, E.S., Nilüfer, B. & Isik, Y. Characterization of molybdenum nitride coatings produced by arc-PVD technique. Surface and Coatings Technology 94-95 (1997) 501-506.

322 Bereznai, M., Tóth, Z., Caricato, A.P., Fernández, M., Luches, A., Majni, G., Mengucci, P., Nagy, P.M., Juhász, A. & Nánai, L. Reactive pulsed laser deposition of thin molybdenum- and tungsten-nitride films. Thin Solid Films 473 (2005) 16-23.

323 He, Y. & Feng, J.Y. Diffusion barrier performances of direct current sputter-deposited Mo and Mo_xN films between Cu and Si. Journal of Crystal Growth 263 (2004) 203-207.

324 Inumaru, K., Baba, K. & Yamanaka, S. Preparation of superconducting molybdenum nitride MoN_x ($0.5 \leq x \leq 1$) films with controlled composition. Physica B 383 (2006) 84-85.

325 Inumaru, K., Baba, K. & Yamanaka, S. Synthesis and characterization of superconducting β-Mo_2N crystalline phase on a Si substrate: An application of pulsed laser deposition to nitride chemistry. Chemistry of Materials 17 (24) (2005) 5935-5940.

326 Roberson, S.L., Finello, D. & Davis, R.F. Synthesis of low oxygen concentration molybdenum nitride films. Materials Science and Engineering A 248 (1998) 198-205.

327 Wu, J.D., Wu, C.Z., Song, Z.M. & Li, F.M. Preparation of molybdenum nitrides by laser-promoted nitridation reaction. Thin Solid Films 311 (1997) 62-66.

328 Shen, L.-H., Cui, Q.-L., Zhang, J., Li, X.-F., Zhou, Q. & Zou, G.-T. A new method for preparation of nanocrystalline molybdenum nitride. Chinese Physics Letters 22 (12) (2005) 3192-3194.

329 Gulbransen, E.A., Andrew, K.F. & Brassart, F.A. Oxidation of molybdenum 550°C to 1700°C. Journal of The Electrochemical Society 110 (9) (1963) 952-959.

330 Lide, D.R. (ed.) CRC Handbook of chemistry and physics. USA: CRC Press, 1999. 80th edition. 2504 p. ISBN 978-0849304804.

331 Li, S. & Lee, J.S. Molybdenum nitride and carbide prepared from heteropolyacid – II. Hydrodenitrogenation of indole. Journal of Catalysis 173 (1998) 134-144.

332 Li, S. & Lee, J.S. Molybdenum nitride and carbide prepared from heteropolyacid – III. Hydrodesulfurization of benzothiophene. Journal of Catalysis 178 (1998) 119-136.

333 Ramanathan, S. & Oyama, S.T. New catalysts for hydroprocessing: transition metal carbides and nitrides. The Journal of Physical Chemistry 99 (1995) 16365-16372.

334 Zhaobin Wei, Z.B., Grange, P. & Delmon, B. XPS and XRD studies of fresh and sulfided Mo_2N. Applied Surface Science 135 (1998) 107-114.

335 Janssen, G.C.A.M., Tichelaar, F.D. & Visser, C.C.G. Stress gradients in CrN coatings. Journal of Applied Physics 100, 093512 (2006) 1-4.

336 Huang, C.-T. & Duh, J.-G. Stress and oxidation behaviours of r.f.-sputtered (Ti,Al)N films. Surface and Coatings Technology 81 (1996) 164-171.

337 Hultman, L. Thermal stability of nitride thin films – Review paper. Vacuum 57 (2000) 1-30.

338 Ylönen, M., Torkkeli, A. & Kattelus, H. In situ boron-doped LPCVD polysilicon with low tensile stress for MEMS applications. Sensors and Actuators A 109 (1-2) (2003) 79-87.

339 French, P.J. Polysilicon: a versatile material for microsystems. Sensors and Actuators A 99 (2002) 3-12.

340 Stoffel, A., Kovács, A., Kronast, W. & Müller, B. LPCVD against PECVD for micromechanical applications. Journal of Micromechanics and Microengineering 6 (1) (1996) 1-13.

341 Yao, Z., Stiglich, J. & Sudarshan, T.S. Molybdenum silicide based materials and their properties. Journal of Materials Engineering and Performance 8 (3) (1999) 291-304.

342 Petrovic, J.J. Mechanical behaviour of $MoSi_2$ and $MoSi_2$ composites. Materials Science and Engineering A192/193 (1995) 31-37.

343 Hawk, J.A., Alman, D.E. & Petrovic, J.J. Abrasive wear of Si_3N_4–$MoSi_2$ composites. Wear 203-204 (1997) 247-256.

344 Iizuka, T. & Kita, H. Oxidation mechanism of Mo_5Si_3 particle in Si_3N_4 matrix composite at 750°C. Materials Science and Engineering A 366 (2004) 10-16.

345 Natesan, K. & Deevi, S.C. Oxidation behaviour of molybdenum silicides and their composites. Intermetallics 8 (2000) 1147-1158.

346 Molarius, J.M.T., Suni, I., Laurila, T., Zeng, K., & Kivilahti, J.K. R.F.-sputtered tantalum-based diffusion barriers between copper and silicon. Superficies y Vacío 9 (1999) 206-209.

347 Oliver, W.C. & Pharr, G.M. Improved technique for determining hardness and elastic modulus using load and displacement sensing indentation experiments. Journal of Materials Research 7 (1992) 1564-1580.

348 Nevas, S., Manoocheri, F. & Ikonen, E. Gonioreflectometer measuring spectral diffuse reflectance. Applied Optics 43 (2004) 6391-6399.

349 Nix, W.D. Elastic and plastic properties of thin films on substrates: nanoindentation techniques. Materials Science and Engineering A234-236 (1997) 37-44.

350 Oliver, W.C. & Pharr, G.M. Measurement of hardness and elastic modulus by instrumented indentation: Advances in understanding and refinements to methology. Journal of Materials Research 19 (1) (2004) 3-20.

351 Schuh, C.A. Nanoindentation studies of materials. Materials Today 9 (5) (2006) 32-40.

352 Li, X. & Bhushan, B. A review of nanoindentation continuous stiffness measurement technique and its applications. Materials Characterization 48 (2002) 11-36.

353 Lee, K.-H. & Takai, O. Nanoindentation study on nanomechanical characteristics of a-CN film deposited by shielded arc ion plating. Diamond & Related Materials 14 (2005) 1444-1450.

354 Zheng, W.T., Sjöström, H., Ivanov, I., Xing, K.Z., Broitman, E., Salaneck, W.R., Greene, J.E. & Sundgren, J.-E. Reactive magnetron sputter deposited CN_x: Effects of N_2 pressure and growth temperature on film composition, bonding, and microstructure. Journal of Vacuum Science & Technology A 14 (5) (1996) 2696-2701.

355 Sun, Y., Bell, T. & Zheng, S. Finite element analysis of the critical ratio of coating thickness to indentation depth for coating property measurements by nanoindentation. Thin Solid Films 258 (1995) 198-204.

356 Xu, Z.-H. & Rowcliffe, D. Finite element analysis of substrate effects on indentation behaviour of thin films. Thin Solid Films 447-448 (2004) 399-405.

357 Chen, X. & Vlassak, J.J. Numerical study on the measurement of thin film mechanical properties by means of nanoindentation. Journal of Materials Research 16 (10) (2001) 2974-2982.

358 Zhang, T.-Y. & Xu, W.-H. Surface effects on nanoindentation. Journal of Materials Research 17 (7) (2002) 1715-1720.

359 Atuchin, V.V., Khasanov, T., Kochubey, V.A., Pokrovsky, L.D. & Senchenko, E.S. Negative dispersion in γ-Mo_2N/Si(100) films. Proceedings

of XII International Conference and Seminar EDM'2011, Section I. 30 June - 4 July 2011, Erlagol, Russia. IEEE (2011) 30-33.

360 Malitson, I.H. Interspecimen comparison of the refractive index of fused silica. Journal of the Optical Society of America 55 (10) (1965) 1205-1209.

361 Kischkat, J., Peters, S., Gruska, B., Semtsiv, M., Chashnikova, M., Klinkmüller, M., Fedosenko, O., Machulik, S., Aleksandrova, A., Monastyrskyi, G., Flores, Y. & Masselink, W.T. Mid-infrared optical properties of thin films of aluminum oxide, titanium dioxide, silicon dioxide, aluminum nitride, and silicon nitride. Applied Optics 51 (28) (2012) 6789-6798.

362 Ordal, M.A., Bell, R.J., Alexander, R.W., Long, L.L. & Querry, M.R. Optical properties of fourteen metals in the infrared and far infrared: Al, Co, Cu, Au, Fe, Pb, Mo, Ni, Pd, Pt, Ag, Ti, V, and W. Applied Optics 24 (24) (1985) 4493-4499.

363 Ordal, M.A., Bell, R.J., Alexander, R.W., Newquist, L.A. & Querry, M.R. Optical properties of Al, Fe, Ti, Ta, W, and Mo at submillimeter wavelengths. Applied Optics 27 (6) (1988) 1203-1209.

364 Rakic, A.D., Djurisic, A.B., Elazar, J.M. & Majewski, M.L. Optical properties of metallic films for vertical-cavity optoelectronic devices. Applied Optics 37 (22) (1998) 5271-5283.

365 Williams, K.R. & Muller, R.S. Etch rates for micromachining processing. Journal of Microelectromechanical Systems 5 (4) (1996) 256-269.

366 Williams, K.R., Gupta, K. & Wasilik, M. Etch rates for micromachining processing – Part II. Journal of Microelectromechanical Systems 12 (6) (2003) 761-778.

367 Kiihamäki, J., Dekker, J., Pekko, P., Kattelus, H., Sillanpää, T. & Mattila, T. "Plug-up" – a new concept for fabricating SOI MEMS devices. Microsystem Technologies 10 (2004) 346-350.

368 Rissanen, A., Blomberg, M. & Kattelus, H. Improved reproducibility in porous silica sol-gel processing using tertiary butanol solvent. Technical proceedings of the 2004 NSTI Nanotechnology Conference and Trade Show. Vol. 3 (2004) 366-369.

369 Golio, M. (ed.) Microwave and RF product applications. USA: CRC Press LLC, 2003. 1st edition. ISBN 0-8493-1732-0.

370 Lucyszyn, L. (ed.) Advanced RF MEMS. United Kingdom: Cambridge University Press, 2010. 1st edition. 412 p. ISBN 978-0-521-89771-6.

371 Aigner, R. MEMS in RF filter applications: Thin-film bulk acoustic wave technology. Wiley Interscience: Sensors Update 12 (2003) 175-210.

372 Gammel, P., Fischer, G. & Bouchaud, J. RF MEMS and NEMS technology, devices, and applications. Bell Labs Technical Journal 10 (3) (2005) 29-59.

373 Barker, N.S. & Rebeiz, G.M. Optimization of distributed MEMS transmission-line phase shifters – *U*-band and *W*-band designs. IEEE Transactions on Microwave Theory and Techniques 48 (11) (2000) 1957-1966.

374 Entesari, K. & Rebeiz, G.M. A differential 4-bit 6.5–10-GHz RF MEMS tunable filter. IEEE Transactions on Microwave Theory and Techniques 53 (3) (2005) 1103-1110.

375 Vähä-Heikkilä, T. & Rebeiz, G.M. A 4–18-GHz reconfigurable RF MEMS matching network for power amplifier applications. International Journal of RF and Microwave Computer-Aided Engineering 14 (4) (2004) 356-372.

376 Peroulis, D., Lu, Y. & Katehi, L.P.B. Highly reliable analog MEMS varactors. Microwave Symposium Digest, 2004 IEEE MTT-S International. Vol. 2 (2004) 869-872.

377 Shah, U., Decrossas, E., Jung-Kubiak, C., Reck, T., Chattopadhyay, G., Mehdi, I. & Oberhammer, J. 500-600 GHz submillimeter-wave 3.3 bit RF MEMS phase shifter integrated in micromachined waveguide. Proceedings of 2015 IEEE MTT-S International Microwave Symposium. IEEE (2015) 4 pp.

378 Shah, U., Decrossas, E., Jung-Kubiak, C., Reck, T., Chattopadhyay, G., Mehdi, I. & Oberhammer, J. Submillimeter-wave 3.3-bit RF MEMS phase shifter integrated in micromachined waveguide. IEEE Transactions on Terahertz Science and Technology 6 (5) (2016) 706-715.

379 Wolffenbuttel, R.F. MEMS-based optical mini- and microspectrometers for the visible and infrared spectral range. Journal of Micromechanics and Microengineering 15 (2005) S145-S152.

380 Graf, A., Arndt, M., Sauer, M. & Gerlach, G. Review of micromachined thermopiles for infrared detection. Measurement Science & Technology 18 (2007) R59-R75.

381 Liddiard, K.C. Application of interferometric enhancement to self-absorbing thin film thermal IR detectors. Infrared Physics 34 (4) (1993) 379-387.

382 Bauer, S., Bauer-Gogonea, S., Becker, W., Fettig, R., Ploss, B., Ruppel, W. & von Münch, W. Thin metal films as absorbers for infrared sensors. Sensors and Actuators A 37-38 (1993) 497-501.

383 Advena, D.J., Bly, V.T. & Cox, J.T. Deposition and characterisation of far-infrared absorbing gold black films. Applied Optics 32 (7) (1993) 1136-1144.

384 Nelms, N. & Dowson, J. Goldblack coating for thermal infrared sensors. Sensors and Actuators A 120 (2005) 403-407.

385 Lenggenhager, R., Baltes, H., Peer, J. & Forster, M. Thermoelectric infrared sensors by CMOS technology. IEEE Electron Device Letters 13 (9) (1992) 454-456.

386 Schneeberger, N., Paul, O. & Baltes, H. Optimized structured absorbers for CMOS infrared detectors. Proceedings of The 8th International Conference on Solid-State Sensors and Actuators, and Eurosensors IX. 25-29 June 1995, Stockholm, Sweden (1995) 648-651.

387 Roncaglia, A., Mancarella, F. & Cardinali, G.C. CMOS-compatible fabrication of thermopiles with high sensitivity in the 3-5 μm atmospheric window. Sensors and Actuators B 125 (2007) 214-223.

388 Blomberg, M. & Lehto, A. A thin film blackbody structure. Proceedings of Eurosensors XIV. 14th European Conference on Solid-State Transducers. 27-30 August 2000, Copenhagen, Denmark (2000) 301-302.

389 Fonseca, L., Santander, J., Rubio, R., Sabaté, N., Figueras, E., Duch, M., Gràcia, I. & Cané, C. Use of boron heavily doped silicon slabs for gas sensors based on free-standing membranes. Sensors and Actuators B 130 (2008) 538-545.

390 Puurunen, R.L. Surface chemistry of atomic layer deposition: A case study for the trimethylaluminum/water process. Journal of Applied Physics 97 (12) (2005) 1-52.

391 Dekker, J., Kolari, K. & Puurunen, R.L. Inductively coupled plasma etching of amorphous Al_2O_3 and TiO_2 mask layers by atomic layer deposition. Journal of Vacuum Science & Technology B 24 (5) (2006) 2350-2355.

392 Schmidt, J.-U., Knobbe, J., Gehner, A. & Lakner, H. CMOS integrable micro mirrors with highly improved drift-stability. Proceedings of MOEMS-MEMS 2007 Micro and Nanofabrication. SPIE (2007) 64670R, 11 pp.

393 Schmidt, J.-U., Friedrichs, M. & Gehner, A. Amorphous TiAl films for micromirror arrays with stable analog deflection integrated on complementary metal oxide semiconductors. Journal of Micro/Nanolithography, MEMS, and MOEMS 7 (2) (2008) 021012.

394 Lin, Y.-C., Tsai, Y.-C., Ono, T., Liu, P., Esashi, M., Gessner, T. & Chen, M. Metallic glass as a mechanical material for microscanners. Advanced Functional Materials 25 (35) (2015) 5677-5682.

395 Heo, N., Lee, J., Shin, H., Yoo, J. & Kim, D. Inverse design of the absorbing layer for detection enhancement in near-infrared range. Optics Express 21 (20) (2013) 23220-23230.

396 Ma, W., Wang, S., Wen, Y., Zhao, Y., Dong, L. & Yu, X. Uncooled focal plane array for multiband IR imaging using optical-readout bimaterial cantilevers. Journal of Microelectromechanical Systems 24 (3) 582-591.

397 Ma, W., Jia, D., Wen, Y., Yu, X., Feng, Y. & Zhao, Y. Diode-based microbolometer with performance enhanced by broadband metamaterial absorber. Optics Letters 41 (13) (2016) 2974-2977.

398 Oishi, K., Yonemaru, S., Akai, D. & Ishida, M. SiO_2/SiN multilayer-stack infrared absorber integrated on $Pb(Zr_{0.4},Ti_{0.6})O_3$ film pyroelectric sensors on γ-Al_2O_3/Si substrate. Sensors and Materials 27 (2) (2015) 217-227.

399 Czarnecki, P. Impact of charging mechanisms on the reliability of RF MEMS devices. Dissertation. Belgium: Katholieke Universiteit Leuven, Faculty of Engineering, 2010.

400 Debogovic, T. & Perruisseau-Carrier, J. MEMS-reconfigurable metamaterials and antenna applications. International Journal of Antennas and Propagation. Article ID 138138 (2014) 8 pp.

401 Dietlein, C.R., Hedden, A.S. & Wikner, D.A. Digital reflectarray considerations for terrestrial millimeter-wave imaging. IEEE Antennas and Wireless Propagation Letters 11 (2012) 272-275.

402 Du, Y., Su, W., Li, X., Huang, Y. & Bao, J. A novel MEMS distributed phase shifter for D-band application. 2016 IEEE International Conference on Microwave and Millimeter Wave Technology (ICMMT), vol. 1. IEEE (2016) 542-544.

403 Fall, M., Fouladi, S., Domingue, F., Dieppedale, C., Reig, B. & Mansour, R.R. High capacitance ratio RF MEMS dielectric-less switched capacitor. Proceedings of the 8th European Microwave Integrated Circuits Conference. 6-8 October 2013, Nuremberg, Germany (2013) 356-359.

404 Ghavanini, F.A., Enokssen, P., Bengtsson, S. & Lundgren, P. Vertically aligned carbon based varactors. Journal of Applied Physics 110 (2011) 021101, 14 pp.

405 Hedden, A.S., Dietlein, C.R. & Wikner, D.A. A 220 GHz reflection-type phased array concept study. Proceedings of Passive Millimeter-Wave Imaging Technology XIV. SPIE Defense, Security, and Sensing. International Society for Optics and Photonics 8022 (2011) 802220N, 12 pp.

406 Hedden, A.S., Dietlein, C.R. & Wikner, D.A. Millimeter-wave electronically scanned reflectarray optimization and analysis. Proceedings of Passive and Active Millimeter-Wave Imaging XV. SPIE Defense, Security, and Sensing. International Society for Optics and Photonics 8362 (2012) 836203, 7 pp.

407 Malmqvist, R., Gustafsson, A., Nilsson, T., Samuelsson, C., Carlegrim, B., Ferrer, I., Vähä-Heikkilä, T., Ouacha, A. & Erickson, R. RF MEMS and GaAs based reconfigurable RF front-end components for wide-band multifunctional phased arrays. Proceedings of the 3rd European Radar Conference. September 2006, Manchester, United Kingdom. IEEE (2006) 319-322.

408 Ouacha, A., Erickson, R. & Malmqvist, R. Technology for ultra broadband reconfigurable beamformer and front-end. Proceedings of the 4th European Radar Conference. October 2007, Munich, Germany. IEEE (2007) 150-153.

409 Perruisseau-Carrier, J. Microwave periodic structures based on micro-electromechanical systems (MEMS) and micromachining techniques. Dissertation. Switzerland: École Polytechnique Fédérale de Lausanne (EPFL), 2007.

410 Perruisseau-Carrier, J. & Skrivervik, A.K. Monolithic MEMS-based reflect-array cell digitally reconfigurable over a 360° phase range. IEEE Antennas and Wireless Propagation Letters 7 (2008) 138-141.

411 Ruan, J.J. Investigation and modeling of the impact of electrostatic discharges on capacitive RF MEMS switches. Dissertation. France: Université de Toulouse, 2010.

Microelectromechanical systems (MEMS) are often based on silicon technology. This thesis studies two molybdenum-based thin films, amorphous Mo-N and Mo-Si-N deposited by reactive sputtering, for an alternative material choice for surface micromachining.

Aalto-DD 23/2017
VTT SCIENCE 147

ISBN 978-952-60-7289-0 (printed)
ISBN 978-952-60-7288-3 (pdf)
ISSN-L 1799-4934
ISSN 1799-4934 (printed)
ISSN 1799-4942 (pdf)

978-951-38-8512-0 (printed)
978-951-38-8509-0 (pdf)
2242-119X
2242-119X (printed)
2242-1203 (pdf)

Aalto University
School of Electrical Engineering
Department of Electronics and Nanoengineering
www.aalto.fi

BUSINESS +
ECONOMY

ART +
DESIGN +
ARCHITECTURE

SCIENCE +
TECHNOLOGY

CROSSOVER

DOCTORAL
DISSERTATIONS